Using Metabolic Medical Imaging to Model Tumour Growth and Response to Therapy



Thaís Soleimani Roque

Supervisors: Prof. Michael Chappell and Prof. Julia Schnabel

Magdalen College

University of Oxford

A thesis submitted for the degree of

Doctor of Philosophy in Engineering Science

June 22, 2018

I would like to dedicate this thesis to my mother, Maria, who has always believed in me, loved me unconditionally and encouraged me to walk on my own feet while always being there to hold my hand. And to my loving, wonderful, and understanding husband, Vinicius, who has been a constant source of support, strength and encouragement during the challenges of this dissertation: I am truly thankful for having you in my life.

This thesis is also for the person, who, without even knowing, inspired me to take the final steps towards completion of this thesis: my son, Arthur. I can't wait to hold your hands.

This thesis is written in memory of Prof. Brian Bellhouse.

Acknowledgements

They say it takes a village to raise a child. I feel like the same applies to completing a PhD - and it is a pretty big village.

I am thankful to my supervisors, Prof. Julia Schnabel and Prof. Michael Chappell, for their guidance and wisdom. From the planning to the writing phase, they nurtured and challenged the scientist in me, always generous with their time, attention and trust. They were key in setting up the collaboration with the Preclinical Imaging Group from the Oxford Institute for Radiation Oncology: thank you for providing me with the foundational data of this thesis.

I am also thankful to Dr. Laurent Risser, who showed me that besides great cheese and wine, France is also a country of brilliant mathematicians and extremely kind and thoughtful people: mille mercis.

And because brilliance is not a french monopoly, I would also like to thank Prof. Waldemar Zylka, whom I count as my long-standing mentor and friend. He is at the origin of my interest in modelling patient-specific tumour growth, back in my Gelsenkirchen days.

The road to this thesis is filled with generous benefactors, both public and private. The *Studienstiftung des Deutschen Volkes* and the Sloane and Robinson scholarship supported me on the MSc in Biomedical Engineering, a key step toward my DPhil. The Oxford-Bellhouse Graduate Scholarship along with EPSRC not only financed my DPhil, but also allowed me to join Magdalen College. At Magdalen I found not just a home, but a major support network: porters, caterers, librarians, bursar, deans - they were always there for me.

My village cuts across several time zones. I thank the friends and family who cheered me forward from places as exotic as Arujá, Caruaru, Recife, Vargem Grande do Sul, São Paulo, Lübbecke, Paris and of course, the most exotic place in the world, Oxford. A special thanks to my lab partners in crime Flora, João, Ana, Johanna, Adam and Jola. Only you guys know what we have been through.

Last but not least, I would not have gotten here without the daily dose of love and encouragement from my ever-so-present mother, my ever-so-loving husband, my ever-so-purring B & B, and, for the last six months, my ever-so-kicking baby. Every kick from within pushed me a step further. You are the most effective deadline.

Abstract

The number of cancer related deaths is predicted to reach over 13.1 million in 2030 [1]. Understanding the spatio-temporal evolution of tumours and their response to therapy is crucial to thwart this gloomy prognosis. Mathematical models have been used to elucidate the biological processes involved in tumour growth, but their complexity severely limits their clinical value. Effective models should base predictions on patient-specific data that can be obtained and tested in the clinic.

This thesis aims to develop novel clinically-relevant methodologies to model solid tumour growth and reaction to therapy. Models are developed that predict the macroscopic tumour evolution as a result of complex biological processes happening at the microscopic scale (such as cell proliferation, hypoxia, necrosis and oxygenation) while retaining simplicity in terms of the number of parameters that require calibration. This facilitates integration of medical imaging-derived tumour descriptor maps (e.g. for cellularity and nutrient availability) to initialise, calibrate and verify the models.

In addition to the models themselves, this thesis contributes to the literature by introducing novel frameworks to 1) derive maps of proliferative, hypoxic and necrotic cells using only Dynamic Contrast Enhanced Magnetic Resonance Imaging data; 2) apply these maps to constrain the models and obtain subject-specific predictions of tumour evolution; 3) account for tumour vascularisation, focusing on the angiogenesis-driven macroscopic changes observed longitudinally on medical imaging scans; and 4) produce a proof-of-concept updated model that could support medical decision in the treatment and management of cancer patients.

The results demonstrate the feasibility of using information derived from imaging data to quantify and predict subject-specific global and local tumour evolution and reaction to therapy. Experimentally validated comparison between model predictions and tumour imaging data obtained at later time points of the tumours' evolution show noticeable improvements in prediction accuracy, model complexity and clinical value over state-of-the-art methods. Nevertheless, additional imaging information on complementary aspects of tumour growth and response to therapy could render our models even more relevant to clinical practice.

Contents

Contents iv

List of Figures viii

List of Abbreviations xi

1 Introduction 1

1.1 Motivation 1

1.2 Mathematical models 2

1.3 Integration of medical imaging data into models of tumour growth 4

1.4 Scientific contributions and thesis outline 5

2 Literature Review 9

2.1 The hallmarks of cancer 9

2.2 Medical imaging of tumours 13

2.2.1 PET and SPECT 14

2.2.2 CT 16

2.2.3 MRI 17

2.3 Cancer therapy 32

2.3.1 Radiotherapy 33

2.3.2 Chemotherapy 37

2.3.3 Anti-angiogenic therapy 39

2.4 Imaging-based models of tumour growth 41
2.4.1 Single-scale models of tumour growth 42
2.4.2 Dual-scale models of tumour growth 46
2.4.3 Multi-scale models of tumour growth 47
2.5 Models of tumour reaction to therapy 50
2.5.1 Modelling the effect of radiotherapy 51
2.5.2 Modelling the effect of chemotherapy 56
2.5.3 Modelling the effect of anti-angiogenic therapy 59
2.6 Conclusions 60

3 3-D Model of Tumour Growth 63

3.1 Methods 64
3.1.1 Tumour growth model 64
3.1.2 Numerical implementation 73
3.1.2.1 Continuous model 73
3.1.2.2 Discrete model 74
3.1.2.3 Alternating Direction Implicit scheme 76
3.1.3 Input and parameter maps 79
3.1.4 Analysis of tumour-specific parameters 80
3.2 Experiments 85
3.2.1 Sensitivity analysis 85
3.2.2 Relationship between SGR and model parameters 86
3.2.3 Simulations 87
3.3 Results 88
3.3.1 Sensitivity analysis 88
3.3.2 Relationship between SGR and model parameters 89
3.3.3 Simulations 91
3.4 Discussion and Conclusions 98

4 Integration of Medical Imaging Data into the Tumour Growth Model 101

4.1 Methods . . . 103

4.1.1 Overview of the method . . . 104

4.1.2 DCE-MRI data to physiological parameters . . . 104

4.1.3 Cellularity maps and related maps . . . 109

4.1.4 Estimation of model parameters . . . 111

4.1.5 Predicting the tumour spatio-temporal growth . . . 112

4.2 Experiments . . . 113

4.2.1 Synthetic data . . . 113

4.2.2 Pre-clinical data . . . 115

4.3 Results . . . 116

4.3.1 Synthetic data . . . 116

4.3.2 Pre-clinical data . . . 118

4.3.3 Cellular evolution simulations . . . 122

4.3.4 3-D growth simulations . . . 123

4.4 Discussion and Conclusions . . . 135

5 3-D Model of Vascular Tumour Growth 140

5.1 Methods . . . 142

5.1.1 Model of vascular tumour growth . . . 143

5.1.2 Estimation of tumour-specific parameters . . . 149

5.1.3 Experiments . . . 150

5.2 Results . . . 152

5.2.1 Sensitivity analysis and parameter optimisation . . . 152

5.2.2 Synthetic data . . . 155

5.2.3 Pre-clinical data . . . 158

5.3 Discussion and Conclusions . . . 171

6 3-D Model of Tumour Response to Therapy 176

6.1 Methods 180

6.1.1 Radiation effect 180

6.1.2 Isoeffective radiotherapy schedules 181

6.1.3 Anti-angiogenic therapy 184

6.1.4 Adding therapy to the model of tumour growth 184

6.2 Experiments 192

6.2.1 Effect of Avastin on treatment outcome 193

6.2.2 Effect of fractionation on radiotherapy outcome 193

6.3 Results 196

6.3.1 Effect of Avastin on treatment outcome 196

6.3.2 Effect of fractionation on radiotherapy outcome 200

6.4 Discussion and Conclusions 203

7 Conclusions and Future Work 208

7.1 Conclusions 208

7.2 Future Work 211

References 221

List of Figures

2.1 The hallmarks of cancer 12
2.2 Fractionation effect on the fraction of surviving cells. 36

3.1 Framework of the multi-scale model of avascular tumour growth . 65
3.2 Schematic diagram of the numerical implementation approach . . 73
3.3 Example of input and parameter maps 79
3.4 The cell cycle 80
3.5 Proliferation rate as a function of the nutrient level 82
3.6 Hypoxic rate as a function of the nutrient level 83
3.7 Hypoxic and necrotic rates as a function of pO_2 84
3.8 Relationship between the diffusion constant and SGR 90
3.9 Effect of apoptosis on tumour volume evolution 92
3.10 Effect of apoptosis on tumour cell number evolution 96
3.11 Simulated tumour cell maps for synthetic cases 97

4.1 Flowchart of a model constrained by data derived from DCE-MRI 105
4.2 Model calibration and verification pipeline 112
4.3 Mean volume and Dice overlap errors 117
4.4 Mean cellularity evolution for the synthetic data 119
4.5 Mean cellularity evolution for the pre-clinical data 121
4.6 Mean DSC overlap. 123
4.7 Mean percent volume error. 124
4.8 True and estimated cell distributions for Case 1. 128
4.9 True and estimated proliferative cell distributions for Case 1. . . . 129
4.10 True and estimated hypoxic cell distributions for Case 1. 130
4.11 True and estimated necrotic cell distributions for Case 1. 131
4.12 True and estimated cell distributions for Case 2. 132
4.13 True and estimated cell distributions for Case 4. 133
4.14 True and estimated cell distributions for Case 6. 134

5.1 Flowchart of a model of vascular tumour growth constrained by data derived from DCE-MRI 143
5.2 Relationship between the diffusion constant and the specific growth rate for the model of vascular tumour growth 153

5.3 Proliferation, hypoxia and necrosis rates as a function of distribution volume . . . 155
5.4 Mean percent volume and DICE error for synthetic data. 156
5.5 Mean cellularity evolution for the synthetic data. 157
5.6 Mean cellularity evolution for the pre-clinical data. 160
5.7 Mean percent volume and DICE error for real data. 161
5.8 True and estimated cell distributions for Case 1 164
5.9 True and estimated proliferative cell distributions for Case 1 . . . 165
5.10 True and estimated hypoxic cell distributions for Case 1 166
5.11 True and estimated necrotic cell distributions for Case 1 167
5.12 True and estimated cell distributions for Case 4 168
5.13 True and estimated cell distributions for Case 6 169
5.14 Comparison between avascular and vascular models for Case 10 . 170

6.1 Model of vascular tumour growth and reaction to therapy 185
6.2 Two-compartment model 186
6.3 Combined treatment schedule 194
6.4 Effect of combined anti-angiogenic and radiotherapy schedule on cellularity evolution 198
6.5 Effect of combined anti-angiogenic and radiotherapy schedule on volume and hypoxia evolution 199
6.6 Effect of fractionated therapy on tumour cellularity evolution . . . 201
6.7 Effect of different α/β-ratios on therapy outcome 202

List of Abbreviations

DSC	Dice similarity coefficient
T_1	Longitudinal relaxation time
T_2	Transverse relaxation time
ADC	Apparent diffusion coefficient
AIF	Arterial input function
AUC	Area under the curve
CA	Contrast agent
CSF	Cerebrospinal fluid
CT	Computed Tomography
DCE	Dynamic contrast enhanced
DTI	Diffusion tensor Imaging
DWI	Diffusion weighted MRI
EC	Endothelial cell
EES	Extracellular-extravascular space
eFAST	Extended Fourier Amplitude Sensitivity Test

FA	Flip angle
FDG-PET	Fludeoxyglucose positron emission tomography
FDG-PET	Fluorodeoxyglucose-PET
FMISO-PET	Fluoromisonidazole positron emission tomography
GBM	Glioblastoma multiforma
LQ-model	Linear Quadratic model
MRI	Magnetic resonance imaging
MTT	Mean transit time
PDE	Partial differential equation
PET	Positron emission tomography
PK	Pharmacokinetic
RF	Radio frequency
RT	Radiotherapy
SGR	Specific growth rate
SPECT	Single photon emission computed tomography
TAF	Tumour angiogenic factor
TE	Echo time
TR	Repetition time
VEGF	Vascular endothelial growth factor

Chapter 1

Introduction

1.1 Motivation

Cancer is a leading cause of death worldwide. Globally, cancer was responsible for 8.8 million deaths in 2015 [1]. The World Health Organization has predicted that this number will reach over 13.1 million in 2030. Cancers of lung, liver, colon, stomach and breast account for the highest number of cancer deaths. The economic impact of cancer is significant and increasing, with an associated total annual economic cost in 2010 estimated at approximately US$ 1.16 trillion [2]. It is estimated that investing in prevention, early detection, and treatment strategies has the potential to save up to 3.7 million lives every year, resulting in an economic benefit of more than US$ 400 billion [3].

Considerable advances in understanding and identifying causes of cancer and developing treatment strategies have been achieved in the past decades. Nevertheless, the prospect of a cure remains a vision in the face of a tough and evasive adversary: the term cancer is used to define a group of more than 200 diseases that can affect any part of the body. At its most basic level, the term cancer

can be used to describe uncontrolled growth and spread of abnormal cells in the body.

In the landmark paper *The Hallmarks of Cancer*, the authors identify six requirements for the progression of this disease: self-sufficiency in growth signals, insensitivity to anti-growth signals, evasion of apoptosis, limitless replicative potential, sustained angiogenesis, and tissue invasion and metastasis [4]. In that sense, cancer can be seen as a progressive, multistep transformation process that incorporates biological changes happening at different spatial and temporal scales.

Knowledge of the biological changes involved in cancer progression has enabled the development of cancer treatments targeting each of the disturbed biological processes. Cancer treatments involve, but are not limited to, surgery, radiation therapy, chemotherapy, immunotherapy and targeted therapy. Most patients receive a combination of treatments, normally chemo- and/or radiotherapy for tumour downsizing, followed by surgery. Understanding of how different therapeutic schemes affect the spatio-temporal tumour evolution is a crucial precondition to successful tumour treatment.

1.2 Mathematical models

Mathematical models of tumour growth and reaction to therapy have emerged as a valuable tool to explore the interplay of the biological changes mentioned previously and potentially support medical decision in the treatment and management of cancer patients. Broadly speaking, these models can be divided into three categories depending on their choice of scale: microscopic, macroscopic and multi-scale.

The first category describes the evolution of each tumour cell by different biologi-

cal functions and activities to elucidate the microscopic aspect of tumour growth. Models can range from simple exponential, logistic and Gompertzian growth laws to elaborate systems of partial differential equations describing the growth of a tumour and its invasion into the surrounding tissue [5, 6, 7, 8]. Their focus resides in describing the evolution of each cell described by different biological functions and activities to elucidate the microscopic aspect of the tumour growth [9].

The second category includes continuum models that describe tumour growth at the macroscopic level. The majority of the current macroscopic models of tumour growth have been applied to the case of glioma growth[10, 11, 12, 13, 14, 15, 16, 17]. Formulated based on Murray's reaction-diffusion formalism [18], they describe the temporal evolution of tumour cell densities at different locations through diffusion and proliferation of cells.

Most recently, a third category, called multi-scale modelling, has emerged as an attempt to incorporate biological processes across a range of physical scales of a tumour into the model framework [19, 20, 21]. The advantage of such approaches is that by describing macroscopic tumour evolution as a result of the underlying phenomena happening at the cellular and sub-cellular scales, they consider the progressive, multistep, multi-scale aspect of tumour evolution. While multi-scale modelling is a promising development, it relies on information across the different scales, that are normally hard to obtain.

Recent advances in non-invasive biomedical imaging techniques offer a potential solution. They can report on the anatomy of bulk tumour and volume, as well as be used to extract quantitative measures of, for instance, tumour vascularity, perfusion, metabolism, hypoxia, cell density and proliferation. Using these quantitative measures extracted from images, which are normally generated with a resolution of around 0.5-5 mm, directly provides data to inform the larger

lenght-scales within multi-scale models. This perspective might ultimately lead to patient-specific predictions of tumour growth and response to therapy.

1.3 Integration of medical imaging data into models of tumour growth

The promising perspective of achieving patient-specific predictions of tumour growth and reaction to therapy has motivated a number of groups to explore the concept of integrating quantitative measures derived from medical imaging into mathematical models of tumour growth.

Most of the existing works focus on the macroscopic scale and take into account information from clinical MR imaging to delineate the tumour boundaries, to extract anatomical information and to estimate the cell density. However, by treating the tumour growth globally, they tend to neglect the metabolic heterogeneity found in all cancer types [10, 12, 22, 23].

Some existing work succeeded in incorporating functional and metabolic information derived from PET scans into a multiscale approach, but they do not include any deformation or expansion happening at the macroscopic level [19, 20]. Their clinical application is therefore limited, since information on the macroscopic evolution of the tumour is crucial to therapy planning.

Ideally, one would aim at the combination of anatomical, functional and metabolic information from clinical imaging data with a multi-scale approach to feed information to both the cellular and macroscopic scales, thereby modelling the tumour as a living system. A few studies were able to demonstrate to some degree the feasibility of parameterising a multi-scale model of tumour growth using informa-

tion from different medical imaging modalities (e.g. CT, MRI, PET). However, their patient-specific prediction ability remains limited due to the complexity of the developed approach [24, 21, 25]; or due to missing data [26, 27]. The latter is especially true for approaches depending on information from many imaging modalities, which might not all be available for each patient. Moreover, the need for multi-modal imaging data may lead to errors arising from the spatial co-localisation as well as from the spatial resolution disparity.

To avoid the problems associated with the need for multi-modal imaging and hence the potential lack of subject-specific data, in this thesis we propose to derive all information needed to constrain a model of tumour growth and response to therapy from a single imaging modality. This modality needs to be able to provide anatomic information (ideally 3D) while allowing for richer information on microscopic phenomena to be extracted. We choose Dynamic Contrast-Enhancement (DCE) magnetic resonance imaging (MRI), which additionally to the anatomic MRI information enables the extraction of physiological parameters related to vessel permeability, blood flow, and tissue volume fractions [28]. It has previously been shown that DCE-MRI has the potential to predict therapeutic response at the cellular level [29] and to assess tumour pathophysiology by estimation of tumour cellularity [30, 23].

1.4 Scientific contributions and thesis outline

This thesis aims to develop new methodologies to model solid tumour growth and response to therapy as well as to provide a framework for the integration of biological information extracted from medical anatomic and metabolic imaging. These methodologies are of great clinical interest, as they can integrate and

quantify the various processes involved in tumour growth; but more importantly, they have the potential to enable the prediction of therapeutic outcomes for each patient.

This work makes five key scientific contributions:

1. We introduce models of tumour growth that are able to account for complex microscopic biological processes while retaining simplicity in terms of the number of parameters that require calibration. As such, these models predict the 3-D macroscopic invasion of the tumour in the host tissue whilst evaluating how each cell group (proliferative, hypoxic and necrotic) contributes to tumour evolution;

2. We develop and introduce a novel way of interpreting DCE-MRI images in terms of tumour descriptors which can be used among other things to constrain models of tumour growth and reaction to therapy;

3. We present and demonstrate how maps of cellularity extracted from medical imaging can be used to feed and calibrate our models to obtain subject-specific predictions of tumour evolution;

4. We introduce a novel model of vascular tumour growth that accounts for vascularisation in an indirect yet pragmatic way: rather than following the migration of each endothelial cell as a response to excretion and diffusion of growth factors, we focus on the macroscopic changes resulting from angiogenesis that can be observed longitudinally on medical imaging scans;

5. We present a method to use our models to explore different schedules and dosing of radiotherapy, to study the effect of anti-angiogenenic therapy on radiation therapy outcome and to determine the most effective dose-scheduling of both treatment modalities.

This thesis is structured as follows. In Chapter 2, we provide the necessary background on topics of relevance to the thesis including 1) biological processes involved in tumour progression and reaction to therapy; 2) the role of different therapies in the management of cancer; 3) the main medical imaging modalities used in the diagnosis and management of cancer, and the information that they can provide on cancer; 4) the state-of-art computational models of tumour growth and reaction to therapy parameterised by medical imaging information.

With the aim of taking a step in the direction of patient-specific modelling of tumour growth, in Chapter 3 we develop and present a subject-specific model of tumour growth based on a set of partial differential equations (PDEs), which allows for the inclusion of anatomical information as well as of different biological activities (proliferation, hypoxia and necrosis) extracted from medical imaging. We also provide the computer implementation used to solve the model equations. A sensitivity analysis of the parameters and a closer examination of each model parameter are also included to allow for a more informed choice about whether and what parameters should be optimised.

In Chapter 4 we use a set of medical images to parameterise the model developed in Chapter 3. The model, which could be driven by any data able to derive cellularity and nutrient maps, is calibrated using a set of longitudinal DCE-MR images of preclinical breast carcinoma. To allow for this calibration, we present a novel method to extract maps of tumour descriptors (such as the number of proliferative, hypoxic and necrotic cells) from DCE-MRI. Our aim is to examine whether the model is able to predict the local and global cell density for different cell sub-populations (proliferative, hypoxic and necrotic), as well as the 3-D macroscopic invasion of the avascular tumour in the host tissue at later time points.

In Chapter 5, the model presented in Chapter 3 and tested in Chapter 4 is extended to account for the effect of angiogenesis on tumour growth. We start off by presenting the model along with its assumptions and the updated model equations. The same methodology in terms of estimation and prediction of tumour-specific parameters is applied to the updated model. Experiments on synthetic and on the same pre-clinical data set used in Chapter 4 are included to allow for comparison between the results obtained with both models.

In Chapter 6, we turn to the clinical application of our work, and introduce an extension of the vascular model introduced in Chapter 5 to investigate the dynamic process of tumour growth and angiogenesis in response to anti-angiogenic therapy and radiotherapy. We choose this model due to its ability to predict vascular tumour growth at a macroscopic level while accounting for processes like proliferation, death and spread of tumour cells, as well as angiogenesis. We include a set of simulations to inspect the effects of hypoxia, anti-angiogenic drugs and fractionated therapy on the response of tumour growth to radiotherapy, and compare our results with behaviours observed in preclinical and clinical studies.

Finally, in Chapter 7, we present our conclusions and discuss the main results of this thesis. We depict possible ways of overcoming limitations of the current methodologies. We suggest some avenues that could be explored, in the hope that our models can become even more relevant to clinical practice and realise their full potential in enabling the prediction of outcomes, and aiding the selection and development of therapy schedules.

Chapter 2

Literature Review

The aim of this chapter is to provide background and context for this work and an introduction to topics of relevance to this thesis. This includes 1) the biological processes involved in tumour progression; 2) a description of the main imaging modalities used to obtain information on these processes, and which are used to manage and treat cancer patients; 3) the role of radio-, chemo- and anti-angiogenic therapy in the management of cancer patients; 4) an overview of contributions to the field of medical imaging based models of tumour growth; and 5) examples of how these models have been expanded to predict the effect of therapy (radio-, chemo- and anti-angiogenic therapy) on tumour growth.

2.1 The hallmarks of cancer

Cancer is a leading cause of morbidity and mortality worldwide, with 8.8 million deaths in 2015 [1]. Moreover, the global cancer burden is expected to exceed 20 million new cancer cases annually by 2025 [2].

The term cancer is used to define a group of more than 100 diseases that can

affect any part of the body. In their landmark paper *The Hallmarks of Cancer*, Hanahan and Weinberg suggest that most types of human cancer share six essential alterations in cell physiology leading to the progressive conversion of normal cells into invasive cancer: self-sufficiency in growth signals, insensitivity to anti-growth signals, evasion of apoptosis, limitless replicative potential, sustained angiogenesis, and tissue invasion and metastasis [4]. These researchers published an updated article, in which they added reprogramming of energy metabolism and evading immune destruction as new emerging hallmarks of cancer [31]. The authors referred to these two hallmarks as emerging because neither of them has been validated. We therefore focus on the original six hallmarks (shown in Fig. 2.1) and subdivide them depending on which spatial scale they can be observed:

The sub-cellular scale: In normal tissue, the progression of a cell from an inactive quiescent state into an active proliferative state depends on mitogenic growth signals (GS) coming from the normal tissue microenvironment. Receptors present on the cell membrane bind these signals and transmit them to genes present in the cell nucleus to regulate the cell evolution. Cancerous cells are able to generate their own signals, which results in a disruption of the homeostatic mechanism needed to ensure an equilibrium between cell proliferation and cell death that preserves the architecture and functionality of the tissue.

Another mechanism responsible for the control of cellular inactivity and for the maintenance of tissue homeostasis is the expression of anti-proliferative signals. Cancer cells are able to circumvent this mechanism by interrupting the signalling circuit necessary to govern the transit of the cell from a proliferative to a quiescent or post-mitotic state. This disruption, known as the tumour suppression loss in cancer, can be observed in a majority of human cancers [4].

The cellular scale: The signals emitted at the sub-cellular scale are not only necessary to regulate cell growth or anti-growth, but also cell proliferation and death, which become evident at a cellular scale. Programmed cell death (apoptosis) is a further mechanism necessary to ensure tissue homeostasis. Tumoural cells acquire the capability to evade apoptosis, which, along with their growth signal autonomy and insensitivity to antigrowth signals, results in a deregulated proliferation programme independent of signals present in the microenvironment [4]. However, this disruption of cell-to-cell signalling alone does not ensure expansive tumour growth. It takes the acquisition of the fourth capability, the limitless replicative potential, in order for a clone of cells to form a tumour of a size visible at the macroscopic scale.

The tissue scale: The gain-of-function mutation in oncogenes and the loss-of-function mutation in tumour suppressor genes described earlier only lead to a self-limited, avascular tumour growth. This is because the growth of tumour cells is limited by substrate availability resulting from cellular proliferation, which in turn depends on nutrients available in the microenvironment of the cells. When the avascular tumour exceeds a critical diameter of a few milimeters, the normal host tissue vasculature is no longer able to support its growth. Consequently, tumour cells lacking oxygen become hypoxic and, as a response, secrete a number of diffusible chemical substances, called tumour angiogenic factors (TAFs), into the surrounding tissue. These substances diffuse into the host tissue and eventually reach endothelial cells (ECs) from surrounding blood vessels, which respond to the TAF gradient by migrating towards the tumour. After some days, the growing tumoural network is linked to the parent vessel, so that this vascular connection is able to provide all the nutrients and oxygen needed for continued tumour progression. This process, known as angiogenesis, is crucial for tumour growth

and progression.

The newly acquired tumour vasculature is known to be tortuous and chaotic, resulting in unbalanced blood supply and, consequently, in perfusion heterogeneities. As a result, many regions within the tumour become hypoxic, resulting in further tumour progression [32].

During the last step of their development, cancer cells acquire the ability to escape the primary tumour mass, invade adjacent tissues and travel to distant sites (metastasis) where they may succeed in forming a new tumour mass. The successful invasion and metastasis depend upon the other five hallmarks. Both processes involve changes in the physical coupling of cells to their mircroenvironment as well as the activation of extracellular proteases, which can act matrix-degrading and facilitate cells invasion into other tissues [4].

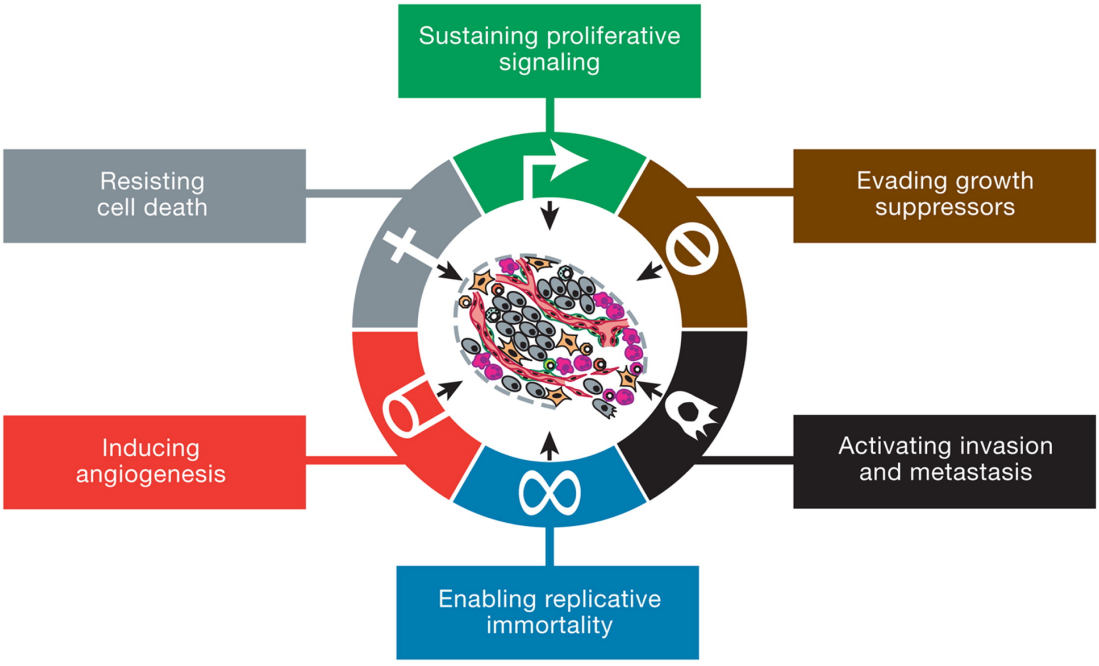


Figure 2.1: This figure illustrates the six hallmark capabilities originally proposed in [4]. Figure extracted from [31] DOI: (10.1016/j.cell.2011.02.013), Copyright 2011 Elsevier Inc. (open archive).

2.2 Medical imaging of tumours

The previous section indicates that tumour growth is an intricate process which involves interwoven mechanisms unfolding at various stages and scales. All these processes are linked by a dynamic, aberrant, heterogeneous system: the tumour microenvironment. Tumour perfusion - the delivery of nutrients, their diffusion and convection into the tumour, and the removal of waste products - is a key aspect that can be used to understand the complex interrelationships between the different constituents of the tumour microenvironment and the tumour cells.

The importance of the microenvironment and perfusion to tumour growth, invasion and metastasis justify the interest in studying their complex relationship. Over the past few decades, different techniques have been developed to image the anatomy, the physiology and the metabolism of cancer [33]. These imaging techniques are now able to quantitatively describe the tumour from the tissue to the sub-cellular scale, including its microenvironment and perfusion.

Information derived from imaging modalities play a crucial role in the care of cancer patients. As such, caregivers can not only identify tumours, but also plan treatments and quantify tumour reaction to therapy. To allow for different aspects to be observed, a number of biological quantities can be measured and assessed using a range of imaging modalities.

We will limit our discussion of the medical imaging of tumours to Positron Emission Tomography (PET), Single Photon Emission Computed Tomography (SPECT), Computed Tomography (CT) and Magnetic Resonance Imaging (MRI). These are the most commonly used imaging modalities in cancer management as well as the ones which have been explored to predict treatment response. Out of these, we will mainly focus on MRI, due to the advantages it offers when

compared with other modalities including lack of ionisation, higher soft tissue contrast, possibility of tissue characterisation and metabolic imaging.

2.2.1 PET and SPECT

Positron Emission Tomography and Single Photon Emission Computed Tomography are functional imaging techniques that can map biological and physiological processes upon injection of radiolabelled molecular tracers into the body. Here, we provide a brief overview of how PET and SPECT can be used to assess biological events such as tumour proliferation, hypoxia and apoptosis. A more comprehensive review on the application of PET and SPECT in the investigation of tumour biology can be found in [34].

PET imaging plays a significant role in the management of cancer patients, as it provides a quantitative measure of mechanisms crucial to tumour growth and its response to therapy. Different tracers have different rates of uptake depending on the type, function and activity of the imaged tissue. For instance, the most commonly used PET tracer in oncology, Fluorodeoxyglucose (FDG-PET), is known to accumulate in areas of increased glucose metabolism, and hence increased cell activity. Using FDG-PET, some pre-clinical and clinical studies were able to demonstrate a correlation to or prediction of treatment response [35].

Another quantitative measure of tumour growth can be derived from PET using Fluordeoxythymidine (FLT), which was developed as a surrogate marker of cellular proliferation. Once transported to the intracellular space, FLT, to which the cell membrane is impermeable, gets trapped. Because FLT depicts higher uptake by rapidly proliferating cells such as tumour cells, it has been used to study treatment response in both preclinical and clinical scenarios [36].

In addition to the activity of the cells, PET can also assess cell inactivity in terms of hypoxia. The main tracer used for this is ^{18}F-Fluorosimonidazole (FMISO), which is retained by hypoxic but not by normoxic cells. Another PET-based method to quantify hypoxia is based on copper(II)-diacetyl-bis(N4-methylthiosemicarbazone), Cu-ATSM, which is able to access the intracellular space. This tracer is stable in normoxic tissue. In hypoxic tissue, however, the copper is reduced and released from the ATSM, becoming trapped in the hypoxic cell. The assessment of hypoxic levels in tumours is crucial to the study of tumour progression and therapy outcome, as hypoxic cells are known not only to initialise angiogenesis but also to be more resistant to chemo- and radiotherapy because of their lack of oxygen [37].

SPECT is similar to PET in that it measures the amount of radionuclide present in the tissue after injection of radiolabelled tracers, which have longer half-life than PET tracers. This longer half-life is an advantage, as it allows more imaging time. However, SPECT has a lower image resolution than PET.

Additional information on tumour activity can be derived from SPECT. For example, SPECT images acquired upon the injection of ^{99m}Tc-HYNIC-anexA5 are an indicator of apoptosis, due to the fact that annexin A5 binds to the plasma membrane of apoptotic cells.

The possibility of detecting changes in molecular biology even prior to anatomic change is the main advantage of functional imaging modalities such as PET and SPECT. However, their low spatial resolution limits their ability to provide detailed anatomical and morphological information. A higher spatial resolution can be achieved with imaging modalities such as CT and MRI.

2.2.2 CT

In contrast to PET and SPECT, modalities such as Computed Tomography (CT) are able to provide high-quality, high-resolution 3D images of tissues, including non-invasive functional and metabolic *in vivo* information.

The first practical CT scanner was developed in 1971 by G. Hounsfield and used to image the brain [38]. Similar to conventional X-ray pictures, CT involves passing X-ray beams through tissues and recording their attenuation profile which depends on tissue density. However, while conventional X-ray pictures are projections through the 3D volume, CT scans are 3D representations where each picture element can be attributed to an individual anatomical structure in the body.

This is accomplished by measuring the attenuation of X-ray beams from hundreds of different angles, with the aid of a rotating X-ray tube and detector. All the data arriving from the different angles are gathered and reconstructed to a 3D image with the help of a reconstruction algorithm such as filtered backprojection. The contrast between the different tissues will depend on the attenuation coefficients. In that sense, the CT scanner produces digital images which consist of a square matrix of elements (pixel), each of which represents a voxel (volume element) of the X-ray linear attenuation coefficient of the patient tissues.

Compared to other imaging modalities, CT scans are very fast, have an excellent dense tissue contrast, a superior spatio-temporal resolution and are low cost. In addition, CT numbers, the Housfield units, are standardised and physically meaningful. The main disadvantages of the CT scans are the high exposure of the patient to x-ray radiation and the limited soft tissue contrast, which is essential in tumour imaging. The latter can be overcome with the help of functional CT, to which we turn in the next section.

Functional CT

The development of fast CT scanners, along with the development of better analysis techniques, has helped to introduce functional CT as a method able to study the physiological function in the human body and disease [39].

Functional CT describes the use of contrast agents to capture physiological parameters that reflect the vasculature within tumours and other tissues. This is obtained by measuring the increase in attenuation or enhancement of the tissue from a series of CT images upon injection of an iodinated contrast agent [40].

Simple measures of tissue contrast enhancement such as peak enhancement value can be used to obtain semi-quantitative metrics of vascular physiology. Pharmacokinetic modelling techniques, on the other hand, enable the extraction of quantitative metrics such as blood flow, blood volume, mean transit time and permeability surface area [40]. A comprehensive review of the approaches that can be used to extract physiological (functional) information about a tissue can be found in [39].

The main advantages of functional CT in comparison to other imaging modalities, such as MRI or PET, are its accessibility and simplicity. There is nevertheless a cost in terms of increased ionisation exposure for the patient, as one generally needs to perform several CT scans. MRI, which does not involve ionising radiation yet enables tissue characterisation as well as extraction of functional information of the human body, can provide a promising alternative to CT.

2.2.3 MRI

Since its introduction to the scientific community in 1973 by Paul C. Lauterbur [41], Magnetic Resonance Imaging has become a widespread, useful tool

for clinical diagnosis and therapy planning. The basic principles of MRI are briefly described below, but a more detailed introductory description can be found in [42].

Basic Principles

MRI exploits the interaction between an applied magnetic field and a nucleus that possesses spin. Almost all elements of the periodic table have one naturally occurring isotope that possesses a spin. Therefore, in theory, nearly all elements can be examined using MR. The human body is made up primarily of water and fat, both of which contain hydrogen. The hydrogen nucleus ^1H, consisting of a single proton, is hence a natural choice when probing the body using MR techniques in a clinical environment.

In addition to its spin, a positively charged nucleus also has a magnetic moment parallel to the axis of the rotation. Within a tissue containing hydrogen protons with spin vector of equal magnitude, each proton is spinning about its axis creating a micro-magnetic field. However, due to their random orientation in all directions, at a macroscopic level the vector addition of these spin vectors produces a zero sum, resulting in a net zero magnetisation. When placed in a strong, external magnetic field, $\mathbf{B_0}$, the normally randomly oriented protons begin to rotate perpendicular to, or precess about, $\mathbf{B_0}$. As there are slightly more spins pointing in the direction of $\mathbf{B_0}$, the resulting net magnetisation $\mathbf{M_0}$ will be parallel to the external magnetic field. The protons precess about the axis (by convention the z-axis) of $\mathbf{B_0}$ at a constant rate which is proportional to the strength of the magnetic field and expressed by the Larmor equation as follows:

$$\omega_0 = \gamma B_0 \tag{2.1}$$

Here, γ denotes the gyromagnetic ratio, a constant for each nucleus in $s^{-1}T^{-1}$.

To observe the precessing nuclear moments of the protons, the longitudinal magnetisation first needs to be tipped away from the z-axis. This is accomplished by applying a radio frequency (RF) pulse, the $\mathbf{B_1}$ field, into the object to be imaged. Choosing an RF pulse with a central frequency ω_0 and an orientation perpendicular to $\mathbf{B_0}$ allows energy to be transferred to the protons. This energy induces $\mathbf{M_0}$ to rotate away from its equilibrium orientation in a direction perpendicular to both $\mathbf{B_0}$ and $\mathbf{B_1}$. If the RF pulse is left on long enough and at a high enough amplitude, the absorbed energy makes the longitudinal magnetisation rotate entirely into the transverse plane.

After switching off the RF pulse, a process called relaxation occurs in which the protons release the absorbed energy and gradually realign with $\mathbf{B_0}$. There are two relaxations processes: the longitudinal (spin-lattice) relaxation, which refers to the return of $\mathbf{M_0}$ to its equilibrium state along the z-axis; and the transverse (spin-spin) relaxation, which represents the spin dephasing along the x-y plane. If a RF receiver coil is placed perpendicular to the transverse plane, a signal produced by the protons during their precession can be recorded.

To allocate the received signal to different regions of space and make the magnetic field spatially dependent, magnetic field gradients are applied to the received signal. These gradients are small perturbations superimposed on the main magnetic field $\mathbf{B_0}$ which encode a spatial location into the signal. Three gradients, one in each of the z, x, and y directions, are used to obtain an image through:

slice selection (G_z), frequency encoding (G_x), and phase encoding (G_y). While G_z is responsible for slice thickness and position, G_x and G_y are responsible for encoding the spatial locations within each slice.

Tissue and Sequence Parameters

As mentioned in the previous section, MR measurements involve an RF pulse used to excite the protons of the probe, making them precess about $\mathbf{B_0}$. The angle by which the net magnetisation $\mathbf{M_0}$ is altered is termed the flip angle, FA, and depends on the strength and on the duration of the RF pulse. During the process of relaxation, two relaxation times can be measured: T_1 and T_2.

The relaxation time T_1, also known as the longitudinal or the spin-lattice relaxation time, is the time required for the longitudinal net magnetisation to return to 63% of the original magnetisation M_z following an excitation pulse. For a flip angle $FA = 90°$, the longitudinal relaxation is described by an exponential growth process:

$$\boldsymbol{M}_z(\tau) = \boldsymbol{M_0}(1 - \exp^{(-\tau/T_1)}) \tag{2.2}$$

where τ is the time following the RF pulse and T_1 the time constant describing the rate of growth.

Similarly, the relaxation time T_2, also known as the transverse or spin-spin relaxation time, is the time required for the transverse magnetisation to decay to 37% of its initial value M_{xy} through irreversible processes such as natural interactions at the atomic and molecular levels within the tissue or specimen. This loss of transverse magnetisation follows an exponential decay:

$$\boldsymbol{M}_{xy}(\tau) = \boldsymbol{M_0}(\exp^{(-\tau/T_2)}) \tag{2.3}$$

where τ is the time following the RF pulse and T_2 the time constant describing the rate of decay, which is a measure for the dephasing of the spins. However, in a real MR acquisition, due to imperfections in the external magnetic field and local variations in magnetic susceptibility, the transverse magnetisation decays much faster than would be predicted by natural atomic and molecular mechanisms. This real decay rate is termed T_2^* and can be considered an "effective" T_2 of the tissue being imaged.

Both time constants, T_1 and T_2, are inherent properties of tissues and therefore constant for a specific tissue at a given magnetic field strength. The transverse relaxation always proceeds at a faster rate than the longitudinal relaxation. T_1 and T_2 values for hydrogen nuclei in various tissues will depend on the size and motion of the molecule in which these nuclei reside. For example, pure liquids like water or cerebrospinal fluid (CSF) have small, rapidly rotating molecules. On the other hand, most of the hydrogen atoms in fat are nestled within long chains of carbon atoms. As a result, it takes longer for the hydrogen atoms of water to recover than the ones in fat and hence the T_1 values for water and CSF are larger than the one for fat.

The repetition time (TR) is the period between two RF pulses. In conjunction with FA, TR controls how far the magnetisation vectors can recover before the next excitation occurs, playing a crucial role on the amount of the T_1-weighting that contributes to the image contrast. Using the example of a T_1-weighted image of the brain, to achieve a contrast between fat and CSF, TR must be short enough so that neither fat nor CSF has sufficient time to fully return to $\boldsymbol{M_0}$. On such

an image, tissues with a short T_1 like fat will appear bright as they regain most of their longitudinal magnetisation during the TR interval and hence contribute more to the image. In contrast, tissues with a long T_1 like CSF will appear dark because they do not regain much longitudinal magnetization during the TR interval and hence do not contribute as much to the formation of the image.

We recall that the T_2 determines the dephasing of the spins after the RF pulse generated from energy transfer between spins. Given its bulky structure, the energy exchange in the hydrogen atoms is more efficient in fat than in water. As a result, hydrogen nuclei in fat lose transverse magnetisation faster than in CSF, which in turn has a larger magnitude of transverse magnetisation. Therefore, on a T_2-weighted image, CSF will have a stronger MR signal and appear very bright in comparison to fat.

Unlike T_1 and T_2, which are parameters intrinsic to the tissue, the sequence parameters (FA, TR and echo time (TE)) can be controlled and altered by the operator to produce different images, emphasising different tissues. Whilst the FA has an effect on the overall contrast in an image (higher flip angles create images with greater contrast), TR and TE can be chosen to focus on measurement of either T_1 or T_2, as described earlier.

Many different techniques can be used to acquire MR images. The pre-clinical data used in this thesis was acquired using a spoiled gradient recalled (SPGR) sequence. This type of sequence uses a smaller FA to allow for reasonable recovery of M_z with a short TR. With a smaller FA, the total scan time can be dramatically reduced. The SPGR sequence is specifically designed to destroy the transverse magnetisation immediately after recording the measurement at time TE, to ensure that there is no residual magnetisation when the new RF pulse is applied. Because TR is chosen to be shorter than the tissue's full recovery time,

and the SPGR sequence has a disruptive character on transverse (T_2) coherences, it is very useful in the production of T_1-weighted images.

The MR signal of an SPGR sequence depends on intrinsic tissue (T_1 and T_2^*) as well as on operator-selected (FA, TR and TE) parameters. Assuming a longitudinal steady-state and perfect spoiling have been achieved, the signal (S) model of an SPGR sequence is given by:

$$S = M_0 \frac{\sin FA(1 - \exp(-TR/T_1)}{(1 - (\cos FA) \exp(-TR/T_1)} \exp(-TE/T_2{}^*) \tag{2.4}$$

The signal depends on $T_2{}^*$ rather than on T_2 because phase shifts resulting from magnetic field inhomogeneities and local variations in magnetic susceptibility are not cancelled at the center of the gradient echo sequences. The measured MR-signal (S) is therefore dictated not by true T_2-relaxation, but by these other factors which constitute $T_2{}^*$. The $T_2{}^*$-weighting is controlled by the parameter TE. The contribution of $T_2{}^*$ can hence be minimised by choosing a small TE, which brings the final term of Eq. 2.2.3 close to unity. The parameter TR, on the other hand, controls T_1-weighting. When TR is small, the term $[\exp(-TR/T_1)]$ approaches unity and T_1-weighting increases. One should note that in practice it is difficult to achieve perfect spoiling. This leads to an approximation which has a direct effect on the estimated parameters (e.g. T_1 values) so that these are in the end approximations, rather than the true, intrinsic tissue values.

Functional information from MRI

Because it does not involve ionising radiation, MRI is often the imaging modality of choice in oncology, especially due to the good soft tissue contrast which enables

differentiation between normal tissue and tumours.

For example, MR protocols can involve the quantification of the self-diffusion of water molecules in tissues (Diffusion Weighted MRI (DWI)) described by an apparent diffusion coefficient (ADC) to measure cell structure and density. A further MR diffusion technique, Diffusion Tensor Imaging (DTI), can be used to noninvasively assess diffusion anisotropy as well as to characterise the structural connectivity of fibres present e.g. in the brain.

In addition to diffusion, MRI techniques have been developed to noninvasively measure tissue perfusion, which refers to the rate of blood flow through the capillary circulation of an organ or tissue. These techniques involve the serial acquisition of MR images upon delivery of an exogenous, intravascular, non-diffusible contrast agent (CA). As the CA enters the tissue of interest, susceptibility effects on the signal echo (Dynamic Susceptibility (DSC) MR Perfusion Imaging) or relaxivity effects on the signal echo can be measured (Dynamic Contrast Enhanced (DCE) MR Perfusion Imaging). In the next section, we will provide a brief description of each of the methodologies mentioned above.

DWI

Diffusion Weighted MRI (DWI) generates images based on the extent of random water motion in tissues. Diffusion can be affected by interactions with cellular membranes, intracellular organelles and macromolecules [43]. Therefore, information on the extracellular-space, on the integrity of cellular membranes and on tissue cellularity can be extracted with the help of this modality. The measured diffusion in tissues, which is lower than in free solution, is termed the apparent diffusion coefficient (ADC) [44, 45, 46].

Preclinical and clinical studies have demonstrated a number of potential roles

of DWI in the detection and characterisation of diseases. Because it provides a measure of tissue microenvironment, DWI has been used to evaluate tumour cellularity. In general, any process (pharmacological, physical or radioactive) that causes cellular necrosis or lysis has been shown to increase water diffusion represented by an increase in ADC value. In contrast, increased cellularity has been associated with a reduction in ADC values due to the restricted diffusion of water molecules [47]. The measured ADC, therefore, correlates inversely with tumour (tissue) cellularity [48].

Several clinical studies have confirmed this general association by comparing tumour ADC values with the histology of the underlying tissue. However, proposed threshold ADC values to differentiate between pathologic processes vary across studies. This variation can be due to the lack of standardisation in DWI acquisition and data analysis, both of which affect ADC values [46].

Nonetheless, studies have demonstrated the potential of DWI to assess tumour response to therapy. For instance, increases in water diffusion upon exposure of tumours to chemo- and/or radiotherapy have been linked to favourable treatment outcome [46]. The observed changes in ADC values due to therapy vary with the biological mechanism of action of the therapy as well as with the timing of the DWI acquisition in relation to treatment delivery [43]. It is therefore important to interpret these analyses with caution. This is specially the case since the influence of water diffusion on DWI measures are to-date not fully validated and an appropriate biophysical interpretation of these measures *in vivo* is still controversial [46]. The assessment of a more mechanistic understanding of therapy induced changes will likely require observations from additional functional imaging modalities such as DCE-MRI and PET.

The main advantages of DWI have to do with 1) its ability to assess response to

treatment of cancer at a cellular level and therefore to potentially detect successful treatment earlier than anatomical measures, and 2) its availability on most clinical MRI systems, making it easy to assess patients with brain cancer. However, especially in its application to the brain, where the tissue organisation leads to anisotropic diffusion of water, DWI is limited. The measured ADC depends on the direction of the applied diffusion gradient, and to obtain the directionality of diffusion, multiple directions need to be applied [47]. We briefly review this approach, termed diffusion tensor imaging (DTI), in the next section.

DTI

DTI is a method used to non-invasively characterise the structural connectivity of tissues. It was proposed as a means to provide information on the extent of diffusion anisotropy and its orientation [49]. Recently, it has become the main modality used to map neuronal fibre tracts *in vivo*, a technique known as diffusion tractography [45]. This modality extracts the 3D fibre trajectories by assuming that the largest principal axis of the diffusion tensor will align with the predominant fibre orientation within a voxel [50].

Both DTI and tractography provide not only ways of investigating structural connectivity of tissues but also of assessing changes due to brain disease. A number of studies have examined how these fibre tracks influence tumour evolution and how, in turn, the progressing tumour changes the fibre tracks. DTI has been mostly used to detect radiation-induced damage in the brain. For instance, infiltrating tumour cells, tumour oedema, or radiation-induced damage all appear to disrupt the normal anisotropy as measured by DTI. However, it remains difficult to allocate each pattern of anisotropy to the underlying cause (e.g. glioma cells infiltration or radiation-mediated damage). These difficulties notwithstanding,

DTI has been proposed as a tool to track treatment-induced damage and aid radiation planning to prevent or reverse that damage [47].

DTI and tractography have been used to provide information to improve patient care in the operating room. For instance, patients operated with DTI integrated neuronavigation have shown higher median survival rate and lower rate of postoperative deficit and dependency when compared with the ones who were operated with anatomic imaging and neuronavigation. Moreover, a decrease in surgery duration, patient fatigue and seizures due to surgery could also be observed [51].

Interpreting DTI results is not always straightforward, and it is therefore important to understand which anatomical information can be extracted with high confidence and which cannot. Limitations of this technique include 1) the fact that microscopic (cellular level) anatomical information is averaged over the relatively large voxel volume, so that for multiple fibre population with different orientations, their contributions to the signal are likely to be averaged; 2) the issue of simplification in tensor calculation caused by the use of only 6 measurements, which could result in large loss of information; and 3) the fact that the assumption that the largest diffusion axis corresponds to the fibre orientation is only true for a single population, as one orientation is not sufficient to represent two fibre populations. These problems could be mostly solved by increasing image resolution and by extracting more parameters from each voxel [52].

Despite these limitations, DTI has proven a useful tool to improve overall patient care in neuroscience and neuro-oncology. More detailed reviews on DTI and its applications in basic neuroscience and in oncology can be found in [51, 52].

DSC-MRI

DSC-MRI is another technique which has become very present in the management of cancer, especially in brain tumours. DSC-MRI is an exogenous contrast-based technique which relies on the intravenous injection of a paramagnetic CA, such as those involving gadolinium (Gd) chelates. This perfusion technique, which is usually based on T_2- or T_2^*-weighted imaging sequence, makes use of very rapid imaging to capture the first pass of the CA, and it is therefore also known as bolus tracking MRI.

Upon injection of the CA, the magnetic field is distorted and T_2 around the vessel is reduced due to an increased susceptibility effect [53]. The CA induced increase in the R_2 relaxation rate in a tissue can be computed as [54]:

$$R_2^* = R_{20}^* + r_2^* \cdot C_b \tag{2.5}$$

where $R_2^* = 1/T_2^*$, R_{20}^* represents the gradient-echo (GE) transverse relaxation rate of the tissue without the CA, r_2^* is the transverse relaxivity of the CA, and C_b is the intravascular concentration of CA in the blood. This relationship can also be applied to a spin-echo sequence as $R_2 = R_{20} + r_2 \cdot C_b$ [55].

When a gradient-echo acquisition is used, microscopic field perturbation and diffusion causes signal losses in large and small vessels, respectively. In the case of spin-echo (SE) acquisition, the signal loss is greatly reduced because the dephasing is partially refocused. As with GE acquisitions, diffusion is the cause of signal losses in small vessels. Thus, SE measurements are mainly sensitive to capillary sized vessels; whereas GE measurements are sensitive to all vessel sizes [54].

Images are acquired before, during, and after CA injection. The time course

images can be divided into the baseline, the first passage of the bolus, and the recirculation period. During the baseline period, images are acquired before the arrival of the CA bolus, and the time course signals are therefore usually constant. During the first passage of the CA, the DSC-MRI signal quickly decreases until the peak signal change, which corresponds to the time of maximum CA concentration. The signal intensity (partially) returns to baseline values. Finally, during the recirculation period, the DSC-MRI signal slowly decreases again, due to re-entering of the CA. After this period, signals theoretically recover up to the baseline. The signal intensity-time curves are converted into concentration-time curves, assuming a linear relationship between the change in relaxation rate, and the concentration [55].

Quantification of tissue perfusion can be performed through model-free approaches that characterise the shape and structure of the signal intensity time curve $S(t)$ as well as through fitting of a model to describe the concentration-time curve. [56]. The latter is normally based on the physical principles of tracer kinetics [57, 58]. Original model assumptions are intact blood-brain barrier (BBB), stable flow during the measurement, and negligible T_1 changes after CA injection. Additional assumptions are no recirculation of the tracer and no dispersion or delay of the bolus for estimating the arterial input function (AIF).

A number of error sources can affect perfusion quantification when using DSC-MRI. The major ones include: the linear assumption for the relationship between signal and concentration of the CA, bolus delay and dispersion, and the breakdown of BBB resulting in leakage of the tracer into the extravascular space. A good review of several studies performed to overcome these limitations can be found in [55].

In conclusion, DSC-MRI measures the intravascular phase of the CA and is used

mainly for perfusion analysis of the brain and diseases of the brain, such as stroke. Outside the brain, however, and especially in tumours, DCE is the method of choice as it captures the extravasation of the CA from the leaky tumour vessels into the extracellular-extravascular space (EES) [59].

DCE-MRI

DCE-MR data are generally obtained with rapid acquisitions of T_1-weighted MR images upon the injection of a gadolinium-based CA, which escapes the leaky tumour vasculature and shortens the T_1 relaxation time of surrounding hydrogen ions. By examining images acquired before and after CA injection, an individual area (or voxels) will demonstrate a characteristic signal intensity time curve, which can be linked to the concentration of CA. Because the CA is unable to cross the cellular membrane, the DCE-MRI measured signal intensity shortening derives mainly from CA that extravasates to the EES.

The DCE-MRI data can be analysed to extract parameters which can be interpreted in terms of physiological tissue characteristics. A multitude of approaches have been developed and used to estimate DCE-MRI related parameters. These can be divided into quantitative, semi-quantitative and model-free approaches.

Quantitative models can be used if the arterial input function (AIF), which describes the concentration of contrast in blood plasma over time, is known. Analysis of the time course of CA uptake and washout may be used to extract parameters pertaining to a model of the tissue vasculature. For example, the dynamics of the CA exchange between the vasculature and the EES can be estimated by fitting of an appropriate pharmacokinetic (PK) tracer analysis model to the measured CA concentration time curve. Using, for example, the first generation of DCE-

MRI models, the model developed by Tofts and colleagues in the 1990s [28], yields parameters related to tissue perfusion and vessel wall permeability (represented by K_{trans}), the total extracellular volume (v_D) and the blood flow (F).

Without an input function, semi-quantitative measures can be used to describe the shape and structure of the signal intensity enhancement curve. These models are simpler than the quantitative ones, as the parameters can be measured directly on the time-intensity curve. Semi-quantitative parameters include bolus arrival time, peak enhancement, area under the curve and time to peak. While they are more straightforward than the quantitative models, their high dependency on the chosen MRI acquisition protocol makes it difficult to interpret the parameters in terms of the underlying physiology of the tissue as well as to compare the obtained values between different patients and scanners [60, 61].

Finally, model-free approaches that characterise the shape and structure of the signal intensity time curve $S(t)$ can also be used to quantify tissue perfusion [56]. These models have the advantage that they produce two independent parameters, flow and mean-transit time, without the need for prior assumptions on the underlying tissue's internal structure. However, they might not provide accurate estimates in the presence of recirculation and extravasation of the CA [59].

Due to its ability to provide the above mentioned information on physiological tissue characteristics, DCE-MRI application to the management of cancer patients is of high interest. It has been shown, for instance, that this technique can be used to investigate tumour grades, the treatment effect of radiotherapy and chemotherapy, as well as to destinguish between patients who will respond and those who will not to a given therapy [32, 62, 55]. A more detailed review on how DCE-MRI is being used to assess tumour growth and treatment response can be found in [62]. A very comprehensive review on DCE-MRI related models as well

as a guideline to address the problem of model selection are provided in [59].

In the next section, we will focus on the different cancer therapy methods, with a special focus on radiotherapy, which plays a central role in the management of cancer patients.

2.3 Cancer therapy

Over the last decades, a huge number of biological processes (as the ones described in Section 2.1) that become disturbed in cancer has been identified. With the understanding of key elements such as cell-cycle, proliferation, hypoxia, apoptosis and angiogenesis, it has become possible to develop cancer treatments targeting each of the disturbed biological process.

Cancer treatments involve, but are not limited to, surgery, radiation therapy, chemotherapy, immunotherapy and targeted therapy. Some patients only receive one treatment. Most patients receive a combination of treatments, such as surgery with chemotherapy and/or radiation therapy. In the next section, we will provide a brief overview of the main treatments which have been considered when modelling tumour growth and reaction to therapy: radiotherapy, chemotherapy and targeted therapy. For the latter, we will focus on anti-angiogenic therapy due to its potential to improve the outcome of radiotherapy [63]. More detailed information on cancer treatments strategies for different tumour types can be found in the book *Treatment of Cancer* [64].

2.3.1 Radiotherapy

Radiation therapy, also known as radiotherapy (RT), uses ionising radiation to cure or stabilise cancer. It is one of the most common tools used to treat cancer and can be used alone or in conjunction with other treatments (e.g. surgery and chemotherapy). The choice to use radiation to treat a particular cancer depends on a wide range of factors, such as the type, location and stage of cancer. It is normally used in cancer's early development, when the tumour is well localised or has only undergone regional spread.

The fundamental challenge in radiation therapy, as in all cancer treatments, is to find the right balance between eliminating the cancer and avoiding unacceptable injury to surrounding healthy tissue. Substantial improvements have already been achieved in this regard with the development of new technologies such as image-guided therapy, by altering the radiotherapy fractionation or by the use of concurrent chemotherapy [65].

To further overcome this challenge and in order to achieve the best outcome possible for the patient, treatment planning should be optimised before radiation delivery. Such optimisation requires understanding of the underlying biological processes that influence and hence determine tumour response to therapy. In the following paragraphs we will therefore describe the biology of radiotherapy (including the "5 R's of radiotherapy"), the effect oxygen has on the radiation outcome and how altering the radiotherapy fractionation can be used to improve therapeutic outcome.

DNA damage and cell killing

Irradiation of any tissue generates a succession of processes with different time-scales. In the physical phase, a high-speed electron takes fractions of a second to traverse the DNA molecule and pass across a cell. There it can either ionise or excite orbital electrons. If sufficient energy is present, ionised electrons may excite or ionise further electrons in atoms near them, initiating a cascade of ionisation events. This process is responsible for the direct damage of radiation on DNA. In the chemical phase, damaged atoms and molecules react with other cellular components by breaking adjacent molecular structures, resulting in the appearance of free-radicals. These reactions are complete within approximately 1ms after radiation exposure and are responsible for indirect damage of radiation on DNA. The last phase, the biological phase, starts with cells trying to repair the damaged acquired from the two previous phases. The vast majority of lesions, for instance in DNA, are successfully repaired. In a case where lesions fail to repair, cell losses in both tumours and normal-tissues will happen within days or weeks after radiation. Other processes include compensatory cell proliferation (as a response to cell killing) and the so-called late reactions. The latter refers to fibrosis, blood-vessel damage and even the appearance of second tumours. Hence, effects of ionising radiation may be observable up to many years after exposure [66].

Both healthy and cancerous tissues are affected by these forms of damage. The key to the efficacy of radiotherapy is to destroy cancer cells and as far as possible leave healthy tissue undamaged. This can be achieved with the help of fraction-ation therapy, which involves dividing the total dose into several smaller doses over a period of several days.

Standard fractionation involves dividing the dose into 30 units delivered every

week day over six weeks. Hyperfractionation divides the same total dose into more doses, giving out treatments more than once a day. Hypofractionation delivers higher doses of radiation in fewer fractions. The rationale behind fractionation is to allow enough irradiation dose to be given to the tumour, while minimising the damage done to the healthy tissue surrounding it.

The biological factors that influence the response of normal and tumour tissues to fractionated radiotherapy can be explained by the "five R's of radiotherapy", first introduced by Withers [67] and expanded by Steel *et al.* [68]:

- **Repair**: Splitting the radiation dose into fractions gives cells time to repair damage in the biological phase. The ability of a cell to recognise damage is suppressed in tumour cells, but present in healthy cells. Fractionation allows healthy cells time to repair themselves before a new dose is delivered. This results in a higher number of tumour cells being killed while limiting the damage to healthy ones (as shown in Fig. 2.2).

- **Reassortment**: The time between fractions allows tumour cells to transition through the cell-cycle phases. The sensitivity of cells to radiation varies depending on the phase they are in. Cells that survive a first treatment fraction will probably be hit in the next treatment, as they progress to a more sensitive phase.

- **Repopulation**: During an extended course of radiotherapy (e.g. six weeks), cells that survive irradiation may proliferate and repopulate the tissue. For the case of healthy tissue, this can mean a reduction in side effects as the tissue as a whole is repairing itself to some degree. However, if tumour cells start to repopulate before the end of therapy, an accelerated growth of the remaining tumour towards the end of the treatment might be observed. A possible way to counteract tumour-cell repopulation might be by using

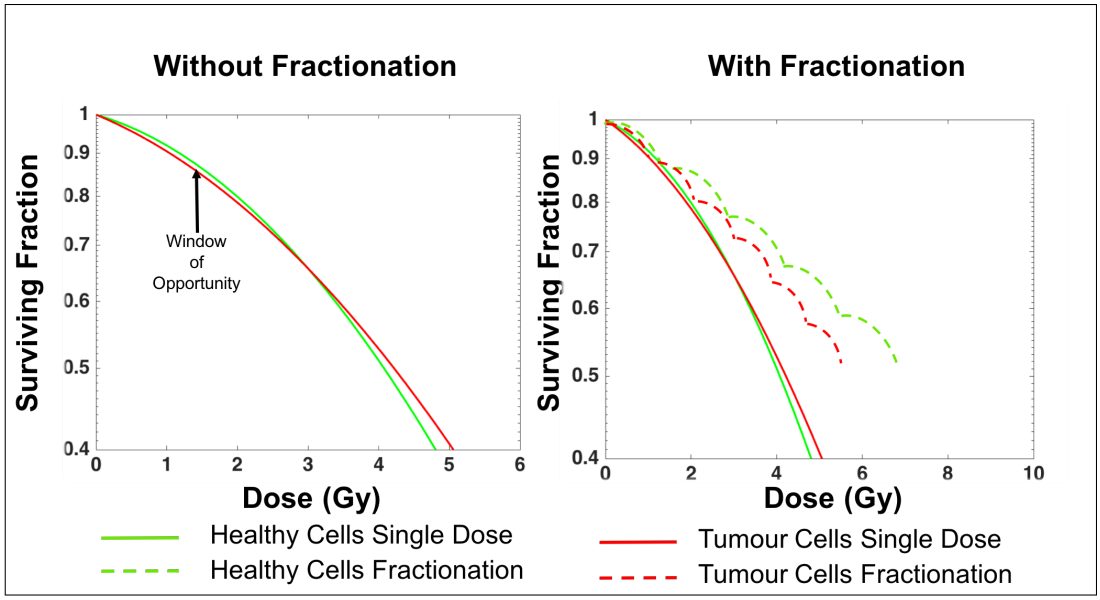


Figure 2.2: For a single dose (left), tumour cells do not repair damage at low doses as well as healthy cells so that the survival fraction of healthy cells (green) exceeds that of tumour cells. At high doses, the survival fraction of tumour cells (red) exceeds that of healthy cells. Fractionation therapy harnesses this effect, delivering radiation at low doses (e.g. typically about 2Gy/fraction) per fraction within this 'Window of Opportunity'. As a result, tumour cells (red, dashed) die in higher numbers while healthy cells (green, dashed) experience limited damage.

accelerated fractionation schedules, in which higher doses are delivered in fewer fractions so that the course of therapy can be reduced.

- **Reoxygenation**: In a tumour, cells that survive a first dose of radiation will tend to be hypoxic. Fractionation allows for potential improvement of their oxygen supply, leading to an increase in radiosensitivity, and, as a result, to a higher probability of these cells dying with the next dose.

- **Radiosensitivity**: Radiosensitivity has been added to the 4 R's by Steel *et al.* [68] after realisation that cell lines from different types of tumour differ in their inherent radiosensitivity and therefore react differently to the same dose schedule. This resulted in adaptation of doses and schedules according to the cell line being irradiated.

The available imaging techniques have improved the ability to quantify the extent

of cancer in a patient and therefore contributed to the delivery of more effective radiotherapy. This is especially important since irradiation is best applied to tumours which are well localised. For the case where the cancer has already spread to other parts of the body, non-localized, diffusely deliverable treatment like chemotherapy needs to be administered. This therapy, which is a common component of many treatment regimes, will be the topic of our next section.

2.3.2 Chemotherapy

Chemotherapy is a cancer treatment that uses drugs to destroy cancer cells. It is one of the most common treatments for cancer, and it can be given alone or before, during or after other treatments (such as surgery and radiotherapy).

As chemotherapeutic agents kill highly proliferating cells present all over the body, it is especially the therapy of choice for cases where cancer cells have metastasised to other parts of the body. It might be delivered every day, every week or every month depending on the type of cancer and on how severe it is.

As with radiotherapy, chemotherapy protocols strive to achieve maximal effectiveness of the drug with tolerable toxicity. Therefore, treatment plans are optimised and take into consideration the time required by healthy cells to recover from toxic damage caused by chemotherapeutic agents. If the time between two treatment cycles is too large, cancer cells will recover from the damage and tumour growth will progress. In contrast, if the treatment cycles are too close together, toxicity might exceed the maximally tolerated dose [69]. Because chemotherapeutic agents target rapidly dividing cells, adverse effects can be observed in normal cells with high proliferation rates. As a result, some degree of bone marrow toxicity, hair loss and damage to the intestinal epithelium (manifested e.g. as nausea and vomiting) can be expected during and after chemotherapy.

There are many types of chemotherapy drugs, which are normally divided into groups based on how they affect cancer cells. Common chemotherapeutic agents are [69]:

- **Alkylating agents**: The oldest type of chemotherapy acts by targeting the DNA of cancer cells to keep them from making more copies of themselves. They include cyclophosphamide, melphalan, and temozolomide and are used to treat leukemia, lymphoma, carcinoma as well as breast, brain, lung, and ovarian cancers.

- **Antimetabolites**: These agents act by interfering with the normal metabolism of cells to make them stop growing. This can be achieved, for instance, by blocking the activity of critical enzymes. Among many others, they include methotrexate and cytosine arabinoside, and are normally used in the treatment of lymphoma, leukaemia and cancer in the breasts, ovaries, and lungs.

- **Antitumour antibiotics**: This group of agents attack the enzymes inside the DNA of cancer cells, preventing them from dividing and growing. Doxorubicin and mitoxantrone are examples of such agents and can be used to treat, among others, lymphoma, mammary tumours and a variety of carcinomas.

- **Plant alkaloids**: These drugs act by preventing cells from making more copies of themselves. They are most commonly derived from periwinkle plant (vinca alkaloids). They include vinblastine and vincristine, and are typically used in the treatment of e.g. lymphoma, non-small cell lung cancer and brain cancer.

Chemotherapy is a common cancer treatment, and has been proven useful to the management of cancer patients. However, the main limitation is the high level

of side effects linked to the fact that it also kills healthy cells all over the body. New drugs able to attack tumour cells while sparing healthy cells have emerged as a means of reducing side effects. Treatment with these drugs is called targeted therapy, and works by targeting specific gene products that control the biological processes associated with cancer such as angiogenesis, cell-cycle control, apoptosis and invasion [64]. Due to the importance of angiogeneis to tumour progression and metastasis, in the next section we will focus on one special type of targeted therapy - anti-angiogenic therapy- which inhibits angiogenesis and has been shown to increase the efficacy of conventional therapies such as radiotherapy [70].

2.3.3 Anti-angiogenic therapy

Due to the significant role of angiogenesis to tumour growth, much research has been conducted to find ways to block angiogenesis with the hope of inhibiting tumour growth. This could for instance be achieved either by inhibiting growth factors (such as the vascular endothelial growth factor (VEGF)) required for ECs proliferation or by directly inhibiting EC migration. This research has led to the development of bevacizumab (Avastin), the first VEGF targeted anti-angiogenesis cancer therapy approved by the U.S. Food and Drug Administration (FDA) [71].

This therapeutic approach has been tested and validated on patients with various types of cancers. Its application either alone or in combination with radio- or chemotherapy has shown to improve progression-free survival while keeping adverse effects at a moderate level [72].

Although Avastin is perhaps the most discussed anti-angiogenesis drug, many other therapeutic strategies targeting some aspects of VEGF signalling have been investigated and are currently in various phases of clinical evaluation [63].

For instance, tyrosine-kinase inhibitors of the VEGF receptors have shown anti-angiogenic effects and are therefore being used as anti-angiogenic agents against pathological angiogenesis [72].

Some studies have suggested that the chaotic and leaky tumour vasculature may undergo normalisation as a response to inhibitors of angiogenesis. This vascular normalisation might improve vessel functionality and result in better perfusion of the remaining tumour mass. The hope was that by reducing tumour hypoxia one could also improve the delivery of chemo- or/and radiotherapy [72].

This hypothesis was tested, for instance, by Dings *et al.* who investigated whether anti-angiogenic drugs (such as Avastin) were able to increase the effect of radiotherapy by transiently normalising tumour vasculature. Their findings showed that anti-angiogenic drugs were able to transiently normalise the tumour vasculature, increase tumour oxygenation and as a result improve the effects of RT on tumour growth. This was observed especially when radiation was delivered at the peak of tumour oxygenation, identified as the first four days of anti-angiogenic treatment [63].

Results like these suggest that while anti-angiogenic drugs have been approved for cancer treatment, the clinical benefits of anti-angiogenic therapy can still be increased by more precise understanding of the morphological changes of the tumour vasculature in response to therapy. Treatment scheduling needs to ensure radiation or chemotherapy is delivered during periods of higher radiosensitivity achieved e.g through pre-delivery of Avastin. However, tumour vasculature is normally highly heterogeneous (both intra- and inter-tumoural), which impinges on the predictability of the patient's response to either anti-angiogenic or combined therapy. This might explain why so far most anti-angiogenic drugs have demonstrated only a moderate effect on the overall patient survival rate, limiting

the clinical benefit of these drugs [71].

There have been many advances in cancer therapy, as briefly outlined in this review. However, just as no two human beings are identical, no two tumours develop and react to therapy in exactly the same way. Given the high cost of these therapies, the ability to predict treatment outcome is not only a clinical need but also an economic requirement. Accommodating the individuality of each patient into cancer management is an objective of personalised medicine. The vision of personalised medicine is not new, but advances in genomics, informatics and medical imaging in oncology have placed this vision closer to reach. There is much potential in the possibility of using medical imaging to constrain mathematical models of tumour growth to predict how a given tumour will progress and respond to an individual treatment schedule. In the following sections, we will review the current state-of-the-art in the field of medical imaging based models of tumour growth and response to therapy.

2.4 Imaging-based models of tumour growth

In order to successfully treat cancer, the influence of the tumour on its microenvironment and vice versa need to be understood. Mathematical models of tumour growth provide a useful tool to evaluate and describe the effect of different components of the microenvironment on tumour growth dynamics. These models can range from simple exponential, logistic and Gompertzian growth laws to elaborate systems of differential equations [5, 6, 7, 8, 73]. Although they can be used to elucidate the microscopic aspect of tumour growth and can provide insights into tumour biology, their clinical value is fundamentally limited. This is because the majority of these models rely on knowledge of processes occurring at the

sub-cellular scales, such as chemotaxis, haptotaxis or growth factors, which are difficult to measure in an intact living system and cannot be observed on medical images.

To overcome this limitation, models of tumour growth can be built *a priori* from data derived from non-invasive biomedical imaging techniques. Imaging techniques not only report on the anatomy of bulk tumour and volume but can also be used to extract quantitative measures of, for instance, tumour vascularity, perfusion, metabolism, hypoxia, cell density and proliferation.

This promising perspective has motivated a number of groups to explore the concept of integrating quantitative measures derived from medical imaging into mathematical models of tumour growth. Macroscopic tumour modelling is most relevant to allow for comparison to human imaging data and potential translation into a clinical scenario. Some of the main contributions to the literature at the interface between mathematical modelling of tumour growth and imaging will be briefly described in the review that follows. The works are divided into subsections adopting modelling based on one, two or various scales.

2.4.1 Single-scale models of tumour growth

The majority of the current medical imaging based models of tumour growth have been applied to the case of glioma. Glioma cells are known to not only proliferate but also to migrate along the white fibres of the brain. The fact that glioma cells migrate beyond the tumour bulk detected by imaging devices displays the peril of this disease and the interest in predicting its further development.

Most glioma growth models describe the evolution of the local tumour cell density by applying the reaction-diffusion approach suggested by Murray [18] as

follows:

$$\frac{\partial c(\mathbf{x},t)}{\partial t} = \nabla \cdot (D \nabla c(\mathbf{x},t)) + p\, c(\mathbf{x},t) \tag{2.6}$$

where $c(\mathbf{x},t)$ is the concentration of glioma cells at position $\mathbf{x}$ and time t, D is the diffusion coefficient associated with glioma cell diffusion and p is the proliferation rate of the glioma cells.

The first efforts towards personalisation of the reaction-diffusion model (Eq. 2.6) involved defining the evolution of glioma cell population based on patient-specific CT scans. For instance, Tracqui *et al.* used a set of CT scans of one glioma patient taken over the course of the patient's terminal year to calibrate a reaction-diffusion model of gliomas. A total of six unknown parameters were optimised to give the best least squares fit of the simulated tumour area to the area observed on the CT scan. The initial tumour cell density was determined through analysis of a biopsy obtained at the time of the first scan [74]. These early approaches demonstrated the feasibility of using information from anatomic medical imaging to parametrise a simple model of tumour growth. However, as their validation was performed on a 2D domain and aspects like the heterogeneity of the brain tissue with respect to grey and white matter were not taken into account, their clinical applicability remained limited.

A model reformulation was proposed by Swanson *et al.* to accommodate the fact that glioma cells migrate more rapidly in white than in grey matter [75, 76]. Using a detailed mapping of the white and grey matter of a virtual brain, they were able to simulate glioma growth on a brain domain which was anatomically accurate. This approach, differentiating between white matter and grey matter diffusion rates, has been adopted by other groups due to its usefulness in defining

expected pathways of invasion by glioma cells.

Another way to account for the heterogeneous structure of the brain is to treat D as an explicit function of space, so that it can be substituted by a tensor of the form $\mathbf{D}(\mathbf{x})$. Exploring the fact that glioma cells preferentially migrate along white fibres of the brain, in [11], the authors derived the aforementioned tensor from DTI. This study demonstrated the importance of integrating structural information available from imaging data to account for tumour cell growth. However, because DTI data was not available on the patient data sets, the authors used DTI data from a healthy volunteer to initialise the model. This lack in patient data constrains the patient-specificity of their model.

Similarly, Clatz *et al.* used DTI to include the anisotropic diffusion process in white matter fibres into a simulation of glioblastoma multiforma (GBM) growth. They also took into account mechanical restrictions presented by certain brain structures by combining a functional atlas with the tumour simulation [12]. To this end, the authors first segmented the images into an expansion component, which does not infiltrate the tissue, and a diffusion component, which invades adjacent structure by a diffusion process as given in Eq. 2.6. These images were then registered to an anatomical brain atlas and simulations were performed using a finite element method, whereby tumour cell density was assigned to each mesh point. Making use of 7 landmarks, the brain deformation (mass effect) induced by the tumour invasion was compared to what was measured on MR images by registration of the predicted tumour to that acquired six months after the initial measurements. The results of these comparisons showed the feasibility of using biomedical imaging data to initialise and constrain a model of glioma growth. However, similarly to [11], the fact that the DTI information was not derived from the patient data used for validation and that an anatomical brain atlas

was used, reduce the patient-specificity of their approach. A more quantitative validation of this approach, which included the computation of image differences between initial images, virtual images and patient images after a period of six months, was provided by Bondiau *et al.* [77].

One of the main advantages of these approaches is that by describing the evolution of cell groups rather than of each individual cell, these models provide a framework which allows for integration of medical imaging data. In order to personalise such a model, the estimation of parameters using longitudinal data can be performed to predict subsequent evolution. Here, evolution can be defined as cellular, volumetric, or tumour delineation progression. Most groups initialise their models with cellular densities but use a macroscopic, observable quantity of interest (e.g. radial or middle slice evolution) for validation [10, 11, 12, 13, 14, 15].

The main limitation of the above presented macroscopic models of tumour growth is that by treating the tumour as a growing bulk of inert mass, they fail to take into account that tumours are living, heterogeneous systems able to adapt to changes happening in their (micro)-environment. By treating p and D as global constants (even as a tensor) that do not change in time, they assume that an initial tumour grows as fast (or slow) as a more developed tumour, thus ignoring the multi-stage, heterogeneous nature of tumour growth described previously.

Additionally, apart from the non-patient-specific DTI data, the results using these models were obtained based solely on anatomical imaging data, so that processes and interactions happening at the microscopic scale were neglected. In order to include these processes, the use of more specific imaging techniques such as PET, SPECT or perfusion MRI could be explored. The resulting information could then be integrated into a mathematical model which accounts for processes happening at the cellular level that collectively lead to a macroscopic evolution

of the tumour. We review some of the efforts performed to link events happening at two different scales to develop clinically relevant models of tumour growth in the following section.

2.4.2 Dual-scale models of tumour growth

The first study to integrate metabolic measures into a model of tumour growth was performed by Szeto *et al.* [22], who investigated the link between biological aggressiveness assessed by a serial MRI with the hypoxic burden assessed on FMISO-PET. For the case of glioma, the growth kinetics were examined using Eq. 2.6. Aggressiveness of the tumour was quantified by the ratio p/D. A high ratio value meant a highly proliferative, well defined tumour bulk. Conversely, a low value represented a highly diffusive tumour behaviour, normally linked to a poorer outcome [78]. Their results demonstrated a possible link between hypoxia (happening at the cellular scale) and the diffusive character of gliomas (happening at the macroscopic scale). However, here again, only a global proliferation and diffusion rate were used, assuming the tumour to be homogeneous and failing to identify regions of higher (proliferative) or lower (hypoxic) metabolic status.

To include tumour heterogeneity, Stamatakos *et al.* employed a cellular automaton able to link interactions happening at the microscopic layer, such as cell proliferation and cell death, to the macroscopic tumour expansion or shrinkage [79]. The basic idea of the model was that tumours consist of biological cells that are in proliferative phases (phases G1, S, G2 and mitosis) and quiescent cells (phase G0). Numerous checkpoints during the cell cycle control cycle progression and check for any DNA damage, e.g. caused by radiation, that needs to be repaired. Cells that cannot repair DNA damage induce apoptosis, and are excluded from the system after a lysis time. Their first results, obtained based on the case of a

tumour spheroid grown *in vitro*, provided insight into the biological mechanisms involved in tumour growth *in vitro*, and motivated the group to extend their model to one clinical case of GBM [24]. Their results demonstrated that their model was able to qualitatively describe GBM growth based on anatomic imaging data derived from MRI. However, the fact that images of the tumour were only used to delineate the apparent boundary of the tumour and not to calibrate their model parameters, is a noticeable limitation of this approach.

As mentioned earlier, in order to understand and account for the crucial phenomena occurring during tumour growth , all three scales - sub-cellular, cellular and tissue - need to be included into the model approach. Some of the groups mentioned in this section have acknowledged this necessity and made some initial efforts to develop a framework able to deal with modelling at each scale. These efforts will be presented in the next section.

2.4.3 Multi-scale models of tumour growth

From a macroscopic point of view, a tumour can be described by its volume, surface area or morphology. Tumour cellularity and vasculature can be used to describe the structure of the tumour at a cellular scale, which in turn includes molecular properties, such as nutrient metabolism and growth factors expression. As demonstrated earlier in this chapter, current medical imaging methods are able to provide information on each of these scales. However, these events are highly interconnected, so that any attempt to develop a multiscale model of tumour growth needs to include parameters able to couple changes happening at different scales.

One example of such a model was developed by Saut *et al.*, who introduced a mathematical model to reproduce the multiscale structure of glioblastoma [80].

In their approach, they accounted for cellular proliferation, angiogenesis as well as for the effects of hypoxia on different cellular phenotypes (i.e. proliferative vs. invasive). Local deficiency in nutrients and oxygen was considered to lead to a switch from the proliferative to the invasive state. They were able to offer insight into the growth of glioblastoma in the presence and absence of angiogenesis but their results were largely qualitative due to the lack of patient information e.g. on the level of oxygen, nutrients as well as vascularity.

An example of how this variability between patients can be taken into acccount was given by Yankeelov *et al.* who used a coupled set of partial differential equations to describe tumour growth (macroscopic scale), angiogenesis (cellular scale), and glucose consumption (sub-cellular scale) [27]. Equations describing the spatio-temporal rate of change of tumour cells, endothelial cells and glucose, were constrained using combined PET-MRI data to predict the evolution of the tumour. Their results demonstrated the possibility of describing patient-specific tumour evolution at all three scales with the aid of medical imaging. The limitations of this approach are that death and proliferation rates of tumour and endothelial cells are assumed to remain constant over time and that data from both PET and MRI are needed in order to constrain and initialise the model. This dual-modality necessity may lead to errors arising from co-localisation as well as from spatial resolution disparity. Moreover, although their model accounts for change in tumour cells, no information on the status of these cells is provided. For instance, information on the level of hypoxia in terms of number of hypoxic cells would be of particular interest.

Swanson *et al.* accounted for hypoxia in their proliferation-invasion-hypoxia-necrosis angiogenesis (PIHNA) model [16]. To quantitatively explore how glioma cells interact with their tissue microenvironment, they updated their previous

proliferation-invasion model to account for the interactions of normoxic and hypoxic glioma cells, vascular endothelial cells, angiogenic factors, and necrosis formation. Using T_1- and T_2- weighted MR images as well as hypoxia assessed through immunohistochemistry from three glioma cases, they tested their model's ability to predict relative amounts of hypoxia and necrosis as well as to perform tumour grading. Although their model provides a proof-of-concept of how both cellular and microenvironmental modelspecific variables can affect glioma growth and grading, the fact that their approach only optimises D and p, while keeping the remaining model parameters constant based on values from literature sources, limits their potential of truly assessing the relative effect of each of the processes (necrosis, hypoxia and angiogenesis) on glioma growth. Moreover, the fact that the hypoxic level was estimated from immunohistochemistry data and described based on a single value for the whole of the tumour, restricts the potential of the model to be used to predict the relative presence of each of the included aspects in the tumour.

An example of how hypoxia can successfully be incorporated into a multi-scale model of tumour growth is given by Atuegwu *et al.*, who used hypoxia as a driver of tumour cell migration [26]. They introduced a new model (the proliferation-apoptosis-migration (PAM) model) described entirely in terms of medical imaging data. To that end, measurements and predictions of cellularity, proliferation, hypoxia and apoptosis were derived from DW-MRI, FLT-PET, FMISO-PET and Tc-Annexin V SPECT, respectively. For the case of a virtual rat brain tumour and using values found in the literature, the authors were able to demonstrate the feasibility of building a model of tumour growth *a priori* from imaging data. One of the main limitations of this approach is that it does not incorporate vascularisation, which is known to be a leading factor in tumour evolution. Due to their lack of patient (animal)-specific data, the authors included parameters

given in other studies performed with different types of cancer. Hence, due to the lack of calibration and validation, their model cannot be considered patient-specific. Their model can, however, serve as a proof-of-concept and motivate other groups to include data from medical imaging in a model able to link tumour growth processes happening at different scales.

The medical imaging models reviewed in this section have the potential of becoming an invaluable research analysis and clinical assessment tool. Not only are these models able to model tumour growth based on a set of scans which are readily available in the clinic, but they can also serve as a tool to design patient-specific treatment plans as well as to predict how each patient will respond to each of these plans. Many of the groups included in this section have also explored how their approaches could be used to model the effect of therapy on tumour growth. In the next section we will provide a brief review on some of the works performed to model tumour reaction to radio-, chemo- and anti-angiogenic therapy.

2.5 Models of tumour reaction to therapy

Imaging-based tumour models can be used to get an insight into tumour growth, but they are also a powerful tool to assess the interplay of underlying biological processes which impact therapeutic response. Models of tumour reaction to therapy have the potential to answer concrete clinical questions such as whether the response of a tumour in terms of size and shape to a given treatment can be predicted over time, or what would be the best treatment schedule for a specific patient regarding modality, dosage, schedule and duration.

Different computer models were designed with the aim of answering such questions, with the hope they could serve as tools for predicting the efficacy of therapy,

optimising patient-specific therapies or improving target volume delineation. In the following sections, we present a general perspective of the use of medical-imaging based models to predict and/or optimise tumour response to radio-, chemo- and anti-angiogenic therapy.

2.5.1 Modelling the effect of radiotherapy

In the same way that most imaging-based models of tumour growth have focused on the case of brain tumours, most clinically oriented models of tumour response to therapy have been dedicated to this type of tumours. As previously mentioned, most of these works have used the reaction-diffusion equation to describe tumour growth. The effect of therapy is usually included in Eq. 2.6 as:

$$\frac{\partial c(\mathbf{x},t)}{\partial t} = \nabla \cdot (D \nabla c(\mathbf{x},t)) + p \cdot c(\mathbf{x},t) - T \cdot c(\mathbf{x},t) \tag{2.7}$$

where $c(\mathbf{x},t)$ is the concentration of cells at position $\mathbf{x}$ and time t, D is the diffusion coefficient associated with tumour cell diffusion, p is the proliferation rate of the tumour cells and T represents a loss term to describe the effect of therapy and exhibits an explicit time as well as dose dependence according to the therapeutic scheme.

Ever since its introduction, the Linear Quadratic (LQ) model of induced cell kill by radiation therapy has been used to predict the relationship between fractionated radiation dose and the probability of cell survival [81]. Cell death can result from an α component, which increases linearly with dose, d, or from a β constant in which cell death increases in proportion to the square of d. The fraction of cells surviving a single dose of radiation d, is hence given by:

$$S(d) = \exp\left(-(\alpha \cdot d + \beta \cdot d^2)\right) \tag{2.8}$$

where α $(1/Gy)$ and β $(1/Gy^2)$ are sensitivity parameters that characterise the initial linear slope and the curvature of the survival curve, respectively.

For the case of radiotherapy, the loss term, T, is generally chosen to be $R(d, \alpha, \beta) = 1 - S(d) = 1 - \exp\left(-(\alpha \cdot d + \beta \cdot d^2)\right)$ and hence to represent the probability of cell death depending on the applied dose and on the sensitivity parameters.

For instance, Rockne *et al.* applied this approach to quantify response to radiotherapy in individual GBM patients as well as to compare how a tumour treated with radiotherapy would compare with an untreated tumour. They used pre-treatment MRI scans to constrain their model, and found a correlation between the net proliferation rate and the radiation response parameter. They were also able to predict tumour size post-therapy within the inter-observer tumour volume uncertainty [82]. Based on these results the authors concluded that their model was able to create virtual *in silico* tumours with growth characteristics similar to the ones observed in patients, so that this approach could be used to predict individual response to any given treatment. However, being a probability, $R(d, \alpha, \beta)$ is a dimensionless quantity, and Eq. 2.9 becomes dimensionally incorrect. To circumvent this problem, Rockne *et al.* [83, 82] proposed that since radiation therapy is delivered daily, the probability of cell death can be considered as a probability rate.

Another use of Eq. 2.6 in the context of radiotherapy has been proposed by Unkelbach *et al.* to aid patient personalisation of the prescribed dose distribution in the periphery of the tumour [84]. According to their model, the density of infiltrating cells drops almost exponentially with distance from the visible gross

tumour volume. Using T_2-weighted images to derive tumour infiltration, the authors introduced the concept of dose fall-off rate to quantify the steepness of the prescription dose fall-off according to their assumed cell distribution. They showed that the dose fall-off rate was given by the inverse of the product of radiosensitivity and infiltration length. They concluded that depending on the radiosensitity and infiltration length of the tumour in each patient, this approach has the potential to personalise the prescribed radiation dose distribution. The success of this approach will highly depend on methods of estimating radiosensitivity and infiltration length on a patient by patient basis.

The need for accurate estimation of the tumour delineation and infiltration is another aspect that needs to be considered when simulating radiation therapy due to the localised aspect of this therapy. With that aim, Swanson *et al.* used their proliferation-invasion model to quantify the extent of tumourous invasion of individual gliomas to include tumour cells in the brain which are not detectable on anatomic medical imaging [76]. They were able to estimate the extent of cells which had spread beyond the invasion defined by standard medical imaging. They hence concluded that such an approach could lead to more accurate planning of therapy regimes as well as to the prediction of potential recurrence.

Clatz et al. [12] have also tackled the problem of correct tumour delineation of the clinical target volume to include isolated malignant cells as well as to account for the additional tumour invasion at treatment time. Their approach consists of two coupled models, one using a reaction-diffusion formulation to describe the evolution of tumour density and a second predicting the mass effect induced by cell proliferation and invasion. Through comparison of their model simulations with the real growth observed on MRIs of a patient taken six months apart, they concluded that the approach was feasible as a method to delineate tumour

invasion. However, they did not include any therapy schedule to test how this delineation would affect treatment outcome.

An extension to the approach of Clatz et al. [12] was proposed by Konukoglu *et al.* with the aim of improving tumour targeting in radiation therapy [85]. Also using a time series of MRIs to parametrise their reaction-diffusion tumour growth model, the authors described a method to extrapolate the invisible infiltration margins of gliomas. Using synthetic images and virtually grown tumours, they also proposed a way to use these margins to create variable irradiation margins which could be adapted to the estimated growth dynamics of each patient.

A further extension of the works of Clatz and Konukoglu *et al.* was recently published by Le *et al.*, who used the previous approaches to optimise radiotherapy planning [86]. In their approach, they combined the model of tumour growth used in [12] with a dose response model, considering a linear approximation of the LQ-model. Using clinical segmentations as input, and taking their uncertainty into account, they found the optimal prescription dose by minimising the number of surviving tumour cells. They tested their approach on MRIs of two high grade glioma patients and showed how their model could be used to compute a patient specific radiotherapy planning depending on tumour infiltration. The authors concluded that their approach served a as a proof of concept for how models of tumour growth combined with a dose response model and information from medical imaging can be used to derive patient-specific dose distribution, better targeting the tumour, and hence sparing other organs by re-distributing the dose. However, their approach did not include the reaction to different therapy fractionation schemes, which form a crucial aspect of radiotherapy planning.

Ever since the publication of their first model, the group led by Stamatakos have published model updates, mainly to simulate the GBM reaction to different

therapy fractionation schemes [87, 21, 88]. For instance, Dionysiou *et al.* used the LQ model to describe cell killing by irradiation and varied the parameters α and β (see Eq. 6.1) to account for the differences in radiosentitivities depending on the cell cycle phase. They performed simulations for the hypothesis of radiosensitive and radioresistant tumour for the standard and hyperfractionated schemes. Their results suggested that hyperfractionation was more effective only for the case of radiosensitive tumour. In another paper, the group also investigated the effects of weekend treatment gaps on the response of fast growing solid tumours [88]. To this end, they compared the continuous and weekend-less hyperfractionated accelerated radiotherapy approaches, using the same total dose and fraction dose, with the only difference being the consideration of weekends as pause in the treatment schedules. Their results suggested that the continuous approach could be advantageous in terms of tumour cell repopulation restrain during therapy. However, because this approach is shorter than the weekend-less one, should the therapy not succeed in eliminating all tumour cells, repopulation of the tumour post-therapy was shown to begin earlier.

Also using a stochastic model, Titz and Jeraj employed FDG-PET/CT data to investigate the effects of oxygenation on radiotherapy outcome [89]. Their anatomical information was derived from a CT scan and the metabolic information on proliferation and oxygenation was derived from FLT-PET and Cu-ATSM-PET, respectively. For the case of head and neck squamous cell carcinoma (HNSCC), their results showed that the greater the hypoxic fraction, the less efficacious the treatment is. Compared to the works described earlier, their main advantage lies in the fact that proliferation was derived locally from metabolic images, instead of globally from anatomical images. However, there are some limitations in their approach in terms of clinical usefulness: (1) because their model is non-deformable, only tumours with minimal morphological changes can be modelled;

(2) due to the missing cell redistribution there is no prediction of tumour growth at the macroscopic level, making a 2D (or 3D) model validation difficult; (3) their calibration was based on cell line specific parameters instead of patient-specific data.

2.5.2 Modelling the effect of chemotherapy

As mentioned in the previous section, the proliferation-invasion model can be easily modified to account for the effect of therapy on the tumour cell evolution. This is not only true for radiotherapy but also for chemotherapy. Swanson *et al.* [76] have for instance extended the proliferation-invasion model to explore the effects of chemotherapy on the spatio-temporal response of gliomas. Accounting for chemotherapy as a cell loss term proportional to the administered dose given at any time t, and assuming homogeneous drug delivery to the brain, Eq. 2.6 was modified to:

$$\frac{\partial c(\mathbf{x},t)}{\partial t} = \nabla \cdot (D \nabla c(\mathbf{x},t)) + p \cdot c(\mathbf{x},t) - G(t) \cdot c(\mathbf{x},t) \tag{2.9}$$

Usually, chemotherapy is delivered in treatment cycles, each one consisting of the administration of drugs for a period of time, t_{chemo}, followed by a waiting period, t_{wait}. Therefore, $G(t)$ defines the temporal profile of the chemotherapy, and is proportional to the drug concentration ($G(t) = 0$ implies that the therapy is off and no drug effect is present).

Swanson *et al.* investigated the cases of homogeneous and heterogeneous drug delivery to the brain, whereby the latter was introduced to account for the effects of heterogeneities in the vascular structure of the brain tissue. Analogous to the case where no treatment was considered, they accounted for differences in cellular

migration in grey and white matter. As a result, for the heterogeneous case, drug delivery was limited by the vascular density present in each region in the brain. Their results showed that chemotherapy was able to reduce the total number of tumour cells but not the extent of invasion of the tumour. With that in mind, the authors concluded that these invasive cells might be the reason for recurrences post-therapy, an effect often clinically observed in the management of gliomas. They further suggested that this diffusive nature of glioma cells might be the most effective mechanism of resistance to therapy, even more so than hypoxia. However, this remains a hypothesis which could for instance be tested with a model accounting for both invasion and hypoxia.

An example of a model that incorporates the effect of hypoxia on tumour growth is given by Stamatakos *et al.* [21], who have expanded their model reviewed in Section 2.4.2 to explore how GBM would react if treated by temozolomide [21]. They used MRI, PET and histopathology information to delineate the tumour, assess the necrotic area and obtain cell cycle duration, respectively. Their model of tumour growth remained unchanged, accounting for processes like cell cycling, necrosis and apoptosis for each geometric cell. Cell survival upon chemotherpay delivery for each geometric cell was predicted based on the drug pharmacodynamics. Therapy was assumed to affect both proliferative and hypoxic cells likewise, due to the fact that temozolide is a cell-cycle non-specific agent. Their predictions of the spatio-temporal activity of a virtual tumour demonstrated qualitative agreement with clinical experience in terms of cell kill due to chemotherapy. However, some limitations of this approach can be pointed out. First, they focused on the main tumour and did not account for the fact that glioma cells infiltrate in the brain, a limitation compared to the work of Swanson *et al.* [76]. Second, by assuming each geometric cell to have the same number of tumoural cells impose an unnatural homogeneity on the model. Finally, due to its complexity, their model

contains many parameters to be derived from medical imaging information.

One example of how medical imaging can be used to parametrise a simple model of tumour reaction to therapy is provided by Atuegwu *et al.* [23], who used DWI and DCE-MRI to estimate tumour cellularity pretreatment, after one cycle, and after completion of all cycles of chemotherapy. The first two sets of images were used to estimate the proliferation/death rate, which was then used in conjunction with the logistic model of tumour growth to predict the number of tumour cells at the conclusion of therapy. The estimations obtained for 28 patients were compared to the number of tumour cells estimated from MR images obtained at the conclusion of therapy. They also tested whether the proliferation rate could be used to differentiate between responders and non-responders. Their results suggested that this approach can be used to predict the total number of cells at the end of the therapy regimen, as well as to separate patients who had complete response from those who did not, as early as the completion of the first cycle of therapy. These results indicate how incorporating quantitative information about tumour properties can lead to potentially clinically relevant information about patient response to therapy. The authors concluded that more work, such as updating their model to include tumour vascularity and nutrient metabolism, was required to improve the predictive ability of their model.

Including vascularisation is especially important when accounting for the delivery of the drug to the tumour as well as for processes such as nutrient delivery, hypoxia and angiogenesis. For example, imaging-based models that account for the effect of anti-angiogenic therapy tend to be multi-scale in order to incorporate these processes in their approach. Some of these models will be briefly reviewed in the next section.

2.5.3 Modelling the effect of anti-angiogenic therapy

Another effort to incorporate serially acquired DW-MRI data into a mathematical model to quantify proliferation and migration rates of human gliomas, as well as to predict progression free survival and overall survival for patients treated with bevacizumab comes from Ellingson *et al.* [25]. Their approach did not involve the simulation of tumour reaction to anti-angiogenic therapy, but rather the use of cell diffusion and proliferation rate maps to differentiate between responders and non-responders. They were able to find strong correlation between mean proliferation rate and progression free and overall survival in anti-angiogenic therapy. They concluded that their results suggested that invasion (represented by their diffusion rate maps) might not be the main cause of patient response (or lack of), as suggested e.g. by Swanson *et al.* in [76]. Nonetheless, they recalled the importance of assessing more infiltrative tumour phenotypes, given the concern that these phenotypes might lead to the failure of bevacizumab results.

As mentioned in Section 2.4.3, one example of such a model which accounts for different phenotypes, including proliferative and invasive, was introduced by Saut *et al.* [80]. Their approach accounting for the grow-or-go phenotype (i.e. under hypoxic conditions cells switch from the proliferative to the invasive phenotype) was not only used to model the growth of GBM, but also to investigate clinical and biological effects of anti-antiogenic drugs on tumour growth. The effect of anti-angiogenic drugs was included in the model by setting the angiogenesis factor, responsible for the growth rate of new vessels, to zero when bevacizumab was delivered. This resulted in lower vascular density in the tumour, a decrease in the number of proliferative cells, and an increase in the numbers of invasive and necrotic cells. Their simulation results suggested that anti-angiogenic therapy lowers the number of proliferative cells not only by necrosis but also by increasing

their switch to the invasive phenotype, offering an apparent explanation for the rapid growth observed in some GBM patients when anti-angiogenesis drugs are discontinued. Given these findings on the role of invasive cells in therapy outcome, the authors proposed the addition of anti-motility agents for a more effective treatment of GBM.

2.6 Conclusions

In this Chapter we have provided the necessary background on topics of relevance to the remainder of this thesis. We have presented cancer evolution as a complex process, which involves interwoven mechanisms unfolding at various stages and scales. We have also described how current medical imaging modalities can be used to extract quantitative information from a tissue to a sub-cellular scale, and how this information is crucial to the development of cancer treatments.

The available imaging techniques have improved the ability to quantify the extent of cancer in a patient and therefore enabling more effective therapy to be delivered. First steps in the direction of individualised treatment schedules (e.g. fractionation, combination therapy) depending on patient and tumour type have already been taken. However, continued development of tools to enable the assessment of the biological differences between tumours and across patients is essential to achieve patient-specific treatment planning.

We then described how imaging-based models of tumour growth and response to therapy have emerged as a powerful tool that could potentially lead to patient-specific treatment planning, and reviewed some of the main contributions in the field. Overall, approaches like the ones included in this review, which are clinically oriented, have shown the feasibility of constraining models using information from

medical imaging to predict tumour growth and response to therapy.

This review demonstrated how the overwhelming majority of the studies presented have been devoted to tumours in the brain (mostly to gliomas). This is because both the rigid structure of the skull and the presence of natural features facilitate the registration needed for the validation of the models. Tumours present in other regions of the human body would likely require the development of new methods.

Most studies focused on anatomic information or used the medical imaging information to delineate the tumour and initialise their simulations. However, their model parameters were not calibrated based on imaging-data so that their predictions depend highly on parameters obtained from the literature and have limited patient-specific prediction ability. This limitation arises primarily from the complexity of the developed approach [21, 25]; or due to missing data [26, 27]. The latter is especially true for approaches relying on information from many imaging modalities.

Future efforts should be directed towards the development of a multi-scale model of tumour growth built *a priori* from data derived preferably from an imaging modality which is routinely used in the clinic, to overcome the limitations related to the lack of patient-specific data. This imaging modality needs to offer both anatomical and metabolic information at a high spatial resolution level. The inclusion of longitudinal data would allow for patient-specific calibration of parameters. Because the system is left intact, measurements (images) can be taken at different time points, thus allowing for validation as well as for updates of the models and ultimately leading to the simulation of the tumour response to different therapy protocols.

The first step in the direction of patient-specific prediction of tumour growth

involves the development of a model of tumour growth. To this end, different approaches were considered. One possible approach is given by the agent-based, stochastic models like the ones described in [79, 89]. However, counting and following each tumour cell through their cell-cycle and motion limits the predictions of such models to the 2D or spheroid cases. Given that our aim is to make the potential translation of our models to the clinic as straight-forward as possible and that growth is ultimately observed at the tissue layer, we discard this approach and use a set of continuous equations instead to describe tumour growth. The resulting model, which focuses on changes that can be inferred from the comparison between longitudinal anatomic images while still accounting for different biological activities (proliferation, hypoxia and necrosis) happening at different scales, ultimately leads to a multi-scale, 3D description of tumour growth. This subject-specific model will be developed and presented in the next chapter.

Chapter 3

3-D Model of Tumour Growth

Even though much progress has been made developing mathematical models of tumour growth, just a small fraction of them have been devoted to the inclusion of clinical data. In order to achieve impact on clinical practice, mathematical models of tumour growth and treatment response need to be able to incorporate quantitative, spatio-temporal data available from non-invasive imaging modalities for an individual patient.

In this chapter, we develop and present a imaging-based model of tumour growth which allows for the inclusion of anatomical information as well as of different biological activities (proliferation, hypoxia and necrosis) derived from medical imaging modalities[1]. Most of the imaging-based models presented in Chapter 2 focused on tumour invasion and morphology without accounting for the aforementioned biological processes [10, 11, 12, 16, 17, 15]. To account for these processes, some groups developed more complex models containing many parameters which could not be derived from medical imaging information [21]. Our model repre-

[1]Large parts of the work presented in this chapter have been published in the following article: T. Roque *et* al, "A DCE-MRI Driven 3-D Reaction-Diffusion Model of Solid Tumour Growth", *IEEE Transactions on Medical Imaging*, Volume: 37, Issue: 3, March 2018 [90].

sents a combination of both: it is able to predict the 3-D macroscopic invasion of the tumour in the host tissue as well as how each cell group (proliferative, hypoxic and necrotic) contributes to tumour evolution while retaining simplicity in terms of the number of parameters that require calibration. Being able to account for both the volume and cellularity evolution is of high clinical interest, given how processes like hypoxia are known to affect further tumour growth (e.g. through angiogenesis) and therapy outcome.

We start off by presenting our PDE-based model of avascular tumour growth along with the numerical implementation used to solve the set of equations. We then examine each model parameter to derive appropriate parameter ranges. Next, we perform a set of experiments on synthetic data considering the cases with and without apoptosis, to understand how this process as well as each model parameter influences the model outcome. Finally, we discuss the results obtained and, considering our findings, draw conclusions about its applicability to real medical imaging data.

3.1 Methods

3.1.1 Tumour growth model

In the section that follows we will describe our tumour growth model, which represents a multiscale 3-D model consisting of three scales: a macroscopic tissue scale to allow for integration of medical imaging data, a cellular scale at which the nutrient is made available to the tumour cells, and a sub-cellular scale in which metabolic processes depending on the nutrient level can lead to cell proliferation, hypoxia or necrosis. Changes in the latter (i.e. mitotic activity, hypoxia and necrosis) result in changes in the microscopic layer (i.e. local cell number), which

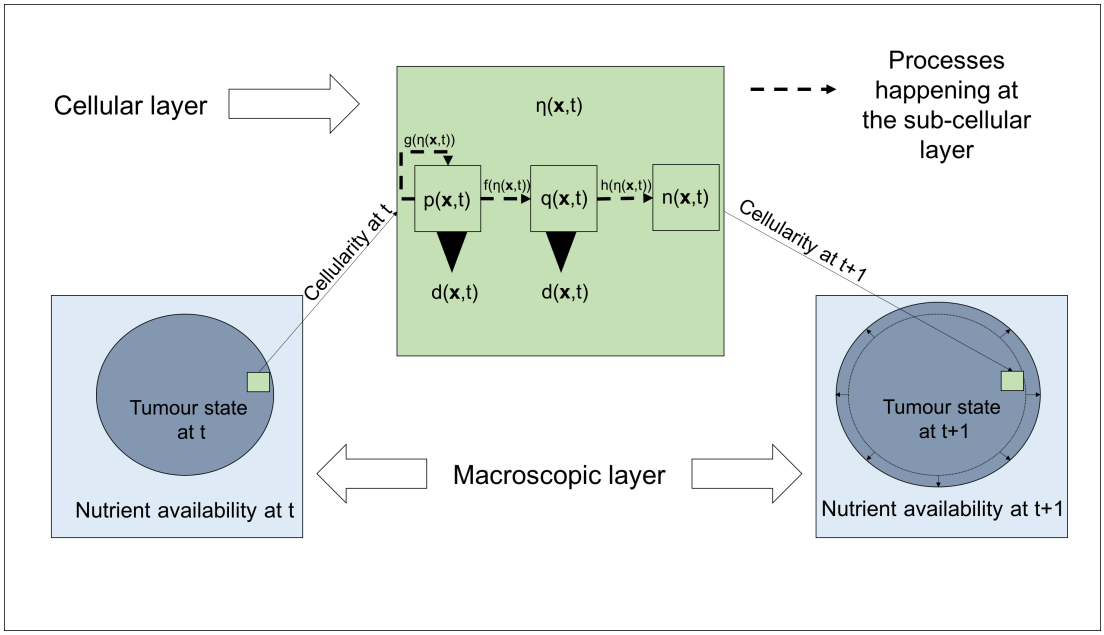


Figure 3.1: Framework of the multi-scale model of tumour growth. At the macroscopic layer, the nutrient is made available to the tumour cells and the tumour shape (volume) can be observed for time point t (left bottom). At the cellular layer, cells can be in one of the following states: proliferating, hypoxic or necrotic. Depending on the local nutrient $\eta(\mathbf{x}, t)$ available to them, proliferating cells can either proliferate or turn hypoxic at the rates $g(\eta(\mathbf{x}, t))$ and $f(\eta(\mathbf{x}, t))$, respectively. If hypoxic, cells can either remain hypoxic or turn necrotic if the nutrient continues to be inadequate at the rate $h(\eta(\mathbf{x}, t))$. The processes of proliferation, hypoxia and necrosis happen at the sub-cellular layer, but can be observed as a change in both the cellular and macroscopic layers. Proliferative and hypoxic cells are assumed to diffuse into the tissue at a rate $d(\mathbf{x}, t)$. Following proliferation, hypoxia, necrosis and diffusion for each grid point, the tumour state and nutrient availability at time point $t + 1$ are both updated and used as input for the computations for the next simulation time step.

in turn affect the tumour at the macroscopic level (i.e. tumour expansion and nutrient distribution). An overview of our model is given in Fig. 3.1.

As depicted in Fig. 3.1, the first step of the framework consists in using information on the nutrient and local cell number for each cell sub-population derived from the medical imaging data as input to the model. Assuming this information is available (in Chapter 4 we will demonstrate how maps of cellularity and nutrient can be extracted from medical imaging), the first process we are interested in at the sub-cellular layer is the proliferation of cells, which will occur if the local nutrient condition is favourable.

Proliferation has been investigated in various mathematical models. The most prominent examples are the logistic [91] and Gompertz [92] models. Both models can be written in the form:

$$\frac{\partial c(t)}{\partial t} = g(c(t))\,, \tag{3.1}$$

where $c(t)$ is the cell number. For the logistic model, $g(c(t))$ can be computed as:

$$g(c(t)) = p \cdot c(t) \cdot \left(1 - \frac{c(t)}{\Theta}\right)\,, \tag{3.2}$$

and for the Gompertz model as [93]:

$$g(c(t)) = p \cdot c(t) \cdot \left(\log(\frac{\Theta}{c(t)+a})\right)\,, \tag{3.3}$$

where a, b and Θ are parameters that can be optimised to describe a particular data set. The logistic model describes the growth of the cell population that is limited by the carrying capacity Θ. It assumes that the proliferation rate, p, decreases linearly with increasing population until it equals zero at Θ. For the case of the Gompertz model, the growth is limited by the carrying capacity $\Theta - a$. It assumes an exponential decay of the proliferation rate. Both models have an S-shape, i.e. an increasing curve with one inflection point that slowly converges to the maximum number of cells dictated by the carrying capacity. Given that for the Gompertz law, an extra parameter is needed to describe the same saturation behaviour, we choose to implement the logistic law in our model of tumour growth.

Tumour cells not only proliferate, but also spatially invade the host tissue. To implement spatial diffusion into pure, temporally proliferating model, Eq. 3.1 needs to be extended by the spatial tumour expansion term. Adopting the model introduced by Murray [18] (see Eq. 2.6), Eq. 3.1 for the logistic model becomes a reaction-diffusion equation as follows:

$$\frac{\partial c(\mathbf{x},t)}{\partial t} = \bigtriangledown \cdot (d(\mathbf{x},t) \bigtriangledown c(\mathbf{x},t)) + p \cdot c(\mathbf{x},t) \cdot \left(1 - \frac{c(\mathbf{x},t)}{\Theta}\right) \tag{3.4}$$

where the carrying capacity, Θ, models the mutual competition between cells for space and nutrients. The diffusion parameter, $d(\mathbf{x},t)$, models isotropic growth, so that if the model were to be started at the implantation time point of the tumour, the resulting shape would be a sphere. Alternatively, anisotropic tumour growth could be modelled with the use of a tensor, as suggested by [11], and linked to a map of different tissue types which could be estimated from various imaging modalities depending on the tumour site and its host tissue (e.g. CT, DTI).

Because tumour growth is not only the result of unrestrained proliferation, but also of disorder in cell death and hypoxia, we also include the evolution of hypoxic and necrotic cells in our model.

At each time step t, depending on the local nutrient $\eta(\mathbf{x},t)$ available to them, proliferating cells can either proliferate or turn hypoxic at the rates $g(\eta(\mathbf{x},t))$ and $f(\eta(\mathbf{x},t))$, respectively. To model the fact that the probability of a cell to proliferate increases with increasing nutrients, but is not infinite, as there is a maximum proliferation rate dictated by the mitotic activity and cell cycle of the cell, we assume that $g(\eta(\mathbf{x},t))$ is represented by a Gompertz function of nutrient. If hypoxic, cells can either remain hypoxic or turn necrotic if the nutrient continues to be inadequate at the rate $h(\eta(\mathbf{x},t))$. In our model, as we will see in

Section 3.1.4, nutrient delivery is represented by the availability of oxygen to the cells. Therefore, quiescent tumour cells are included in the number of hypoxic cells. The hypoxic and necrotic rates are assumed to follow an exponential decay, to account for the fact that the probability for a cell to turn hypoxic or necrotic increases with decreasing nutrient. The local cell division g, the hypoxia transition f and the necrosis transition h rates are directly related to the local nutrient level $\eta(\mathbf{x}, t)$, as follows:

$$g(\eta(\mathbf{x},t)) = G_{max} \exp(-\exp(-c_{g_0} \cdot (\eta(\mathbf{x},t) - ip)) \tag{3.5}$$

$$f(\eta(\mathbf{x},t)) = F_{max} \exp\left(-c_{f_0} \cdot \eta(\mathbf{x},t)\right) \tag{3.6}$$

$$h(\eta(\mathbf{x},t)) = H_{max} \exp\left(-c_{h_0} \cdot \eta(\mathbf{x},t)\right). \tag{3.7}$$

where c_{g_0} represents the slope of the Gompertz function and ip is the position of the steepest increase of the nutrient, and therefore the inflection point of the Gompertz curve. The decay constants c_{f_0} and c_{h_0} dictate the dependency of the local hypoxic and necrotic rates on the local nutrient level, respectively. The constants G_{max}, F_{max} and H_{max}, measured in $hour^{-1}$, are the maximum possible proliferation, hypoxic and necrotic rates, respectively.

Expressed as a set of PDEs, the processes described above can be modelled as follows [7]:

$$\frac{\partial p(\mathbf{x},t)}{\partial t} = \bigtriangledown \cdot (d(\mathbf{x},t) \bigtriangledown p(\mathbf{x},t)) + g(\eta(\mathbf{x},t)) \cdot p(\mathbf{x},t) \cdot \left(1 - \frac{r(\mathbf{x},t)}{\Theta}\right) - f(\eta(\mathbf{x},t)) \cdot p(\mathbf{x},t) \quad (3.8)$$

$$\frac{\partial q(\mathbf{x},t)}{\partial t} = \bigtriangledown \cdot (d(\mathbf{x},t) \bigtriangledown q(\mathbf{x},t)) + f(\eta(\mathbf{x},t)) \cdot p(\mathbf{x},t) - h(\eta(\mathbf{x},t)) \cdot q(\mathbf{x},t) \quad (3.9)$$

$$\frac{\partial n(\mathbf{x},t)}{\partial t} = h(\eta(\mathbf{x},t)) \cdot q(\mathbf{x},t) \quad (3.10)$$

where $p(\mathbf{x},t)$, $q(\mathbf{x},t)$, $n(\mathbf{x},t)$ and $r(\mathbf{x},t)$ represent the number of proliferative, quiescent (hypoxic), necrotic and total cells, with t denoting time and $\mathbf{x}$ a spatial coordinate in a three-dimensional domain. Note that, other than in Eq. (3.4) and in most reaction-diffusion models of tumour growth [10, 11, 12, 13, 22, 14, 17, 23] where the proliferation rate has a global value, here the proliferation rate, $g(n(\mathbf{x},t))$, is a function of the nutrient distribution (Eq. 5.2) and hence, of time and space. To account for the lysis of cells, we assume that once necrotic, cells are removed from the tumour after a period of 40 hours [8].

The processes of proliferation, hypoxia and necrosis happen at the sub-cellular layer, but when accounted for as a set of PDE like ours, can be observed as a change in both the cellular and macroscopic layers. Proliferative and hypoxic cells are assumed to diffuse into the tissue at a rate $d(\mathbf{x},t)$. Following proliferation, hypoxia, necrosis and diffusion for each spatial coordinate, the tumour

state (represented by the total number of cells and tumour volume) and nutrient availability at time point $t+1$ can be updated and used as computation inputs for the next simulation time step.

To update the nutrient distribution $\eta(\mathbf{x})$, we follow the reduced model proposed by Sherrat and Chaplain [7], which relates the local nutrient to the total number of tumoural cells and the proliferation cells (which consume the nutrient) as follows:

$$\eta(\mathbf{x}) = \eta_0 \cdot [(1 - \alpha \cdot r(\mathbf{x}))]/[1 + (p(\mathbf{x})/\gamma)] \tag{3.11}$$

where η_0 represents the level of nutrient of the host tissue (in the absence of a tumour cell population), which is equal to the maximum of the nutrient that can be made available to cells within the tumour. Due to the importance of oxygen to tumour evolution (e.g. in terms of hypoxia and necrosis), we choose the nutrient to represent the local partial pressure of oxygen, pO_2, which has the potential of being derived from medical imaging. However, $\eta(\mathbf{x})$ could represent any other factors which contribute to cellular growth, for example glucose.

The constants α and γ are chosen, for simplicity, to be the inverse of the maximum of the total cell number r and of the proliferative cell number p, respectively. This is the quasi-steady state solution to:

$$\frac{\partial \eta(\mathbf{x})}{\partial t} = D_\eta \nabla \eta(\mathbf{x}) + k_1 \cdot \eta_0 (1 - \alpha \cdot (r(\mathbf{x}))) - k_1 \cdot \eta(\mathbf{x}) - k_2 \cdot p(\mathbf{x}) \cdot \eta(\mathbf{x}), \tag{3.12}$$

where $\gamma = k_1/k_2$. This quasi-steady state assumption can be justified by the disparity in time-scale between the dynamics of the nutrient field and cell-cycle

(the diffusion time of oxygen across one cell is on the order of seconds while cell division occurs on the order of hours). The first term of the right-hand side can be set to zero, as the nutrient can be assumed to be completely consumed by local cells and not by cells in the neighbourhood.

The next, and final aspect which we need to consider at the macroscopic level is the tumour expansion which is the result of the diffusion of both proliferative and hypoxic cells (see Fig. 3.1). In [27], the authors assumed that cell diffusion was mechanically coupled to the host tissue structure through a stress tensor and an empirical coupling constant. The stress tensor was, in turn, influenced by an expansive force caused by the changes in mass associated with cell proliferation. To simplify this relationship, and using the fact that the stress tensor is linked to cell density, here we assume a direct relationship between the isotropic diffusion coefficient d and the total cell number r. We compute the local diffusion coefficient for both proliferative and hypoxic cells as follows:

$$d(\mathbf{x}, t) = D_0 \exp\left(-r(\mathbf{x}, t)/\kappa\right) \quad \cdot \tag{3.13}$$

We choose coupling constant, κ, to be the maximum of the total cell number. D_0 is a parameter to be optimised to model the fact that tumours expand at different rates.

As explained in Chapter 2, the tumour evolution is not only a result of increased proliferation but also of reduced programmed cell death (apoptosis) in cancer cells. To account for the fact that cell death does not only occur due to the lack of nutrients or oxygen (necrosis), we also include the process of apoptosis in our model as a cell loss rate added to the RHS of the equations for both proliferating (Eq. 3.8) and hypoxic (Eq. 3.9) cells. Hence, when apoptosis is included, the

rates of change in the concentration of proliferating, hypoxic and necrotic cells (Eq. 3.8-Eq.3.10) become:

$$\frac{\partial p(\mathbf{x},t)}{\partial t} = \bigtriangledown \cdot (d(\mathbf{x},t) \bigtriangledown p(\mathbf{x},t)) + g(\eta(\mathbf{x},t)) \cdot p(\mathbf{x},t) \cdot \left(1 - \frac{r(\mathbf{x},t)}{\Theta}\right) - f(\eta(\mathbf{x},t)) \cdot p(\mathbf{x},t) - c_{apop} \cdot p(\mathbf{x},t) \quad (3.14)$$

$$\frac{\partial q(\mathbf{x},t)}{\partial t} = \bigtriangledown \cdot (d(\mathbf{x},t) \bigtriangledown q(\mathbf{x},t)) + f(\eta(\mathbf{x},t)) \cdot p(\mathbf{x},t) - h(\eta(\mathbf{x},t)) \cdot q(\mathbf{x},t) - c_{apop} \cdot q(\mathbf{x},t) \quad (3.15)$$

$$\frac{\partial n(\mathbf{x},t)}{\partial t} = h(\eta(\mathbf{x},t)) \cdot q(\mathbf{x},t) \quad (3.16)$$

In these equations for proliferative and hypoxic cell concentration (Eq. 3.14 and Eq. 3.15) we not only account for cell loss due to hypoxia and necrosis, but also account for spontaneous cell death due to apoptosis with a rate given by c_{apop}. Cells dying due to apoptosis are assumed to be removed directly (within the same simulation time step) by local macrophages, justified by the fact that the steps of apoptosis including cellular membrane disruption, breaking down of cytoplasmic and nuclear skeletons, extrusion of the cytosol, chromosome degradation and fragmentation of the nucleus all happen in a span of 30 to 120 min [4]. These cells therefore do not contribute to the number of necrotic cells, and hence the equation describing the necrotic cell concentration evolution remains unchanged.

3.1.2 Numerical implementation

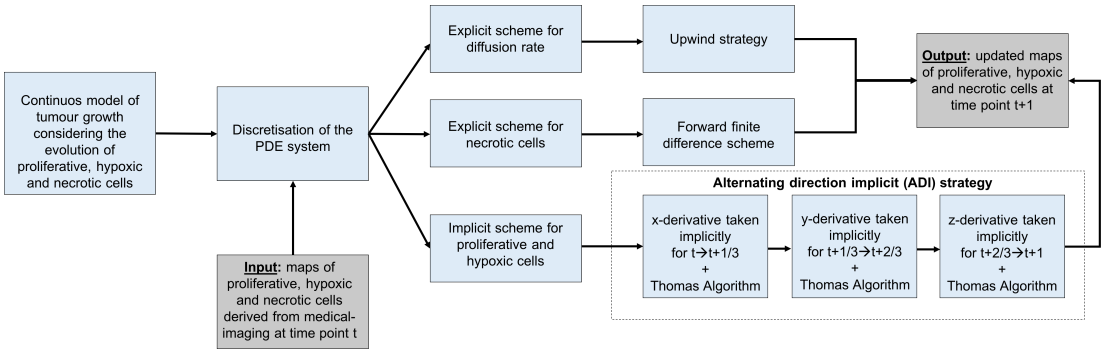


Figure 3.2: Schematic diagram of the numerical implementation approach to solve the system of equations: Eq. 3.8, 3.9 and 3.10. The first step consists of discretisation of the PDEs. A mix of implicit and explicit schemes are chosen to solve the set of PDEs. To solve the set of discretised equations on a 3D domain, an Alternating Direction Implicit (ADI) scheme [94], which consists of splitting the equations into three sets of equations in each direction x,y and z. Using this scheme allows for fast solution of the discretised equations as it results in equations of tridiagonal matrices. These matrices can then be inverted using the Thomas Algorithm [95]. Maps of proliferative, hypoxic and necrotic cells of time point t can be used as input into the discretised model, so that after solution over the whole 3D domain, maps of proliferative, hypoxic and necrotic cells for $t+1$ are obtained as an output.

3.1.2.1 Continuous model

Next, we present the numerical strategy developed to solve the system of equations, in particular Eq. 3.8, 3.9 and 3.10. An overview of the strategy is shown in Fig. 3.3. We recall that the system of section 3.1.1 predicting the tumour dynamics in Eq. 3.8-3.10 at each spatial location $\mathbf{x}$ and each time t is:

$$\begin{cases} \frac{\partial p}{\partial t} &= \bigtriangledown(d \bigtriangledown p) + g(\eta)p\left(1 - \frac{r}{\Theta}\right) - f(\eta)p - c_{apop}p \\ \frac{\partial q}{\partial t} &= \bigtriangledown(d \bigtriangledown q) + f(\eta)p - h(\eta)q - c_{apop}q \\ \frac{\partial n}{\partial t} &= h(\eta)q\,, \end{cases}$$

where p, q, n are the amount of proliferating, hypoxic and necrotic cells, respectively. Note that these scalar fields are defined for each $(\mathbf{x}, t)$. The diffusion coefficient d was modelled by a scalar field $d = D_0 \exp(-r/\kappa)$ in Eq. 3.13, where r is the total number of cells ($r = p + q + n$) and D_0 is a model parameter. Local proliferation, hypoxia and necrosis rate g, f and h are given by Eq. 3.5-3.7 and are directly related to the nutrient distribution η (Eq. 3.11). Finally, given the motivation of constraining the model using medical-imaging, we choose each grid point to correspond to an imaging voxel so that Θ represents the volume of a voxel divided by the volume of a tumour cell, as defined in section 4.1.3. On a 3D domain, this system is therefore:

$$\begin{cases} \frac{\partial p}{\partial t} &= \frac{\partial d}{\partial x}\frac{\partial p}{\partial x} + \frac{\partial d}{\partial y}\frac{\partial p}{\partial y} + \frac{\partial d}{\partial z}\frac{\partial p}{\partial z} + d\frac{\partial^2 p}{\partial x^2} + d\frac{\partial^2 p}{\partial y^2} + d\frac{\partial^2 p}{\partial z^2} + A \\ \frac{\partial q}{\partial t} &= \frac{\partial d}{\partial x}\frac{\partial q}{\partial x} + \frac{\partial d}{\partial y}\frac{\partial q}{\partial y} + \frac{\partial d}{\partial z}\frac{\partial q}{\partial z} + d\frac{\partial^2 q}{\partial x^2} + d\frac{\partial^2 q}{\partial y^2} + d\frac{\partial^2 q}{\partial z^2} + B \\ \frac{\partial n}{\partial t} &= C\,, \end{cases}$$

where, at each point $(\mathbf{x}, t)$, $A = (1 - r/\Theta)gp - fp - c_{apop}p$, $B = fp - hq - c_{apop}q$, and $C = hq$.

3.1.2.2 Discrete model

We denote $s^{\tau}_{i,j,k}$ the value of a scalar field s at voxel (i, j, k) and at time $t = \tau\Delta t$, where s is p, q, n, r or d in practice. When solving partial differential equations using finite difference schemes, one necessary condition for the convergence of numerical solutions is to consider the Courant-Friedricks-Lewy (CFL) condition [96]. This condition states that the time step length must be kept small enough so that information from a given grid point only propagates to its immediate neighbours during this time step. If this condition is not met, information can travel through two or more grid points at each time step and this can affect convergence neg-

atively. Because implicit schemes use the entire domain to calculate each time step, they lack a CFL condition. To avoid managing CFL conditions, we adopt an implicit finite differences strategy to make the scheme for solving the non-linear PDE set more stable than when using an explicit scheme.

For proliferating cells p we then use:

$$\begin{aligned}\frac{p^{\tau+1}_{i,j,k} - p^{\tau}_{i,j,k}}{\Delta t} &= \delta_x(d^{\tau}_{i,j,k}) \cdot \frac{p^{\tau+1}_{i+1,j,k} - p^{\tau+1}_{i-1,j,k}}{2\Delta x} \\ &+ \delta_y(d^{\tau}_{i,j,k}) \cdot \frac{p^{\tau+1}_{i,j+1,k} - p^{\tau+1}_{i,j-1,k}}{2\Delta y} \\ &+ \delta_z(d^{\tau}_{i,j,k}) \cdot \frac{p^{\tau+1}_{i,j,k+1} - p^{\tau+1}_{i,j,k-1}}{2\Delta z} \\ &+ d^{\tau}_{i,j,k} \cdot \frac{p^{\tau+1}_{i+1,j,k} - 2p^{\tau+1}_{i,j,k} + p^{\tau+1}_{i-1,j,k}}{\Delta x^2} \\ &+ d^{\tau}_{i,j,k} \cdot \frac{p^{\tau+1}_{i,j+1,k} - 2p^{\tau+1}_{i,j,k} + p^{\tau+1}_{i,j-1,k}}{\Delta y^2} \\ &+ d^{\tau}_{i,j,k} \cdot \frac{p^{\tau+1}_{i,j,k+1} - 2p^{\tau+1}_{i,j,k} + p^{\tau+1}_{i,j,k-1}}{\Delta z^2} \\ &+ A^{\tau}_{i,j,k}\,, \end{aligned} \tag{3.17}$$

where an upwind strategy [97] approximates the first-order derivatives δ_x, δ_y, and δ_z of $d^{\tau}_{i,j,k}$, *e.g.*:

$$\delta_x(d^{\tau}_{i,j,k}) = \begin{cases} \dfrac{d^{\tau}_{i,j,k} - d^{\tau}_{i-1,j,k}}{\Delta x}, & \text{if } p^{\tau}_{i+1,j,k} \leq p^{\tau}_{i-1,j,k} \\ \dfrac{d^{\tau}_{i+1,j,k} - d^{\tau}_{i,j,k}}{\Delta x}, & \text{otherwise} \end{cases} \tag{3.18}$$

We note that these spatial derivatives are the only ones which are estimated explicitly. This allows for a much simpler solution of the PDE than when using an implicit formulation, given that d is relatively stable in space (see Eq. 3.13).

The equation for hypoxic cells q is the same as Eq. 3.17 except for p and A which are replaced by q and B. For the necrotic cells n, we finally have $n^{\tau+1}_{i,j,k} =$

$n^{\tau}_{i,j,k} + \Delta t \cdot C^{\tau}_{i,j,k}$. In what follows, we only explain how we solve the evolution of proliferative cells, using the fact that the equations for proliferative and hypoxic cells are analogous, and the equation for necrotic cells can be solved using a simple Euler scheme as it does not contain any spatial derivative.

3.1.2.3 Alternating Direction Implicit scheme

Directly solving Eq. 3.17 on a 3D domain can be extremely time consuming as it requires the inversion of a large (square of the number of image voxels) block tridiagonal matrix at each considered τ. One way to efficiently solve these equations it to use the Alternating Direction Implicit (ADI) scheme [94] , which consists of splitting the finite difference equations into three sets of equations which are solved in three steps: first, x is taken implicitly from τ to $\tau + 1/3$, then y is taken implicitly from $\tau + 1/3$ to $\tau + 2/3$; and finally, z is taken implictily from $\tau + 2/3$ to $\tau + 1$. The advantage of the ADI scheme is that it results in equations where only tridiagonal matrices need to be inverted. These can be solved efficiently using the Thomas Algorithm [95]. Following this strategy, Eq. 3.17 is then solved as follows:

(Step 1: Sweep in x) For all (j,k):

$$\begin{pmatrix} p^{\tau+1/3}_{1,j,k} \\ p^{\tau+1/3}_{2,j,k} \\ \vdots \\ p^{\tau+1/3}_{I,J,K} \end{pmatrix} = \begin{pmatrix} w^{\tau}_{1,1,j,k} & w^{\tau}_{2,1,j,k} & & 0 \\ w^{\tau}_{3,2,j,k} & w^{\tau}_{1,1,j,k} & \ddots & \\ & \ddots & \ddots & w^{\tau}_{2,I-1,j,k} \\ 0 & & w^{\tau}_{3,I,j,k} & w^{\tau}_{1,I,j,k} \end{pmatrix} \cdot \left[\begin{pmatrix} p^{\tau}_{1,j,k} \\ p^{\tau}_{2,j,k} \\ \vdots \\ p^{\tau}_{I,J,K} \end{pmatrix} + \begin{pmatrix} A^{\tau}_{1,j,k} \\ A^{\tau}_{1,j,k} \\ \vdots \\ A^{\tau}_{I,J,K} \end{pmatrix} \right], \quad (3.19)$$

(Step 2: sweep in y) For all (i,k):

$$\begin{pmatrix} p^{\tau+2/3}_{i,1,k} \\ p^{\tau+2/3}_{i,2,k} \\ \vdots \\ p^{\tau+2/3}_{I,J,K} \end{pmatrix} = \begin{pmatrix} w^{\tau+1/3}_{1,i,1,k} & w^{\tau+1/3}_{4,i,1,k} & & 0 \\ w^{\tau+1/3}_{5,i,2,k} & w^{\tau+1/3}_{1,i,2,k} & \ddots & \\ & \ddots & \ddots & w^{\tau+1/3}_{4,i,J-1,k} \\ 0 & & w^{\tau+1/3}_{5,i,J,k} & w^{\tau+1/3}_{1,i,J,k} \end{pmatrix} \cdot \left[\begin{pmatrix} p^{\tau+1/3}_{i,1,k} \\ p^{\tau+1/3}_{i,2,k} \\ \vdots \\ p^{\tau+1/3}_{I,J,K} \end{pmatrix} + \begin{pmatrix} A^{\tau+1/3}_{i,1,k} \\ A^{\tau+1/3}_{i,2,k} \\ \vdots \\ A^{\tau+1/3}_{I,J,K} \end{pmatrix} \right], \quad (3.20)$$

(Step 3: sweep in z) For all (i,j):

$$\begin{pmatrix} p_{i,j,1}^{\tau+1} \\ p_{i,j,1}^{\tau+1} \\ \vdots \\ p_{I,J,K}^{\tau+1} \end{pmatrix} = \begin{pmatrix} w_{1,i,j,1}^{\tau+2/3} & w_{6,i,j,1}^{\tau+2/3} & & 0 \\ w_{7,i,j,2}^{\tau+2/3} & w_{1,i,j,2}^{\tau+2/3} & \ddots & \\ & \ddots & \ddots & w_{6,i,j,K-1}^{\tau+2/3} \\ 0 & & w_{7,i,j,K}^{\tau+2/3} & w_{1,i,j,K}^{\tau+2/3} \end{pmatrix} \cdot \left[\begin{pmatrix} p_{i,j,1}^{\tau+2/3} \\ p_{i,j,2}^{\tau+2/3} \\ \vdots \\ p_{I,J,K}^{\tau+2/3} \end{pmatrix} + \begin{pmatrix} A_{i,j,1}^{\tau+2/3} \\ A_{i,j,2}^{\tau+2/3} \\ \vdots \\ A_{I,J,K}^{\tau+2/3} \end{pmatrix} \right], \quad (3.21)$$

where:

$$\begin{aligned}
w_{1,i,j,k}^{\tau} &= 1 + \tfrac{2\Delta t}{3\Delta x^2} \cdot d_{i,j,k}^{\tau}, \\
w_{2,i,j,k}^{\tau} &= -\tfrac{\Delta t}{3} \cdot \left(\tfrac{\delta_x(d_{i,j,k}^{\tau})}{2\Delta x} + \tfrac{d_{i,j,k}^{\tau}}{\Delta x^2} \right), \\
w_{3,i,j,k}^{\tau} &= -\tfrac{\Delta t}{3} \cdot \left(-\tfrac{\delta_x(d_{i,j,k}^{\tau})}{2\Delta x} + \tfrac{d_{i,j,k}^{\tau}}{\Delta x^2} \right), \\
w_{1,i,j,k}^{\tau+1/3} &= 1 + \tfrac{2\Delta t}{3\Delta y^2} \cdot d_{i,j,k}^{\tau+1/3}, \\
w_{4,i,j,k}^{\tau+1/3} &= -\tfrac{\Delta t}{3} \cdot \left(\tfrac{\delta_z(d_{i,j,k}^{\tau+1/3})}{2\Delta z} + \tfrac{d_{i,j,k}^{\tau+1/3}}{\Delta x^2} \right), \\
w_{5,i,j,k}^{\tau+1/3} &= -\tfrac{\Delta t}{3} \cdot \left(-\tfrac{\delta_y(d_{i,j,k}^{\tau+1/3})}{2\Delta y} + \tfrac{d_{i,j,k}^{\tau+1/3}}{\Delta y^2} \right), \\
w_{1,i,j,k}^{\tau+2/3} &= 1 + \tfrac{2\Delta t}{3\Delta z^2} \cdot d_{i,j,k}^{\tau+2/3}, \\
w_{6,i,j,k}^{\tau+2/3} &= -\tfrac{\Delta t}{3} \cdot \left(\tfrac{\delta_z(d_{i,j,k}^{\tau+2/3})}{2\Delta z} + \tfrac{d_{i,j,k}^{\tau+2/3}}{\Delta z^2} \right), \\
w_{7,i,j,k}^{\tau+2/3} &= -\tfrac{\Delta t}{3} \cdot \left(-\tfrac{\delta_z(d_{i,j,k}^{\tau+2/3})}{2\Delta z} + \tfrac{d_{i,j,k}^{\tau+2/3}}{\Delta z^2} \right).
\end{aligned}$$

The equations 3.19, 3.20 and 3.21 are solved using the Thomas Algorithm [95].

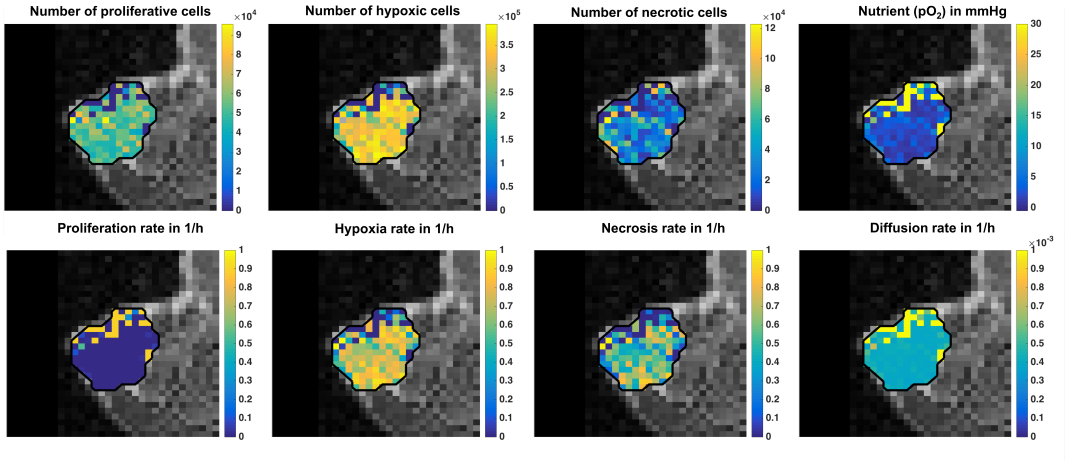


Figure 3.3: Example of cellularity and nutrient maps used as input in the model (top row). Using these input maps and, Eq. 3.5, Eq. 3.6, Eq. 3.7 and Eq. 3.13, initial maps of proliferation (g), hypoxia (f), necrosis (h) and diffusion (d) rates can be computed, respectively (bottom).

3.1.3 Input and parameter maps

Different maps are needed to initialise, calibrate and verify our reaction-diffusion model: The number of proliferating cells (p), the number of hypoxic cells (q), the number of necrotic cells (n), the total number of tumour cells (r) and the nutrient distribution (η). These maps could in theory be derived from multiple imaging modalities as discussed in Chapter 2. Here, we use example input maps for one pre-clinical case of the data set which will be introduced, described and evaluated in Chapter 4 (see Fig. 3.3 (top)).

Using these input maps in Eq. 3.5, Eq. 3.6, Eq. 3.7 and Eq. 3.13, initial maps of proliferation (g), hypoxia (f), necrosis (h) and diffusion (d) rates can be computed, respectively (see Fig. 3.3 (bottom)). These maps as well as the computation of the cellularity maps for the next simulation time point depend on the choice of the following parameters: c_{g_0}, c_{f_0}, c_{h_0} and D_0. To allow for a more conscious choice about whether and what parameters should be optimised, in the section that follows we perform a closer examination of each model parameter.

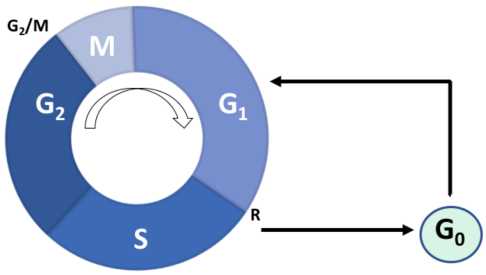


Figure 3.4: Cell cycle dynamics including proliferation phases (G1, S, G2, M), quiescent phase (G0) and checkpoints (R and G2/M).

3.1.4 Analysis of tumour-specific parameters

One of the most important aspects of tumour growth is given by the proliferation of cells. To complete proliferation, cells need to pass through a series of stages, known collectively as the cell cycle. The cell cycle shown in Fig. 3.4 contains proliferating phases (G1, S, G2, M), a resting phase (G0) and numerous checkpoints which control cycle progression and check any DNA damage. Successful progression from one phase to the next depends highly on nutrient availability. In particular, for insufficient pO_2 at the restriction (R) checkpoint after the G1 phase, the cell might exit the cell cycle and enter a quiescent state, i.e. the G0 phase. If conditions improve, quiescent cells might re-enter the cell cycle. However, in case of sustained low pO_2 level, apoptosis or necrosis might be induced as a response to hypoxia [98].

To account for cell-cycle dynamics, in [79, 21], the authors assume that cells progress from one phase to another with given probabilities. Because they follow each tumour cell through each phase of its cell-cycle, and a tumour consists of billions of cells, their approach is very computationally expensive. To overcome this limitation, while accounting for cells with different activities within a single voxel, here we simplify the cell-cycle and differentiate only between a proliferation phase (combining phases G1, S, G2 and mitosis), a hypoxic phase (G0) and a

necrotic phase.

As oxygen (pO_2) is the driving nutrient for this model, cells progress through the cell-cycle, i.e. divide, turn quiescent (included as part of the hypoxic cells) or die depending on their local oxygen level. Because the data used in this thesis is of pre-clinical nature, we assume the nutrient in the host tissue, η_0, to be $30mmHg$, a common value found for subcatenous tumours in mice [99].

As mentioned earlier, cells which are in proliferation phases are subject to numerous checkpoints during the cell-cycle to control cycle progression and check for any DNA damage. That means that not all cells which are in a nutrient rich environment will undergo cell division. But, it also allows for some cells where the nutrient level is just about sufficient to proceed, if they are successful at the different checkpoints. To mimic this behaviour, the proliferation rate, $g(n)$, is modelled as a function of pO_2 distribution following a Gompertz evolution given by Eq. 3.5. In this function, the maximum local proliferation rate is given by G_{max}. Since $g(n)$ will vary with space, as it depends on the local pO_2, and c_{g_0} dictates the rate of this dependency, G_{max} can be set as a constant. Common values for the proliferation rate found in the literature range e.g. from 6.4 $year^{-1}$ [100] to 97.44 $year^{-1}$ [15]. To allow for our proliferation rates to be within this range, and taking into account that here we measure the proliferation rate in 1/hour, G_{max} is set to $1hour^{-1}$. This results in a range for $g(n)$ of $[0, 1]$ $hour^{-1}$. We note that this value alone would amount to a doubling time that is very much less than the ones expected in cancer biology (typically 1 day^{-1}). However, the fact that G_{max} is still multiplied by the term $\exp(-\exp(-c_{g_0} \cdot (\eta(\mathbf{x}, t) - ip))$, the *de facto* global doubling time (which can be seen as an average over the proliferation rate map produced with this model given the dependency of c_{g_0} on the local $\eta(\mathbf{x}, t)$) counteracts this disparity. The parameter ip represents the oxygen

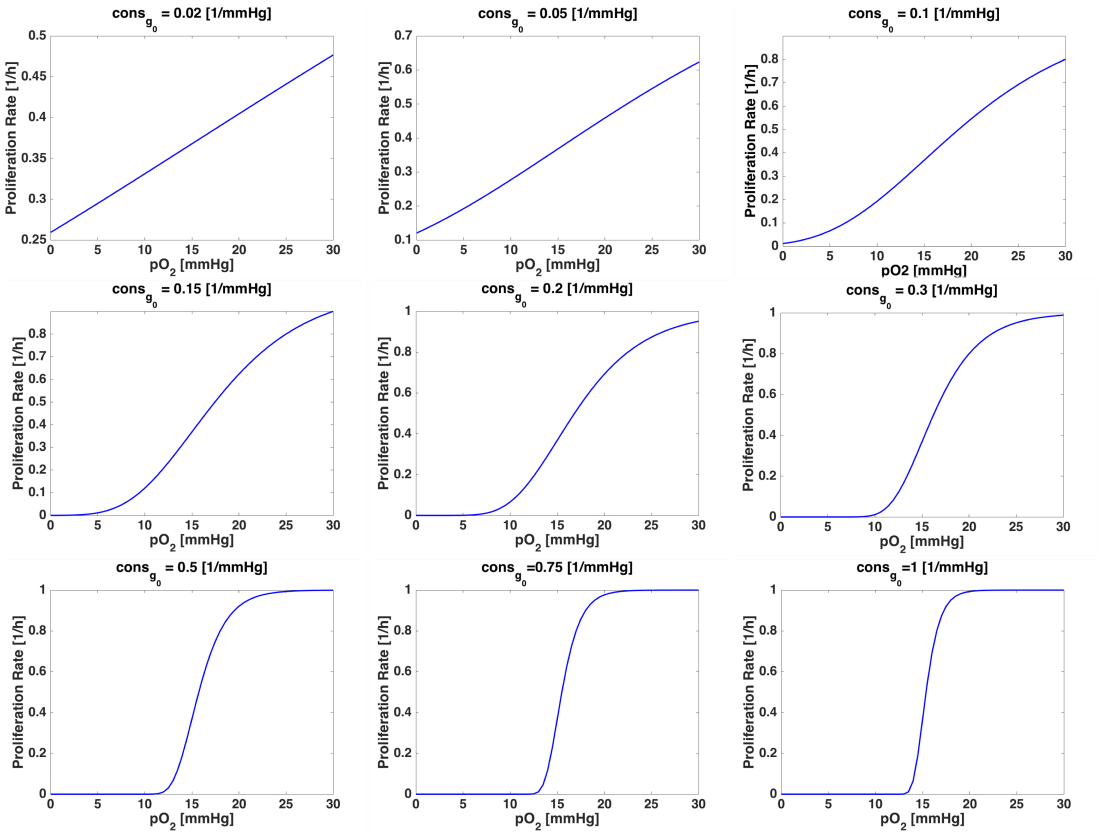


Figure 3.5: Proliferation rate in 1/h as a function of local pO_2 level for different values of c_{g_0}. The values range from 0.05 to 1 $mmHg^{-1}$.

level at the inflection point, which we take to be at the centre of the curve, so that $ip = 15mmHg$.

To analyse the behaviour of $g(n)$ in function of c_{g_0}, the proliferation rate distributions $g(\eta)$ for different values of c_{g_0} are shown in Fig. 3.5. For very small values of c_{g_0} (top row), the Gompertz evolution is almost a straight line for the given nutrient range (0-30$mmHg$) meaning that cells will divide at lower levels of oxygen, at a small proliferation rate. For higher values of c_{g_0} (bottom row), all cells which have access to a nutrient amount above the critical value (given by ip) will be proliferating at the G_{max} value. However, cells will not proliferate ($g = 0$) below this critical value. The graphs in the middle row represent a compromise between the conditions in the top and the bottom rows: proliferative cells might

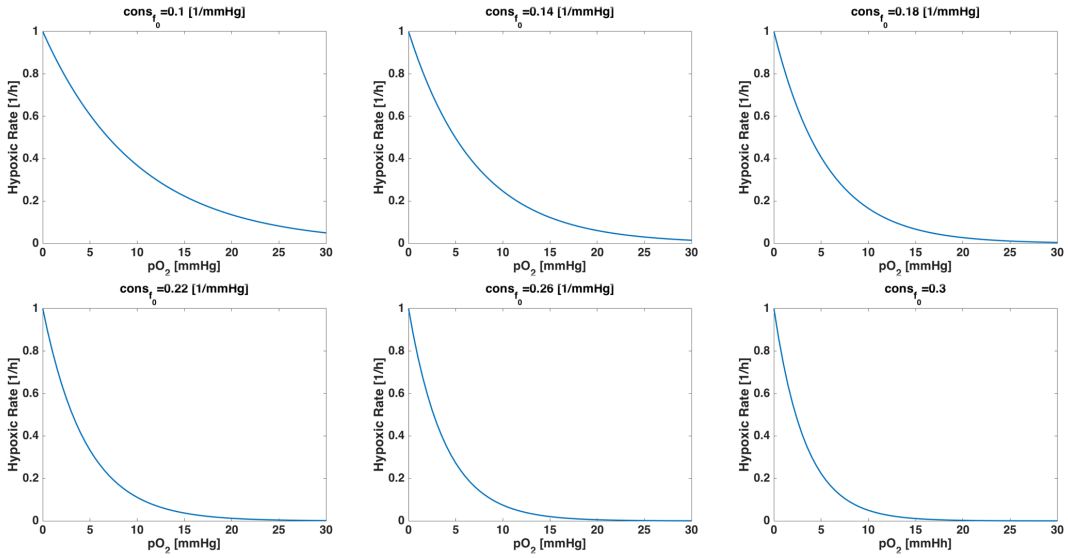


Figure 3.6: Hypoxic rate in 1/h as a function of local pO_2 level available for different values of c_{f_0}. The values range from 0.1 to 0.3 $mmHg^{-1}$ showing that the higher c_{f_0} (bottom row), the smaller the range for which hypoxic cells will be created (for instance for $c_{f_0} = 0.3mmHg^{-1}$ no proliferative cells above $15mmHg$ will turn hypoxic). The graphs for smaller c_{f_0} (top row) represent a state in which even in nutrient rich environments hypoxic cells would be created at a small rate.

not achieve their maximum cell division potential, G_{max}; however, the transition between not proliferating and proliferating is smoother, allowing for cells which might be in a voxel containing $10mmHg$, for instance, to proliferate, but at a much lower rate than the ones seen for smaller values of c_{g_0}. Following this analysis, we choose the range for this parameter to be $c_{g_0} = [0.15 - 0.3]\, mmHg^{-1}$, to model the fact described above that cells with moderate pO_2 might successfully progress through the cell-cycle.

Similarly to the analysis for the proliferation rate, Fig. 3.6 demonstrates how the rate at which proliferative cells turn hypoxic depend on pO_2 and the parameter c_{f_0}. The values range from 0.1 to 0.3 $mmHg^{-1}$ showing that the higher c_{f_0} (bottom row), the smaller the range for which hypoxic cells will be created (for instance for $c_{f_0} = 0.3mmHg^{-1}$ no proliferative cells above $15mmHg$ will turn hypoxic). The graphs for smaller c_{f_0} (top row) represent a state in which even in nutrient rich environments hypoxic cells are created at a small rate.

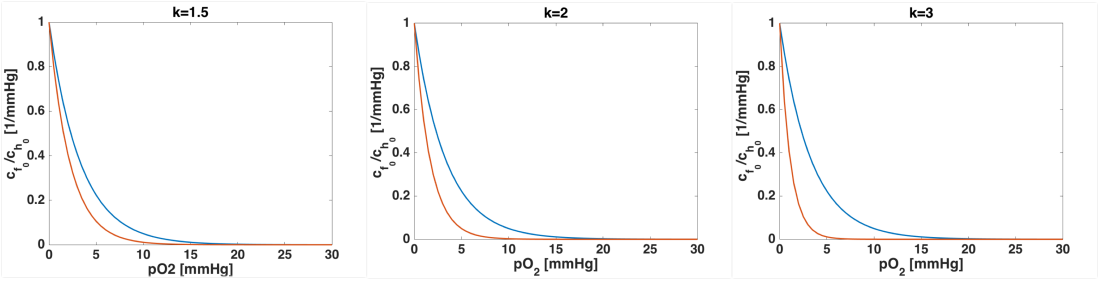


Figure 3.7: Hypoxic (blue) and necrotic rates (red) (1/mmHg) as a function of local pO_2. To ensure that necrosis will occur at a lower nutrient level than hypoxia, a linear relationship, $c_{h_0} = kc_{f_0}$, between the two constants is explored. The graphs show this relationship for different values of k, with $k > 1$. For all three figures, $c_{f_0} = 0.3mmHg^{-1}$ was used.

To model the fact that necrosis occurs at a lower nutrient level than hypoxia, and to prevent that during optimisation c_{h_0} gets assigned a value smaller than c_{h_0} (which would lead to necrosis occurring at a higher nutrient level than hypoxia), we set the relationship $c_{h_0} = kc_{f_0}$ with $k > 1$. Fig. 3.7 depicts this relationship for different values of k. For $k = 1.5$ (left), the transition between hypoxia and necrosis is not as clear as for the case where $k = 3$ (right), as the curves are still too close together. For $k = 3$, the range of pO_2 values within which necrosis is allowed to happen is too small; the situation is even more pronounced for large values of c_{f_0}. Under these observations, $k = 2$ (middle) represents a compromise between the other two, as it allows for necrosis to happen for a wider range of po_2 values while providing for a clear, smooth transition between necrosis and hypoxia. Setting k as a constant has the added benefit of further reducing the number of parameters that need calibration.

In addition to proliferation, hypoxia and necrosis, our model also considers the process of apoptosis in terms of a cell loss rate. To find an appropriate range for this parameter, we turn to the literature on apoptotic rates, and find values that range from 0 to 15% [101, 102]. Apoptotic rates are measured in %. However, to ensure Eq. 3.14 and Eq. 3.15 are dimensionally correct, our apoptotic rate needs to be in $hour^{-1}$. Our previous assumption that apoptotic cells disappear within

one hour (during a simulation time step) allows us to simply convert the values found in the literature into a range for our c_{apop} measured in $hour^{-1}$.

Tumour growth is not only a result of cell proliferation, hypoxia and necrosis, but also of cell invasion into the host tissue. Our model accounts for this effect in terms of a diffusion process, as given in Eq. 3.13. Common values for the diffusion rate found in the literature range e.g. from $7 \cdot 10^{-4}\, mm^2/day$ to $0.03\, mm^2/day$ [17, 15]. Taking these values and the fact that our diffusion rate is measured in $mm^2/hour$ into account, yields a range for D_0 of around $[1 \cdot 10^{-5}, 1 \cdot 10^{-3}]\ mm^2/hour$.

Summarising, the analysis presented in this section results in the following ranges for our model parameters:

$$\begin{aligned} 0.15\, mmHg^{-1} &\leq c_{g_0} \leq 0.50\, mmHg^{-1} \\ 0.05\, mmHg^{-1} &\leq c_{f_0} \leq 0.3\, mmHg^{-1} \\ 0\, hour^{-1} &\leq c_{apop} \leq 0.15\, hour^{-1} \\ 1 \cdot 10^{-5}\, mm^2/h &\leq D_0 \leq 1 \cdot 10^{-3}\, mm^2/h \end{aligned} \tag{3.22}$$

In the next section, we describe experiments which include a more detailed analysis of how each parameter influences the model output.

3.2 Experiments

3.2.1 Sensitivity analysis

To explore whether all of our model parameters explained in the previous section influence our model outcome, we performed a sensitivity analysis using the eFAST

method as described in [103]. The reference outputs were the number of total cells, number of necrotic cells and the estimated tumour volume, r, n, and vol_s, respectively. To determine the significance of the eFAST first-order indices, we followed the procedure described in [103] and included a dummy parameter into the analysis. Parameters with a sensitivity index with less than that of the dummy parameter should not be considered significantly different from zero.

3.2.2 Relationship between SGR and model parameters

Given that all our parameters have an influence on tumour volumetric growth, we explore whether a relationship between the volumetric growth can be found. Such a relationship would yield a more conscious choice on the parameter ranges, as the volumetric growth is a measure that can be directly extracted from two consecutive medical imaging scans. In the clinic, tumour growth is usually expressed by the tumour volume doubling time. However, the authors in [104] were able to demonstrate that the specific growth rate (SGR) is biologically more relevant than the doubling time and a convenient measure of tumour growth when there is uncertainty in the estimation of the growth rate, and hence it should be used to quantify tumour growth [105]. For a tumour assumed to grow exponentially, the growth rate is proportional to its volume, V, as follows:

$$\frac{dV}{dt} = SGR \cdot V \tag{3.23}$$

The solution of this equation yields the well-known exponential equation of tumour volumetric growth:

$$V(t_2) = V(t_1) \cdot \exp\left(SGR \cdot (t_2 - t_1)\right), \tag{3.24}$$

so that SGR can be computed as:

$$SGR = \log(V(t_2)/V(t_1))/(t_2 - t_1). \tag{3.25}$$

To this end, 1000 tumours were generated using random parameters within the ranges given in Eq. 3.22, their volumetric growth after 24 hours simulated and the SGR for each of the 1000 cases computed. The simulated volume, vol_s was obtained by producing an apparent boundary on the simulated tumour based on $r(x, t_2)$. Due to the diffusion term, all voxels on the image might contain some tumour cells even though those would not be visible on a scan. In order to delineate the tumour, we assume that if a voxel contains less than 500 tumour cells, then this voxel is not a part of the tumour as only 0.1% of its capacity will be made out of tumour cells. We then multiplied the number of voxels by the voxel volume to obtain the vol_s in mm^3.

Because we are also interested in understanding how apoptosis influences tumour volumetric growth, we include two sets of experiments: one in which an apoptotic rate is chosen within the range given in Eq. 3.22 and one where the apoptotic rate is set to zero, and hence does not affect the simulation outcome.

3.2.3 Simulations

In order to evaluate how different sets of model parameters influence tumour growth, we performed simulations with 20 different synthetic tumours generated using 20 different parameter sets (see Tab. 3.1) within the ranges given in Eq. 3.22. Each tumour was initialised using maps from one of the available preclinical DCE-MRI cases (see Chapter 4) and simulations were performed for 96

hours, whereby a simulation time step of 1 hour was adopted. To test the effect of apoptosis on overall tumour growth, we also account for the case without apoptosis ($c_{apop} = 0\, hour^{-1}$).

	Parameters			
Cases	$c_{g_0}(1/mmHg)$	$c_{f_0}(1/mmHg)$	$D_0(mm^2/h)$	$c_{apop}(1/h)$
1	0.280	0.1889	$4.88e-4$	0.059
2	0.1567	0.0737	$2.80e-5$	0.086
3	0.476	0.157	$8.04e-5$	0.076
4	0.227	0.127	$4.12e-5$	0.012
5	0.181	0.232	$1.58e-5$	0.028
6	0.341	0.099	$2.0\ e-4$	0.107
7	0.302	0.089	$8.16e-5$	0.066
8	0.335	0.107	$1.88e-5$	0.041
9	0.463	0.102	$3.5\ e-4$	0.026
10	0.174	0.149	$3.3\ e-4$	0.070
11	0.177	0.051	$7.46e-5$	0.052
12	0.219	0.211	$2.91e-4$	0.100
13	0.374	0.189	$4.23e-4$	0.022
14	0.262	0.280	$4.45e-5$	0.022
15	0.186	0.183	$3.29e-4$	0.122
16	0.346	0.089	$1.59e-5$	0.114
17	0.300	0.096	$1.68e-5$	0.064
18	0.399	0.299	$1.85e-4$	0.148
19	0.380	0.248	$2.75e-4$	0.095
20	0.482	0.152	$4.55e-4$	0.061

Table 3.1: Parameters used to generate 20 synthetic tumours. For the case where no apoptosis was included in the model, c_{apop} is set to 0, but all the remaining parameters are the same. These parameters were generated randomly in the range given in Eq. 3.22.

3.3 Results

3.3.1 Sensitivity analysis

The sensitivity analysis on the tumour volume, for a total of 1285 model evaluations, yielded first-order sensitivity indices as listed in Tab. 3.2. The highlighted values represent the parameters that had the largest influence on the model out-

	Parameters				
Output	$c_{g_0}(1/mmHg)$	$c_{f_0}(1/mmHg)$	$D_0(mm^2/h)$	$c_{apop}(1/h)$	dummy
vol_s	0.3944	0.1904	**0.5161**	0.2056	0.0954
n	0.1886	**0.8613**	0.1229	0.3073	0.2631
r	0.3423	0.2268	**0.4227**	0.4032	0.1690

Table 3.2: First-order sensitivity indices for parameters of avascular tumour growth using the eFAST method as described in [103]. The reference outputs were vol_s, n and r.

puts (estimated volume, total and necrotic cell numbers). These results show that parameter with the most influence on tumour volume evolution is the diffusion rate. When considering total cell number as model output, the parameters with the most influence are diffusion and apoptosis rates. For the case where the necrotic cell number was considered as output, the highest sensitivity index was observed for the hypoxic rate.

These results imply that our tumour growth is mostly influenced by the diffusive character of the cells. Because this is also the parameter which has the largest range (across dimensions) we explored whether a case-specific range for the diffusion parameter could be obtained based on the specific growth rate (SGR). The results of this analysis are presented in the next section.

3.3.2 Relationship between SGR and model parameters

A total of 1000 tumours were generated using random parameters within the ranges given in Eq. 3.22. Using Eq. 3.2.2 and the resulting volumes, the SGR for each of the 1000 cases were computed. We performed a Pearson correlation analysis between SGR and all model parameters. Without apoptosis, this analysis yielded Pearson correlation coefficients of 0.0157, 0.1577 and 0.8816 for c_{g_0}, c_{f_0} and D_0, respectively. When apoptosis was included, the correlation coefficients were 0.0927, 0.2203, 0.8453, -0.20 for c_{g_0}, c_{f_0}, D_0, c_{apop}, respectively. For both

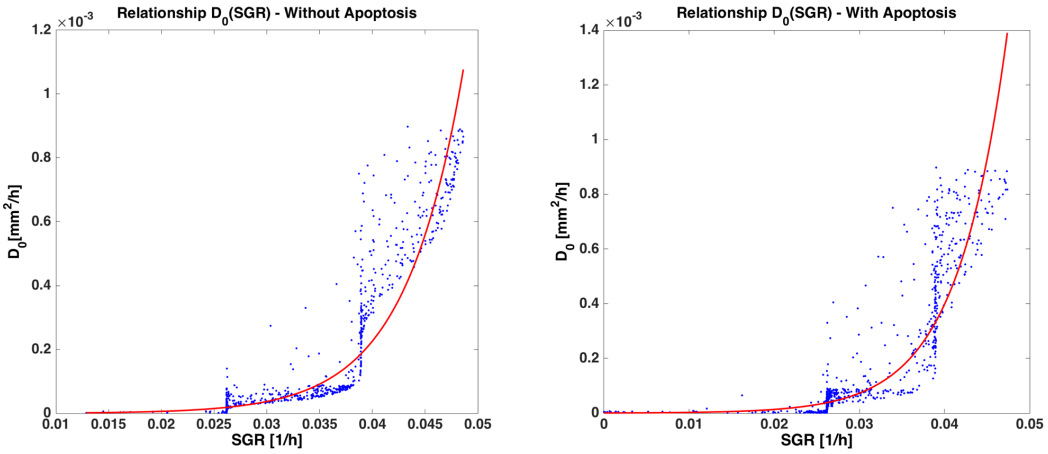


Figure 3.8: Plots of the results of 1000 simulations to determine the relationship between the diffusion constant, D_0, and SGR. We use exponential fitting curves and with a 99.99% confidence interval we obtain the minimum and maximum values for the exponential rate and the initial value of the functions, as shown in Eq. 3.26 and Eq. 3.27 for the cases without and with apoptosis, respectively.

cases the parameter D_0 demonstrated a much higher influence on SGR than all other parameters. We plot the values of D_0 as a function of SGR in Fig. 3.8. The observed straight lines (e.g. at $SGR = 0.038 hour^{-1}$) are probably related to the fact that different combinations of the proliferation (c_{g_0}) and diffusion (D_0) rates can lead to tumours of equal size. This effect has been reported in other studies which led to either the proliferation or the diffusion rate being kept constant in order to find an unique solution to the optimisation problem [10, 17]. This figure also shows that D_0 grows non-linearly with increasing SGR. We hence fitted the data to an exponential curve (Fig. 3.8). Using a 99.99% confidence interval for the fitting yielded a customised range, $[d_{min}(SGR), d_{max}(SGR)]$, of:

$$\begin{aligned} d_{min}(SGR) &= 5.46 \cdot 10^{-8} \cdot exp(SGR \cdot 166.6482)\, mm^2/h \\ d_{max}(SGR) &= 2.69 \cdot 10^{-7} \cdot exp(SGR \cdot 195.4765)\, mm^2/h \end{aligned} \tag{3.26}$$

for the case without apoptosis, and of:

$$\begin{aligned} d_{min}(SGR) &= 2.47 \cdot 10^{-7} \cdot exp(146.7288 \cdot SGR)\, mm^2/h \\ d_{max}(SGR) &= 9.53 \cdot 10^{-7} \cdot exp(173.7549 \cdot SGR)\, mm^2/h \end{aligned} \tag{3.27}$$

when apoptosis was accounted for.

3.3.3 Simulations

The effect of apoptosis on tumour volume is shown in Tab. 3.3. On average, apoptosis has the effect of reducing tumour volume for all time points, as indicated by the negative mean values.

To further illustrate this effect, Fig. 3.9 shows the comparison between the volumes obtained for simulations with and without apoptosis for Cases 1, 10, 11, 15, 16 and 17. These cases were chosen as examples of:

Relative volume difference	Day 2	Day 3	Day 4	Day 5
Mean	-0.04219	-0.08683	-0.0909	-0.08614
Std	0.10355	0.05989	0.0696	0.05999

Table 3.3: This table lists the mean and standard deviation (std) values for the relative tumour difference due to apoptosis for the 20 synthetic cases. The negative values indicate that apoptosis has a reducing effect on tumour volume for all time points (Days 2 to 5).

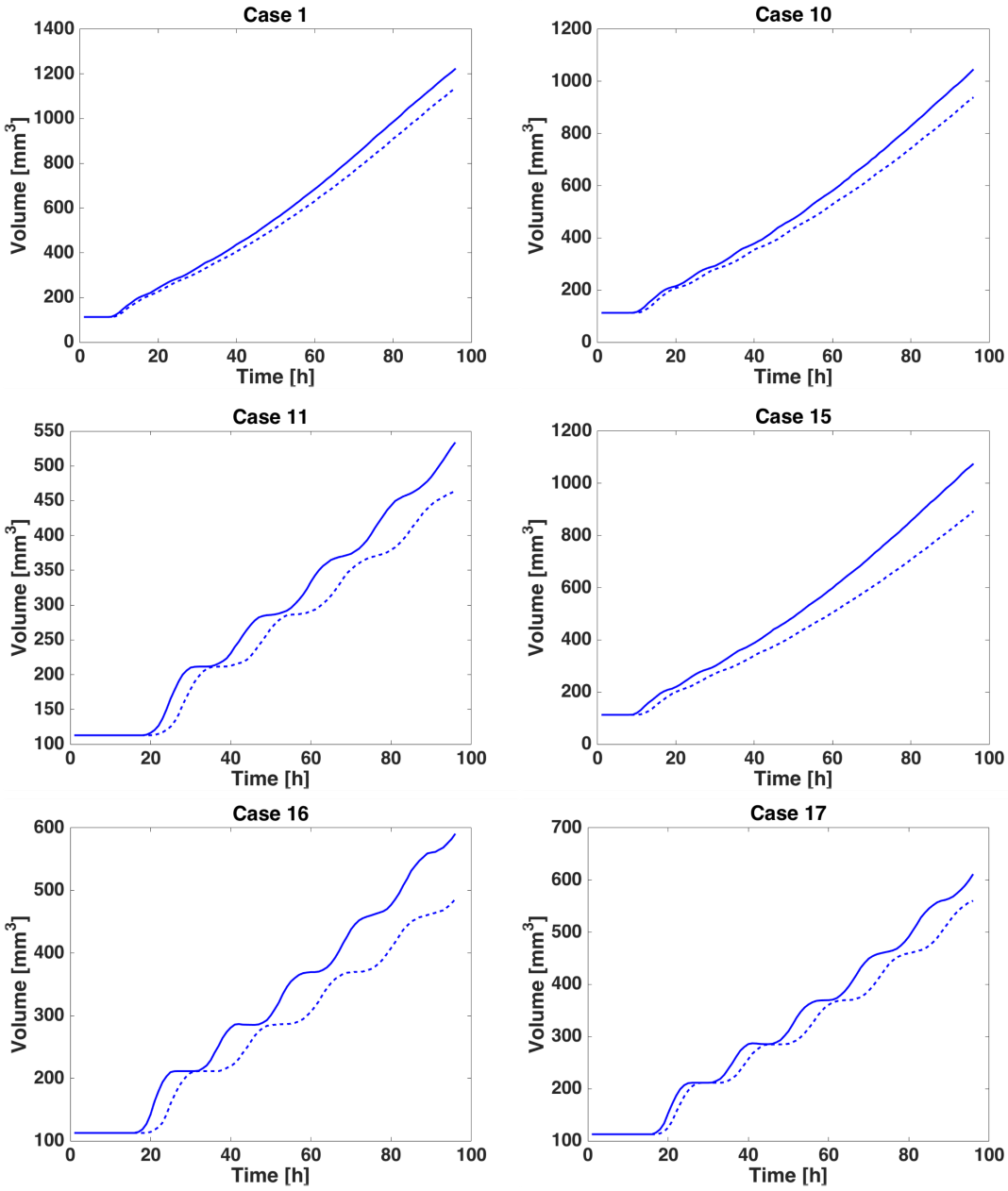


Figure 3.9: The effect of apoptosis on tumour volume evolution is shown for a range of synthetic cases. For all cases, the volume evolution graphs obtained when including apoptosis (dashed lines) were less steep than the ones where no apoptosis was included. The volume difference is larger for later simulation time points.

- Case 1: high c_{g_0}, high c_{f_0}, high D_0 and low c_{apop};
- Case 10: low c_{g_0}, intermediate c_{f_0}, high D_0 and low c_{apop};
- Case 11: low c_{g_0}, low c_{f_0}, low D_0 and low c_{apop};
- Case 15: low c_{g_0}, high c_{f_0}, high D_0 and high c_{apop}.
- Case 16: high c_{g_0}, low c_{f_0}, low D_0 and high c_{apop};
- Case 17: high c_{g_0}, low c_{f_0}, low D_0 and low c_{apop};

From this figure a trend can be observed, in which cases with higher D_0 (Cases 1, 10 and 15) depict a faster volume evolution and a higher tumour volume at the end of the simulation, than the ones with lower D_0 (Cases 11, 16 and 17). The latter demonstrate a gradual growth as opposed to the continuous growth observed for the ones with higher D_0. This gradual growth can be observed as elevations, which suggest that cells need to proliferate for a certain amount of time (e.g. 10 hours) until the tumour has enough pressure generated by the cells to expand again (given the dependency of the *de facto* local diffusion rate and the local cell number). For all cases, apoptosis has the effect of reducing the overall tumour volume evolution according to its magnitude - the higher the apoptosis, the higher the effect.

The cell evolution for each sub-population can also be obtained as a model output. For the Cases listed above, Fig. 3.10 depicts the evolution of proliferating (blue), hypoxic (green), necrotic (red) and total (black) cell numbers with and without apoptosis (dashed lines). In general, apoptosis has the effect of reducing total cell number. However, closer evaluation of each Case depending on its parameter set combination yields a more detailed understanding of how each parameter influences cellular evolution and the effect of apoptosis. In more detail:

- Case 1: From the analysis performed on Fig. 3.5 it became evident that

for high c_{g0}, the proliferation rate, $g(\eta)$ depicts a steeper shape, so that under a given pO_2 threshold no cells will proliferate. This along with a higher diffusion rate results in a larger tumour (volume) with a more pronounced proliferating rim (since cells within the tumour will not have access to enough pO_2 to undergo mitosis). As c_{f_0} is also high, and nutrient will be low inside the tumour (due to the higher tumour volume), more of the cells will turn hypoxic explaining why hypoxia (the green line) is the main contributor to total cell growth (black). For this combination of parameters, apoptosis has the largest effect on hypoxic cells. A rather counter-intuitive finding is that while apoptosis has an effect of hypoxic, necrotic and total cell number, it has a positive effect on proliferation, observed as an increase in the number of proliferating cells especially after Day 3.

- Case 10: The combination of high D_0 and low c_{g_0} results in more proliferating cells spread all over the tumour. However, an intermediate c_{f_0} value results in less hypoxia, as there is a curve displacement towards the left side, and proliferative cells will turn hypoxic only for very low levels of pO_2 (see Fig. 3.6). The effect of apoptosis is mostly seen on necrotic cells, as a lower number of hypoxic cells directly affects the number of necrotic cells.

- Case 11: Apoptosis demonstrates a smaller effect on cell number (as compared with the other cases). Especially, there is no effect on proliferating cells as the graphs practically overlap. When all parameters are low, we have less cell spread (smaller D_0), more contained tumour volume, and hence, more nutrients available to all voxels. This, in combination with a small c_{g_0} (smoother $g(\eta)$), results in a small number of proliferation cells being present all over the tumour. The same holds for c_{f_0}: cells will turn hypoxic all over the tumour, but at a smaller rate. This results in necrosis

happening across the tumour volume, however at a higher rate, resulting in a higher contribution of the necrotic cells to the total cell number.

- Case 15: The highest effect of apoptosis on total cell number is due to the effect observed on the hypoxic cell number. As for Case 10, the combination high D_0 and low c_{g_0} results in more proliferating cells spread all over the tumour. However, a high c_{f_0} results in more hypoxic cells (than e.g. in Case 10) because a higher diffusion results in more voxels with lower nutrient.

- Case 16: The combination of a high c_{g_0} with a low D_0 results in less proliferative cells but in a more pronounced proliferative rim. A low c_{f_0} leads to more hypoxic cells but also to more necrotic cells (due to lower c_{h_0}). The highest effect of apoptosis is observed for the necrotic cells number.

- Case 17: Due to a similar parameter set, the cellular evolution is similar to the one obtained for Case 16. The main difference is in the c_{apop} which is smaller for Case 17, resulting in a milder effect of apoptosis on the necrotic cells and hence on the total cell number.

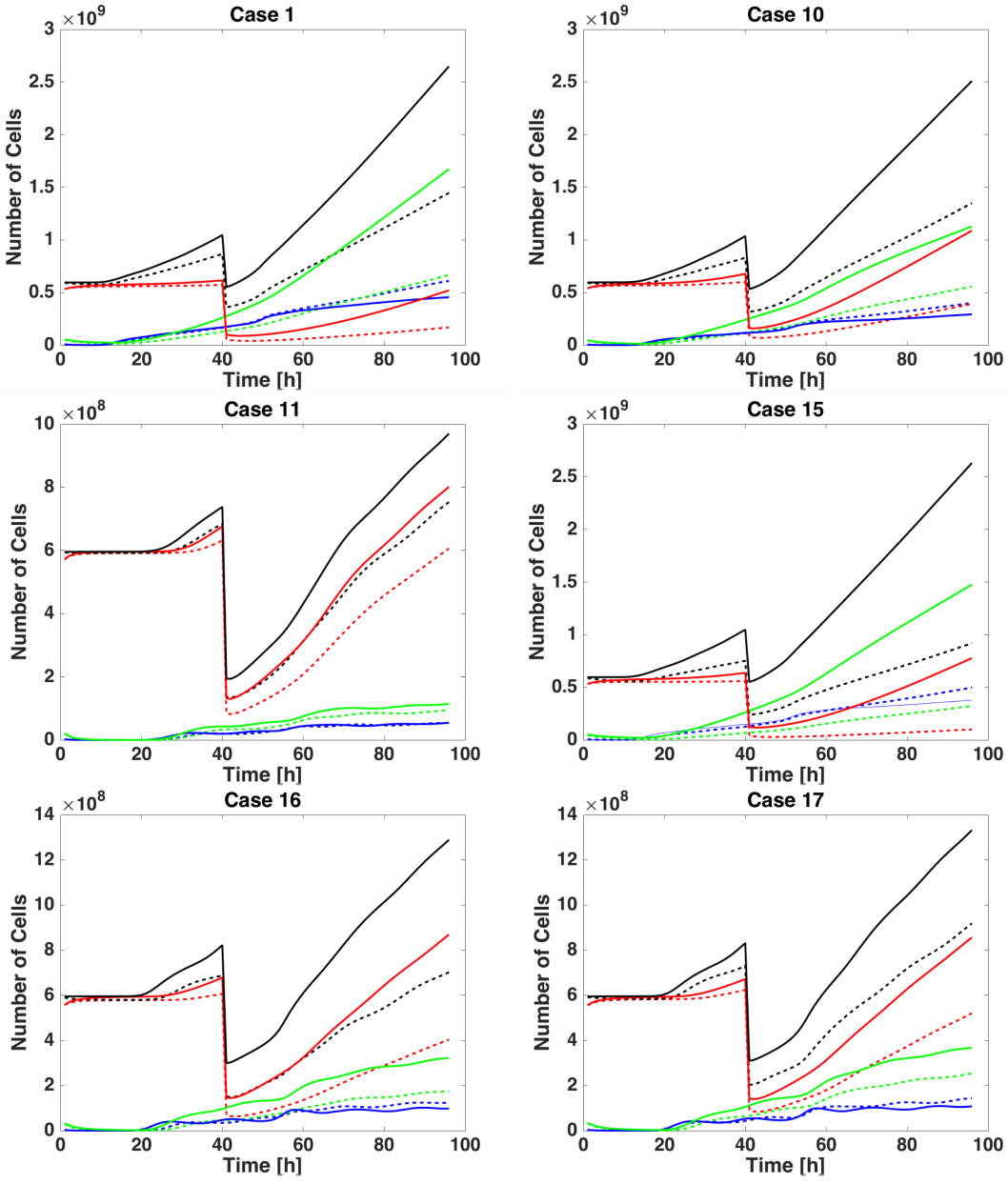


Figure 3.10: The effect of apoptosis on the number of proliferating (blue), hypoxic (green), necrotic (red) and total (black) cell is shown for a range of synthetic cases. For all cases, the total, hypoxic and necrotic cell evolution graphs obtained when including apoptosis (dashed lines) were less steep than the ones where no apoptosis was included. However, the proliferative cell numbers increased in the presence of apoptosis, especially for Cases 1, 10 and 15.

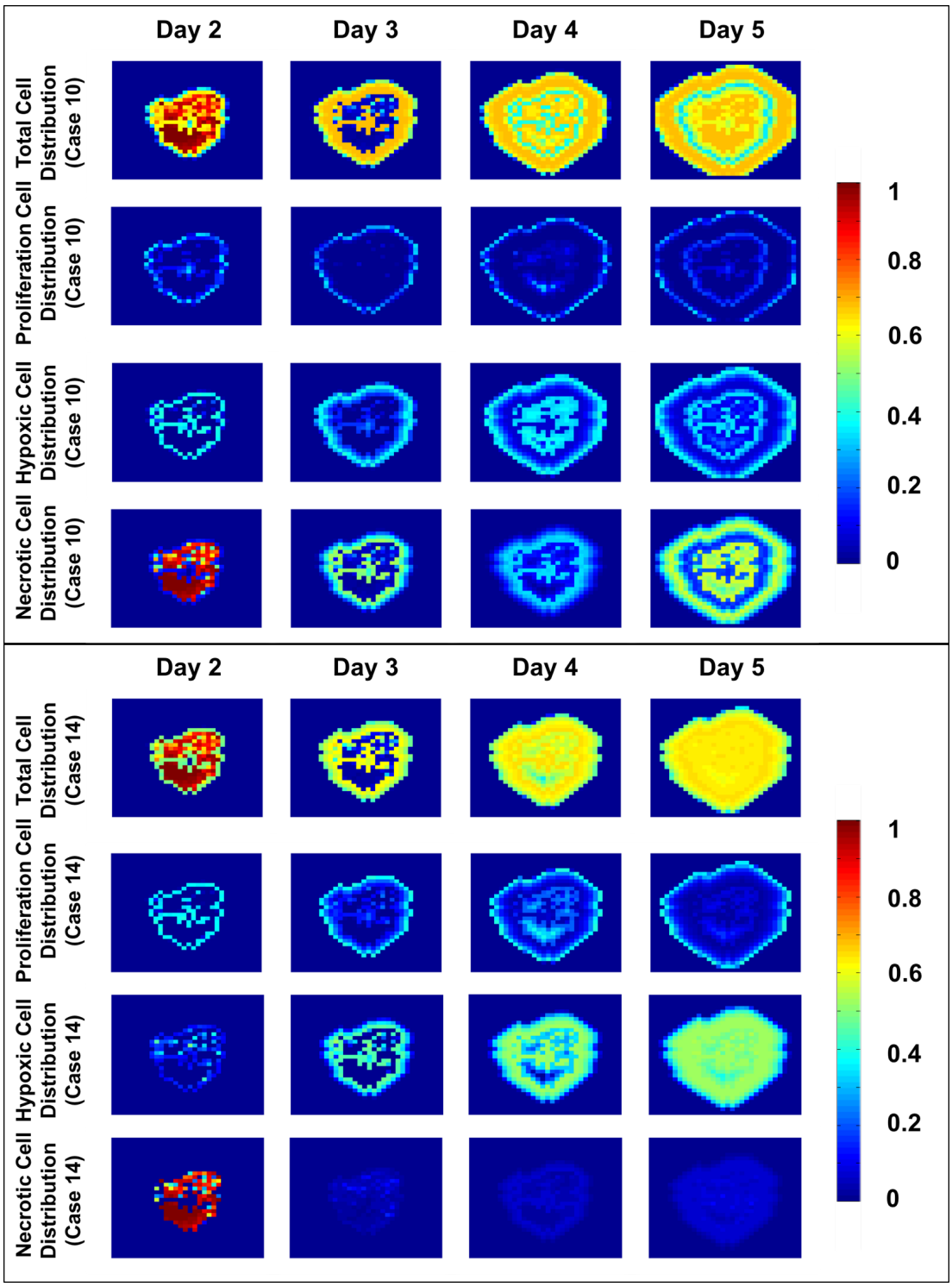


Figure 3.11: Simulated maps for total, proliferative, hypoxic and necrotic cells for a central slice of the tumour volume for cases 10 (top) and 14. The maps for Days 2 to 5 represent relative values obtained by dividing the cell maps of $t = 24h, t = 48h, t = 72h$ and $t = 96h$ by Θ, respectively.

In addition to the estimation of the global cellularity evolution and the volumetric tumour growth, our model allows for the assessment of the local distribution of cells within the tumour borders. In Fig. 3.11 we compare the local distribution of cells for distinct tumours, represented by their own set of parameters, using Cases 10 and 14 as examples. Case 10, with its higher D_0 and smaller c_{g_0}, results in a larger tumour with larger necrotic core. Case 14, with its higher c_{g_0} and lower D_0, depicts a smaller tumour with a more predominant proliferation rim (represented by the bright blue rim). For later time points, Case 14 exhibits a higher number of hypoxic cells due to the more homogenous spread of nutrient within the tumour, as compared to a very invasive tumour. There is also a smaller number of necrotic cells distributed homogenously across the tumour. As a result of the homogeneous distribution of hypoxic cells, all over the tumour, hypoxic cells will turn necrotic at a small necrotic rate (due to the higher c_{f_0} and consequently, the higher c_{h_0}).

3.4 Discussion and Conclusions

In this chapter we have presented a multi-scale, reaction-diffusion model of avascular tumour growth which can be constrained by quantitative imaging data to predict tumour spatio-temporal growth. The main advantage of our model is its ability to predict the 3-D macroscopic invasion of the tumour in the host tissue while evaluating how each cell group (proliferative, hypoxic and necrotic) contributes to tumour evolution.

We first performed an analysis of the model parameters to make a conscious choice about the ranges we use for simulations. From this analysis, we were able to set a relationship between D_0 and SGR. This relationship, which to the

best of our knowledge has never been presented before, represents a step in the direction of model personalisation, as it allows a reduction of the search space of the parameter using tumour volumes extracted from imaging scans.

Accounting for different cell groups and using parameter maps rather than global values are further strengths of the current model compared to other works where all cells within the tumour or a given voxel are assumed to be active and divide at the same proliferation rate [12, 16, 15]. Accounting for these different cell populations allows different aspects of tumour growth, like e.g. angiogenesis, to be integrated in a future version of the model.

This model has the potential to be applied to tumours present in other regions of the human body, as it neither assumes any a priori information on the direction of cellular spread nor it depends on information available only to brain tissue.

Using maps of cellularity extracted from medical imaging scans to initialise the model is another advantage of our strategy when compared to models which used geometric cells of set dimensions, initialised with an assumed, constant number of tumour cells to simulate tumour growth [79]. This is especially important as matching the spatial resolution of our models with the ones found in medical images makes the model more clinically oriented. The small number of model parameters (4 in total), is another advantage of our model when compared to complex models like the stochastic models introduced in [19] and [21], which contain too many parameters to be extracted from medical imaging information.

Our model allowed us to assess the effect of apoptosis, a process happening at the sub-cellular scale, on the macroscopic tumour growth. Our results indicated that apoptosis has the effect of reducing tumour volume evolution. This is not surprising as we have added apoptosis in our model as a cell loss rate, and the cell distribution is directly related to the tumour volume. However, Fig. 3.10 shows that

for some parameter combinations, apoptosis has the effect of increasing proliferative cells. This increase is rather counter-intuitive but might explain why higher level of apoptosis were associated with more aggressive tumours [102].

In this chapter we have presented our model formulation along with the processes it emulates and the relevant assumptions. We have also performed a thorough evaluation of the model parameters, analysed how each parameter affects the model output as well as how the parameter ranges can be customised. This was especially important for the diffusion parameter which we found to have the highest influence on the model outcome. We have also shown how different sets of parameters affect the local distributions for proliferative, hypoxic and necrotic cells. All this information is crucial when applying the model to medical imaging data; however, no verification of the model on real data was attempted. From the analysis we have also identified that the local nutrient availability (e.g. pO_2), the cellularity and the diffusion rate are the parameters that influence the model the most. As mentioned in Chapter 2, medical imaging modalities can be used to extract these parameters. For instance, one could use DWI to derive cellularity measures [26], DTI or CT in combination with a stiffness map to assess the direction of diffusion [11, 129], and PET related measures to investigate nutrient availability [20]. In the next chapter, we will therefore verify the model's ability to use medical imaging data in order to obtain subject-specific predictions of tumour evolution based solely on the imaging information.

Chapter 4

Integration of Medical Imaging Data into the Tumour Growth Model

As described in Chapter 2, independent of whether their parametrisation is based on the cellular density evolution or on a tumour delineation progression, most of the current medical imaging based macroscopic models of tumour growth focus on the integration of anatomical medical imaging. Some studies have included structural information from Diffusion Tensor Imaging (DTI) to model the fact that glioma cells preferentially migrate along white fibres of the brain, but no information on the metabolic and activity status of the cell densities has been included [11, 12].

A few studies have integrated metabolic measures from medical imaging modalities into a multi-scale model of tumour growth. This was done, for example, by linking the biological aggressiveness assessed by a series of MRI with the hypoxic burden assessed on FMISO-PET [22]; by using PET-MRI data to constrain a cou-

pled set of partial differential equations to describe tumour cell proliferation, angiogenesis, and glucose consumption [27]; by using hypoxia as a driver of tumour cell migration described in terms of imaging data (MRI, PET and SPECT) [26]; or by using Diffusion Weighted MRI and Dynamic Contrast-Enhancement (DCE)-MRI to parametrise a logistic model of tumour model and predict the cellular evolution as well as the reaction of tumour to therapy [23].

These studies were able to demonstrate to some degree the feasibility of parametrising a model of tumour growth using information from imaging data. However, their model parameters were not calibrated based on patient-specific imaging-data so that their predictions depend highly on parameters obtained from the literature and have limited patient-specific prediction ability. This limitation arises primarily due to the complexity of the developed approach [21, 25]; or due to missing data [26, 27]. The latter is especially true for approaches depending on information from many imaging modalities, which might not all be available for a single patient. Moreover, the need for multi-modal data may lead to co-registration errors arising from spatial misalignment between different modalities as well as from the different spatial resolutions of the devices.

In Chapter 3 we have developed a multi-scale, reaction-diffusion model of avascular tumour growth which is able to simulate the 3-D macroscopic tumour evolution while evaluating how each cell group (proliferative, hypoxic and necrotic) contributes to this evolution. We have shown how maps of cellularity and nutrient distribution can be used to initialise the model. These maps could be derived from a number of imaging modalities (e.g DWI-MRI, FMISO-PET, etc). However, to circumvent the above mentioned limitations related to multi-modal data, in this chapter we attempt to derive these maps from a single imaging modality which is routinely used in the clinic. This modality needs to be able to pro-

vide anatomic information (ideally 3D) while allowing for richer information on microscopic phenomena to be extracted. Given its ability to provide anatomic information while allowing for the extraction of physiological parameters related to vessel permeability, blood flow, and tissue volume fractions [28], we use Dynamic constrast-enhanced (DCE)-MRI.

The aim of this chapter is therefore to explore whether we can use DCE-MRI data to extract quantitative measures to feed our multi-scale model of Chapter 3 to obtain predictions of tumour evolution. We start off by demonstrating how DCE-MRI data can be used to derive the cellularity, nutrient and parameter maps needed to initialise our model. Using a set of synthetic data, we then test our calibration and verification methodologies in terms of model parameter recovery and tumour evolution prediction. Finally, we use a set of longitudinal DCE-MRI images of preclinical breast carcinoma to test the feasibility of using maps of cellularity derived from DCE-MR real data to feed and calibrate tumour growth models as well as to predict animal-specific tumour evolution[1].

4.1 Methods

In this section, we will introduce a novel method to use DCE-MRI data to derive tumour-specific parameters which can be used to parametrise and verify a model of tumour growth such as the one developed in Chapter 3.

[1]The methodology presented in this chapter has been published in the following article: T. Roque *et* al, "A DCE-MRI Driven 3-D Reaction-Diffusion Model of Solid Tumour Growth", *IEEE Transactions on Medical Imaging*, Volume: 37, Issue: 3, March 2018 [90].

4.1.1 Overview of the method

The general pipeline is summarised in Fig. 4.1. Firstly, local physiological properties of the same tumour at two consecutive time points, $TP1$ and $TP2$, are extracted from a time series of DCE-MR images (section 4.1.2) and then converted into input and parameter maps (section 4.1.3). The tumour evolution between the time points is assumed to follow the PDE model outlined in section 3.1.1. To personalise this model, parameters are calibrated by maximising the similarity between the transformed cellularity maps of $TP1$ and the observed cellularity maps at $TP2$ using a simulated annealing optimisation technique (section 4.1.4). The PDE model of section 3.1.1 is finally used to predict the tumour development after $TP2$ (section 4.1.5) and compared to the tumours observed in the scans of these time points (section 4.3).

4.1.2 DCE-MRI data to physiological parameters

As mentioned in Section 2.2.3, DCE-MR perfusion imaging is based on the application of an exogeneous, intravascular, non-diffusible CA and consists of taking several sequential T_1-weighted MR images over a short period of time upon the injection of a CA. The most common CA used is the low-molecular-weight gadolinium-diethylenetriamine pentaacetic acid (Gd-DTPA), which is able to transverse the vessel walls, thus entering the EES. However, it is unable to cross the cellular membrane, limiting its volume of distribution (v_D) to the interstitial space. As a result, DCE-MRI signal intensity changes derive mainly from CA that extravasates to the EES, which locally enhances the signal intensities by shortening of the longitudinal relaxation time according to its concentration:

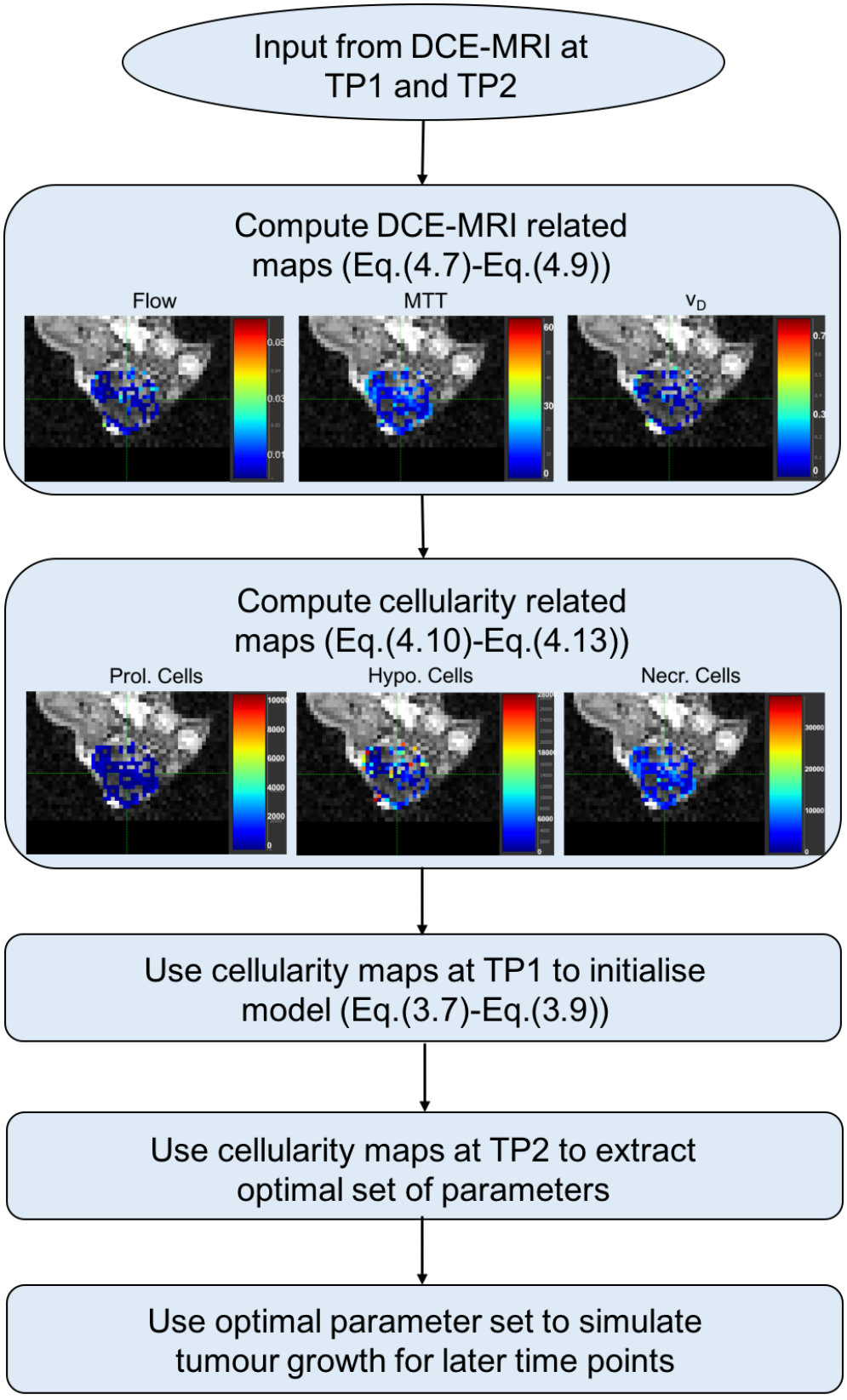


Figure 4.1: Overview of a tumour growth model using information from DCE-MRI perfusion imaging data for calibration and validation. DCE-MRI related physiological maps are used to compute proliferating, hypoxic and necrotic cell maps which in turn are used to initialise the model outlined in Section 3.1.1. This model is solved at each time step and at each voxel to compute the cellularity maps and tumour volume at a later TP. The true tumour volume at TP2 is used to optimise a set of parameters, which in turn is used to predict the tumour evolution at a later TP.

$$\frac{1}{T_1} = \frac{1}{T_{10}} + r_1 C(t) \tag{4.1}$$

Here, T_{10} is the relaxation time T_1 prior to the injection of CA, r_1 the relaxivity constant specific to CA, and C(t) the total concentration of CA at time t.

A usual DCE-MRI experiment assumes a tissue sample with a single inlet through which the arterial plasma flow F enters the tissue. The measured time curves, the tissue concentration $C(t)$ and the concentration in the blood plasma of the feeding artery (the arterial input function, AIF), are related by convolution with an unknown, tissue-characteristic impulse response function $I(t)$:

$$C(t) = I(t) \otimes AIF \tag{4.2}$$

Several models have been developed to estimate DCE-MRI related parameters (see 2.2.3). The first generation dates back to the works of Tofts and colleagues in the 1990s [28], who used a pharmacokinetic tracer analysis model to fit $C(t)$ and extract perfusion related parameters (e.g. exchange rates between individual subspaces). Model-free approaches that characterise the shape and structure of the signal intensity time curve $S(t)$ can also be used to quantify tissue perfusion [56]. Further, semi-quantitative parameters (e.g. bolus arrival time, area under the curve and time to peak) can be computed directly from the $S(t)$ [60].

For our strategy we are interested in the following physiological quantities from the DCE-MRI time series obtained at each time point:

- The maximum enhancement peak of the concentration time curve (mEP),
- the distribution volume (v_D) defined as the fraction of tissue accessible to the CA,

- the blood flow (F),
- the Mean Transit Time (MTT) which relates v_D to the arterial inlet to the space carrying the plasma flow.

Model-free analysis allows the extraction of the latter two parameters without the need for prior assumptions on the internal structure of the tissue [59]. Therefore, to extract these parameters, we adopt a combination of the model-free deconvolution method with a semi-quantitative approach. Note that in this subsection, t indexes the images of a single DCE-MRI time sequence and not different time points TPn, so that time intervals are much smaller here than in section 3.1.1.

First, $S(t)$ is converted into CA concentration time curve $C(t)$ using:

$$C(t) = \frac{1}{r_1}\left(\frac{-1}{TR}\ln\left\{\frac{E(E_{10}-1)+E_{10}[1-\cos(FA)]}{1+\cos(FA)[E(E_{10}-1)-1]}\right\}-\frac{1}{T_{10}}\right)$$

where $E_{10} = \exp(-TR/T_{10})$, $E = S(t)/S_0$ and r_1 is the longitudinal relaxivity (contrast agent property) assumed to be 3.9 $mM^{-1}s^{-1}$ [106, 107]. TR is the repetition time (time between two excitation pulses), FA denotes the flip angle and S_0 is the signal at the baseline. It follows that the $C(t)$ can be extracted from the observed signal enhancement E, provided that r_1, T_{10} and TR are known. The maximum enhancement peak of the concentration time curve mEP is then defined as equal to $\max_t(C(t))$.

Next, the distribution volume v_D (the fraction of tissue accessible to the CA) map for each TP is computed using Eq. 4.3 as given in [59]:

$$v_D = \frac{\int_0^\infty C(t)dt}{\int_0^\infty AIF(t)dt} \quad . \tag{4.3}$$

The AIF is known to vary between individuals and visits due to variation in phys-

iological parameters such as cardiac output, renal function, and also in external parameters such as injection timing. Therefore, ideally one would like to compute a subject-specific AIF to ensure that the model is personalised to each patient. However, measuring AIF is of great challenge in a pre-clinical scenario, so that the use of a population-based AIF becomes a helpful tool. The population based AIF given in [108] is used. The approach used in [108] was to decompose the input function into a bolus model and a body transfer function. In principle, these two elements can take any form but to enable sensible calculations suitable mathematical functions are chosen. Based on [108], we choose to model AIF by a bi-exponential input function of the type:

$$AIF(t) = D(a_1 \exp(-m_1 \cdot t) + a_2 \exp(-m_2 \cdot t)) \tag{4.4}$$

with time-point t=0 set to the beginning of signal enhancement. D is the administered CA dose in $mmol/kg$, a_1 and a_2 are amplitudes in kg/l, m_1 is the distribution rate constant in $1/min$ and m_2 the vascular elimination rate constant in $1/min$. These parameters are chosen based on pre-clinical values given in [109], so that: $D = 0.7350 mmol/kg$, $a_1 = 9.2 kg/l$, $a_2 = 4.2 kg/l$, $m_1 = 2.31/min$ and $m_2 = 0.051/min$.

Following Eq. 4.2, the deconvolution of the measured $C(t)$ with the obtained AIF yields an estimate for the impulse function $I(t)$, defined as:

$$I(t) = F \cdot R(t) \quad \cdot \tag{4.5}$$

Here, $R(t)$ represents the residue function, the fraction of CA remaining in the voxel at a time t after its arrival. For the deconvolution, we choose the block-circulant singular value decomposition (oSVD) method, due to its ability in pro-

viding flow estimates which are insensitive to tracer arrival time differences [110]. Applying oSVD to Eq. 4.2 and 4.5, yields the blood flow F as the maximum of $I(t)$.

The MTT for each voxel can be computed using the central-volume theorem [111]:

$$MTT = \frac{v_D}{F} \quad \cdot \tag{4.6}$$

All these parameters quantify the tumour metabolic status, which is important for the tumour further development.

4.1.3 Cellularity maps and related maps

Different maps are needed to initialise, calibrate and verify our reaction-diffusion model: The number of proliferating cells (p), the number of hypoxic cells (q), the number of necrotic cells (n), the total number of tumour cells (r) and the nutrient distribution (η).

Aryal *et al.* were able to demonstrate that DCE-MRI derived v_D values were significantly, negatively correlated with tumour cellularity [30]. Building on these findings, to estimate the total number of tumour cells r at a given voxel location $\mathbf{x}$, we assume that as the number of cells increases, v_D decreases. Hence, an inverse relationship between cellularity and v_D is assumed:

$$r(\mathbf{x}) = (1 - v_D(\mathbf{x})) \cdot \Theta \quad \cdot \tag{4.7}$$

In [112], the authors were able to demonstrate a positive correlation between the mitotic index and the peak of maximum enhancement. Based on these findings, we assume the number of proliferating cells, p, to be proportional to the peak of

maximum enhancement mEP. It follows that an initial map giving the number of proliferating cells can be estimated assuming following relationship:

$$p(\mathbf{x}) = \frac{mEP(\mathbf{x})}{max(mEP(\mathbf{x}))} \cdot r(\mathbf{x})\,. \tag{4.8}$$

Following a simplified cell-cycle, cells within a voxel that are not proliferating can either be in a dormant state (hypoxic) or dead (necrotic). In order to obtain the number of necrotic cells n, we assume that low blood flow F, and hence low nutrient availability, results in high cell death rate. We hence estimate the number of necrotic cells as follows:

$$n(\mathbf{x}) = \left(1 - \frac{F(\mathbf{x})}{max(F(\mathbf{x}))}\right) \cdot (r(\mathbf{x}) - p(\mathbf{x})) \tag{4.9}$$

where the last term on the RHS represents the total number of cells which are not proliferating, and can hence be either hypoxic or necrotic. The first term on the RHS of the equation represents the percentage out of the non-proliferating cells which are necrotic as a function of blood flow.

Finally, given that we assume a voxel to be made of v_D and tumoural cells only, the number of hypoxic cells q can be estimated as the difference between the total cell number $r(\mathbf{x})$ and the sum of $p(\mathbf{x})$ and $n(\mathbf{x})$:

$$q(\mathbf{x}) = r(\mathbf{x}) - p(\mathbf{x}) - n(\mathbf{x})\,. \tag{4.10}$$

Once the total number of cells in each voxel is known, the nutrient distribution $\eta(\mathbf{x})$ can be computed using Eq. 3.11, which corresponds to the reduced model proposed by Sherrat and Chaplain [7], as outlined in Section 3.1.1.

Next, we will demonstrate how these maps of cellularity and nutrient can be used to estimate the model parameters within the ranges obtained in Section 3.1.4.

4.1.4 Estimation of model parameters

In order to predict the evolution of specific tumours, the parameters c_{g_0}, c_{f_0}, D_0 and c_{apop} need to be calibrated. For this, we use cellularity maps and tumour volumes extracted from scans of two consecutive time points, denoted as $TP1$ and $TP2$. Based on the information obtained in Sections 3.1.4 and 3.3, our estimation problem can be defined as:

$$\begin{aligned} \min_{c_{g_0}, c_{f_0}, D_0, c_{apop}} \quad & vol_e(c_{g_0}, c_{f_0}, D_0, c_{apop}) \\ \text{s.t.} \quad & 0.15 \leq c_{g_0} \leq 0.50 \quad mmHg^{-1} \\ & 0.05 \leq c_{f_0} \leq 0.3 \quad mmHg^{-1} \\ & d_{min}(SGR) \leq D_0 \leq d_{max}(SGR) \quad mm^2/h \\ & 0 \leq c_{apop} \leq 0.15 \quad hour^{-1} \end{aligned} \tag{4.11}$$

where $vol_e = |(vol_s - vol_t)/vol_t|$ is the relative volume estimation error between the volume observed at the true scans in $TP2$ which have been manually delineated by a radiologist (vol_t), and the simulated volume, vol_s, obtained by producing an apparent boundary on the simulated tumour based on $r(x, TP2)$. The cellularity maps are simulated solving the set of PDEs (Eq. 3.8-Eq. 3.10). Their initial states are computed at $TP1$ using the methods described in 4.1.2 and 4.1.3.

Both $d_{min}(SGR)$ and $d_{max}(SGR)$ are found using the relationship derived between D_0 and the specific growth rate (SGR) (see Section 3.3.2). Due to the diffusion term, all voxels of $r(x, TP2)$ might contain some tumour cells even if they would not be visible on a scan. In order to delineate the simulated tumour,

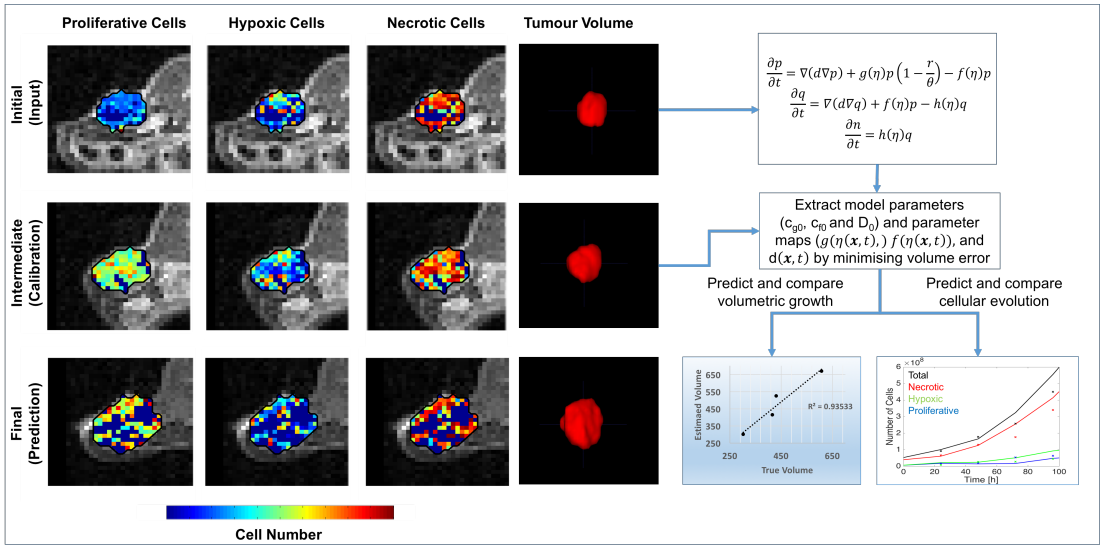


Figure 4.2: Cellularity maps (proliferative, hypoxic and necrotic cells) can be estimated from medical imaging modalities (e.g DCE-MRI, ADC maps and PET-scans) obtained at three time points during tumour growth. Maps of the initial time point can be used as input in the PDE-based model of tumour growth to estimate the tumour volumetric and cellularity growth at future time points. Using the tumour cellularity maps and the tumour volume at the second time point, the model parameters related to the proliferation, hypoxic and diffusion rates can be estimated and used to predict future cellularities and tumour volumes, which enables comparison with the true data at future time points (plots).

we assume a voxel x to be outside the tumour if less than 1% of its carrying capacity is made out of tumour cells, i.e. if $r(x, TP2) < 0.01\Theta$. Note that this PDE-constrained optimisation problem is non-convex and computing vol_e gradients would be costly. We therefore use a global optimisation strategy, the built-in simulated annealing MATLAB function [113], to optimise Eq. 4.11 and hence estimate c_{g_0}, c_{f_0}, D_0 and c_{apop}.

4.1.5 Predicting the tumour spatio-temporal growth

The model parameters are estimated using data from two early time points in tumour evolution, $TP1$ and $TP2$. The obtained values after optimisation are used as input for the tumour growth simulation for later time points. After simulation, the output, represented by the simulated cellularity maps and the

simulated tumour volume, can be compared to the maps acquired at the respective time points. An overview of this analysis pipeline is provided in Fig. 4.2.

We also compare the simulated tumour volumes with the volumes observed in the actual scans in terms of the Dice similarity coefficient DSC. This statistical validation metric, normally used to test the performance of segmentation tools in terms of spatial overlap accuracy, can be calculated using $DSC = \frac{2A \cap B}{A+B}$, where A is the simulated tumour image and B the true tumour image at a given TP.

4.2 Experiments

4.2.1 Synthetic data

In order to evaluate our framework in terms of its capacity to successfully recover model parameters, tests with 20 generated synthetic tumours were performed. To this end, we used the same 20 parameter sets given in Tab. 3.1 and maps for $TP1$ from one of the available pre-clinical DCE-MRI to grow tumours for four days, *i.e.* up to $TP5$.

Different groups reported that different combinations of the proliferation and diffusion rates might yield the same results [10, 17]. The results of our own sensitivity and parameter analyses performed in the previous chapter showed that the diffusion rate, D_0, was the parameter with the most influence on the model output in terms of both tumour volume and total cellularity. We therefore decide to fix c_{g_0} for further analyses. We add simulations cases where $c_{g_0} = 0.15 mmHg^{-1}$ and $c_{g_0} = 0.3 mmHg^{-1}$ to account for the fact that even if the pO_2 conditions are favourable, a small number of cells could turn hypoxic due to the different check points present in the cell cycle. Our sensitivity analysis also demonstrated that

our output volume was also sensitive to c_{apop}. But this influence was not as high as the one observed for D_0. We therefore investigate whether adding c_{apop} to the model leads to more accurate predictions, and consider both cases, $c_{apop} = 0$ and c_{apop} as a parameter to be optimised.

Finally, our sensitivity analysis showed that our model was sensitive to c_{f_0} when the necrotic cell number was considered as a model output. We also explore the case where c_{f_0} is optimised. We do so by first estimating D_0 (and c_{apop}) when the volumetric error, vol_e, is minimised. We then use the recovered value as a constant input to optimise c_{f_0} by minimising an error related to the sum of square errors in the $r(x,t)$, defined as $cell_{error} = \left(r_t(x,TP2) - r_e(x,TP2)\right)^2/\Theta$, where $r_t(x,TP2)$ and $r_e(x,TP2)$ represent the true and simulated total cell maps at $TP2$, respectively.

This is an important analysis to be performed, since the more parameters that need estimation, the higher the computational cost related to the optimisation process. We therefore perform synthetic experiments for a total of eight different optimisation routines: four routines without (I-IV) and four with apoptosis (V-VIII), as listed in Tab 4.1. For the optimisation routines I and V, both c_{f_0} and c_{g_0} are kept constant at $0.15 mmHg^{-1}$. For the routines II and VI, we set $c_{g_0} = 0.15 mmHg^{-1}$ and optimise c_{f_0} as described above. For routines III and VII, both c_{f_0} and c_{g_0} are kept constant at $0.30 mmHg^{-1}$. And finally, for routines IV and VIII we set $c_{g_0} = 0.30 mmHg^{-1}$ and optimise c_{f_0}.

The simulation results using the recovered parameter values for each optimisation routine are compared with the true data at future time points and shown in Section 4.3.1.

	Parameters			
Optimisation Routine	$c_{g_0}(mmHg^{-1})$	$c_{f_0}(mmHg^{-1})$	$D_0(mm^2/h)$	$c_{apop}(hour^{-1})$
I	constant at 0.15	constant at 0.15	optimised	constant at 0
II	constant at 0.15	optimised	optimised	constant at 0
III	constant at 0.30	constant at 0.30	optimised	constant at 0
IV	constant at 0.30	optimised	optimised	constant at 0
V	constant at 0.15	constant at 0.15	optimised	optimised
VI	constant at 0.15	optimised	optimised	optimised
VII	constant at 0.30	constant at 0.30	optimised	optimised
VIII	constant at 0.30	optimised	optimised	optimised

Table 4.1: Optimisation routines used for synthetic experiments. A total of eight routines were used: four routines without (I-IV) and four with apoptosis (V-VIII).

4.2.2 Pre-clinical data

Ten mice, in which CaNT (breast carcinoma) tumour cells were injected, were imaged at five consecutive days over the tumour growth cycle (starting 10 days after injection). To match the denotation used in this chapter, we denote TPn the time point of the nth acquisition. DCE-MRI was performed at 4.7 T (Varian VNMRS) with 60 repeats (DCE frame rate of 10-15 seconds) of a cardio-respiratory (CR-) gated RF and gradient spoiled 3-D gradient echo scan (TR=1.4 ms, TE=0.64 ms, FOV=54×27×27 mm^3, matrix=128×64×64, hard pulse=16 µs and FA=5°). Anaesthesia was maintained with 1-3% isoflurane in a 1:5 O2:air mixture. Respiration was monitored using a pressure balloon. ECG needles were placed subcutaneously in the chest. Motion artefact was minimised with automatic and immediate reacquisition of data corrupted by respiration motion. Gd-DTPA-BMA (Omniscan) was automatically infused into the lateral tail vein triggered at the start of scan 11/60. Sporadically, the Gadolinium injection failed, which hindered the acquisition of the DCE-MRI for $TP1$ for Case 3, $TP2$ for Cases 8 and 9, $TP3$ for Case 1, $TP4$ for Case 9 and $TP5$ for Cases 3 and 4. T_{10} was determined prior to DCE-MRI from a variable flip angle (VFA) scan [114] with the same CR-gated 3-D gradient echo scan and 16 nominal FAs ranging from 1°to 7°in steps of

0.4°. 3-D B1 maps to quantify FA prescription were acquired with a respiration gated actual flip angle imaging (AFI) scan [115] and TR1=10 ms, TR2=100 ms, TE=0.42 ms and nominal FA=64°. Due to missing information for $TP2$ Cases 8 and 9 were excluded from the analysis. Likewise, Case 7 needed to be excluded because the tumour did not grow but shrank between $TP1$ and $TP2$.

4.3 Results

The calibration process takes on average 10.79±4.50 hours running for 1500 iterations over the 3D growth simulation between $TP1$ and $TP2$ or until convergence is achieved. In terms of prediction post $TP2$, each run takes up to 5 minutes depending on the size of the tumour being modelled. The code was written in Matlab (Mathworks, Natick, MA) and all simulations performed on a 3.4 GHz Intel Xeon machine with 32GB of RAM, providing scope for reducing the optimisation time using more efficient implementations or parallelization.

4.3.1 Synthetic data

Table 4.2 lists all parameter estimation mean errors and standard deviations for the eight different optimisation routines. The smaller errors in recovery were observed for optimisation routine IV (without apoptosis, $c_{g_0} = 0.30 mmHg^{-1}$ and c_{f_0} as a model parameter).

Figure 4.3 depicts the mean relative errors (top) and the mean DICE overlaps for time points ($TP2 - 5$), illustrated as a block-diagram for the optimisation routines without apoptosis (left) and with apoptosis. The blue, green, yellow and red blocks represent routines I and V; II and VI; III and VII; and IV and VIII; for the cases without and with apoptosis, respectively.

Optimisation Routine	Parameters			
	$c_{g_0}(mmHg^{-1})$	$c_{f_0}(mmHg^{-1})$	$D_0(mm^2/h)$	$c_{apop}(hour^{-1})$
I	0.440±0.206	0.457±0.434	2.23±1.551	N/A
II	0.440±0.206	0.791±0.889	2.23±1.551	N/A
III	0.331±0.262	0.457±0.434	1.582±0.888	N/A
IV	**0.331±0.262**	**0.407±0.253**	**1.582±0.888**	N/A
V	0.440±0.205	0.457±0.434	2.166±1.457	0.908±0.752
VI	0.441±0.206	0.821±0.809	2.166±1.457	0.908±0.752
VII	0.331±0.262	0.457±0.434	1.812±1.300	0.92±1.755
VIII	0.331±0.262	0.448±0.317	1.812±1.300	0.92±1.755

Table 4.2: Mean parameter recovering errors for a total of eight different optimisation routines: four routines without (I-IV) and four with apoptosis (V-VIII).

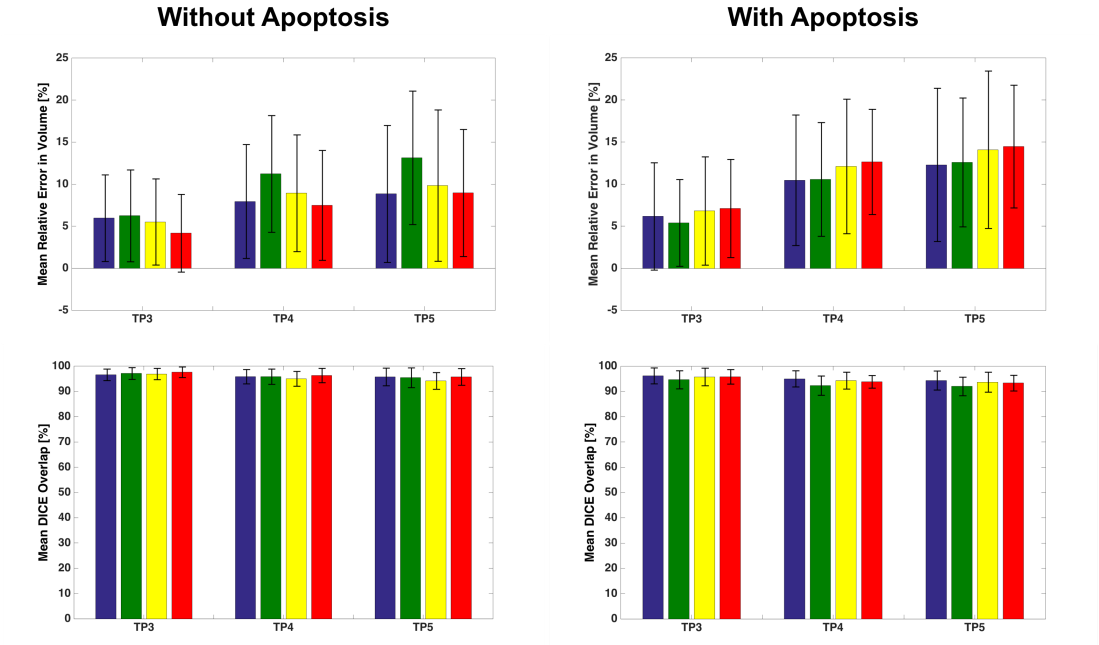


Figure 4.3: The mean relative errors (top) and the mean DICE overlaps for time points ($TP2-5$) are illustrated as a block-diagram for the case where no apoptosis (left) and apoptosis has been included in the model. The blue blocks represent the cases where $c_{f_0} = 0.15mmHg^{-1}$ and $c_{g_0} = 0.15mmHg^{-1}$, for the green ones $c_{f_0} = 0.15mmHg^{-1}$ and $c_{g_0} = 0.30mmHg^{-1}$, the yellow and red ones represent the cases where c_{f_0} is optmised and $c_{g_0} = 0.15mmHg^{-1}$ and $c_{g_0} = 0.30mmHg^{-1}$, respectively. Whilst there is no striking difference between the DICE overlap for the cases with and without apoptosis, much higher volume errors can be observed for the cases where apoptosis was included.

The diagrams show that adding apoptosis as a free parameter to the model increased volume error and slightly decreased the DICE overlaps. For the case without apoptosis, using optimisation routine IV (c_{f_0} optmised and $c_{g_0} = 0.30mmHg^{-1}$)

yielded overall smaller volume errors, followed by optimisation routine I (c_{f_0} and c_{g_0} kept constant at $0.15 mmHg^{-1}$).

We hence use optimisation routines I and IV to compare the outcomes in terms of cellularity estimation. Fig. 4.4 depicts the mean evolution of the 20 synthetic tumours for total, proliferative, hypoxic and necrotic cells between $TP1$ and $TP5$ (a total of 96 hours). The red lines represent the true mean and standard deviation values and the blue bounds the mean estimated values along with their standard deviations. Results obtained for the case where $c_{g_0} = 0.15 mmHg^{-1}$ and $c_{f_0} = 0.15 mmHg^{-1}$ (top row) are generally better, especially for the estimation of proliferating and hypoxic cells. However, using $c_{g_0} = 0.30 mmHg^{-1}$ and c_{f_0} as a model parameter yielded better results for the estimation of necrotic cells, at the cost of an underestimation in both proliferating and hypoxic cells.

4.3.2 Pre-clinical data

Considering the results for the synthetic data experiments, we now apply the two optimisation routines (I and IV) that yielded the best results in terms of both parameter recovery and estimation error to the pre-clinical data described in Section 4.2.2. Because we found that apoptosis mainly had the effect of reducing tumour volume and that adding it as a model parameter did not increase the model's predictive power, we eliminate this parameter and are left with a total of one (for optimisation routine I) and two (for optimisation routine IV) parameters that need to be optimised. In order to obtain subject-specific parameter ranges, needed to solve the optimisation problem, we derive $d_{min}(SGR)$ and $d_{max}(SGR)$ from the pre-clinical data using Eq. 3.27 (without taking apoptosis into account). The values obtained for each pre-clinical case are listed in Tab. 4.3.

The parameter values obtained after optimisation with each of the optimisation

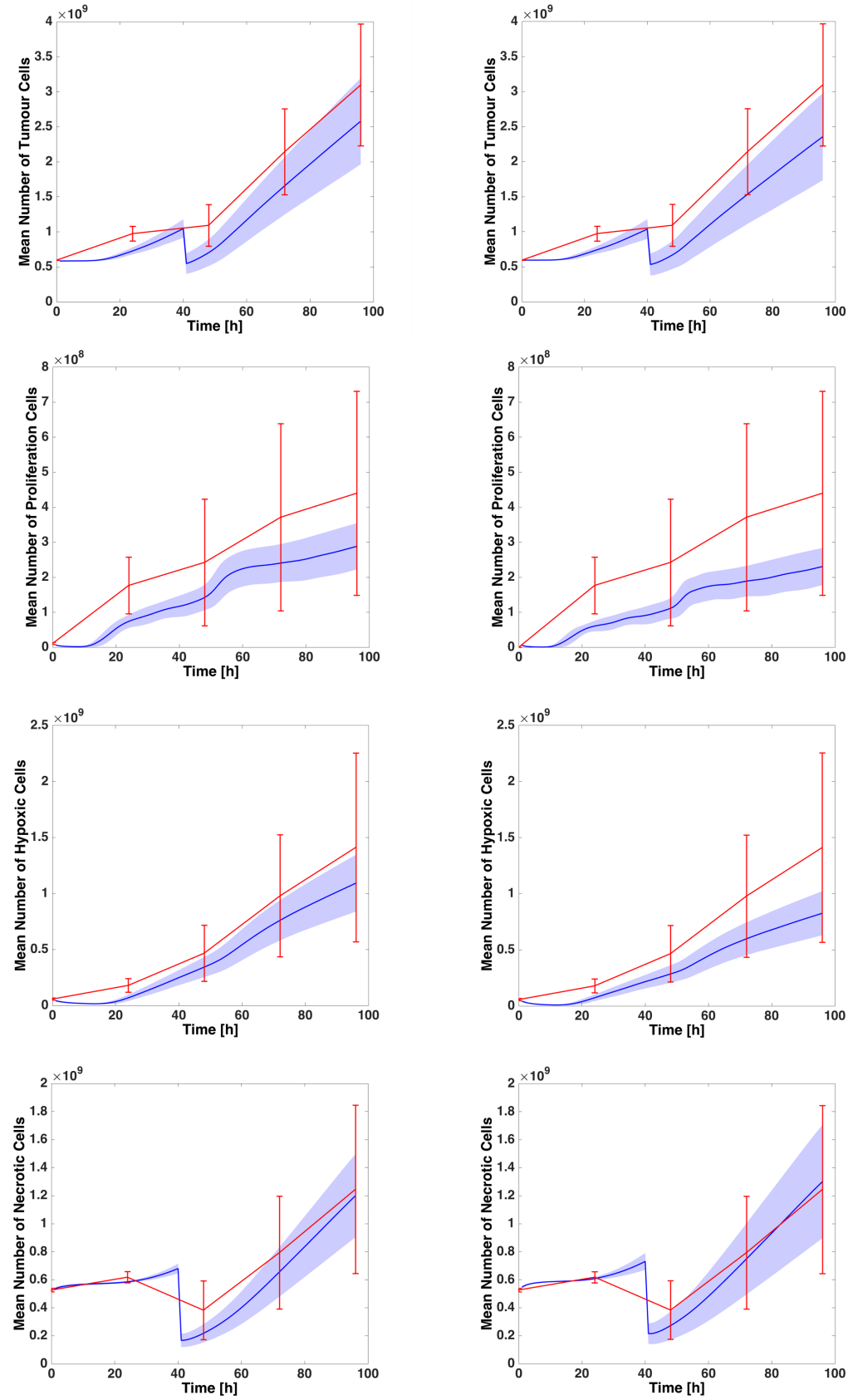


Figure 4.4: Mean cellularity (total, proliferative, hypoxic and necrotic) evolution for synthetic tumour growth for optimisation routines I (LHS) and IV for the time between $TP1$ and $TP5$. Blue bounded lines and the red lines depict the mean and standard deviation values for the estimated and true 20 tumour cases, respectively.

	Volumes (mm^3)				
Cases	TP1	TP2	SGR ($hour^{-1}$)	$d_{min}(SGR)(mm^2/h)$	$d_{max}(SGR)(mm^2/h)$
1	271.63	302.12	0.004	1.063E-07	5.879E-07
2	64.06	98.75	0.010	2.890E-07	1.899E-06
3	178.06	248.65	0.014	5.629E-07	4.1521E-06
4	171.37	221.164	0.011	3.414E-07	2.3098E-06
5	13.37	22.004	0.021	1.807E-06	1.631E-05
6	23.96	35.67	0.0167	8.827E-07	7.038E-06
10	60.23	73.52	0.008	2.071E-07	1.285E-06

Table 4.3: Tumour volume for $TP1$ and $TP2$ for seven breast carcinoma pre-clinical cases. For some cases and time points, no imaging was available due to failure in the contrast agent injection (denoted as N/A). For all cases, the Specific Growth Rate ($SGR = ln(V2/V1)/(t2 - t1)$) was computed as an estimate of the average tumour growth rate using volumes of $TP1$ and $TP2$ [105]. For Case 3 where $TP1$ was not available we used $TP2$ and $TP3$ to estimate SGR.

Parameter	Case 1	Case 2	Case 3	Case 4	Case 5	Case 6	Case 10
$D_0[mm^2/h]$	1.92E-06	1.54E-04	1.30E-04	1.02E-04	1.79E-06	9.06E-05	2.00E-04

Table 4.4: Optimised model parameter values used to simulate tumour growth between $TP2$ and $TP5$ for optimisation routine I. The parameters c_{g_0} and c_{f_0} are kept fixed at $c_{g_0} = 0.15 mmHg^{-1}$ and $c_{f_0} = 0.15 mmHg^{-1}$ for all pre-clinical cases.

Parameter	Case 1	Case 2	Case 3	Case 4	Case 5	Case 6	Case 10
$c_{f_0}[mmHg^{-1}]$	0.299	0.299	0.138	0.210	0.057	0.062	0.117
$D_0[mm^2/h]$	6.5E-07	8.88E-05	7.59E-05	6.03E-05	2.52E-05	5.27E-05	1.90E-04

Table 4.5: Optimised model parameter values used to simulate tumour growth between $TP2$ and $TP5$ for optimisation routine IV. c_{g_0} was kept fixed at $c_{g_0} = 0.30 mmHg^{-1}$ for all pre-clinical cases.

routines, listed in Tab. 4.4 and Tab. 4.5, were used as input for the tumour growth simulation between $TP1$ and $TP5$. Next, we compare the simulated cellularity maps and the simulated tumour volume with the maps and volumes acquired at the respective time points. We also compare the simulated tumour volumes with the true volumes observed in the actual scans in terms of DSC.

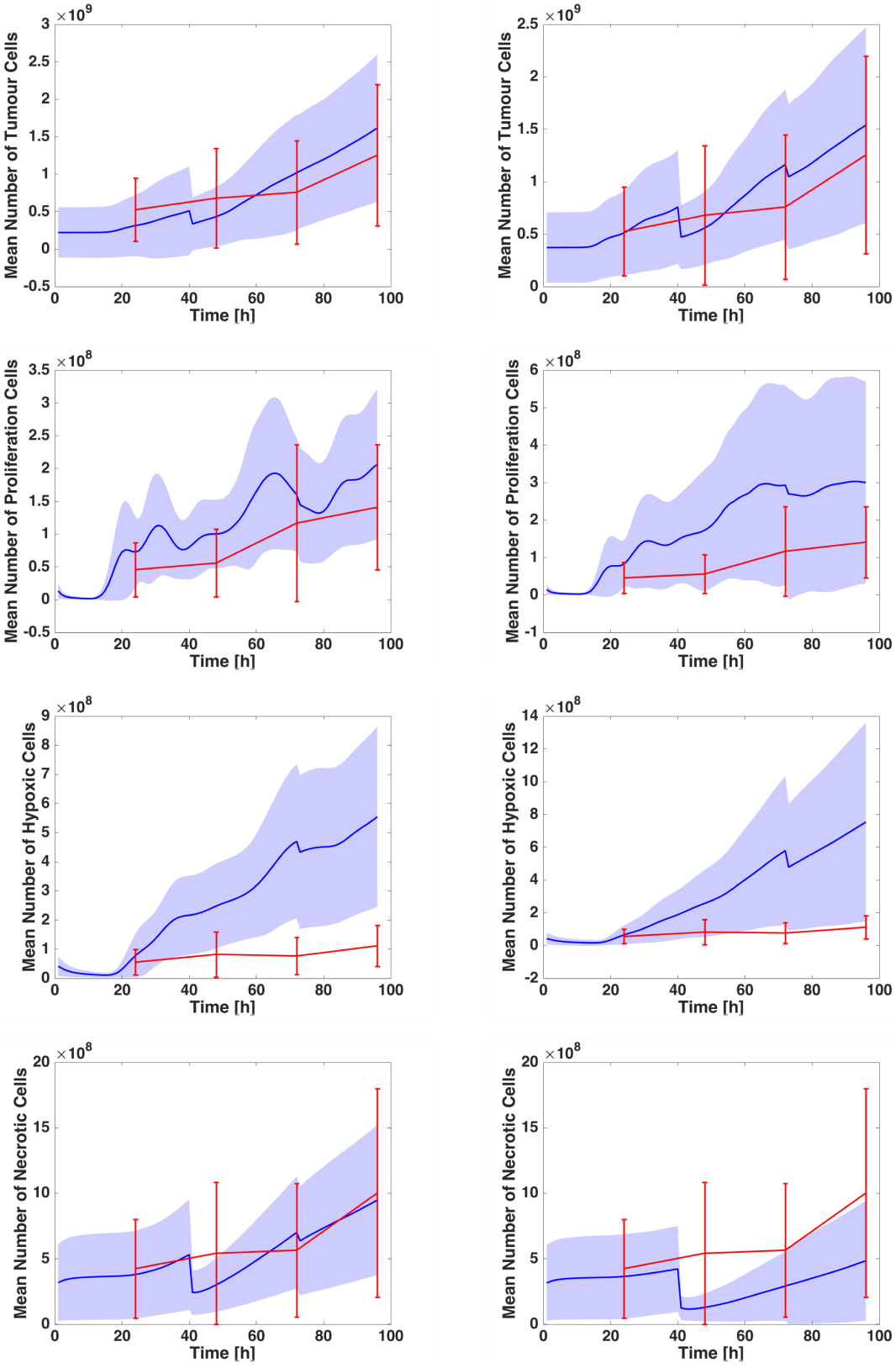


Figure 4.5: Mean cellularity (total, proliferative, hypoxic and necrotic) evolution for tumour growth for optimisation routines I (LHS) and IV for the time between $TP1$ and $TP5$. Blue bounded lines and the red lines depict the mean and standard deviation values for the estimated and true pre-clinical data, respectively.

4.3.3 Cellular evolution simulations

The initial total cell number is computed as the sum of the cells over the voxels within the tumour boundaries at $TP1$. Using the optimised parameters given in Tab. 4.4 and in Tab. 4.5 for the simulations, for each time step, the total cell number for each sub-population was computed and used as input for the consecutive simulation time step.

The mean cellularity (total, proliferative, hypoxic and necrotic) evolution for optimisation routines I (left) and IV for the time points $TP1$ to $TP5$ are shown in Fig. 4.5. Blue bounded lines represent the estimated mean values and standard deviations for the simulated tumours. Red lines depict the true mean and standard deviation values for cellularity evolution for the included pre-clinical data. For both optimisation routines, the highest difference between true and estimated values was observed in the hypoxic cell number. The overestimation in hypoxic cells resulted in an overestimation in the total cell number.

To draw a more quantitative comparison between optimisation routines I and IV, we compute the mean relative errors in cellularity for $TP3$ to $TP5$ (see Tab. 4.6). For most time points and cell sub-populations, optimisation routine IV yielded smaller mean relative errors than optimisation routine I. The mean errors and standard deviations for the hypoxic were many-fold larger than for the necrotic and proliferative cells, quantifying the trend observed for the hypoxic cell evolution in Fig. 4.5. Independently of the optimisation routine used, except for the necrotic cells, the estimation error tended to increase with time, so that predictions for later time points ($TP5$) had higher errors than for earlier time points ($TP3$).

4.3.4 3-D growth simulations

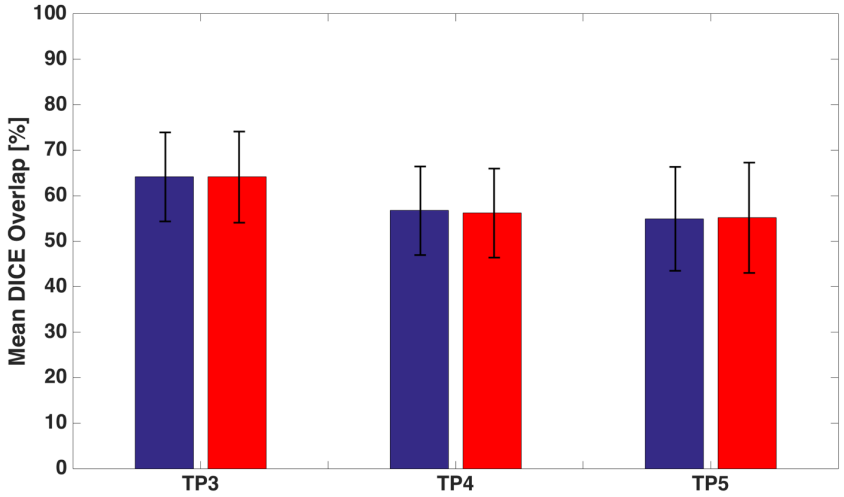


Figure 4.6: Mean DSC overlap between the true and estimated tumours for all cases for optimisation routines I (blue) and IV (red).

Relative Error in Cell Number	TP3	TP4	TP5
Proliferative (I)	0.917±1.271	1.133±2.182	1.345±2.883
Proliferative (IV)	**0.056±1.400**	**0.542±1.134**	**0.6634±0.974**
Hypoxic (I)	**1.395±1.281**	3.686±2.795	4.494±2.799
Hypoxic (IV)	1.647±2.321	**2.814±3.379**	**2.133±4.561**
Necrotic (I)	-0.466 ±0.468	-0.268±0.762	**-0.024±0.956**
Necrotic (IV)	**-0.194±0.340**	**0.1533±0.262**	0.113±0.452
Total (I)	-0.169±0.216	**0.280±0.2286**	0.407±0.378
Total (IV)	**0.064±0.238**	0.462±0.507	**0.342±0.669**

Table 4.6: Mean relative errors in cell number prediction for $TP3$-$TP5$ using optimisation routines I and IV. bold values highlight best results for the comparison between both optimisation routines. Negative values indicate an underestimation in the specific sub-population cell number.

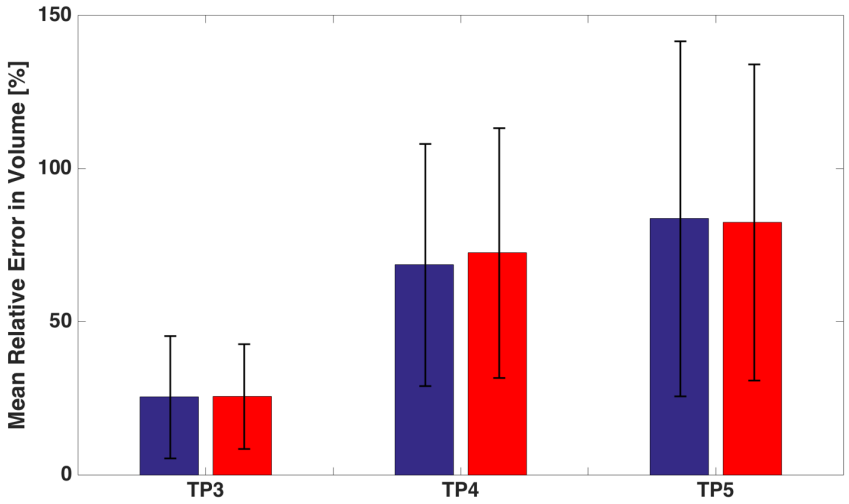


Figure 4.7: Mean percent error between the true and estimated volume values for all cases for optimisation routines I (blue) and IV (red).

Our model outcome does not only allow for the estimation of the global cellularity evolution, but also for the prediction of volumetric tumour growth as well as of the local distribution of cells within the tumour borders. As illustrated in Fig. 4.6, a slight decrease in the mean DSC values can be observed for both optimisation routines. On average, for all seven cases using optimisation routine I (blue) resulted in a DSC 64.20±9.79%, 56.78±9.73% and 54.93±11.43%, for $TP3$, $TP4$ and $TP5$, respectively. When using optimisation routine IV, the DSC values were 64.15±9.99%, 56.20±9.78% and 55.18±12.10%, for $TP3$, $TP4$ and $TP5$, respectively.

The mean relative volume errors are given in Tab. 4.7 and illustrated in Fig. 4.7. For both optimisation routines, an increase in the errors can be observed as simulation time increases. For $TP3$ and $TP4$, keeping c_{f_0} constant (optimisation routine I) yielded slightly better results than when c_{f_0} was added as a model parameter (optimisation routine IV). The opposite was true for $TP5$.

The cellularity distribution for four of the pre-clinical cases (1, 2, 4 and 6) are

	Relative Volume Errors	
Time Points	Optimisation Rule I	Optimisation Rule IV
TP3	**0.254±0.199**	0.256±0.171
TP4	**0.686±0.395**	0.725±0.407
TP5	0.836±0.580	**0.824±0.516**

Table 4.7: Mean relative volume errors for $TP3$-$TP5$ using optimisation routines I and IV. bold values highlight best results for the comparison between both optimisation routines.

shown in Fig. 4.8, Fig. 4.12, Fig. 4.13 and Fig. 4.14 to further illustrate the comparison between optimisation routines I (top) and IV. The true (left columns) and the estimated (middle columns) relative cell distributions are shown for $TP2$, $TP3$, $TP4$ and $TP5$. In the right columns, for a central slice of the tumour volume, the residual maps obtained by subtracting the true maps from the estimated maps are shown. The black outlines displayed within the residual images represent the true tumour delineation. For the true and estimated maps, the colour bar represents the number of cells relative to the voxel cell capacity and hence, ranges from 0 to 1. For the residual maps the colour bar ranges from -1 to 1 whereby negative and positive values represent a local underestimation and overestimation in the cell number, respectively.

The different parameter values obtained for each optimisation routine and case resulted in distinct estimated maps. While the sizes of the estimated tumours did not differ substantially (as expected given the small differences in volumetric errors), the distribution of cells within the tumour borders depicted a difference depending on the optimisation routine, and hence the parameter values, used for the simulation. This difference becomes more evident as simulation time progresses, for instance for $TP4$ and $TP5$. For all cases, especially for $TP4$ and $TP5$, areas of overestimation can be generally observed at the periphery of the tumours. Areas of underestimation can be observed in central parts of tumours, due to an underestimation in the necrotic cell numbers as seen in Tab. 4.6.

From all cases included, Case 1 depicted the best result in terms of growth prediction (Fig. 4.8) independently of the optimisation routine applied. However, a difference in the distribution of the cells within the tumour depending on the optimisation routine can be observed. To further explore this difference, the distribution of proliferative, hypoxic and necrotic cells for Case 1 are displayed in Fig. 4.9-Fig.4.11.

Using optimisation routine I yields a more predominant proliferation level in the outer rim of the tumours ($TP3$ and $TP4$) than when using optimisation routine IV, as shown in Fig. 4.9. The level of proliferation, represented by both the higher values of the colour bar and the wider areas of proliferation, is much higher for the maps obtained with optimisation routine IV. Overall optimisation routine I yields a better prediction of the proliferative cells.

A more homogeneous spread of hypoxic cells for optimisation routine IV can be observed in Fig. 4.10. Optimisation routine I yielded areas of hypoxia which are more prominent in the rim than in the tumour center. As for the distribution of proliferative cells, overall optimisation routine I yields a better prediction of the hypoxic cells than optimisation routine IV when compared to the true maps.

In Fig. 4.11, a much greater underestimation in necrotic cell numbers as well as a more homogeneous distribution can be observed for optimisation routine IV. The numbers of necrotic cells are much smaller for optimisation routine IV than for optimisation routine I. For instance, for $TP5$, the maximum is approximately 0.1 of the voxel capacity as compared to 0.9 in true maps and 0.6 when using optimisation routine I. This may be due to the estimation of c_{f_0} which will affect $cons_{h_0}$ and hence the number of necrotic cells. Not all voxels inside the tumour are at their maximum capacity, and hence the number of proliferative, necrotic and hypoxic cells will not necessarily add up to 1. Nonetheless, in terms of maps estimation,

keeping c_{f_0} constant (optimisation rule I) yielded better results. This is also represented in the higher $cell_{error}$ depicted in Tab. 4.8. This error, related to the sum of square errors in the $r(x,t)$, is defined as $cell_{error} = \left(r_t(x,TP2) - r_e(x,TP2)\right)^2/\Theta$, where $r_t(x,TP2)$ and $r_e(x,TP2)$ represent the true and simulated total cell maps at $TP2$, respectively. It can be seen as a measure of variation between the predicted and true cellularity maps.

	$cell_{error}$	
Time Points	Optimisation Rule I	Optimisation Rule IV
TP3	**4.03E+14 ± 3.18E+14**	4.21E+14 ± 3.62E+14
TP4	**4.69E+14 ± 2.76E+14**	4.80E+14 ± 3.55E+14
TP5	**6.65E+14 ± 4.17E+14**	7.24E+14 ± 5.07E+14

Table 4.8: Mean $cell_{error}$ for $TP3$-$TP5$ using optimisation routines I and IV. Bold values highlight best results for the comparison between both optimisation rules.

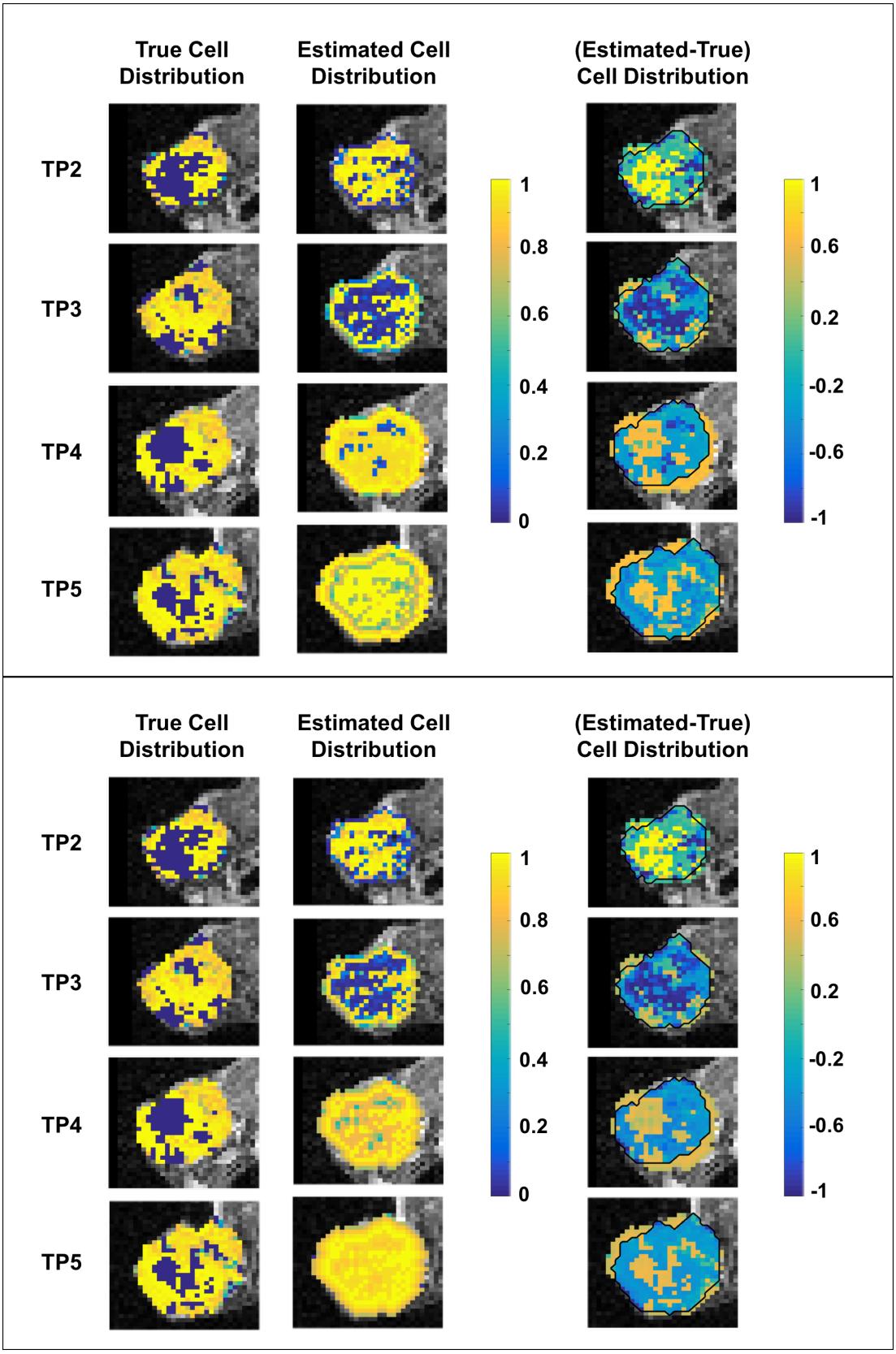


Figure 4.8: True and estimated cell distributions for Case 1 obtained using optimisation routine I (top) and optimisation routine IV. The true (left column) and the estimated (middle column) relative cell distributions for an example pre-clinical case are shown for $TP2$, $TP3$, $TP4$ and $TP5$. In the right column, for a central slice of the tumour volume, we show the residual maps obtained by subtracting the true maps from the estimated maps. The black outlines displayed within the residual images represent the true tumour delineation.

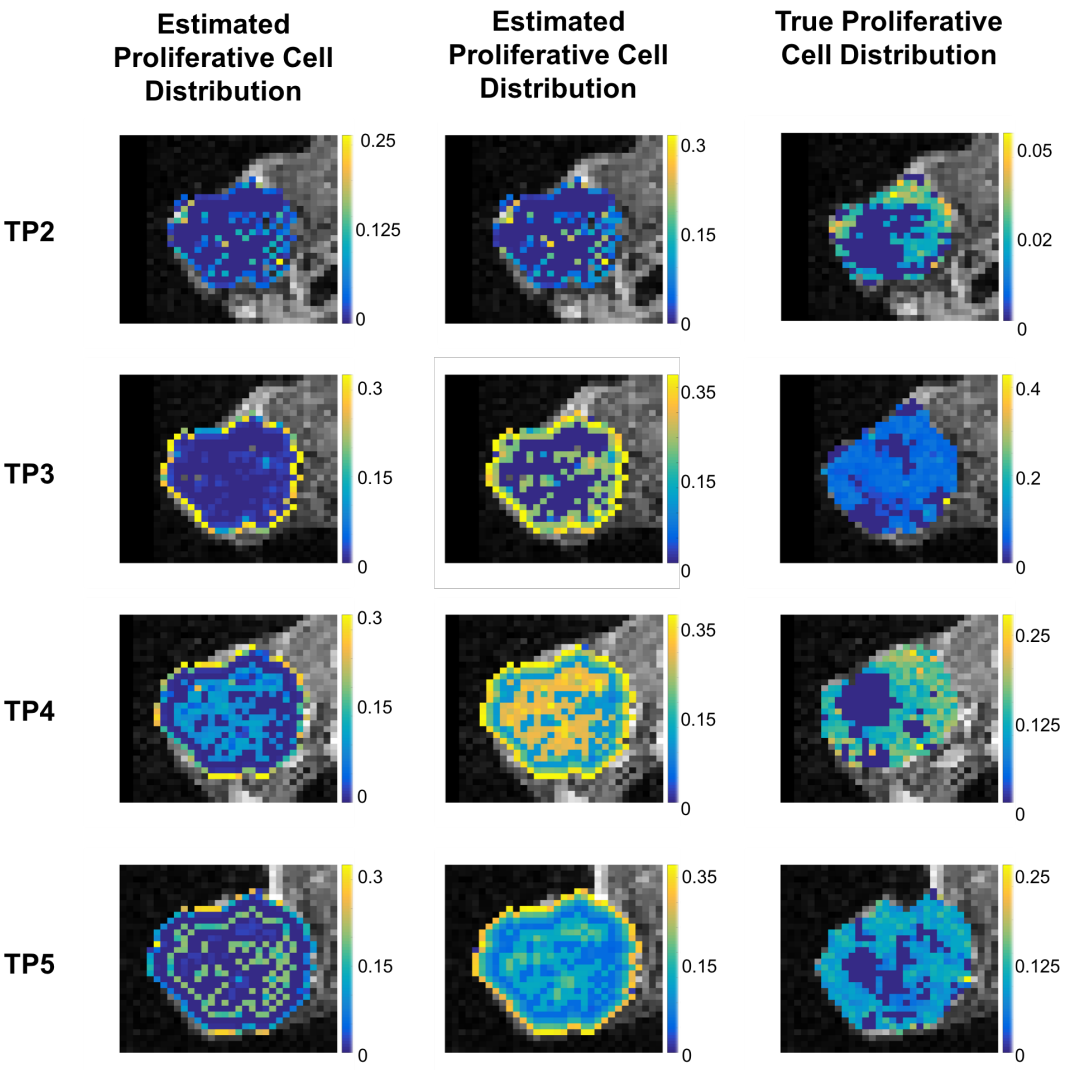


Figure 4.9: True and estimated proliferative cell distributions for Case 1. The estimated (left and middle columns) relative proliferative cell distributions for an example pre-clinical case are shown for $TP2$, $TP3$, $TP4$ and $TP5$ for optimisation routine I and IV, respectively. The true relative maps for proliferative cells are shown in the right column.

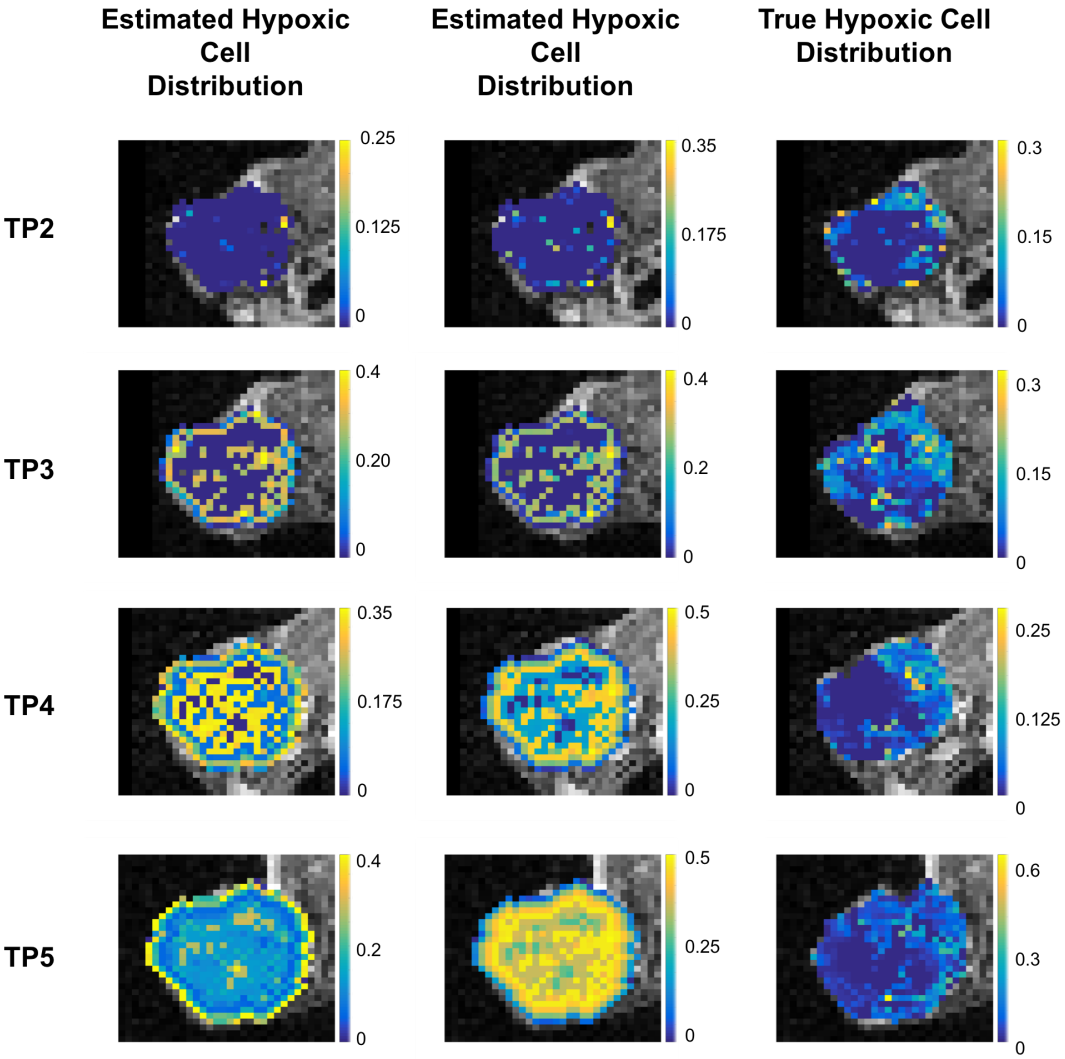


Figure 4.10: True and estimated hypoxic cell distributions for Case 1. The estimated (left and middle columns) relative hypoxic cell distributions for an example pre-clinical case are shown for $TP2$, $TP3$, $TP4$ and $TP5$ for optimisation routine I and IV, respectively. The true relative maps for hypoxic cells are shown in the right column.

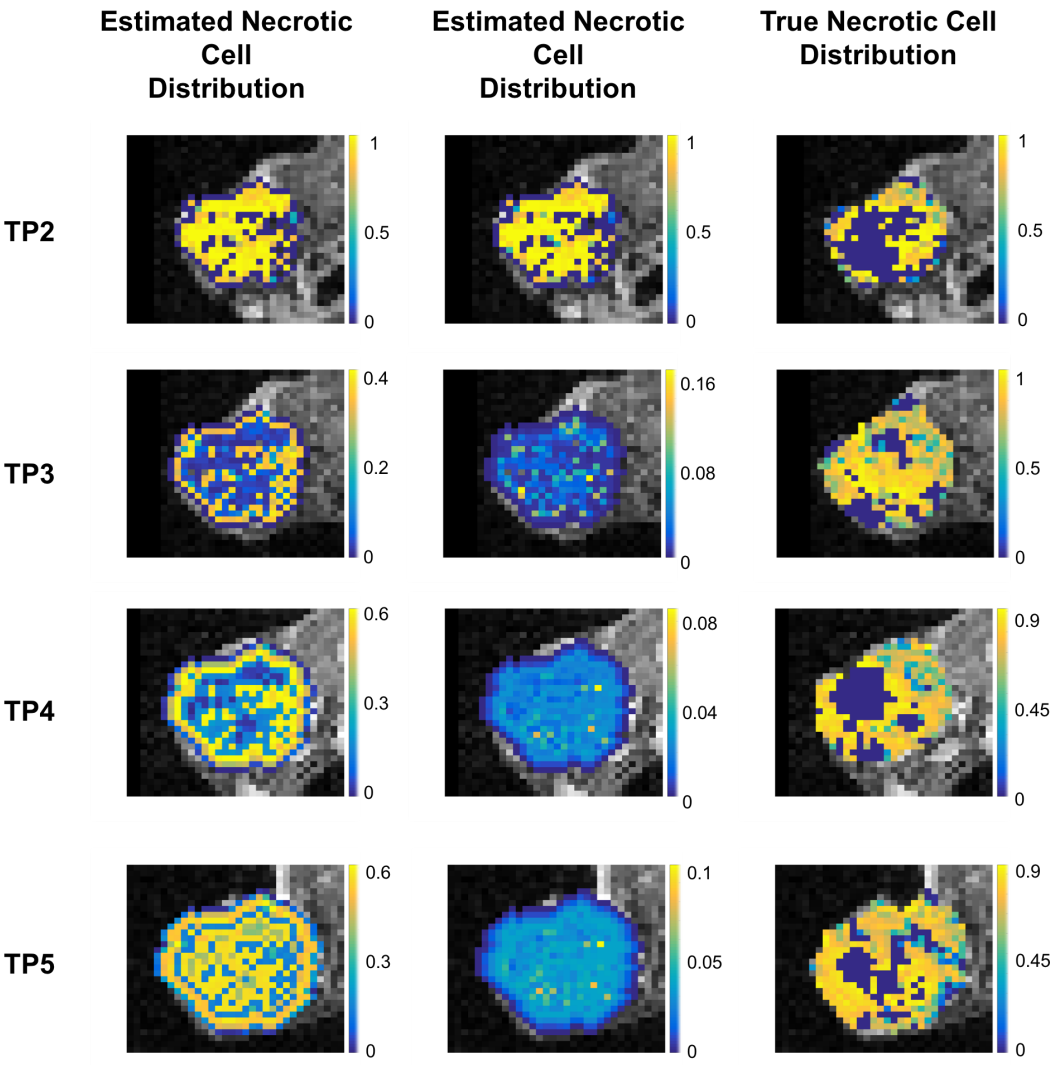


Figure 4.11: True and estimated necrotic cell distributions for Case 1. The estimated (left and middle columns) relative necrotic cell distributions for an example pre-clinical case are shown for $TP2$, $TP3$, $TP4$ and $TP5$ for optimisation routine I and IV, respectively. The true relative maps for necrotic cells are shown in the right column.

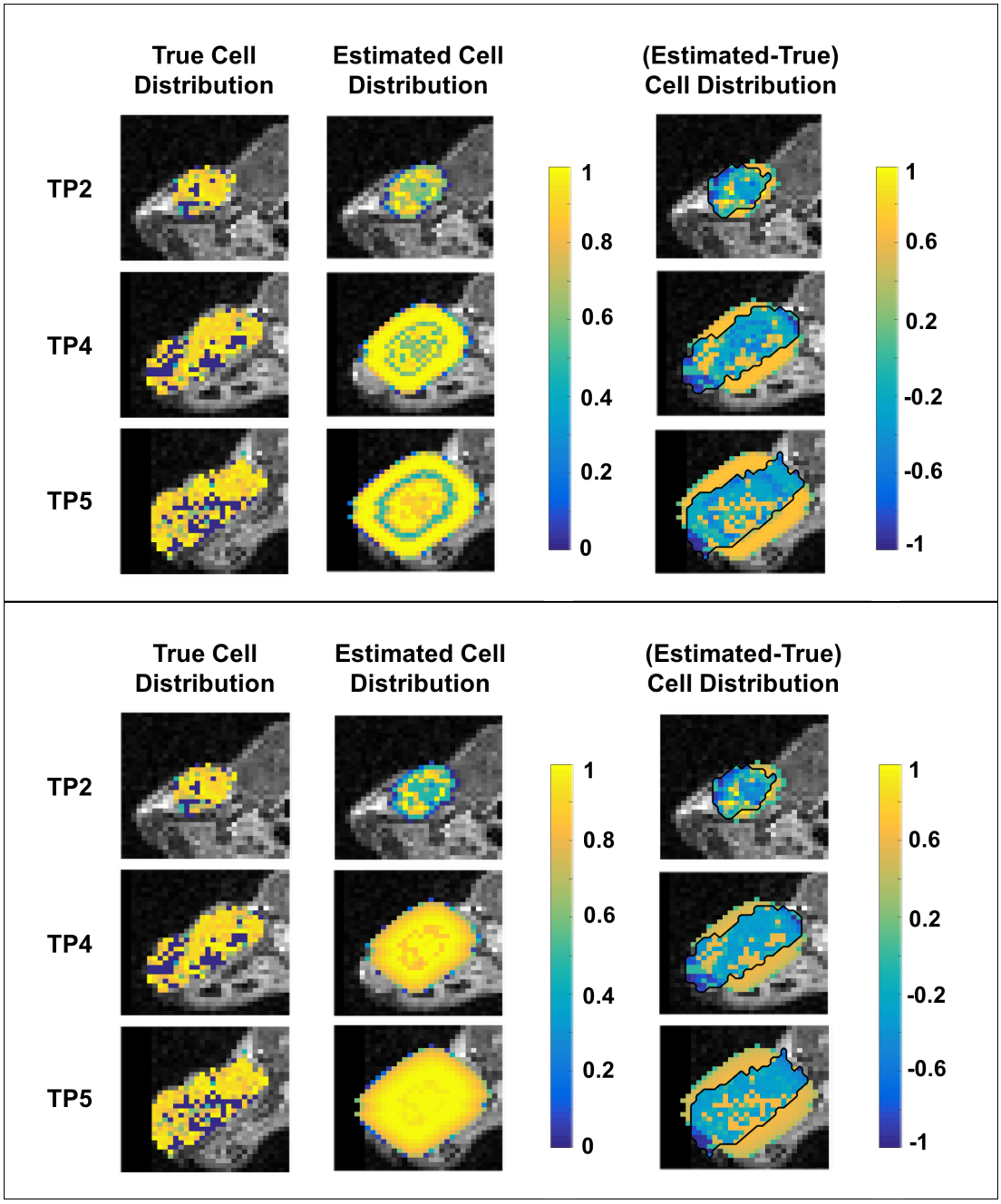


Figure 4.12: True and estimated cell distributions for Case 2 obtained using optimisation routines I (top) and IV. The true (left column) and the estimated (middle column) relative cell distributions for an example pre-clinical case are shown for $TP2$, $TP3$, $TP4$ and $TP5$. In the right column, for a central slice of the tumour volume, we show the residual maps obtained by subtracting the true maps from the estimated maps. The black outlines displayed within the residual images represent the true tumour delineation.

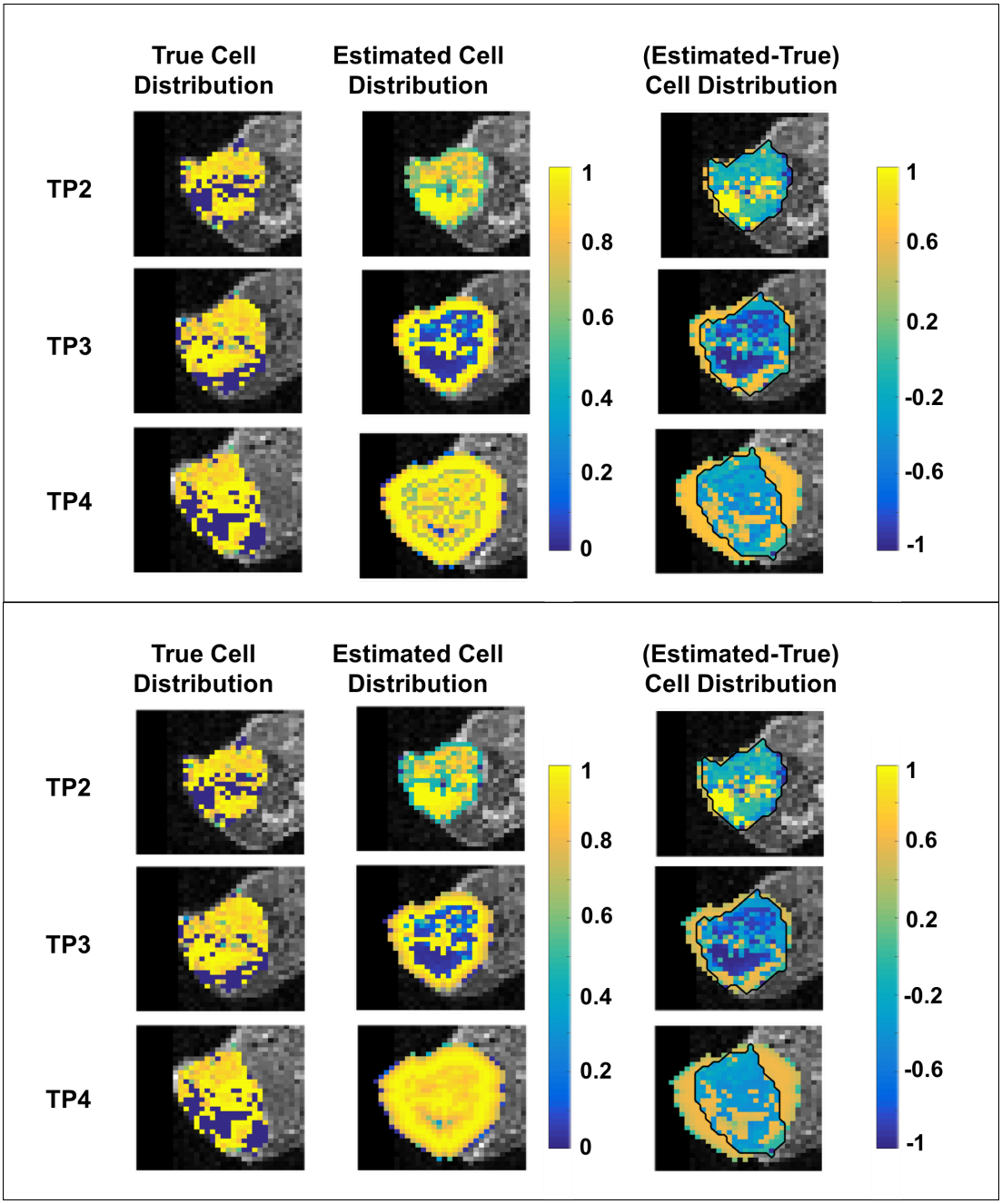


Figure 4.13: True and estimated cell distributions for Case 4 obtained using optimisation routines I (top) and IV. The true (left column) and the estimated (middle column) relative cell distributions for an example pre-clinical case are shown for $TP2$, $TP3$, $TP4$ and $TP5$. In the right column, for a central slice of the tumour volume, we show the residual maps obtained by subtracting the true maps from the estimated maps. The black outlines displayed within the residual images represent the true tumour delineation.

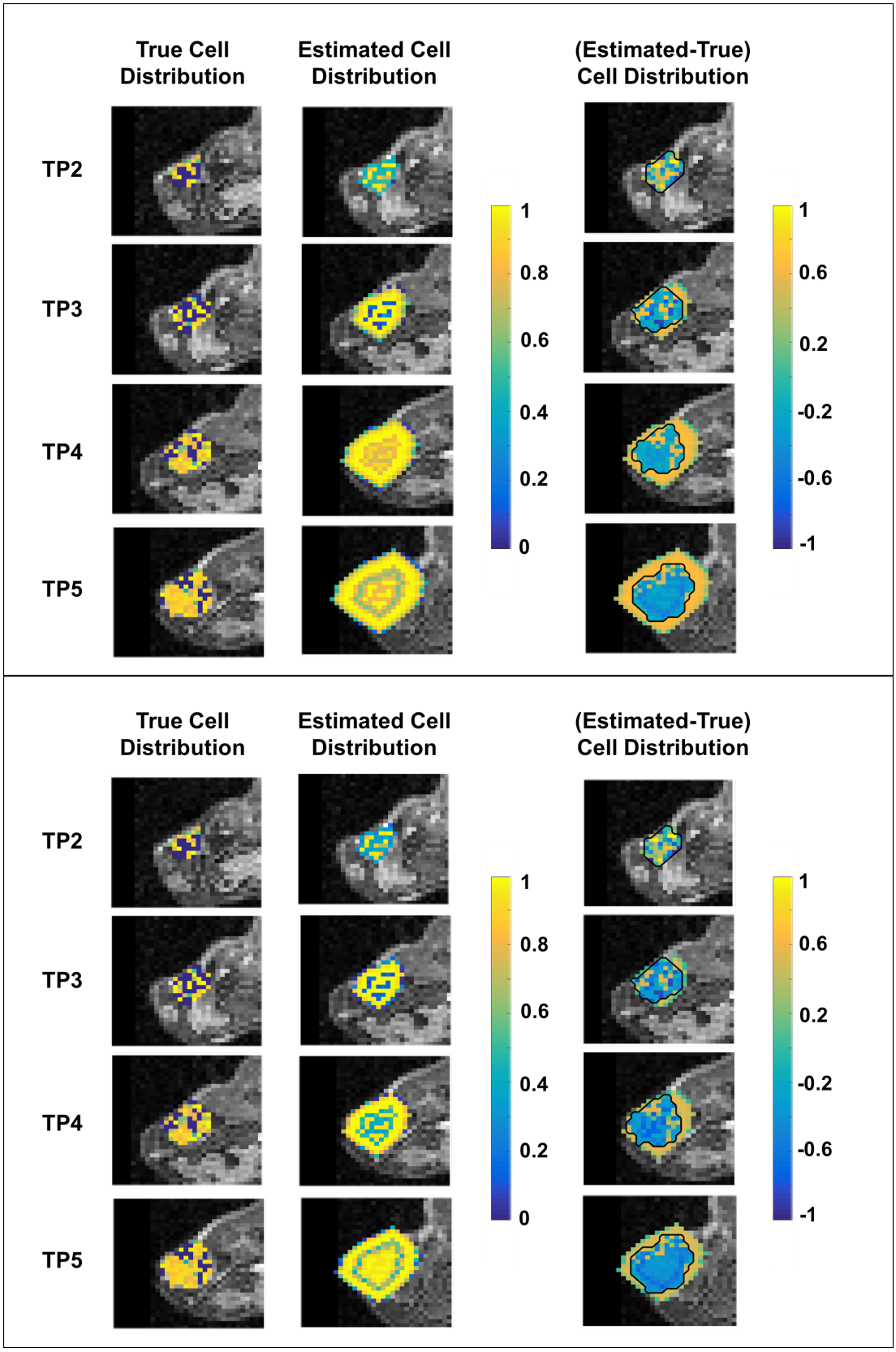


Figure 4.14: True and estimated cell distributions for Case 6 obtained using optimisation routines I (top) and IV. The true (left column) and the estimated (middle column) relative cell distributions for an example pre-clinical case are shown for $TP2$, $TP3$, $TP4$ and $TP5$. In the right column, for a central slice of the tumour volume, we show the residual maps obtained by subtracting the true maps from the estimated maps. The black outlines displayed within the residual images represent the true tumour delineation.

4.4 Discussion and Conclusions

In this chapter, we have presented a methodology to parametrise a reaction-diffusion model of avascular tumour growth using quantitative data extracted from DCE-MRI data. We first tested our methodology on synthetic data. The results showed that using our methodology we were able to accurately predict future tumour growth, manifested in small volume errors and large Dice values. Encouraged by these results, we applied our model to data obtained from DCE-MR images for seven pre-clinical cases of breast carcinoma. Overall, our results demonstrated the feasibility of using maps of cellularity obtained from DCE-MRI analysis to feed and calibrate a model of tumour growth to obtain subject-specific predictions of tumour evolution.

Using synthetic data allowed us to compare many different optimisation routines. The comparison between the two with the smallest parameter recovery and volumetric errors led to the conclusion that while using a smaller c_{g_0} and fixing c_{f_0} may result in more accurate distribution of the cells, using a higher c_{g_0} and estimating c_{f_0} yielded better results in terms of both volume and dice overlap errors. We further compared these two optimisation routines to assess whether adding c_{f_0} and hence increasing the number of parameters and the computational cost of the model led to better results on real data.

Figure 4.5 and Tab. 4.6 demonstrated that using cellularity maps from two early time points of tumour development we were able to predict within a reasonable error margin the overall number of cells at later time points. Accounting for each sub-population evolution in addition to the overall volume growth is a strength of the current model compared to other works where all cells within the tumour or a given voxel are assumed to be active and divide at the same proliferation rate [12, 16, 15]. For instance, in our results, the biggest increase was seen in the

number of necrotic cells suggesting that most of our tumour growth was due to the emergence and growth of necrotic rather than proliferative areas. In addition, the hypoxic cell numbers could be used to aid treatment planning, as hypoxia is known to play an important role in treatment outcome.

However, our results demonstrated that even if the model can predict the total cell evolution within a small range of errors, it is not able to distribute the cells into the three sub-categories correctly, represented especially by an overestimation in the number of hypoxic cells. In terms of global cellularity estimation, optimisation routine IV yielded in general smaller errors than optimisation routine I. Especially the errors for the estimation of hypoxic cells were smaller when c_{f_0} was calibrated, demonstrating the importance of this parameter to the model as it influences the rate at which proliferative cells turn hypoxic but also the rate at which hypoxic cells turn necrotic.

The pre-clinical data analysis demonstrated greater volume errors and smaller Dice values compared to our synthetic experiments. Both optimisation routines perform similarly, with optimisation routine I yielding slightly better results. These results are similar to the ones presented by [15] for their *in vivo* experiments. However, the fact that they assumed that all cells within a given voxel or even within the tumour will follow the same proliferation rules is a major limitation of their approach when compared to ours.

Independently of the optimisation routine used, the cellular prediction and relative volume errors tend to increase with time, so that predictions for later time points ($TP5$) depicted higher errors than for earlier time points ($TP3$). This trend may be due to two reasons. Firstly, the period between the images used for calibration was one day ($TP1$ until $TP2$), so that using the optimised parameters for simulation from $TP2$ onwards might only allow us to predict the volume of

the tumour for the same period, i.e. up until $TP3$. Secondly, for later time points we expect the tumour to have undergone angiogenesis. Our model, however, does not include angiogenesis, and as such only simulates avascular tumour growth. The fact that we already account for hypoxic cells can aid in the introduction of vascularization to the model, as hypoxia is known to play a crucial role in the process of angiogenesis.

A major strength of our model when compared to the existent literature (e.g. [16], [12], [17], [15]) is that it does not only allow for the assessment of global values, such as the Dice, the volume error and the total cell number; but it also allows for the assessment of local cell density distribution as well as local tumour activity represented by proliferation, hypoxia and necrosis.

Our results in Fig. 4.8- 4.14 demonstrated that our model performs better for some cases (e.g. Cases 1 and 6) than others (Case 2 and 4), showing that even within a controlled experiment - the same cell line was injected in subjects belonging to the same species (mice) - tumour progression can vary hugely due to subject-specific microenvironmental aspects. Our model seems to perform better for cases with a more spherical tumour shape (Cases 1 and 6, e.g.) than for finger-shaped tumours like the ones observed in Cases 2 and 4. For the latter, a larger overestimation in the tumour peripheries can be observed. This is because our model does not include information from the surrounding to decide the direction of tumour expansion and a diffusion law is assumed to govern tumour expansion.

Even when lysis time is considered, the model fails at predicting some necrotic areas (such as the ones seen in the true maps shown in Fig. 4.8- 4.14). This might be linked to our assumption that the tumour centre of mass remains constant over its evolution, so that voxels in the centre of the tumour are assumed to correspond over time. When this is not the case, voxels which were necrotic (and hence

empty) at $TP1$ but populated in $TP2$ might not be the corresponding voxels. As a result, in the simulated cell maps for $TP2$ the voxels will be populated and their cells will continue to proliferate, turn hypoxic or die depending on their nutrient level.

At a global level, adding an extra parameter, c_{f_0}, slightly improved the prediction results. At a local level, however, keeping c_{f_0} constant yielded better results, as seen in Fig. 4.9-Fig. 4.11. This was especially true for the estimation of the necrotic cell distribution. Given that we are not only interested in how the tumour expands globally but also in how it changes locally, it follows that there is no added benefit in increasing the number of parameters to be estimated. The fact that we only have one model parameter, D_0, is an additional strength of our model which can capture the complexity in tumour growth including localised cell number evolution, hypoxia, necrosis and proliferation yet remain simple and hence computationally efficient.

There are a few limitations in this current approach. The first limitation has to do with the data set itself. The high spatial resolution comes at the cost of a low temporal resolution which effects the results for the extracted DCE-MR related maps, especially the flow maps. Given the relationship between flow and the derived necrotic cell distributions, the low temporal resolution may explain the higher underestimation in the necrotic cell numbers, observed for instance in Fig. 4.11 and in Tab 4.6.

Another limitation is the fact that a population-based AIF rather than measurements for each individual case was used. The AIF is known to vary between individuals and visits due to variation in physiological parameters such as cardiac output, renal function, and also in external parameters such as injection timing. It has also been shown that using a standard population-averaged AIF

for all patient scans at all time-points can lead to large errors in PK parameter values [116]. Therefore, in a clinical scenario, it would be better to compute a patient-specific AIF to ensure that the model is personalised to each patient. It would also be desirable to have data with high temporal resolution to ensure better fitting of the contrast enhancement curve and thus improved values of flow and volume of distribution. However, measuring AIF is of great challenge in a pre-clinical scenario, so that the use of a population-based AIF becomes a helpful tool.

Accurate estimation of the volume of distribution may also be influenced by data truncation when determined by Eq. 4.3 [59]. Having more confidence in the parameter estimation approach is especially important as errors in this parameter will result in errors in the cellularity maps used to calibrate and validate the model. An alternative would be to extract this parameter through compartmental modelling. This comes, however, at the cost of strong assumptions on the distribution of the CA inside the tissue. The choice of the model and the parameters that can be estimated depend greatly on the quality of the data available.

In conclusion, our pre-clinical data experiments suggest that the reactiondiffusion model introduced in Chapter 3 can be parametrised by DCE-MRI data to estimate local and global tumour evolution. However, the fact that the errors reported in this chapter are larger than the ones found in our synthetic experiments suggests that this model provides an incomplete description of tumour growth and should be amended to provide better predictions, especially for later time points. Therefore, to investigate whether including angiogenesis to the model would result in better estimations, an updated version of this model, which includes angiogenesis, will be introduced and analysed in the next chapter.

Chapter 5

3-D Model of Vascular Tumour Growth

In Chapter 2 we have provided a detailed description of tumour growth and the biological processes involved in it. In the first stage of tumour growth, the nutrients needed for cells to proliferate are provided by simple diffusion from the surrounding into the tumour. As a result, there is typically a maximum size (several millimetres) to which the tumour can grow. Due to the higher proliferation activity in tumours, oxygen demand is surpassed by oxygen supply creating a hypoxic environment. At this stage, the tumour shifts from its avascular phase towards the vascular phase. The hypothesis that angiogenesis is responsible for this later stage of tumour growth was first put forward by Folkman [117] in 1971. In his study he hypothesised that the tumour-angiogenesis factor (TAF) is responsible for the stimulation of new capillaries in tumours and hence for the vascular phase of tumour growth. Hypoxic cells within the tumour are known to play an important role in this process by releasing TAFs. These factors diffuse towards nearby vessels, degrade the basal membrane of the blood vessels and

promote migration of the endothelial cells (ECs) towards the source of TAFs, i.e. the tumour. Hypoxia is also involved in this process by inducing EC proliferation and supporting the maturation of the newly created vessels.

Most of the mathematical models accounting for angiogenesis concentrate on tracking the EC migration as a response to a stimulus provided by the TAFs [118, 119, 120]. These models do not account for nutrient delivery to the tumour tissue by the emerged vasculature and focus mainly on the creation of the capillaries than on their effect on tumour growth. To overcome this limitation, coupled models of angiogenesis and tumour growth have been proposed [121, 122, 123, 124]. These approaches normally track each individual endothelial or cancer cell, and hence, their simulations come at a very high computational cost which limits their application to the one-dimensional or two-dimensional domains. In spite of their limitations in terms of clinical use, these models do provide a means to examine the interactions between different physical mechanisms (e.g. rate of TAF production, strength of chemoctatic response, the rate of capillary formation), angiogenesis and tumour growth.

The aim of this chapter is to develop and evaluate a model of vascular tumour growth which is able to account for tumour vascularisation and its effect on tumour growth while remaining computationally tractable. To this end, we extend the model presented and tested in Chapters 3 and 4 to include the effect of angiogenesis on tumour growth. Our model differs from the above mentioned ones in that it does not explicitly model the vascular network or follow the migration of each EC as a response to TAF excretion and diffusion. Instead, we focus on the macroscopic changes that can be observed longitudinally on medical imaging scans. To account for the fact that angiogenesis affects tumour growth, while tumour cells affect angiogenesis through changes in the tumour microenvironment,

we present a coupled model of angiogenesis and tumour growth.

In a similar way to Chapter 3, we start off by presenting the model along with its assumptions and equations. Next, we perform experiments including synthetic and pre-clinical data. Finally, we discuss the results achieved and also compare them to the the ones obtained in Chapter 4.

5.1 Methods

In the section that follows we will describe how the model presented in Chapter 3 has been modified to account for vascular tumour growth. Instead of modelling tumour-induced angiogenesis in all its complexity, we propose a simplified model which is still able to capture the essence of the complicated physical reality of processes involved in angiogenesis and tumour growth. An overview of the model is given in Fig. 5.1. DCE-MRI related physiological maps are used to compute v_D, proliferating, hypoxic and necrotic cell maps. These maps are used to initialise the model as outlined in Section 5.1.1. At the macroscopic layer, information is extracted from the maps about cellularity and v_D level (A). This information is used to initialise the model at the microscopic layer, where proliferation, hypoxia, necrosis and vascularisation take place (B). We account for angiogenesis as an increase in v_D. This increase starts after τ_{HB}, a time delay introduced to account for the time between TAFs expression and the neovascularisation. For each time step, the cellularity and nutrient maps are updated following proliferation, hypoxic and necrotic processes which happen in dependence of v_D, which includes the vasculature and hence the nutrients needed for tumour growth (C). Solving Eq. 5.5-Eq. 5.8 for each point in time and space results in a tumour growth observable at the macroscopic layer.

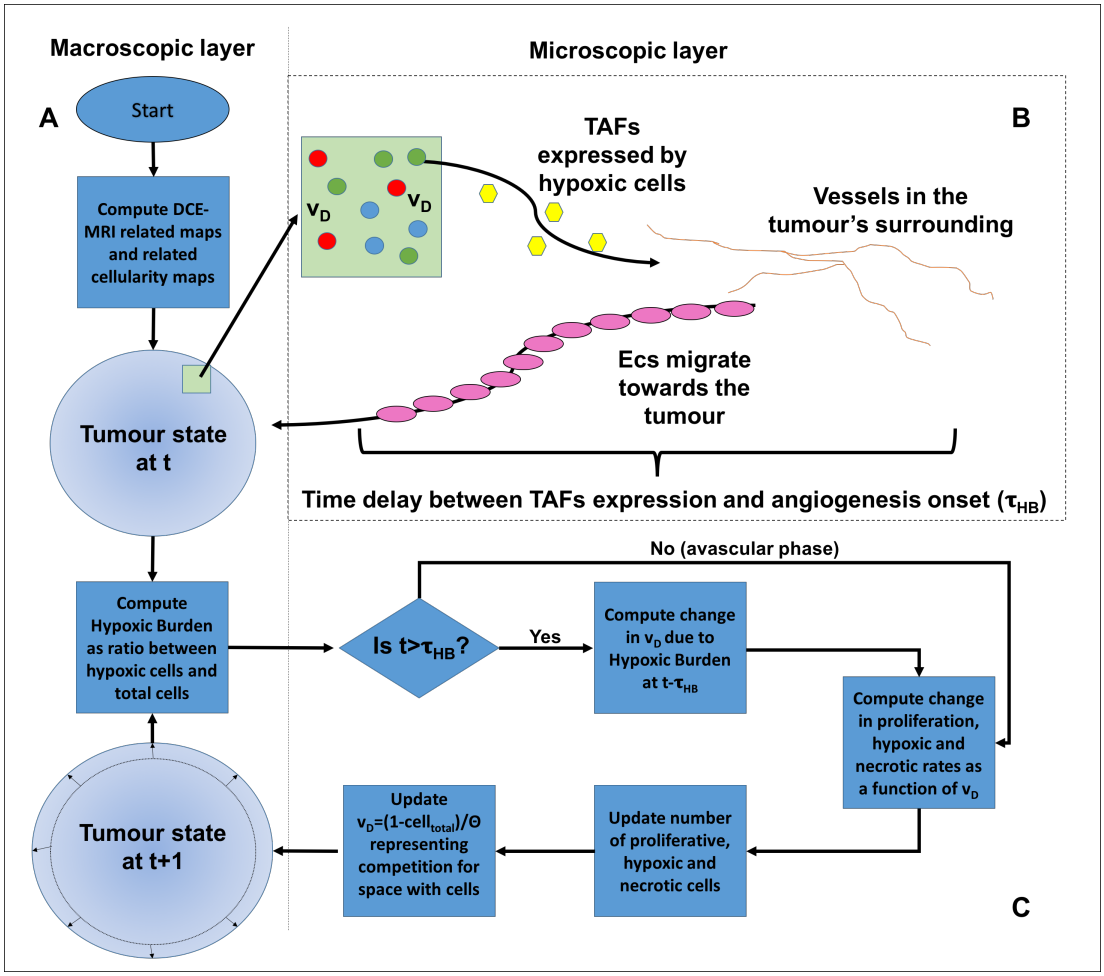


Figure 5.1: Overview of the vascular tumour growth model. This model represents a multiscale 3-D model informed by DCE-MRI and includes a macroscopic tissue, a cellular and a sub-cellular layer. Metabolic processes which depend on the local nutrient level can lead to cell proliferation, hypoxia or necrosis. In return, the activity status of tumour cells can lead to the creation of new vasculature, which in turn affects the nutrient distribution and hence further tumour growth. A more detailed figure description can be found in Section 5.1.

5.1.1 Model of vascular tumour growth

Hypoxia is known to play a crucial role in cancer progression, angiogenesis and resistance to therapy [117, 125, 126]. We therefore use the fact that the model developed in Chapter 3 already accounts for hypoxia and use it as the foundation for our vascular model. Assuming that the extracellular extravascular space remains constant [127], angiogenesis induced volume plasma change can be directly represented by changes in v_D. Hence, we propose to include hypoxia as the cause

of angiogenesis observed as a change in v_D.

We first quantify the level of hypoxia in the tumour by introducing a new term, the Hypoxic Burden (HB), which can be computed for each time step as:

$$HB(t) = \sum \frac{q(t)}{r(t)}, \tag{5.1}$$

where $q(t)$ represents the total number of hypoxic cells and $r(t)$ the total number of tumour cells within the tumour margins.

Similar to the tumour growth model in Chapter 3, the model including angiogenesis accounts for processes happening at the cellular layer including the evolution of proliferating, hypoxic and necrotic cells. However, instead of assuming a nutrient distribution like the one used in Chapter 3 (see Eq. 3.11), here we explore the fact that all nutrients available to the tumour cells within the tumour will come from the vasculature and hence from v_D, and assume that proliferation, hypoxia and death rates will depend on v_D directly. The maps for the cell division probability g, the hypoxia transition f and the necrosis transition h are thus directly related to the volume of distribution v_D, as follows:

$$g(v_D(\mathbf{x},t)) = G_{max} \exp(-\exp(-c_{g_0} \cdot (v_D(\mathbf{x},t) - ip)) \tag{5.2}$$

$$f(v_D(\mathbf{x},t)) = F_{max} \exp\left(-c_{f_0} \cdot v_D(\mathbf{x},t)\right) \tag{5.3}$$

$$h(v_D(\mathbf{x},t)) = H_{max} \exp\left(-c_{h_0} \cdot v_D(\mathbf{x},t)\right) \tag{5.4}$$

where c_{g_0}, c_{f_0} and c_{h_0} are model parameters which influence the response of the proliferation, hypoxia and necrosis rate to v_D, and v_D values lie between 0 and 100

%. We recall that the constant c_{g_0} represents the slope of the Gompertz function and ip is the position of the steepest increase of the nutrient, and therefore the inflection point of the Gompertz curve. The constants G_{max}, F_{max} and H_{max}, measured in $1/h$, are the maximum possible proliferation, hypoxic and necrotic rates, respectively.

Tumour-induced angiogenesis is generated by endothelial cells which migrate from surrounding blood vessels towards the tumour as a response to tumour angiogenic factors (TAFs) expressed by hypoxic cells. Because these processes happen at the microscopic level, they cannot be observed with imaging modalities such as DCE-MRI. Therefore we choose not to follow the TAFs journey towards the closest vasculature present in the tumour surrounding or the dynamics of the endothelial cells as a response to the TAFs, but instead to look at the end result of this process: the changes in the tumour vasculature represented by a change in v_D.

This whole process from the hypoxic cells extracting the TAFs to the endothelial cells forming the new tumour vasculature takes certain amount of time. For instance, [128] suggests that the ECs migrate at a speed of 0.36mm/day. This also means that depending on the distance of the surrounding vasculature, each tumour will become vascularised at a different point in its evolution. Hence, we introduce a model parameter, τ_{HB}, to account for the delay between emergence of hypoxia and the increase in v_D and to determine the time point in which the transition between the avascular and the vascular phases happens.

As long as t is smaller than or equal to τ_{HB}, the tumour remains avascular and there is no increase in v_D due to angiogenesis. Once t overtakes τ_{HB}, angiogenesis, and hence the vascular phase of tumour growth starts (see Fig. 5.1, C).

Similarly to tumour cells, endothelial cells not only proliferate but also migrate

to create the vascular network. This behaviour can be captured by the reaction-diffusion model as shown in [16]. We hence introduce a further PDE to model the change in v_D as a result of tumour hypoxia (represented by the Hypoxic Burden (HB)) and the time delay τ_{HB} as follows:

$$\frac{\partial v_D(\mathbf{x},t)}{\partial t} = \bigtriangledown \cdot (d(\mathbf{x},t) \bigtriangledown v_D(\mathbf{x},t)) + k_{HB} \cdot HB(t-\tau_{HB}) \cdot v_D(\mathbf{x},t) \qquad (5.5)$$

with t denoting time, $\mathbf{x}$ a spatial coordinate in a three-dimensional domain and k_{HB} a proportionality rate constant to relate HB to the change rate in v_D. This constant (here assumed to be 1 $hour^{-1}$) will have an impact on the potential oscillations that could arise from introducing the time delay τ_{HB} to Eq. 5.5.

Tumoural cells can proliferate, turn hypoxic or die depending on their oxygen and nutrient levels. Due to the diffusion limit of oxygen, functional cells must be located within 100µm of a capillary blood vessel [4]. Therefore, the amount of v_D and, consequently of oxygen, in each voxel is assumed to have a local influence on cell growth and death. With that in mind, and based on the fact that tumoural cells do not only undergo changes in activity but also spread over time, we can update the reaction-diffusion equations of Chapter 3 describing the proliferative, hypoxic and necrotic cellularity evolution in terms of their v_D dependency as follows:

$$\frac{\partial p(\mathbf{x},t)}{\partial t} = \bigtriangledown \cdot (d(\mathbf{x},t) \bigtriangledown p(\mathbf{x},t)) + g(v_D(\mathbf{x},t)) \cdot p(\mathbf{x},t) \cdot \left(1 - \frac{r(\mathbf{x},t)}{\Theta}\right) - f(v_D(\mathbf{x},t)) \cdot p(\mathbf{x},t) \qquad (5.6)$$

$$\frac{\partial q(\mathbf{x},t)}{\partial t} = \bigtriangledown \cdot (d(\mathbf{x},t) \bigtriangledown q(\mathbf{x},t)) + f(v_D(\mathbf{x},t)) \cdot p(\mathbf{x},t) - h(v_D(\mathbf{x},t)) \cdot q(\mathbf{x},t) \quad (5.7)$$

$$\frac{\partial n(\mathbf{x},t)}{\partial t} = h(v_D(\mathbf{x},t)) \cdot q(\mathbf{x},t) \quad (5.8)$$

where $p(\mathbf{x},t)$, $q(\mathbf{x},t)$, $n(\mathbf{x},t)$ and $r(\mathbf{x},t)$ represent the number of proliferative, quiescent (hypoxic), necrotic and total cells, with t denoting time and $\mathbf{x}$ a spatial coordinate in a three-dimensional domain. The dependence on $v_D(\mathbf{x},t))$ yields a dependence on time and space for the proliferation and hypoxic rates. This dependency indirectly relates the rates to the total number of cells (given that v_D and cells are competing for space), which eliminates the need to explicitly account for an eventual dependence of the proliferation rate $g(v_D(\mathbf{x},t))$ on the number of proliferative cells. Similarly to the model in Chapter 3, necrotic cells are removed from the tumour after a lysis time of 40 hours [8]. To this end, necrotic cells are registered according to their age, and eliminated once their respective lysis time has elapsed.

The number of total tumoural cells can then be updated using:

$$r(\mathbf{x},t) = p(\mathbf{x},t) + q(\mathbf{x},t) + n(\mathbf{x},t) \quad (5.9)$$

Once the new number of total tumour cells is known, Eq. 4.7 can be solved for v_D as follows:

$$v_D(\mathbf{x}) = 1 - \frac{r(\mathbf{x})}{\Theta}. \tag{5.10}$$

This is a necessary step to account for the fact that v_D and r will be competing for space and that their sum cannot be larger than the total voxel volume. For the vascular phase, the value of $v_D(\mathbf{x})$ after Eq. 5.10 can be smaller than the value obtained with Eq. 5.5. This is a reasonable hard boundary condition which accounts for the loss rate that would usually be added in the LHS of Eq. 5.5 accounting for the loss of vasculature due to collapse, necrosis or the competition with other cells for space [16]. For the avascular phase, this is the only time where v_D is updated, and hence its change in $t+1$ will be simply due to the competition with tumoural cells represented by Eq. 5.10 rather than due to angiogenesis as represented by Eq. 5.5.

Finally, the isotropic diffusion coefficient d for v_D, q and p are assumed to be related to the total cell number r as follows:

$$d(\mathbf{x}, t) = D_0 \exp\left(-r(\mathbf{x}, t)/\kappa\right) \quad \cdot \tag{5.11}$$

As in Chapter 3, κ is chosen to be the maximum of the total cell number and D_0 is a parameter to be optimised.

We use the numerical strategy developed in Section 3.1.2 to solve the system of equations presented in this section, in particular Eq. 5.5-Eq. 5.8. We update the numerical strategy to account for Eq. 5.5, so that for Eq. 3.17-Eq. 3.21 v_D is used instead of p.

5.1.2 Estimation of tumour-specific parameters

Following the procedure derived in Sections 4.1.2 and 4.1.3, parameter maps derived from DCE-MR images at $TP1$ are used to initialise the vascular model. In order to predict the tumour evolution beyond $TP2$ using the model developed in the previous section, the model parameters c_{g_0}, c_{f_0}, c_{h_0}, D_0 and τ_{HB} need to be estimated. The parameters c_{g_0}, c_{f_0} and c_{h_0} are used in Eq. 5.1.1 in the same manner as the ones introduced in Chapter 3 with the difference that Eq. 5.1.1 depends on v_D instead of on pO_2.

Based on this analogy, we keep the ranges for these parameters as the ones used in Chapter 3, hence our estimation problem can be defined as:

$$\begin{aligned} \min_{c_{g_0},c_{f_0},c_{h_0},D_0,\tau_{HB}} \quad & vol_e(c_{g_0}, c_{f_0}, c_{h_0}, D_0, \tau_{HB}) \\ \text{s.t.} \quad & 0.15 \leq c_{g_0} \leq 0.5 \\ & 0.05 \leq c_{f_0} \leq 0.3 \\ & 0.1 \leq c_{h_0} \leq 0.6 \\ & 1 \cdot 10^{-6}\, mm^2/h \leq D_0 \leq 9 \cdot 10^{-4}\, mm^2/h \\ & 2\, h \leq \tau_{HB} \leq 23\, h \end{aligned} \tag{5.12}$$

where $vol_e = |(vol_s - vol_t)/vol_t|$ is the relative volume estimation error between the volume observed at the true scans in $TP2$ which have been manually delineated by a radiologist (vol_t), and the simulated volume, vol_s, obtained by producing an apparent boundary on the simulated tumour based on $r(x, TP2)$. The cellularity maps are simulated solving the set of PDEs (Eq. 5.6-Eq. 5.8). Their initial states are computed at $TP1$ using the methods described in 4.1.2 and 4.1.3. We use the built-in simulated annealing MATLAB function [113] to optimise Eq. 5.12 and hence estimate c_{g_0}, c_{f_0}, c_{h_0}, D_0 and τ_{HB}.

To enable a more personalised estimation of parameters, we examine whether it is feasible to include a case-specific range for the diffusion parameter, D_0, by exploring its relationship with the specific growth rate (SGR). To this end, 1000 tumours were generated using random parameters within the ranges given in Eq. 5.12, their volumetric growth after 24 hours simulated and the SGR for each of the 1000 cases computed.

5.1.3 Experiments

Sensitivity analysis

To explore which parameters influence our model outcome the most, a sensitivity analysis using the eFAST method as described in [103] was performed. The reference outputs were the total cell number, $r(\mathbf{x})$, and the estimated volume at TP2, vol_s. To determine the significance of the eFAST first-order indices (S_i), the procedure described in [103] was followed and a dummy parameter included in the analysis. Parameters with a sensitivity index with less than that of the dummy parameter should not be considered significantly different from zero, and hence will not have a significant influence on the model outcome.

Synthetic data

In order to evaluate our model in terms of its capacity to estimate the parameters correctly, tests with 20 synthetic tumours were performed. To this end, we used the same 20 parameter sets used for the synthetic tumours of Chapter 3 to allow for the comparison of the results using both models. For the parameter τ_{HB} random values within the range given in Eq. 5.12 were used (see Tab. 5.1). For each tumour, the model was initialised using maps for $TP1$ from one of the available

pre-clinical DCE-MRI extracted as outlined in section 4.1.3 and simulations were performed for four days, *i.e.* up to $TP5$.

	Parameters			
Cases	c_{g_0}(unitless)	c_{f_0} (unitless)	$D_0(mm^2/h)$	$\tau_{HB}(h)$
1	0.280	0.1889	$4.88e-4$	13
2	0.1567	0.0737	$2.80e-5$	21
3	0.476	0.157	$8.04e-5$	7
4	0.227	0.127	$4.12e-5$	8
5	0.181	0.232	$1.58e-5$	4
6	0.341	0.099	$2.0\ e-4$	22
7	0.302	0.089	$8.16e-5$	16
8	0.335	0.107	$1.88e-5$	12
9	0.463	0.102	$3.5\ e-4$	16
10	0.174	0.149	$3.3\ e-4$	13
11	0.177	0.051	$7.46e-5$	16
12	0.219	0.211	$2.91e-4$	13
13	0.374	0.189	$4.23e-4$	17
14	0.262	0.280	$4.45e-5$	13
15	0.186	0.183	$3.29e-4$	23
16	0.346	0.089	$1.59e-5$	6
17	0.300	0.096	$1.68e-5$	4
18	0.399	0.299	$1.85e-4$	4
19	0.380	0.248	$2.75e-4$	3
20	0.482	0.152	$4.55e-4$	10

Table 5.1: Parameters used to generate 20 synthetic tumours using the model of vascular tumour growth.

Pre-clinical data

To explore how our updated model compared to the model introduced in Chapter 3, we performed analysis on the pre-clinical data set described in Section 4.2.2. We recall that this dataset is composed of seven mice in which breast carcinoma tumour cells were injected. These mice were imaged under anaesthesia at five consecutive days ($TP1$-$TP5$) over the tumour growth cycle (starting 10 days after injection).

	Parameters				
Sensitivity Index	c_{g_0}	c_{f_0}	$D_0(mm^2/h)$	$\tau_{HB}(h)$	dummy
e-Fast S_i $(r(\mathbf{x}))$	0.0148	0.0481	**0.5330***	**0.3586***	0.0069
e-Fast S_i (vol_s)	0.0086	0.0168	**0.4986***	**0.4413***	0.0044

Table 5.2: Sensitivity indices for the analysis on the model of vascular tumour growth. The top two parameters are highlighted. Values with (*) are significant; i.e., p¡0.05.

5.2 Results

5.2.1 Sensitivity analysis and parameter optimisation

The sensitivity analysis on the total cell number and tumour volume yielded first-order sensitivity indices, S_i, as listed in Tab. 5.2. Other than in Chapter 3, where our volumetric and cellular tumour growth were mostly influenced by D_0, here, the newly introduced parameter τ_{HB}, which accounts for the delay between hypoxia and angiogenesis and the transition between the avascular and the vascular phases, is found to play an almost equally important role in the tumour evolution as demonstrated by its sensitivity indices.

To deduce a personalised range for D_0, we used the relationship between D_0 and the specific growth rate (SGR), as described in Section 5.1.2. Performing a Pearson correlation analysis between SGR and c_{g_0}, c_{f_0}, D_0 and τ_{HB} yielded correlation coefficients of -0.0114, 0.0149, 0.6260 and 0.6313, respectively. Similarly to the sensitivity analysis, the parameters D_0 and τ_{HB} demonstrated a higher influence on the tumour volumetric growth (represented by SGR) than all other parameters. Since the aim is to minimise the range of D_0, we plotted the values of D_0 over SGR and fitted the data with an exponential function. The data points along with the fitting curves are shown in Fig. 5.2. In a similar way to Chapter [**?**], straight lines can be observed at e.g. $SGR = 0.027 hour^{-1}$. This effect is probably related to the observation presented in other studies that dif-

ferent combinations of the proliferation (c_{g_0}) and diffusion (D_0) rates can lead to tumours of equal size [10, 17]. This figure shows how D_0 increases non-linearly with increasing SGR. We hence fitted the data to an exponential curve, and sing a 99.99% confidence interval for the fitting yielded a customised range, $[d_{min}(SGR), d_{max}(SGR)]$, of:

$$\begin{aligned} d_{min}(SGR) &= 9.73e-6 \cdot exp(59.9731 \cdot SGR)\, mm^2/h \\ d_{max}(SGR) &= 2.72e-5 \cdot exp(81.4229 \cdot SGR)\, mm^2/h \end{aligned} \tag{5.13}$$

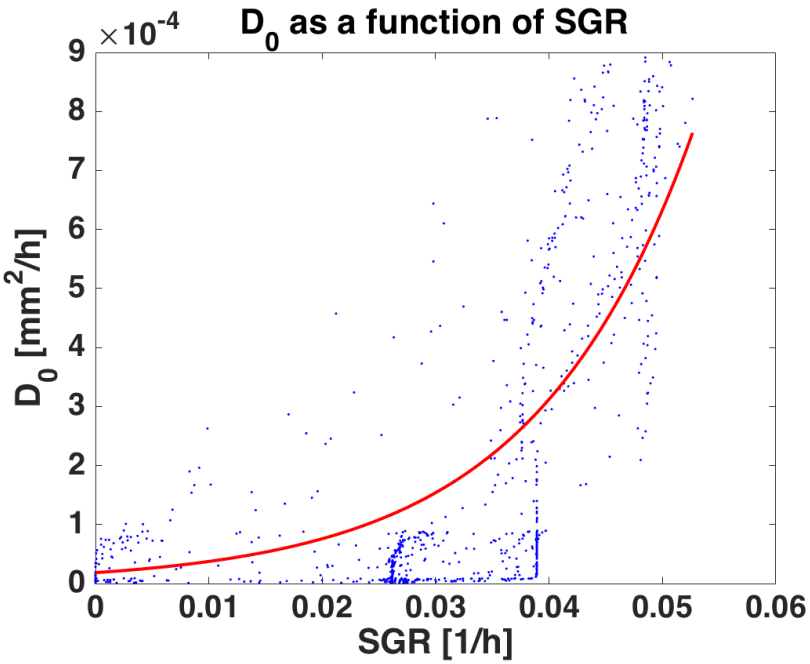


Figure 5.2: Plot of the result of 1000 simulations to determine the relationship between the diffusion constant D_0 and SGR using the updated model of tumour growth. We use exponential fitting curves and with a 99.99% confidence interval we obtain the minimum and maximum values for the exponential rate and the initial value of the functions, as shown in Eq. 5.2.1.

Based on these results and on the information gained from Chapter 4 that there was no added benefit in estimating c_{f_0}, for the analysis that follows both c_{f_0} and c_{g_0} were kept constant. We are thus left with only two model parameters to be optimised, D_0 and τ_{HB}.

The majority of tumour models are interested in estimating the proliferation rate as a measure of different growth patterns between tumours. Since our analysis indicated that this parameter should be kept constant, to still allow for the comparison between different proliferation rates, we perform simulations and calibration of the remaining model parameters using $c_{g_0} = 0.15$ and $c_{g_0} = 0.30$. The hypoxia rate related parameter is kept at $c_f = 0.15$. Following the rationale discussed in Section 3.1.4, to ensure that necrosis always occurs at a lower level of v_D than hypoxia, we set $c_{h_0} = k \cdot c_{f_0}$ with $k = 2$, and hence $c_{h_0} = 0.30$. The chosen values allow for a clear transition between necrosis, hypoxia and proliferation as seen in Fig. 5.3, which depicts the proliferation ($g(v_D)$), hypoxia ($f(v_D)$) and necrosis ($h(v_D)$) as a function of v_D for $c_{g_0} = 0.15$ (Fig. 5.3-a) and $c_{g_0} = 0.30$ (Fig. 5.3-b). The constants G_{max}, F_{max} and H_{max} are set to 1 ($hour^{-1}$) which gives a range of proliferation, hypoxic and necrotic rates. These ranges compare with the values found in the literature and measured in $year^{-1}$ [17, 16, 15]. However, the values in the literature are normally global and do not change with the localisation within the tumour and the nutrient available at this localisation. We are thus left with two optimisation routines: I) $c_{g_0} = 0.15$, $c_{f_0} = 0.15$, and D_0 and τ_{HB} as model parameters; and II) $c_{g_0} = 0.30$, $c_{f_0} = 0.15$, and D_0 and τ_{HB} as model parameters.

For both synthetic and real data, once the parameters D_0 and $\tau_H B$ were estimated between time points $TP1$ and $TP2$, the obtained values were used as input for the tumour growth simulation between $TP1$ and $TP5$. After simulation, the estimated cellularity maps and the tumour volume were compared to the true images of the respective time points. Akin to the previous chapter, the simulated tumour volumes were also compared with the true volumes observed in the actual scans in terms of the Dice similarity coefficient DSC.

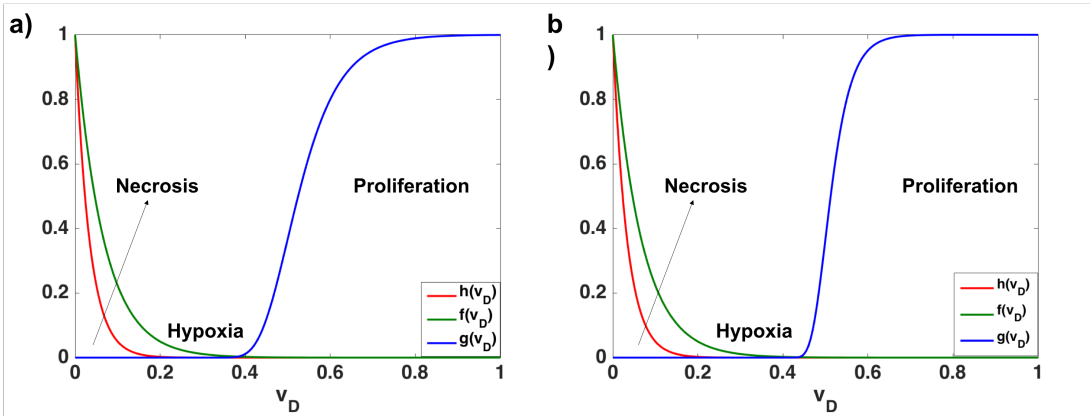


Figure 5.3: Proliferation, hypoxia and necrosis rates [1/h] as a function of the distribution volume (v_D) within a voxel. The maximum value for v_D is 1 (100%), which would give the maximum proliferation, as well as minimum hypoxia or necrotic rates achieved for cells in a nutrient rich environment. There are clear transition points between necrosis and hypoxia, and hypoxia and proliferation. Values for the graphs in a) for c_{g_0}, c_{f_0} and c_{h_0} are 0.15, 0.15 and 0.30, respectively. In b), values are the same, except for $c_{g_0} = 0.30$.

The calibration process for the updated model took on average 24.22±6.77 hours for the synthetic; and 36.52± 20.81 hours for the real data. It took around 1500 iterations over the 3D growth simulation between $TP1$ and $TP2$ until convergence was achieved. Depending on the size of the tumour being modelled, it took up to 3 minutes to simulate the tumour growth between $TP2$ and $TP5$.

5.2.2 Synthetic data

Using synthetic data enables the assessment of the present methodology in recovering known parameters. To this end, simulations using the parameters given in Tab. 5.1 were performed, and the outcome saved in terms of cellularity maps. We optimised D_0 and τ_{HB} by minimising the volumetric error, vol_e. Using $TP1$ and $TP2$ for calibration yielded mean relative errors between true and estimated parameter values of 1.376±2.003 and 1.348±2.324 for D_0, when c_{g_0} was kept constant at 0.15 and 0.30, respectively. The mean relative errors between true and estimated values for τ_{HB} were of 0.454±0.889 and 0.407±0.423 for $c_{g_0} = 0.15$ and

$c_{g_0} = 0.30$, respectively.

Using the optimised parameter values for simulations, we can compute the cellularity maps and tumour volumes at later time points. Figure. 5.4 depicts the mean relative volume errors and DICE values for optimisation routine I ($c_{g_0} = 0.15$, blue) and optimisation routine II ($c_{g_0} = 0.30$, green) for $TP3$ to $TP5$. Overall, a similar performance can be observed for both optimisation routines, with the volume errors increasing and the DICE values decreasing over simulation time.

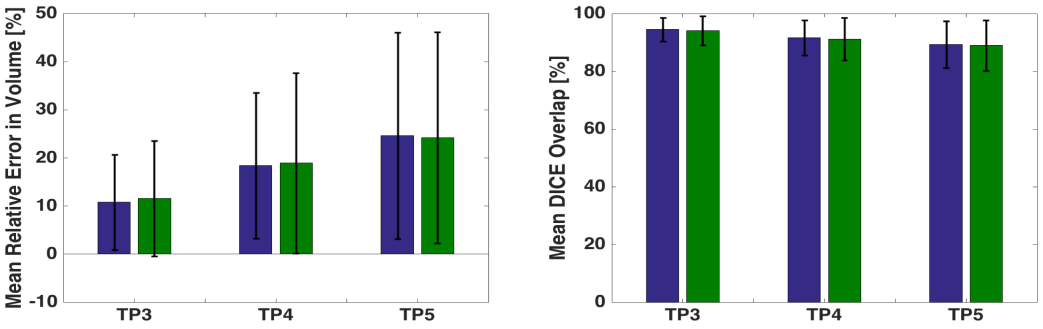


Figure 5.4: Mean percent volume and DICE errors between the true and estimated volume values for all synthetic cases for optimisation routine I (blue) and optimisation routine II (green).

To further compare these two optimisation routines, in Fig. 5.5 we display the mean cellularity (total, proliferative, hypoxic and necrotic) evolution for the time between $TP1$ and $TP5$. Blue bounded lines represent the estimated mean values and standard deviations for the simulated pre-clinical cases. Red lines depict the true mean and standard deviation values for cellularity evolution for the true generated synthetic data. Using the two different optimisation routines yielded virtually the same results in terms of cellularity evolution prediction. Small differences can be observed in the number of hypoxic cells and proliferating cells, with optimisation rule I performing slightly better as seen by the overlap of the mean target and mean estimated number of hypoxic cells and the smaller difference between the maximum target and maximum estimated proliferating

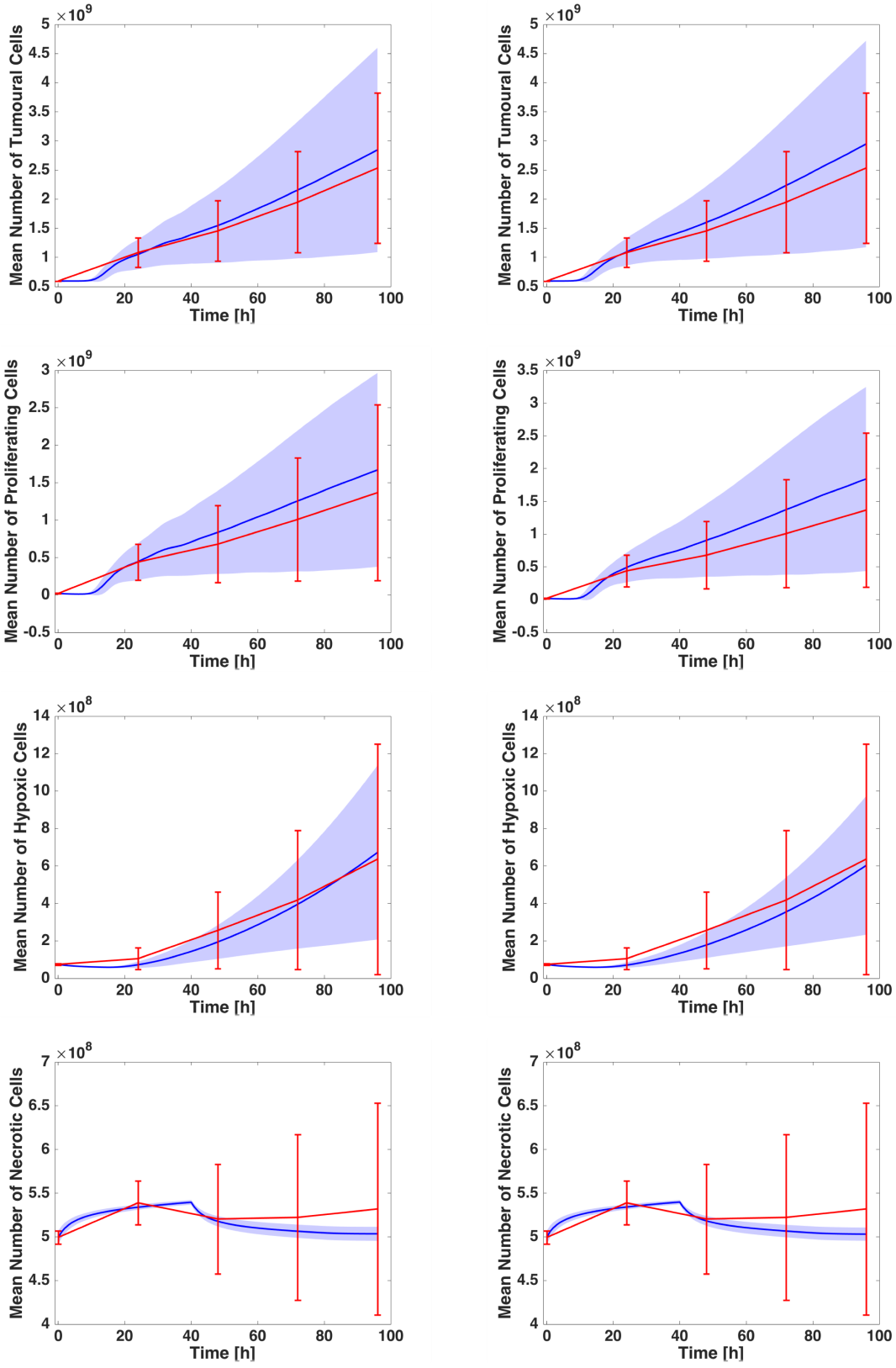


Figure 5.5: Mean cellularity (total, proliferative, hypoxic and necrotic) evolution for optimisation routines I (left) and II for the time between $TP1$ and $TP5$. Blue bounded lines represent the estimated mean values and standard deviations for the simulated pre-clinical cases. Red lines depict the true mean and standard deviation values for cellularity evolution for the true synthetic data. The changes observed at $t = 40h$ in the necrotic cell evolution are directly related to the first completion of the lysis cycle.

Parameter	Case 1	Case 2	Case 3	Case 4	Case 5	Case 6	Case 10
$D_0[mm^2/h]$	1.275e-05	1.448e-4	1.178e-4	3.985e-05	1.121e-4	1.088e-4	4.748e-05
$\tau_{HB}[h]$	8.70	8.081	12.130	14.700	4.584	6.300	7.776

Table 5.3: Optimised model parameter values used to simulate tumour growth between $TP2$ and $TP5$. For all pre-clinical cases,c_{g_0} and c_{f_0} were kept fixed at 0.15. Values for τ_{HB} have been rounded to the nearest integer for use in the simulations.

Parameter	Case 1	Case 2	Case 3	Case 4	Case 5	Case 6	Case 10
$D_0[mm^2/h]$	5.966e-05	1.360e-4	7.032e-05	1.742e-4	1.094e-4	6.318e-05	4.748e-05
$\tau_{HB}[h]$	7.298	10.290	13.932	4.821	5.486	13.172	7.776

Table 5.4: Optimised model parameter values used to simulate tumour growth between $TP2$ and $TP5$. For all pre-clinical cases, c_{g_0} and c_{f_0} were kept fixed at 0.30 and 0.15, respectively. Values for τ_{HB} have been rounded to the nearest integer for use in the simulations.

cells. The changes observed at $t = 40h$ in the necrotic cell evolution are directly related to the first completion of the lysis cycle.

5.2.3 Pre-clinical data

Given the results achieved on the synthetic data, we applied the same methodology to the pre-clinical data outlined in Section 4.2.2. The two optimisation routines yielded the optimised parameters listed in Tab. 5.3 and Tab. 5.4. Using these parameters, for each time step, the total cell number for each sub-population as well as the tumour volume were computed and used as input for the consecutive time step. The initial total cell number for each sub-population and total cell number were computed as the sum of the cells over the voxels within the tumour boundaries at $TP1$.

The mean evolution of the total, proliferating, hypoxic and necrotic cells for the time between $TP1$ and $TP5$ obtained using optimisation routines I and II are shown in Fig. 5.6. Blue bounded lines represent the estimated mean values and standard deviations for the pre-clinical cases. The true mean and standard

deviation values for cellularity evolution for the true observed data are represented by the red lines.

Similarly to the synthetic case, using the two different optimisation routines yielded small differences in terms of prediction of the cellularity evolution. These differences can be mainly observed in the estimation of hypoxic cells, with optimisation routine I performing slightly better as seen by the larger overlap of the lower bound of the mean estimated with the upper bound of the mean target number of hypoxic cells. Overall the estimated cellularity evolution followed the trend of the true cellularity evolution, however an overestimation in the total cell number can be observed for the results obtained using both optimisation routines. This overestimation arises mainly through an overestimation in the proliferative cell number followed by an overestimation in the hypoxic cell number. For the necrotic cells, an underestimation could be observed for early time points, followed by an overestimation for later time points. The changes observed at $t = 40h$ are directly related to the first completion of the lysis cycle. However, this overestimation was smaller than the ones observed for the proliferative and hypoxic cases, and hence had little influence on the total cell number overestimation.

While there was no striking difference in terms of volumetric error and DICE overlap between the two optimisation routines for the synthetic data, for the real data using $c_{g_0} = 0.30$ (optimisation rule II) resulted in smaller volume errors and larger DICE values, as shown in Fig. 5.7. As expected, the smallest volume error and largest DICE overlap was obtained for $TP3$, since $TP1$ and $TP2$ were used for calibration.

In addition to the estimation of the global cellularity evolution and the volumetric tumour growth, our model allows for the assessment of the local distribution of cells within the tumour borders.

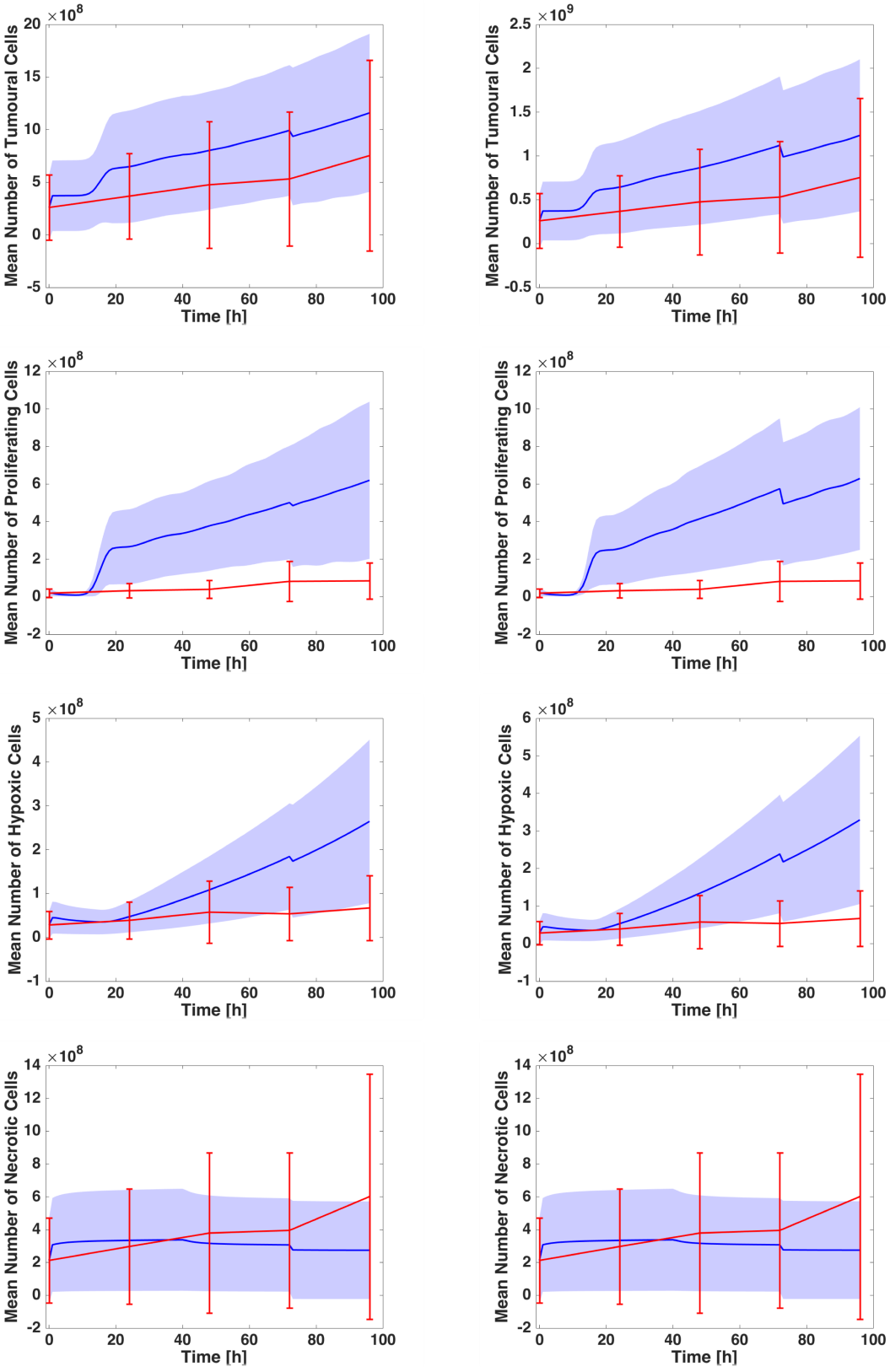


Figure 5.6: Mean cellularity (total, proliferative, hypoxic and necrotic) evolution for optimisation routines I (left) and II for the time between $TP1$ and $TP5$. Blue bounded lines represent the estimated mean values and standard deviations for the simulated pre-clinical cases. Red lines depict the true mean and standard deviation values for cellularity evolution for the true pre-clinical data. The changes observed at $t = 40h$ in the necrotic cell evolution are directly related to the first completion of the lysis cycle.

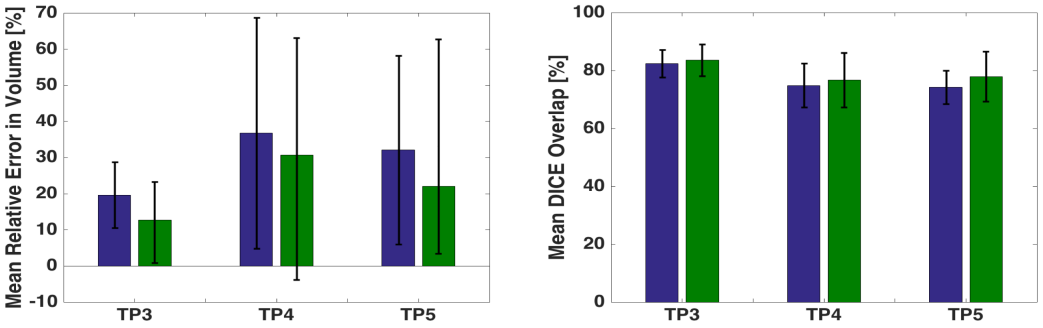


Figure 5.7: Mean percent volume and DICE errors between the true and estimated volume values for all pre-clinical cases for optimisation rule I (blue) and optimisation rule II (green).

To allow for a comparison across cases and optimisation routines, the cellularity distribution for three pre-clinical cases (1, 4 and 6) are illustrated in Fig. 5.8, Fig. 5.12, and Fig. 5.13. These figures include a comparison between optimisation routine I (top) and optimisation routine II. The true (left columns) and the estimated (middle columns) relative cell distributions are shown for $TP2$, $TP3$, $TP4$ and $TP5$. In the far right columns, the residual maps obtained by subtracting the true maps from the estimated maps are shown for a central slice of the tumour volume. The black outlines displayed within the estimated and the residual images represent the true tumour delineation at the respective TP. For the true and estimated maps, the colour bar represents the number of cells relative to the voxel cell capacity and hence, ranges from 0 to 1. For the residual maps, the colour bar ranges from -1 to 1 with negative and positive values representing a local underestimation and overestimation in the cell number, respectively.

For Case 1 (Fig. 5.8), using $c_{g_0} = 0.30$ resulted in slightly larger tumours, and consequently, smaller volumetric errors than using $c_{g_0} = 0.15$. Overall, an overestimation in the necrotic areas could be observed. To allow for a more detailed assessment of the local cellularity, we have included a comparison between the proliferation, hypoxic and necrotic cellularity maps in Fig. 5.9-Fig. 5.11. This breakdown into different sub-populations demonstrates that the model correctly

accounts for the cells in these areas of overestimation to be necrotic.

In Fig. 5.9, an overestimation in the proliferative cell number can be observed. However, using the updated model resulted in a spread of proliferative cells in areas one would expect to be proliferative, so that areas closer to the border demonstrate higher levels of proliferation than central areas within the tumour. A very good agreement between estimated and true hypoxic maps, especially for $TP2$ and $TP3$, can be seen in Fig. 5.10. There was a slight underestimation in the hypoxic cell number, especially at $TP5$. The estimated necrotic maps plotted in Fig. 5.11 showed less change over time than the hypoxic and proliferative cell maps. In terms of numbers, however, these maps were overall closer to the true cell number, as also depicted in Fig. 5.6. The necrotic cells in the maps obtained with $c_{g_0} = 0.30$ (optimisation rule I) are more spread out as compared with the ones obtained using $c_{g_0} = 0.15$, showing that even at the more peripheral parts of the tumour a small number of necrotic cells could be observed. However, for both optimisation routines, tumours had as much as 90% of the centre voxels made of necrotic cells, which would be expected in a necrotic core.

Comparing Case 4 (Fig. 5.12) with Case 1, it becomes evident that the model performs better for some cases than others, depending on the shape of the tumour. The model was not able to predict finger-shaped tumours like the ones seen in Case 4. Both areas of overestimation (yellow areas) and underestimation (blue areas) can be observed on the peripheries of the tumour, so that even if the volumetric error was small, the DICE value showed that the volumes do not overlap accordingly.

Case 6 is an example of a tumour with a slower growth pattern than the other tumours shown in this section. For this case, using $c_{g_0} = 0.30$ resulted in slightly larger areas of overestimation (yellow areas in the residual maps) but also in

some areas of underestimation (blue areas). Overall, the estimation captured well the sizes and shapes of the true tumour, and very small errors can be seen for this case, demonstrating the model's ability to estimate fast- and slow-growing tumours alike.

In Fig. 5.14 we used Case 10 to compare the performance of the avascular (Chapter 4) and the vascular models using optimisation routine I. A real increase in prediction accuracy in terms of both shape and size can be seen for the simulations using the model which includes angiogenesis (bottom). Moreover, there were smaller areas of overestimation (yellow areas) in the images where the difference between estimated and true cell distribution is shown.

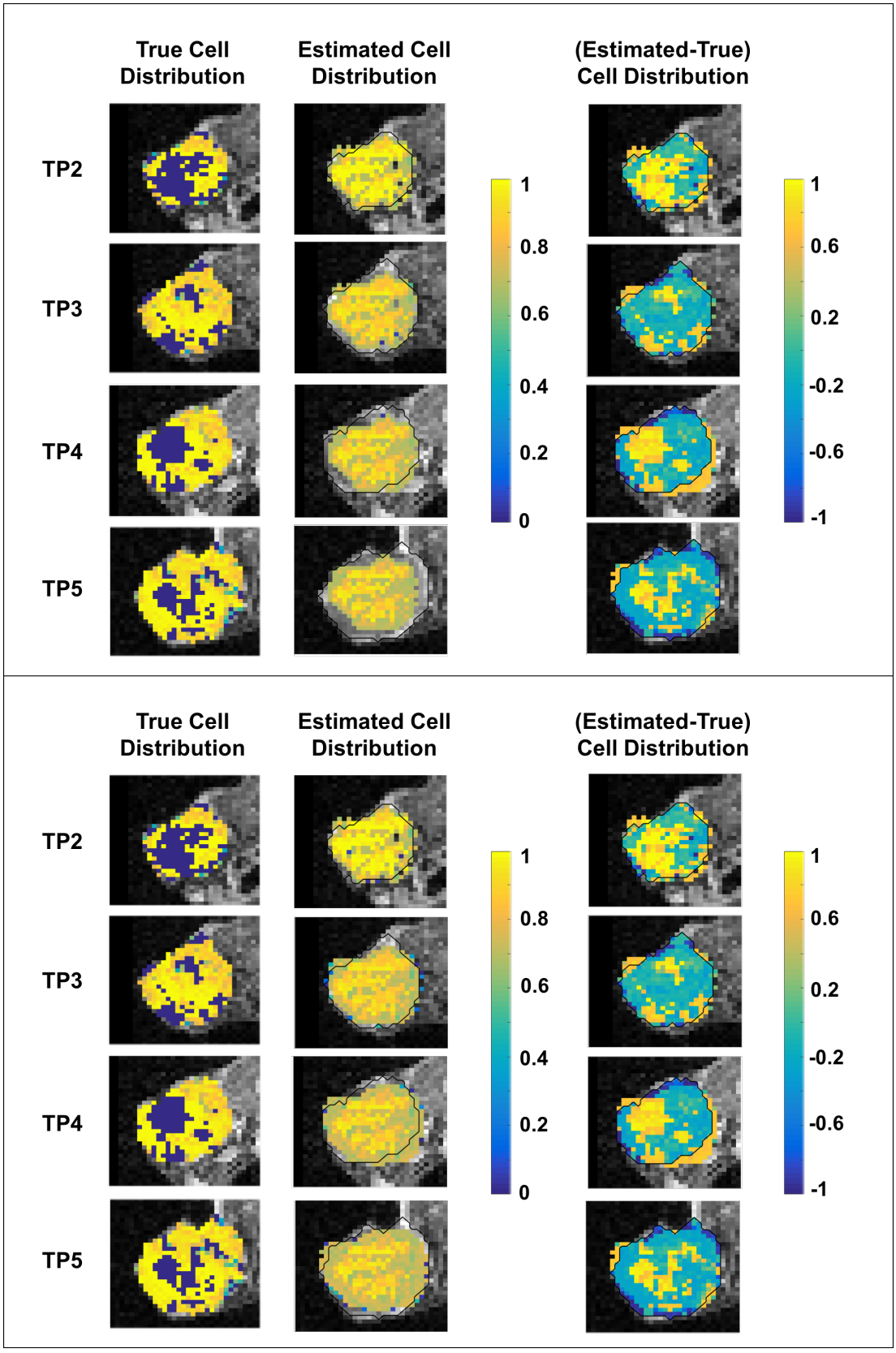


Figure 5.8: True and estimated cell distributions for Case 1 obtained using optimisation routine I (top) and optimisation routine II. The true (left column) and the estimated (middle column) relative cell distributions for an example pre-clinical case are shown for $TP2$, $TP3$, $TP4$ and $TP5$. In the right column, for a central slice of the tumour volume, we show the residual maps obtained by subtracting the true maps from the estimated maps. The black outlines displayed within the residual images represent the true tumour delineation.

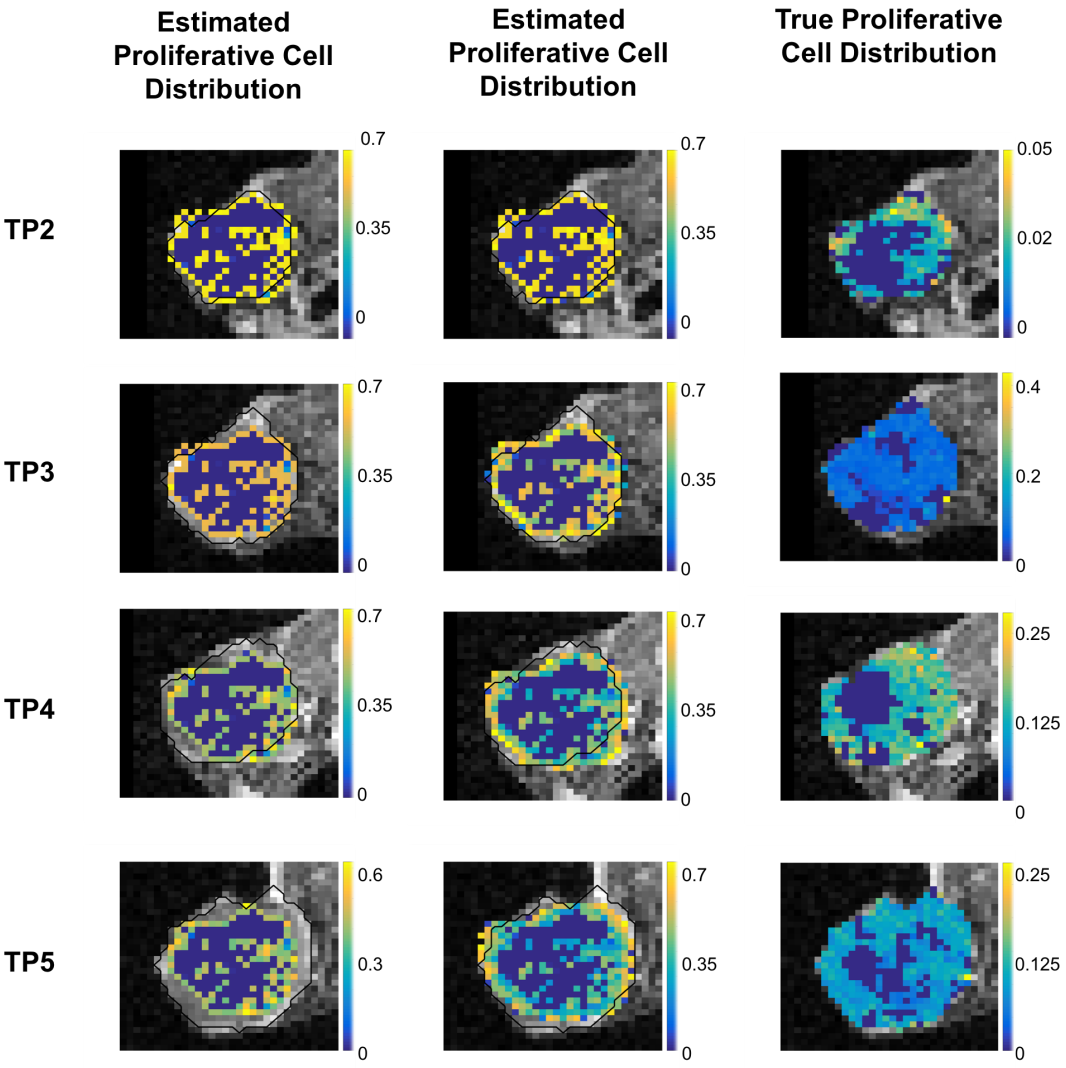


Figure 5.9: True and estimated proliferative cell distributions for Case 1. The estimated (left and middle columns) relative proliferative cell distributions for an example pre-clinical case are shown for $TP2$, $TP3$, $TP4$ and $TP5$ for optimisation routines I and II, respectively. The true relative maps for proliferative cells are shown in the right column.

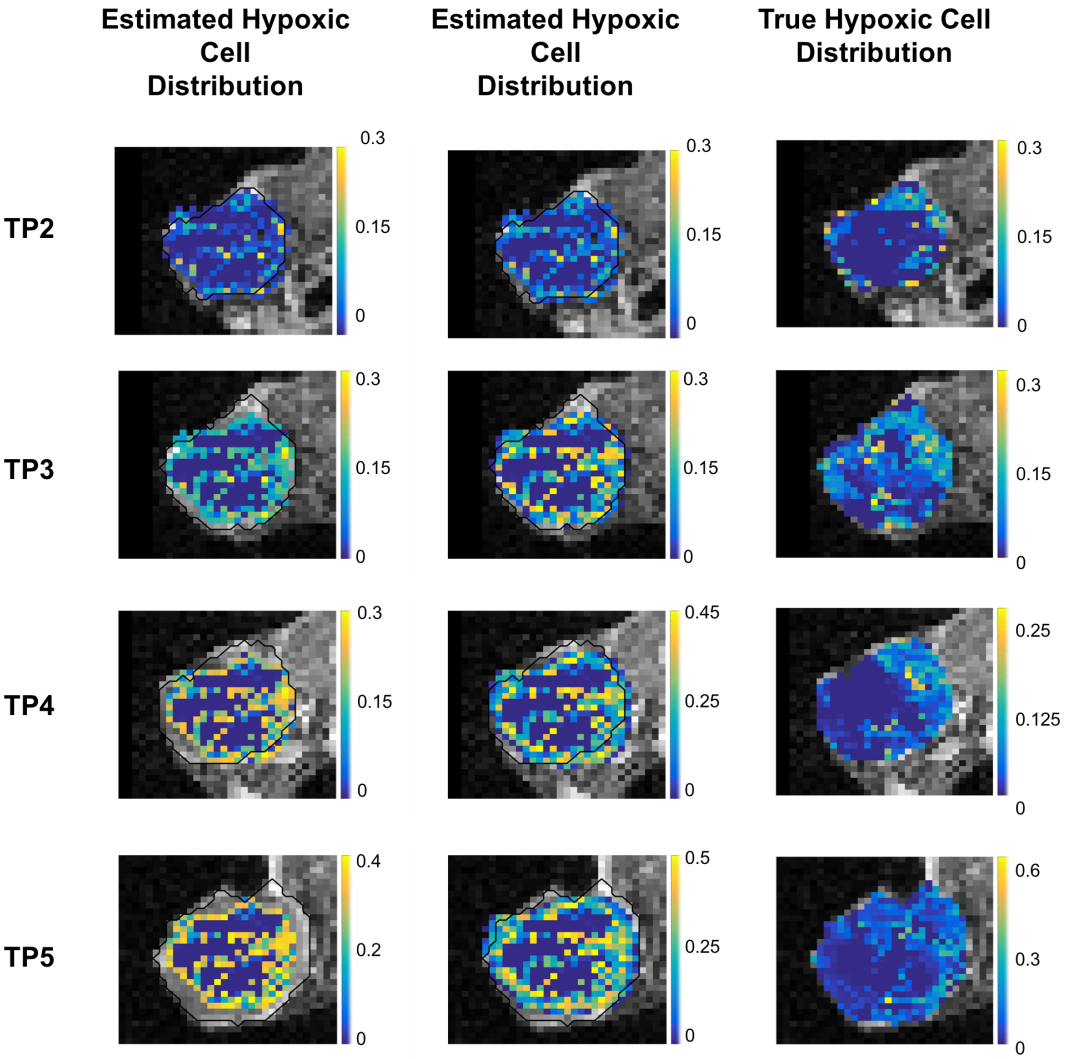


Figure 5.10: True and estimated hypoxic cell distributions for Case 1. The estimated (left and middle columns) relative hypoxic cell distributions for an example pre-clinical case are shown for $TP2$, $TP3$, $TP4$ and $TP5$ for optimisation routines I and II, respectively. The true relative maps for hypoxic cells are shown in the right column.

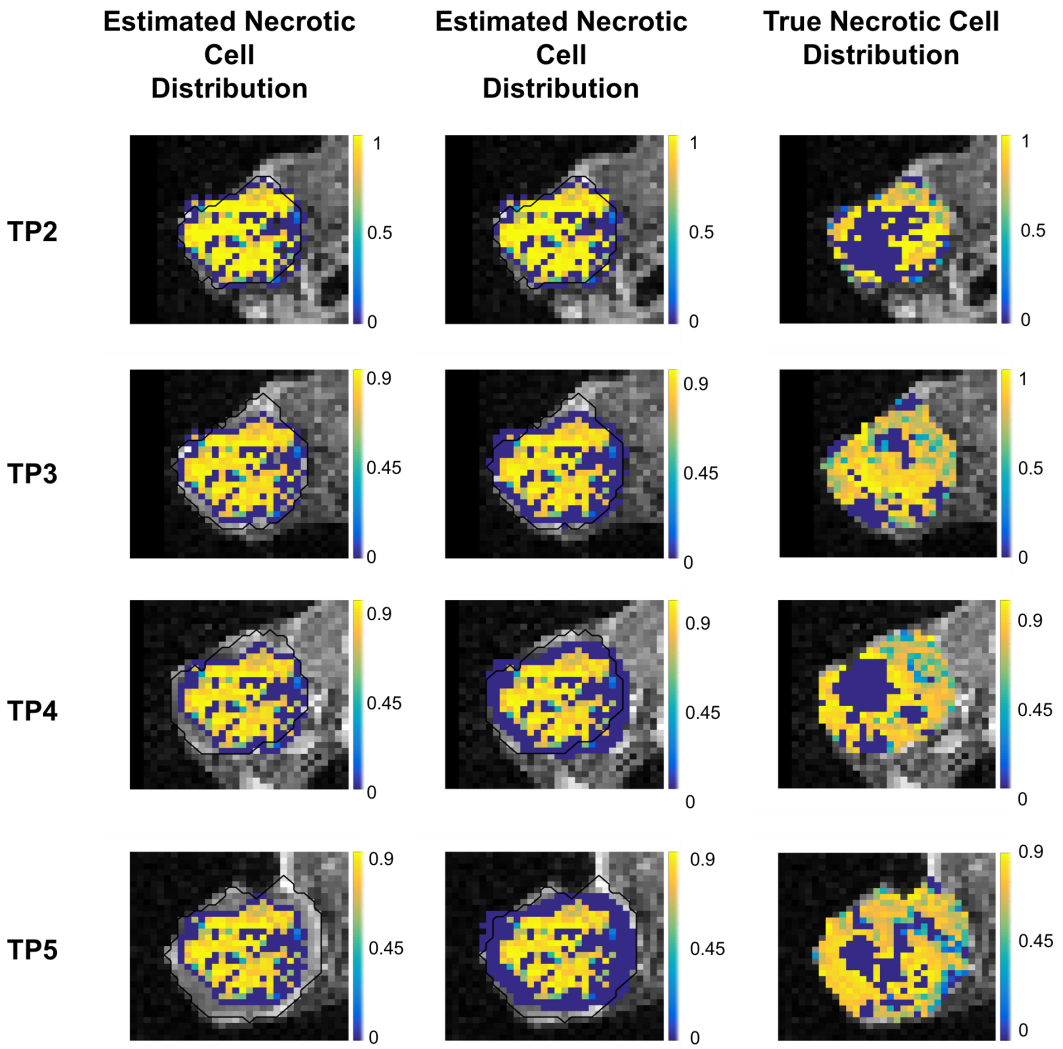


Figure 5.11: True and estimated necrotic cell distributions for Case 1. The estimated (left and middle columns) relative necrotic cell distributions for an example pre-clinical case are shown for $TP2$, $TP3$, $TP4$ and $TP5$ for optimisation routines I and II, respectively. The true relative maps for necrotic cells are shown in the right column.

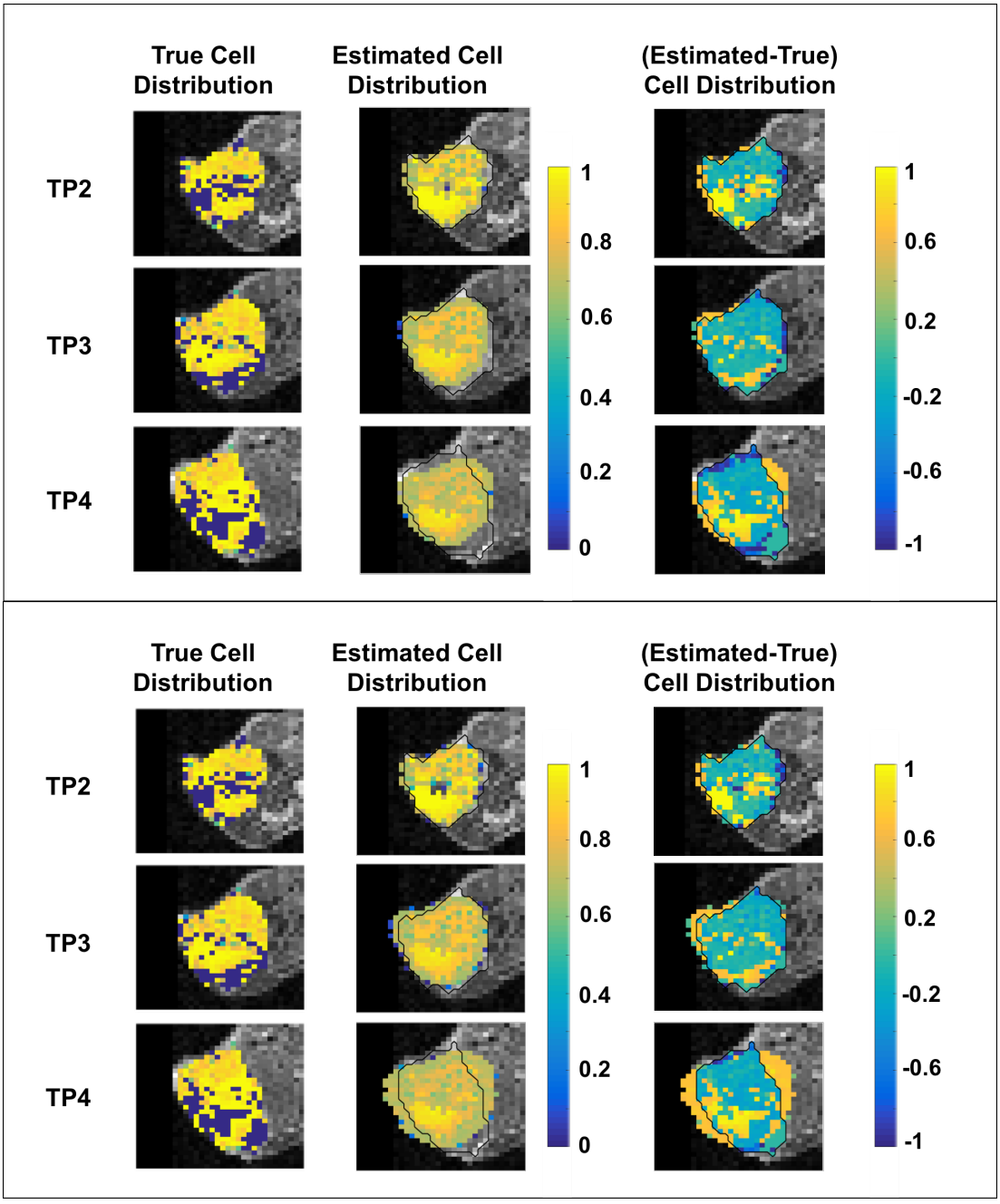


Figure 5.12: True and estimated cell distributions for Case 4 obtained using optimisation routine I (top) and optimisation routine II (bottom). The true (left column) and the estimated (middle column) relative cell distributions for an example pre-clinical case are shown for $TP2$, $TP3$, $TP4$ and $TP5$. In the right column, for a central slice of the tumour volume, we show the residual maps obtained by subtracting the true maps from the estimated maps. The black outlines displayed within the residual images represent the true tumour delineation.

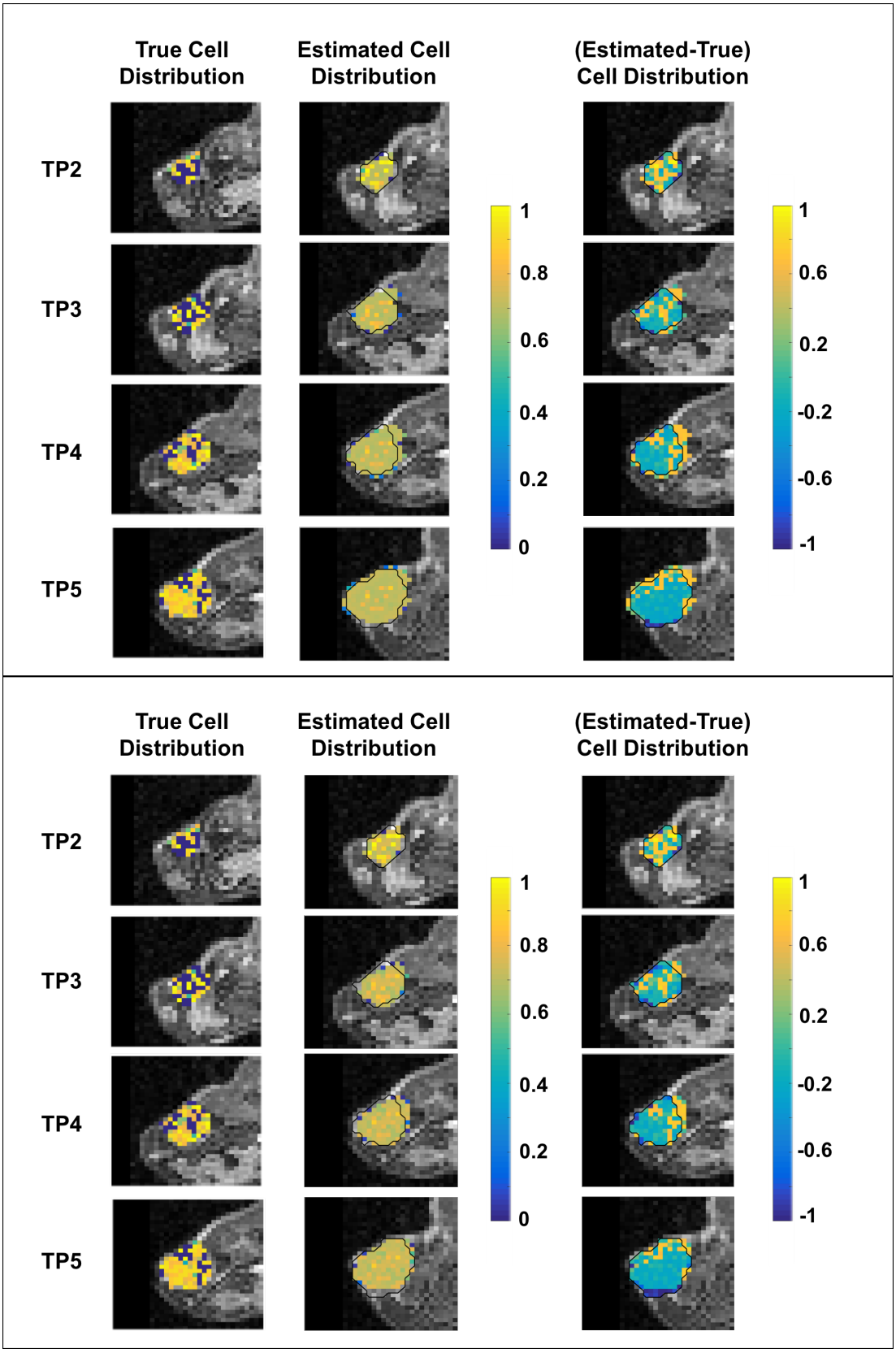


Figure 5.13: True and estimated cell distributions for Case 6 obtained using optimisation routine I (top) and optimisation routine II. The true (left column) and the estimated (middle column) relative cell distributions for an example pre-clinical case are shown for $TP2$, $TP3$, $TP4$ and $TP5$. In the right column, for a central slice of the tumour volume, we show the residual maps obtained by subtracting the true maps from the estimated maps. The black outlines displayed within the residual images represent the true tumour delineation

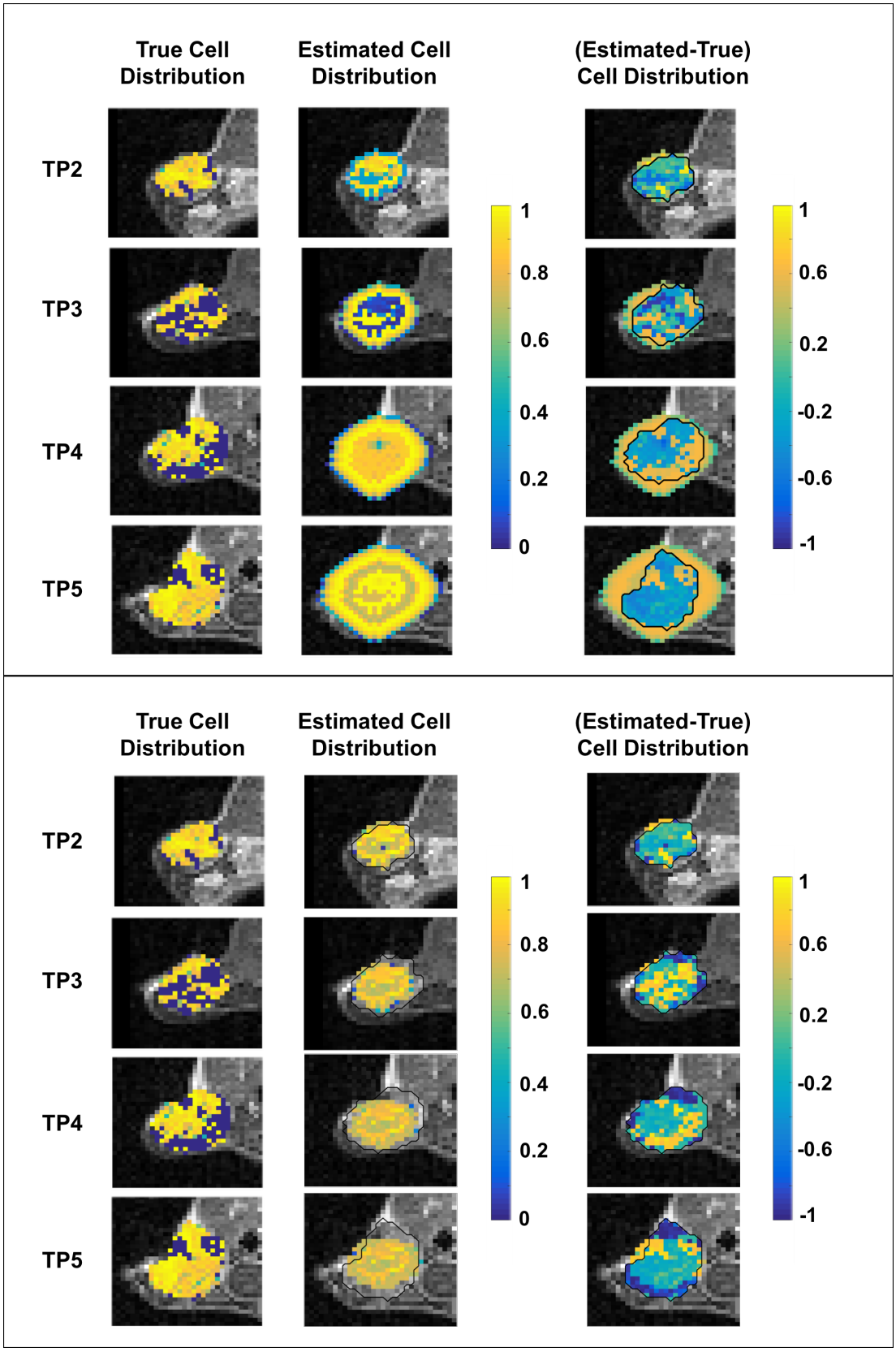


Figure 5.14: True and estimated cell distributions for Case 10 obtained using the avascular (top) and the vascular models. The true (left column) and the estimated (middle column) relative cell distributions for an example pre-clinical case are shown for $TP2$, $TP3$, $TP4$ and $TP5$. In the right column, for a central slice of the tumour volume, we show the residual maps obtained by subtracting the true maps from the estimated maps. The black outlines displayed within the images represent the true tumour delineation.

5.3 Discussion and Conclusions

In the present chapter, we have introduced, calibrated and tested a novel model of vascular tumour growth. This model allows for proliferation, death and spread of tumour cells, as well as for angiogenesis measured implicitly as an increase in v_D, a parameter which can be observed on DCE-MRI longitudinal scans. Tumour specific parameters are estimated from two early time points and used to predict the spatio-temporal evolution of the tumour volume and cell densities at later time points. We first tested our parameter estimation approach on synthetic data from 20 generated tumours. Encouraged by the results, we applied our model to seven pre-clinical cases of breast carcinoma. The obtained results are promising, especially when compared with the results achieved Chapter 4 and the ones found in the literature. Our results demonstrated the feasibility of using maps of cellularity obtained from DCE-MRI analysis to feed and calibrate a model of vascular tumour growth to obtain subject-specific predictions of tumour evolution.

Our *in silico* study resulted in small volume errors ($< 20\%$) and high Dice overlaps ($>88\%$). However, these values are not as good as the ones obtained in Chapter 4 using the avascular model. One reason for this is that instead of one parameter (D_0), here we have two parameters (D_0 and τ_{HB}) strongly influencing the volumetric growth. This results in uncertainties in the recovery of both parameters and hence may lead to a less accurate prediction of tumour growth.

While the results for the synthetic data were slightly poorer than the ones found for the avascular tumour model (Chapter 4), the results from real data for the vascular model outperformed the ones obtained with the avascular model. As such, the pre-clinical data analysis demonstrated smaller volume errors and larger Dice values when compared to the results in Chapter 4.

Using optimisation routine I yielded better results in terms of volumetric prediction and DICE values. These results outperform the ones found in the literature. For instance, [15] reported a volume prediction error for their experiments of as large as 50.1% using days 2 and 4 (which would correspond to our $TP3$ and $TP5$) for calibration. Our volume prediction errors are as large as 36.78% and 30.66% for optimisation routines I and II, respectively. Their results are only comparable to ours when using days 0 and 4 for calibration, which yielded errors smaller than 34.4%. However, in a clinical scenario one would hardly have data of nine consecutive scans allowing for the use of such a large time between measurements for calibration and then for verification.

Normally, one would expect the volume errors to increase over time, since the estimation in based on $TP1$ and $TP2$. However, using the updated model resulted in smaller errors for the prediction of $TP5$ than for the prediction of $TP4$. That behaviour can be linked to the fact that the model does not have a linear growth (nor has a tumour), so that is possible for the model to e.g overestimate the volume at $TP4$ to then correctly predict the volume at $TP5$. Since the results show an average behaviour over the different cases included, this will only happen for some cases. Since in the clinic we are mostly interested in the tumour state at the next time point, this behaviour does not represent a major limitation of the current approach.

Another improvement can be seen in our results in terms of the DICE values obtained between the true and estimated tumours. In [15], their real data analysis yielded values larger than 62%. Our analysis, as a comparison, resulted in values larger than 75% and 78% for optimisation I and II, respectively. This is especially important in terms of prediction of the direction of the growth. Even if the volume errors are small, if the DICE overlap is small too, this is an indication that the

predicted tumour shape does not coincide with the true shape observed in the scans. In order to be able to plan therapy adequately one would need not only to know how much a tumour is growing but also what areas of the host tissue it is invading.

As mentioned earlier, a major strength of our model when compared to the existing literature (e.g. [16], [12], [17], [15]) is its capacity to assess local cell density growth as well as local tumour activity (represented by proliferation, hypoxia and necrosis) in addition to global values (such as the DICE, the volume error and the total cell number). As such, our updated model, does not only resulted in better predictions in terms of volumetric error and DICE values, but also in estimated maps which resemble the true maps more than the ones obtained with the avascular model. For instance, using the updated vascular model resulted in a more realistic spread of proliferative cells in areas of proliferation and not as homogeneous as the previous model. The areas of necrosis were identified as being closer to the tumour centre than the periphery. Finally, hypoxic areas were observed as being spread out more heterogeneously than in the maps obtained with the avascular model. This improvement in the performance of the vascular model over the avascular model used in Chapter 4, can be seen in Fig. 5.14. Using Case 10 as an example, a real increase in prediction accuracy in terms of both shape and size can be seen using the model which includes angiogenesis (bottom). Hence, we can conclude that adding angiogenesis to the model in fact resulted in more realistic results in terms of both volume and cellularity prediction.

Even though adding angiogenesis to the model allowed for the prediction of tumour shapes which are closer to the ones observed in the true images, our model does not have the same performance for all tumour shapes. One of the limitations of the current model is that it cannot account for finger-shaped tumours like the

ones seen in Case 4. One potential way of overcoming this limitation could be by adding information from the surrounding, like stress or pressure, and follow the path of least resistance for the tumour expansion. One could for instance extract this information from MRI-elastography and follow the relationship provided in [129] between cell density and Young's modulus of the tissue to decide the path of growth (following the path of least resistance). Alternatively, one could also include a constitutive equation such the one used by [12] to model the biomechanics of tumour growth. However, due to the need of imaging modalities such as DT-MR imaging, such an approach maybe more applicable to brain tumours [12, 11, 130].

A further limitation of the model has to do with the fact that unlike the previous model, which could have been parametrised using any modality or modalities able to extract information on cellularity and cell metabolism, the model presented in this chapter is built *a priori* from DCE-MRI data. The fact that we have modelled angiogenesis as a direct increase in v_D allowed us to model the biological process in a simplified way but also restricted the methodology to the case of DCE-MRI. However, one could amend this model by introducing an equation to model the evolution of the vascular space in terms of endothelial cell densities as a function of hypoxia, represented by our introduced parameter, τ_{HB}. This equation could then be linked to a nutrient evolution equation (e.g. pO_2) which ultimately would influence proliferation, hypoxia and necrosis in a similar way as in our avascular model. A similar approach has been adopted by Swanson *et al.* in [16].

In this chapter we have introduced a novel model of vascular tumour growth that accounts for angiogenesis in an indirect yet efficient way: instead of following the migration of each EC, we focus on the angiogenesis-related macroscopic changes that can be observed longitudinally on medical imaging scans. The re-

sults obtained with this model are promising and open up a myriad of clinical applications, including predictive modelling, growth pattern research and diagnostic assistance. One particular application is of planning therapy with the aid of such a model. In our next chapter, we will therefore focus on this application and demonstrate how our vascular model could be expanded to account for a tumour's response to therapy.

Chapter 6

3-D Model of Tumour Response to Therapy

Radiation therapy plays an important role in the management of cancer. The aim is to deliver the highest possible dose of irradiation to eliminate cancer, while avoiding unacceptable injury to surrounding healthy tissue. Several factors impact the effectiveness of the treatments, such as optimum dosing and scheduling of therapy. Substantial improvements have already been achieved in this regard with the development of new technologies such as image-guided therapy, by altering the radiotherapy fractionation or by using concurrent chemotherapy [65]. The employment of mathematical models might provide a way of testing different treatment regimens for each patient.

In the past few decades many groups have devoted themselves to the modelling of biological phenomena related to tumour growth and response to radiotherapy. Mathematical models like the ones developed by Byrne *et al.* [131, 6, 132] are very useful to gain valuable insight into the biological phenomena underlying tumour growth, but are limited in their application to clinical practice. In [27], the

authors suggest that this limitation has to do with the fact that the parameter values used in these models are constrained by values from published literature since they cannot be measured in an actual patient.

Patient-specific, imaging based information obtained pre-, during and post-therapy could be used to initialise, calibrate and validate models of tumours response to therapy. The predictions could first be tested retrospectively on data available for each patient and once confirmed and adjusted be used to optimise the design of future clinical trials. Such a model can be used to estimate the distinct contributions of physical changes and parameter variations to therapy outcome. As such, imaging-based models of reaction to therapy could be used to identify potentially dangerous treatment plans, optimise therapy schedules and design better clinical trials [133].

Similar to imaging-based models of tumour growth, most groups have focused on the case of gliomas when modelling tumour reaction to therapy [79, 87, 88, 21, 134, 135, 100, 85, 136]. This has mainly to do with the availability of imaging data (such as DTI-MRI, PET/CT, DWI-MRI, etc). Further reasons are related to the fact that gliomas are known to practically never metastasise [130], that the brain offers many fiducial landmarks and that the skull provides a structure that keeps the possible deformation due to tumour growth within an acceptable range.

Some of these models are based on the reaction-diffusion mechanism and represent therapy reaction as a loss term in the cell evolution equation [134, 135, 100, 85, 136]. They can be very helpful to study the effects of radiotherapy when applied to brain tumours accounting for a variety of tumour delineations, which might include or exclude the undetected portion of cells spread around the tumour bulk. They can also be used to study different therapy dosing and schedules. However,

the fact that these models do not account for biological processes such as hypoxia and angiogenesis, both of which are known to affect the delivery of therapy (e.g. chemotherapy) and oxygenation (necessary for efficient radiotherapy) to the tumour, is a considerable shortcoming of these approaches.

In contrast, some models have simulated effects of tumour oxygenation on radiation response through the use of cell-line and cell-cycle phase specific parameters [79, 87, 88, 21, 89]. For example, in [89], for the case of head and neck squamous cell carcinoma, the authors employed cell-line-specific biological parameters and functional information extracted from pre-therapy PET/CT to simulate effects of tumour oxygenation on radiation therapy response. Their tumour model accounted for biological processes such as proliferation, hypoxia, apoptosis and radiation-induced necrosis. Their results, which were verified against *in vitro* and preclinical data, showed that hypoxic cells required significantly higher doses in order to achieve the same response to therapy as proliferative cells. Although their approach demonstrates how patient-specific data can be transformed into voxel-based biological information and be used to investigate biologically optimised dose prescriptions, the fact that each tumour cell is simulated renders the applicability of their model to the clinical case virtually impossible.

Pre-clinical studies have found a positive interaction between angiogenesis inhibition and radiotherapy characterised by a stronger growth delay when mice were also treated with angiogenic inhibitors as opposed to radiotherapy alone [137]. In [70], the hypothesis was raised that this positive effect was due to certain anti-angiogenisis agents inducing a normalisation of the abnormal structure of the chaotic tumour vasculature and hence making it more efficient for oxygen and drug delivery. The author suggested that these drugs can alleviate hypoxia and increase the efficiency of conventional therapies, like radiotherapy, if both ther-

apies are carefully scheduled. The hypothesis was that during anti-angiogenesis therapy there is a transient period of vessel normalisation which occurs when the misbalance between anti- and pro-angiogenesis factors in the tumour microenvironment is restored. The term 'normalisation window' was hence coined to describe this transient period of vasculature normalisation. Although the hypothesis raised in [70] could be supported by pre-clinical findings [137, 138, 63, 139], it remains a challenge to determine when the normalisation window occurs in patients and hence to translate these findings to clinical practice.

The model developed and evaluated in Chapter 5 represents a compromise between the clinically oriented models (such as the reaction-diffusion glioma models mentioned above) and the cell-cycle specific models, since it accounts for the macroscopic evolution of the tumour, yet still considering hypoxia, necrosis, proliferation and angiogenesis. The purpose of this chapter is therefore to explore whether we can expand the model of Chapter 5 to 1) explore different schedules and dosing of radiotherapy using the example of breast and brain tumours; 2) study the effect of anti-angiogenenic therapy on radiation therapy outcome and by doing so 3) explore whether the model can serve as a tool to determine the normalisation window time point. Due to the lack in data obtained pre-, during and post-therapy, we compare our results to findings in the literature. Thus, this chapter serves as a proof of concept of how models accounting for proliferation, hypoxia, necrosis and angiogenesis due to hypoxia have the potential to serve as a valuable tool to support medical decision making in the treatment and management of cancer patients.

6.1 Methods

6.1.1 Radiation effect

The linear quadratic (LQ) model is the most commonly used model for studying survival response in radiotherapy [81]. Deduced from first principles, this model assumes that radiation produces sublesions within the cell which are directly proportional to the absorbed dose. Cell death can result from an α component, which increases linearly with dose, d, or from a β constant in which cell death increases in proportion to the square of d. The fraction of cells surviving a single dose of radiation d is hence given by:

$$S(d) = \exp\left(-(\alpha \cdot d + \beta \cdot d^2)\right) \tag{6.1}$$

where α $(1/Gy)$ and β $(1/Gy^2)$ are sensitivity parameters that characterise the initial linear slope and the curvature of the survival curve, respectively. The ratio of these parameters, α/β, is the dose when the number of cells killed by the linear component, α, is the same as the number of cells killed by the quadratic constant, β. This ratio is a measure for the fractionation sensitivity and hence depends on the type of cancer being modelled.

It was initially thought that the linear component of the LQ model represented the double strand breaks caused by a single track of radiation, and that the quadratic component was the result of two distinct radiation tracks causing separate single strand breaks in such close proximity that a double strand break occurred [81]. However, the main problem with this idea is that at the standard 2 Gy dose (delivered within a standard fractionation), there is negligible chance of two electron tracks running sufficiently close together for this to happen. Even

without a current biological basis, the LQ model remains the most commonly used one for quantitative predictions of dose and fractionation dependencies in radiotherapy. The main reasons for this might be that it has sufficiently few parameters and that it is reasonably well experimentally validated for a dose up to about 10 Gy [140].

Another factor that can influence the radiation effect is related to the presence or lack of oxygen. Hypoxic cells are known to be less radiosensitive than proliferative cells. This protective effect of hypoxia on cells against radiation is generally expressed as the oxygen enhancement ratio (OER), which represents the ratio of the doses needed to achieve the same cell survival rate at different oxygen availabilities, and is defined as:

$$OER = \frac{\text{dose in hypoxia}}{\text{dose in oxygen}} \tag{6.2}$$

One possible way to account for this difference in radiosensitivity is to adjust the sensitivity parameters, so that the values found in the literature are used for the proliferative (oxygenated) cells and for the hypoxic cells, $\alpha_h = \alpha_p/OER$ and $\beta_h = \beta_p/OER^2$ can be used.

6.1.2 Isoeffective radiotherapy schedules

Radiation therapy is usually delivered in fractions. Studies have demonstrated that each fraction of a fractionated therapy schedule is equally effective. The LQ-model represents a pragmatic method to assess the effect E of n fractions, expressed as the negative logarithm of $S(d)$ as:

$$\begin{aligned} E = -\log(S(d))^n &= -n \cdot \log(S(d)) \\ &= n(\alpha \cdot d + \beta \cdot d^2) \\ &= \alpha \cdot D + \beta \cdot dD \end{aligned} \tag{6.3}$$

In clinical practice, one is often interested in knowing the required change in total radiation dose when the dose per fraction is changed. This can be dealt with using the LQ approach and by dividing both sides of Eq. 6.3 by α:

$$BED = \frac{E}{\alpha} = n \cdot d \left[1 + \frac{d}{\alpha/\beta}\right] \tag{6.4}$$

where n is the number of fractions, d is the dose applied per fraction and the ratio α/β represents the tissue-specific fractionation sensitivity. The Biological Effective Dose (BED), which represents the dose required for a given effect when delivered by infinitely small doses per fraction, has been widely used in clinical calculations.

The BED formulation, which assumes that full repair occurs between fractions so that the biological effect of each fraction is the same, allows easy comparison between different schemes of radiotherapy. Given a fractionated treatment with a fixed BED value, the dose per fraction d for a different, isoeffective fractionated therapy schedule delivering n fractions can be computed as [141]:

$$d = \frac{\alpha/\beta}{2}\left(\sqrt{1 + \frac{4BED/n}{\alpha/\beta}} - 1\right) \tag{6.5}$$

Following therapy delivery, different types of tissue and tumour express damage at different time points. On the one hand, for early-responding tissues, which demonstrate damage days to weeks after irradiation, the α/β-ratios range typically from 7-20 Gy. Gliomas, carcinomas of head and neck, and lung, are examples of early-responding tumours. On the other hand, late-responding tissues express their damage months to years after irradiation and have α/β-ratios ranging from 0.5-6 Gy. Breast and prostate tumours belong to the late-responding tumours [142]. Normal tissue α/β-ratios are normally smaller (1-4 Gy) than those for many human tumours [133].

A typical, standard fractionated scheme in the clinic comprises a dose of 2 Gy per fraction. Therefore, the simplest method for comparing the effectiveness of different schedules is to express each schedule into an equivalent schedule in 2 Gy fractions for a given isoeffect. Considering the different response of tissues, an increase or a decrease in dose per fraction relative to a dose of 2 Gy can be prescribed. The LQ-model has been used to compare therapeutic advantages of different radiation schedules including: 1) hyperfractionation, the use of smaller fraction doses delivered in multiple daily treatments; and 2) hypofractionation, the use of a larger dose per fraction.

For the case of hyperfractionation, a higher total dose of radiation can be achieved in a total treatment time that is about the same duration as for standard radiotherapy. It is therefore associated with increased biological effect, unless the interval between fractions is sufficiently long allowing for full recovery between fractions. The basic idea with this scheme is to take advantage of the difference in the shapes of the cell survival curves between tumours and late-responding normal tissues in order to deliver a higher overall dose of radiation without increasing the late effects of treatment.

Assuming the same treatment effect, hypofractionation is attractive as it allows for the delivery of the treatment in a shorter period of time and at less cost. For some tumour types (such as breast cancer), it can lead to more sustained schedules in terms of both tumour control and effects on normal tissue [143, 142].

6.1.3 Anti-angiogenic therapy

The resistance to therapy not only depends on the tissue being irradiated but can also be partly linked to the effects of the therapy on the vasculature. The inhibition of angiogenesis through anti-angiogenic therapy can potentiate the effects of radiotherapy and as such is generally recognised as a promising approach in the management of cancer patients [144].

As discussed in our previous chapter, in the hypoxic tumour environment there is a surplus of vessel growth factors which results in activation of angiogenesis and hence vascular growth. During anti-angiogenic treatment, the balance between pro- and anti-angiogenesis factors is restored, which causes vessel normalisation and improves tissue oxygenation. However, prolonged treatment results in an excess of angiostatic factors which induces vessel regression and a decreased tissue oxygenation, ultimately leading to increased tumour hypoxia and thus a reduced response to radiotherapy. Hence, effective combination therapy depends highly on proper dose-scheduling of both treatment modalities.

6.1.4 Adding therapy to the model of tumour growth

In this section we expand the model developed and evaluated in Chapter 5, which accounts for the macroscopic evolution of the tumour under consideration of hypoxia, necrosis, proliferation and angiogeneis, to include the tumour response

to therapy, including radiation and anti-angiogenic therapies. A model overview is given in Fig. 6.1.

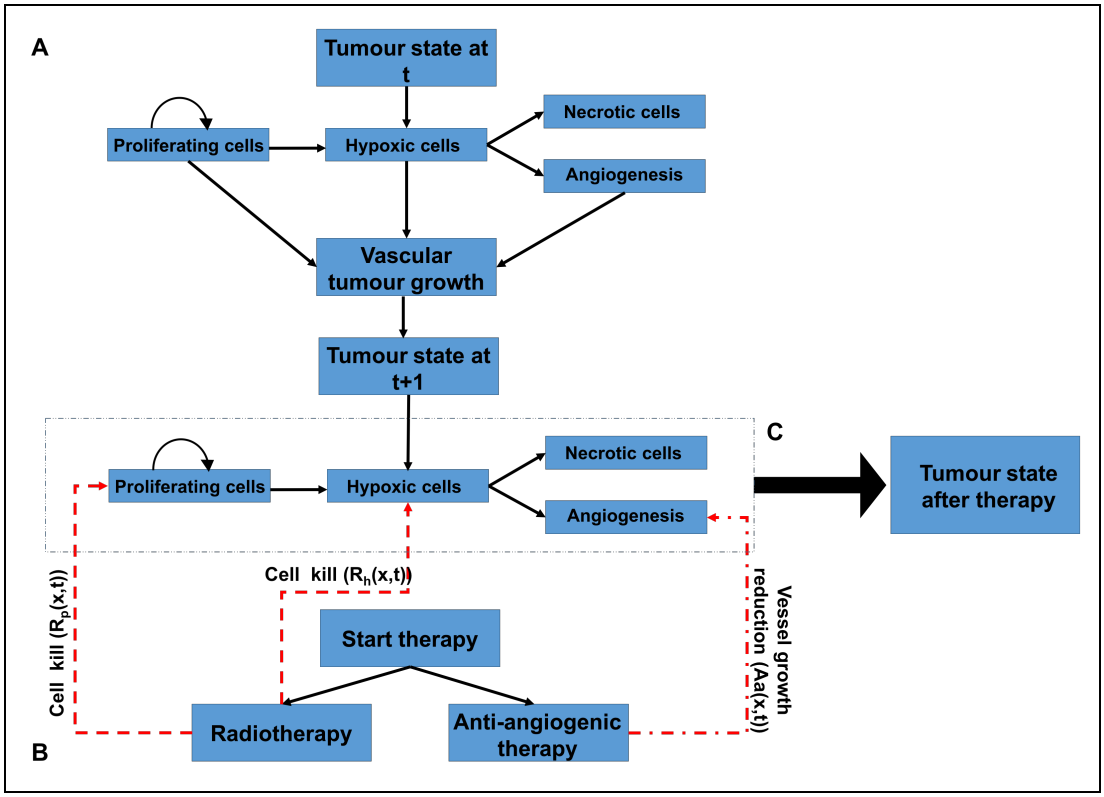


Figure 6.1: Model of vascular tumour growth and reaction to therapy. A) We start from the model used in the previous chapter which accounts for vascular tumour growth. Using tumour images at TP1, we let the tumour grow for 24 hours before applying therapy. B) Radiation therapy has a cell loss effect on the proliferative and hypoxic cells, represented by the terms $R_p(x,t)$ and $R_h(x,t)$, respectively. These terms differ to account for the fact that hypoxic cells are more resistant to radiotherapy than proliferative cells. Anti-angiogenic drugs (e.g. Avastin) acts by preventing the creation of new vessels and hence its effect is considered as a vessel growth reduction in the updated model. Different schedules can be administered and their outcome compared using either radiotherapy alone or in combination with anti-angiogenic drugs. After simulation, the tumour state after therapy C) can be assessed in terms of cellularity, volume growth or reduction, and growth delay.

First, we introduce the changes needed to account for anti-angiogenic therapy. We consider the case of Avastin (Bevacizumab), designed to block vascular endothelial growth factors, and hence to prevent the growth of new blood vessels. Avastin is normally delivered in a single intravenous (IV) dose, and it has been observed that its plasma concentration time curve ($C_p(t)$) following IV administration does not decline linearly as a single, first-order rate process [145]. This non-linear con-

centration time curve is attributed to the distribution of the drug at different rates into different tissue groups, and can be modelled using a two-compartment pharmacokinetic (PK) model. For that case, the plasma concentration time curve shows that the plasma drug concentration declines bi-exponentially as the sum of two first-order processes: distribution and elimination. This is attributed to distribution of the administered drug between the central compartment and tissue (peripheral compartment), as shown in Fig. 6.2-A. The central compartment includes blood and the highly perfused organs and tissues such as the heart, the brain and the kidney in which the administered drug usually equilibrates rapidly. The peripheral compartment includes less well-perfused organs such as the adipose tissue and the skeletal muscle, and therefore the administered drug will equilibrate more slowly.

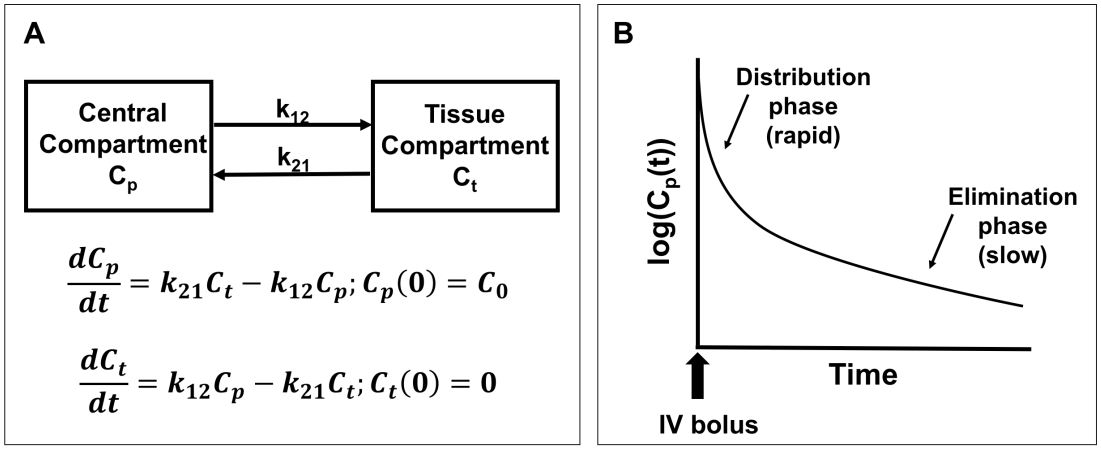


Figure 6.2: Figure A shows the distribution of the administered drug between central and peripheral compartment. k_{12} and k_{21} are first-order rate constants that govern the rate of drug change in and out of the compartments (tissues). The equations in Fig. A can be used to calculate the change in drug concentration in the tissue with time. A typical bi-exponential response curve is shown in Fig. B for the drug in the central compartment.

Hence, when a single dose of the drug is injected intravenously, the time course of drug concentration can be expressed as the sum of two mono-exponential terms:

Dose (mg/kg)	CL (mL/kg/day)	V_C (mL/kg)	V_SS (mL/kg)	$t_{1/2\alpha}$ (h)	$t_{1/2\beta}$ (h)	MRT (days)	AUC (mg.h/mL)
9.3	15.7	53.0	152	28.8	6.81	9.69	14.22

Table 6.1: PK parameters for mice receiving intravenous dose of Avastin extracted from [145] and used to derive the the specific concentration of Avastin in plasma as a function of time (Eq. 6.7. Abbreviations: CL, clearance; V_C, volume of central compartment; V_SS, volume of distribution at steady-state; $t_{1/2\alpha}$, initial half-life; $t_{1/2\beta}$, terminal half-life; MRT, mean residence time; and AUC, area under the plasma drug concentration-time curve.

$$C_p(t) = A\exp\left(-k_\alpha \cdot t\right) + B\exp\left(-k_\beta \cdot t\right) \tag{6.6}$$

The constants A and B represent the intercepts on the y axis (see Fig. 6.6-B) obtained from a semilog plot of plasma concentration versus the time after IV bolus. The constants k_α and k_β are the initial (distribution) and terminal (elimination) rate constants, respectively. We obtain the PK model parameters from the data provided by the European Medicines Agency scientific discussion on Avastin's effect on mice [145]. Using these parameters (listed in Tab. 6.1) as inputs in the two-compartment model equations provided in [146, 147], we derive the specific concentration of Avastin in plasma as a function of time after drug delivery as:

$$C_{Aa}(t) = 0.0351\exp\left(-0.0241 \cdot t\right) + 0.1404\exp\left(-0.0042 \cdot t\right) \tag{6.7}$$

Anti-angiogenic agents are unable to directly sensitise tumour cells to radiation but do exhibit varying levels of radiosensitisation on endothelial cells, leading to improved radiation response [63]. To model this behaviour we thus account for anti-angiogenesis as a direct reduction in vessel creation but not as a direct effect cell proliferation or death. The aim is to investigate whether by normalising the vasculature, and hence allowing for better oxygenation of the cells, an indirect

effect on tumour cells radiosensitivity can be observed.

Using the temporal concentration of the drug in the tumour tissue, the effect of Avastin on the vasculature can be derived. We assume that the anti-angiogenic drug will have a counter-effect on the angiogenesis by blocking VEGF and hence a negative contribution to the v_D evolution equation (Eq. 5.5) introduced in Chapter 5. Since the drug is delivered locally by v_D (since v_D includes the vasculature), the response to anti-angiogenic therapy can be introduced as a loss term and hence the updated version of Eq. 5.5 becomes:

$$\frac{\partial v_D(\mathbf{x},t)}{\partial t} = \bigtriangledown\cdot(d(\mathbf{x},t)\bigtriangledown v_D(\mathbf{x},t)) + HB(t-\tau_{HB})\cdot v_D(\mathbf{x},t) - Aa(t)\cdot v_D(\mathbf{x},t) \quad (6.8)$$

with $Aa(t) = k_{Aa}\cdot C_{Aa}(t)$ representing the local and temporal loss rate of vasculature due to the Avastin concentration in the tissue at time point t after injection. It is important to note that this term captures the decrease but not the normalisation effect on vasculature. The constant k_{Aa} is assumed to be $k_{Aa} = 100/AUC$ (see 6.1) to match the units. The value 100 was chosen, so that the effect of Aa is at its maximum (at $t = 1h$) around 1 which will decrease with time post delivery, as it directly depends on $C_{Aa}(t)$. However, ideally k_{Aa} should be calibrated if data pre-, during and post-therapy were available.

Next, we consider the effect of radiotherapy on tumour cells by adjusting the reaction-diffusion equations used in Chapter 5 to include the effect of the cell death rate due to ionising radiation. The reaction-diffusion equation including the radiotherapy effect on cells is generally described by:

$$\frac{\partial c(\mathbf{x},t)}{\partial t} = \bigtriangledown\cdot(d(\mathbf{x},t)\bigtriangledown c(\mathbf{x},t))+p\cdot c(\mathbf{x},t)\cdot\left(1-\frac{c(\mathbf{x},t)}{\Theta}\right)-R(d,\alpha,\beta)\cdot c(\mathbf{x},t) \quad (6.9)$$

The radiotherapy effect is generally chosen to be $R(d,\alpha,\beta) = 1 - S(d) = 1 - \exp\left(-(\alpha\cdot d+\beta\cdot d^2)\right)$ [83, 82] and hence to represent the probability of cell death depending on the applied dose and on the sensitivity parameters. However, being a probability, $R(d,\alpha,\beta)$ is a dimensionless quantity, and Eq. 6.9 becomes dimensionally incorrect. To circumvent this problem, Rockne *et al.* [83, 82] proposed that since radiation therapy is delivered daily, the probability of cell death can be considered as a probability rate. Although this might be a valid reinterpretation, Borasi *et al.* derived a straightforward method to evaluate the cell death rate due to ionising radiation, $R(d)$, starting from the LQ-model [148]. Considering a single treatment, the suggested expression to be introduced in 6.9 is:

$$R(\tau) = -(\alpha\cdot I + 2\beta\cdot I^2\cdot\tau), \quad (6.10)$$

where I represents the constant dose rate at which radiotherapy is delivered for time τ for the duration of $\Delta\tau$. This expression can be useful to explore the cell concentration during the short period of irradiation (of the order of minutes). However, the sampling of the total time t is longer than $\Delta\tau$, for example in the order of one day. In this case the mean value of Eq. 6.10 over the irradiation time $\Delta\tau$ needs to be considered, so that:

$$R = -(\alpha\cdot I + \beta\cdot I\cdot d), \quad (6.11)$$

where $d = I\cdot\Delta\tau$ indicates the cumulative dose delivered at the end of irradiation.

This is the correct expression to be used in Eq. 6.9, for the case where the total sampling time from the starting from the irradiation is longer than the irradiation time [148]. In [148], $\Delta\tau = 1\ day$. Considering our simulation time step of 1 hour, we therefore assume $\Delta\tau = 1h$, so that $I = d\ (Gy/h)$.

As already mentioned, hypoxic cells are known to be less radiosensitive than proliferative cells. To account for this, we adjust the sensitivity parameters as outlined in Sec. 6.1.1 and use for all simulations $OER = 3$ based on findings by [149]. Two distinctive radiotherapy effects can be defined depending on whether cells are proliferating or hypoxic. For the proliferation case we have:

$$R_p(\alpha_p, \beta_p, d) = \begin{cases} 0 \quad \text{if} \quad t \quad \notin t_{therapy} \\ \\ -(\alpha_p \cdot I + \beta_p \cdot I \cdot d) \quad \text{otherwise} \end{cases} \tag{6.12}$$

And for the hypoxic case, 6.11 becomes:

$$R_h(\alpha_h, \beta_h, d) = \begin{cases} 0 \quad \text{if} \quad t \quad \notin t_{therapy} \\ \\ -(\alpha_h \cdot I + \beta_h \cdot I \cdot d) \quad \text{otherwise} \end{cases} \tag{6.13}$$

We can now update the reaction-diffusion equations of Chapter 5 describing the proliferative, hypoxic and necrotic cellularity evolution in terms of their v_D dependency and the loss rate due to radiotherapy R as follows :

$$\begin{aligned} \frac{\partial p(\mathbf{x},t)}{\partial t} &= \bigtriangledown \cdot (d(\mathbf{x},t) \bigtriangledown p(\mathbf{x},t)) + g(v_D(\mathbf{x},t)) \cdot p(\mathbf{x},t) \\ &\cdot \left(1 - \frac{r(\mathbf{x},t)}{\Theta}\right) - f(v_D(\mathbf{x},t)) \cdot p(\mathbf{x},t) - R_p(\alpha_p, \beta_p, d) \cdot p(\mathbf{x},t) \end{aligned} \tag{6.14}$$

$$\frac{\partial q(\mathbf{x},t)}{\partial t} = \bigtriangledown \cdot (d(\mathbf{x},t) \bigtriangledown q(\mathbf{x},t)) + f(v_D(\mathbf{x},t)) \cdot p(\mathbf{x},t) - h(v_D(\mathbf{x},t)) \cdot q(\mathbf{x},t) - R_h(\alpha_h, \beta_h, d) \cdot q(\mathbf{x},t) \quad (6.15)$$

$$\frac{\partial n(\mathbf{x},t)}{\partial t} = h(v_D(\mathbf{x},t)) \cdot q(\mathbf{x},t) + R_p(\alpha_p, \beta_p, d) \cdot p(\mathbf{x},t) + R_h(\alpha_h, \beta_h, d) \cdot q(\mathbf{x},t) \quad (6.16)$$

where $p(\mathbf{x},t)$, $q(\mathbf{x},t)$, $n(\mathbf{x},t)$ and $r(\mathbf{x},t)$ represent the number of proliferative, quiescent (hypoxic), necrotic and total cells, with t denoting time and $\mathbf{x}$ a spatial coordinate in a three-dimensional domain. The dependence on $v_D(\mathbf{x},t)$ yields a dependence on time and space for the proliferation and hypoxic rates. For the case of therapy, we assume a lysis time of 10 hours [79]. R_p and R_h represent the cell loss rate due to radiotherapy for proliferative and hypoxic cells, respectively. For the untreated case, R_p and R_h are both set to 0 at all times.

The total number of tumoural cells can then be updated using:

$$r(\mathbf{x},t) = p(\mathbf{x},t) + q(\mathbf{x},t) + n(\mathbf{x},t) \quad (6.17)$$

Once the new number of total tumour cells is known, v_D is updated using:

$$v_D(\mathbf{x}) = 1 - \frac{r(\mathbf{x})}{\Theta}. \quad (6.18)$$

As in the simulation cases, any voxel with less than 1% of capacity cells is considered empty, so that tumours might regress in size due to therapy.

6.2 Experiments

Our pre-clinical data used to validate the models of Chapters 3 and 5 do not include exposure to any form of therapy. Therefore, in this chapter we focus on *in silico* experiments, with the aim of demonstrating the feasibility of including response to radiation therapy to the model developed in Chapter 5. To this end, a series of simulations corresponding to various treatment schedules are performed.

To test the simulation model of vascular tumour growth and reaction to therapy, the cases of a breast and brain tumours are considered. Our experiments include 1) the effect of combined anti-angiogenic (Avastin) and radiotherapy (RT) schedule on tumour evolution; and 2) the effect of fractionation radiotherapy on tumour evolution. For both sets of experiments, we use $\alpha/\beta = 4Gy$ and $\alpha/\beta = 10Gy$ representing typical values for breast [150] and brain [134] tumours, respectively. We recall that the sensitivity parameters are characteristic of different types of tissues and tumours.

For all simulations, we use Case 5 as input and assume that the parameters optimised in Chapter 5 and listed in Tab. 5.4 remain constant over the evolution of the tumour and hence use them for the simulations included in this chapter. Most groups modelling tumour growth and response to therapy rely on this assumption to be able to predict tumour growth and response to therapy at future time points [12, 16, 23, 15]. However, other than in the models found in the literature, our proliferation and hypoxic rates depend on the nutrient which in turn depends on time and space. Therefore, our *de facto* local proliferation and hypoxic rates do not remain constant over time, as the nutrient field (represented here by v_D) evolves with time.

All codes were written in Matlab (Mathworks, Natick, MA) and all simulations performed on a 3.4 GHz Intel Xeon machine with 32GB of RAM. Simulations took up to 40 minutes due to the longer period of interest being modelled.

6.2.1 Effect of Avastin on treatment outcome

We study the effect of anti-angiogenenic (Avastin) therapy on tumour oxygenation and on radiation treatment by varying the schedules of anti-angiogenic and radiation therapies. To be able to choose schedules which have been tested and validated in pre-clinical studies, and to compare our results to a ground truth, we assume three specific treatment schedules reported by [63]. In this study tumour-bearing mice were treated with Avastin either two days before a single dose irradiation of 5 Gy or two days after radiation therapy. Fig. 6.3 shows the three treatment schedules included in this analysis: a single dose of RT (5 Gy) delivered at day 4, a single dose of Avastin (9.3mg/kg) delivered two days before RT (5 Gy), and a single dose of Avastin (9.3mg/kg) delivered two days after RT (5 Gy). For all three schedules, we simulate tumour growth for 14 days (336 hours) to be able to assess the growth delay effect of each treatment schedule.

6.2.2 Effect of fractionation on radiotherapy outcome

Next, we use the example of breast ($\alpha/\beta = 4\ Gy$, $BED = 15\ Gy$) and brain tumours ($\alpha/\beta = 10\ Gy$, $BED = 12\ Gy$) to explore the effect of different, iso-effective treatment schedules and dosing on radiotherapy. In the clinic, these treatments are normally repeated for for a number of consecutive weeks (typically 4 to 6 weeks). Here, we consider the cases of standard therapy (5 doses delivered daily), hypo-fractionated therapy (3 doses delivered every other day), hyper-

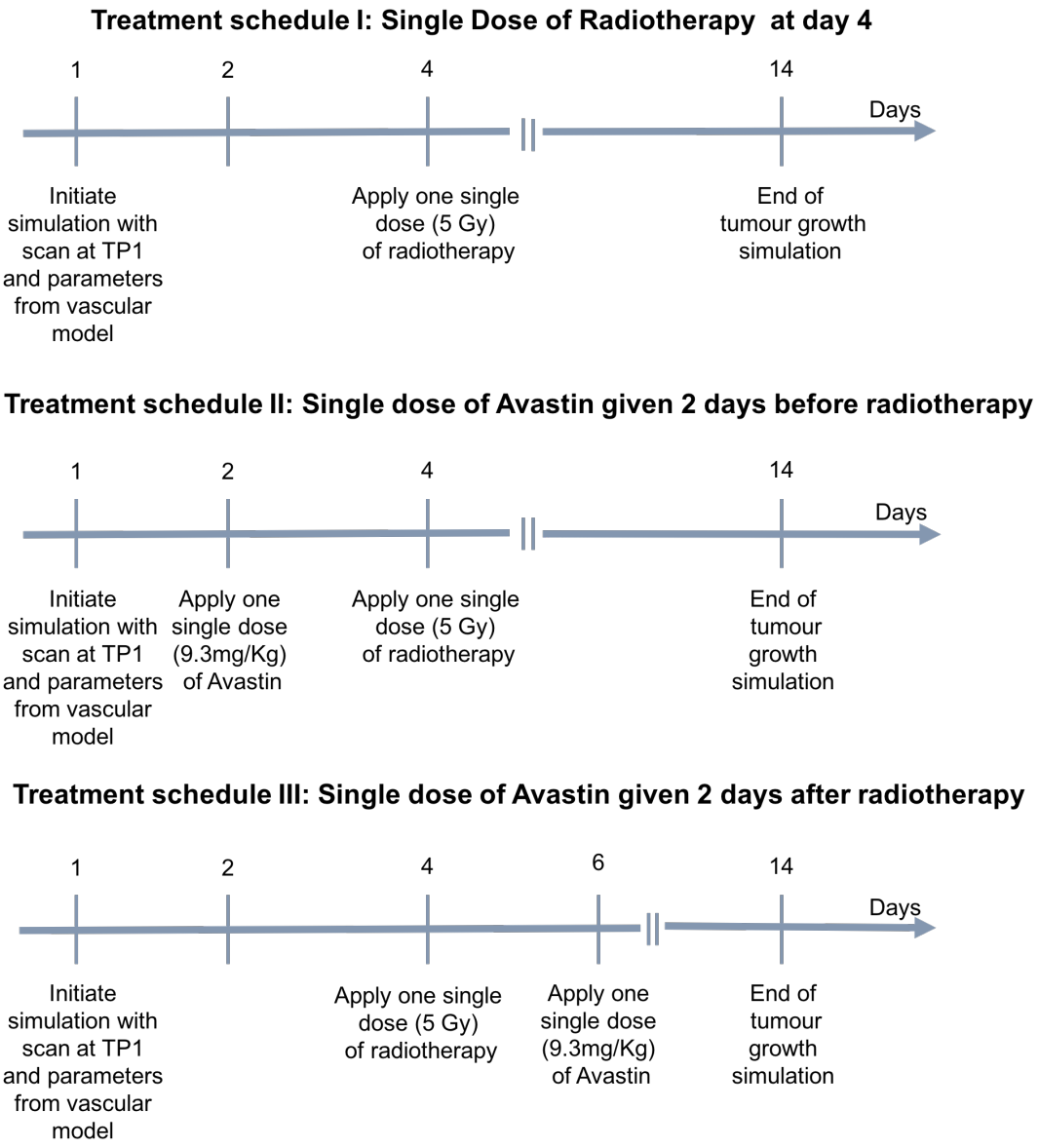


Figure 6.3: Combined anti-angiogenic (Avastin) and radiotherapy (RT) schedule. Before treatment starts the growth of an untreated tumour (Case 5) is simulated using the parameters obtained in Chapter 5. Treatment schedule I (top) involves a single dose of RT and serves as the baseline for comparison of the effectiveness of Avastin on irradiation outcome. Treatment schedule II (middle) and III involve a single dose of Avastin delivered two days before and after RT, respectively. For all three schedules we simulate tumour growth for 14 days (336 hours).

Schedule	Tumour	
	Breast ($\alpha/\beta = 4\,Gy$)	Brain ($\alpha/\beta = 10\,Gy$)
Standard therapy (n=5)	$BED = 15\,Gy*$ $d = 2\,Gy$	$BED = 12\,Gy$ $d = 2\,Gy$
Hypo-fractionated therapy (n=3)	$BED = 15\,Gy$ $d = 2.899\,Gy$	$BED = 12\,Gy$ $d = 3.0623\,Gy$
Hyper-fractionated therapy (n=10)	$BED = 15\,Gy$ $d = 1.1623\,Gy$	$BED = 12\,Gy$ $d = 1.0828\,Gy$
Single dose (n=1)	$BED = 15\,Gy$ $d = 6\,Gy$	$BED = 12\,Gy$ $d = 7.0416\,Gy$

Table 6.2: Radiotherapy treatment schedules for the simulation of the reaction to RT for two theoretical cases: breast and brain tumours. These cases differ in their α/β-ratios and hence in their BED values. * BED values were calculated using Eq. 6.4. The isoeffective dose corresponding to each schedule and maintaining the same BED value was computed using Eq. 6.5.

fractionated (10 doses delivered twice a day) and a single dose. The isoeffective doses corresponding to each schedule and maintaining the same BED value were computed using Eq. 6.5 and are listed in Tab. 6.2. For all cases, the growth of an untreated tumour (Case 5) is simulated using the parameters obtained in Chapter 5 for 24 hours before treatment starts. All simulations run for 288 hours. The first (or single) dose of each treatment is assumed to be delivered on a Monday, so that the consecutive doses are all given during the same week.

The values for α/β are normally extracted through fitting of the cell survival curve. However, these values are often not very accurate, as a range of combinations of the two parameters might fit the data almost equally well. To visualise the effect of this uncertainty on the therapy outcome, we include two sets of parameters that result in the same ratios: we choose $\alpha = 0.08\ Gy^{-1}$ [150] and $\alpha = 0.36\ Gy^{-1}$ [135]; and $\alpha = 0.027\ Gy^{-1}$ [134] and $\alpha = 0.4\ Gy^{-1}$ [87] for breast and brain tumours, respectively.

6.3 Results

6.3.1 Effect of Avastin on treatment outcome

In order to study the influence of anti-angiogenic drug Avastin on tumour growth and reaction to radiotherapy, we tested three treatment strategies with different injection times. For all figures and tables in this section, the abbreviations RT, AvRT and RTAv correspond to treatment schedules I, II and III (see Fig. 6.3), respectively. We also include the case where no therapy has been delivered, and hence of an untreated tumour, to serve as a baseline. However, we do not consider the effect of Avastin alone.

The numbers of tumour cells with different activities (proliferative, hypoxic and necrotic) at different time step are presented as curves in Fig. 6.4. The number of total tumour cells and hypoxic cells increase continually with time in the simulation. However, for the cases of RT and no therapy, the number of proliferative cells have a slight reduction in the period of $t = 250h$ to the end of the simulation. At the same time, necrotic cells remain constant after therapy sessions due to the small lysis time chosen for the simulations. Little effect can be observed on the total cell evolution for the case of a single dose of RT (5 Gy) compared with the case of an untreated tumour. Moreover, a slightly higher number in proliferation cells can be seen for RT, demonstrating that the tumour is more active after recovering from the single RT dose. The strong effect observed on the cellular evolution for the case when Avastin was delivered two days (48 hours) before RT (blue curve) is linked to the much smaller number of hypoxic cells. At the end of the simulation time, the number of proliferative cells is just slightly lower than the one observed for the cases of untreated tumour and RT alone. There is some reduction effect on the overall cellularity when Avastin was delivered after RT.

This effect is a result of the smaller number of hypoxic cells, given that the final number of proliferative cells was larger than the ones observed with the other simulated cases.

The above mentioned observations hold for both the hypothetical breast and brain tumours. The different α/β-ratios seem to have limited effect on the reaction to therapy in terms of cellularity for these three treatment strategies. As depicted in Fig. 6.4, RT alone had a small effect on the total cell number evolution for the case of $\alpha/\beta = 4\ Gy$. For $\alpha/\beta = 10\ Gy$, on the other hand, no effect can be seen which is demonstrated by the overlap of both curves. The biggest effect of different α/β-ratios can be seen for the number of necrotic cells, as demonstrated by a higher final number of necrotic cells for the untreated and RT alone cases for $\alpha/\beta = 10\ Gy$.

Lack of oxygen, hypoxia, reduces cell death effect due to therapy. Consequently, reduction in hypoxia, as the one seen in Fig. 6.4 for the case where Avastin was delivered previous to RT, is expected to reduce tumour volume growth. To examine whether our model is able to mimic this, we include Fig. 6.5 which shows a direct comparison between hypoxia (measured by HB) and volume evolution. A comparison between the different therapy schedules yields higher reaction to therapy in terms of volume growth when Avastin was delivered 2 days before RT, for both $\alpha/\beta = 4\ Gy$ and $\alpha/\beta = 10\ Gy$. This is probably linked to the reduction in hypoxia as seen in the bottom graphs, and agrees with findings reported by [63]. This also suggests that the application of RT 48 hours later than Avastin delivery probably fell within the normalisation window. Both curves belonging to anti-angiogenic drug delivered either pre- or post-RT show a plateau in the hypoxia evolution after the time point of Avastin injection. In contrast, RT applied alone has just a small effect on the hypoxic burden level, but does not change the curve

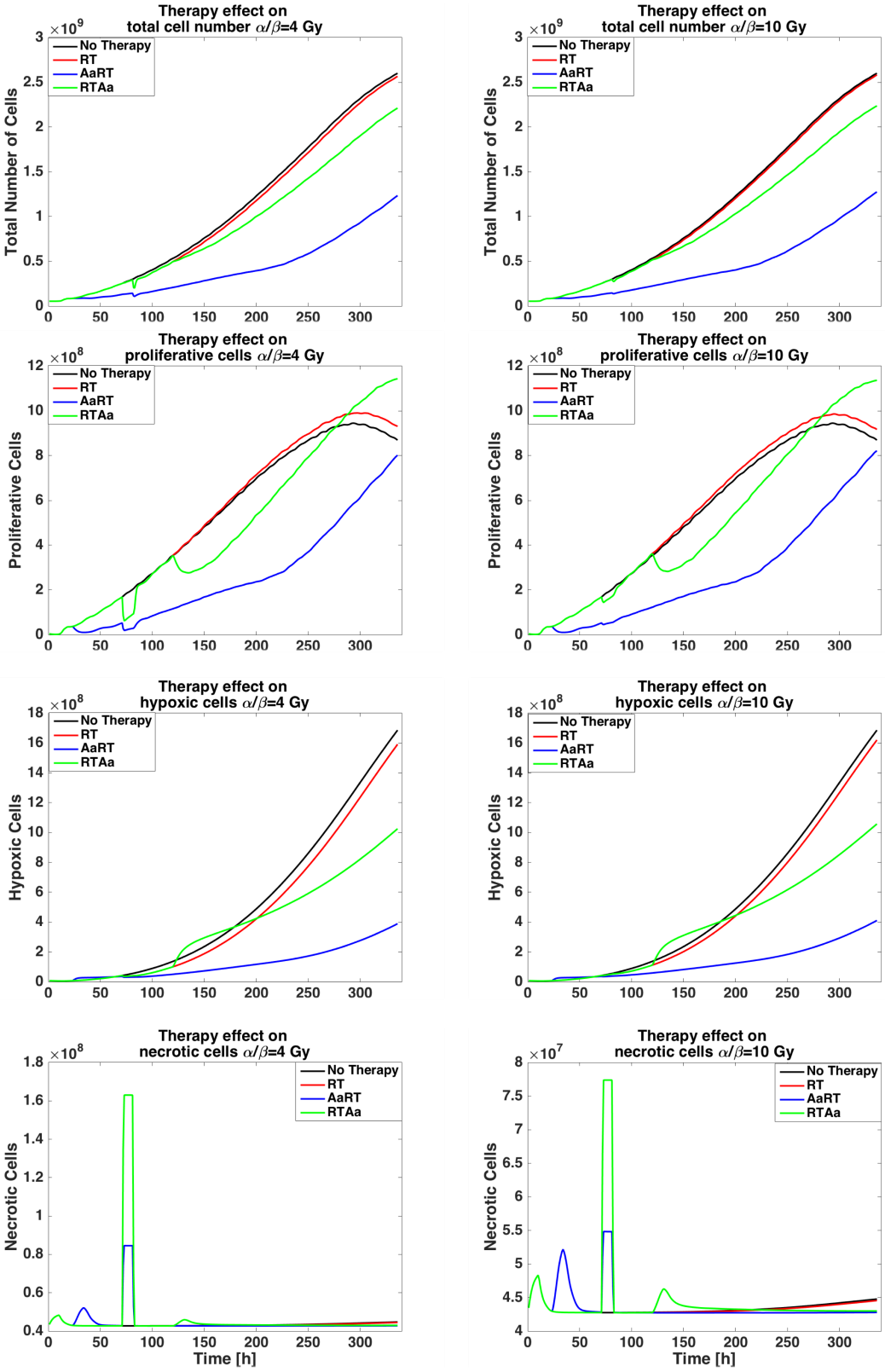


Figure 6.4: Effect of combined anti-angiogenic (Avastin) and radiotherapy schedule on cellularity evolution for $\alpha/\beta = 4\ Gy$ and $\alpha/\beta = 10\ Gy$. For all three schedules and the untreated case we simulate tumour growth for 14 days (336 hours) to be able to assess the growth delay effect of each treatment schedule.

evolution.

In terms of volume and HB there is not a very obvious impact of the ratio α/β on the results. However, $\alpha/\beta = 10\ Gy$ resulted in slightly more hypoxia for when RT was delivered before Avastin. In addition, the final volume for RtAa is smaller for $\alpha/\beta = 10\ Gy$, showing that our fictitious breast (late-responding) tumour is more sensitive to RT applied before Avastin than the fictitious brain (early-responding) tumour.

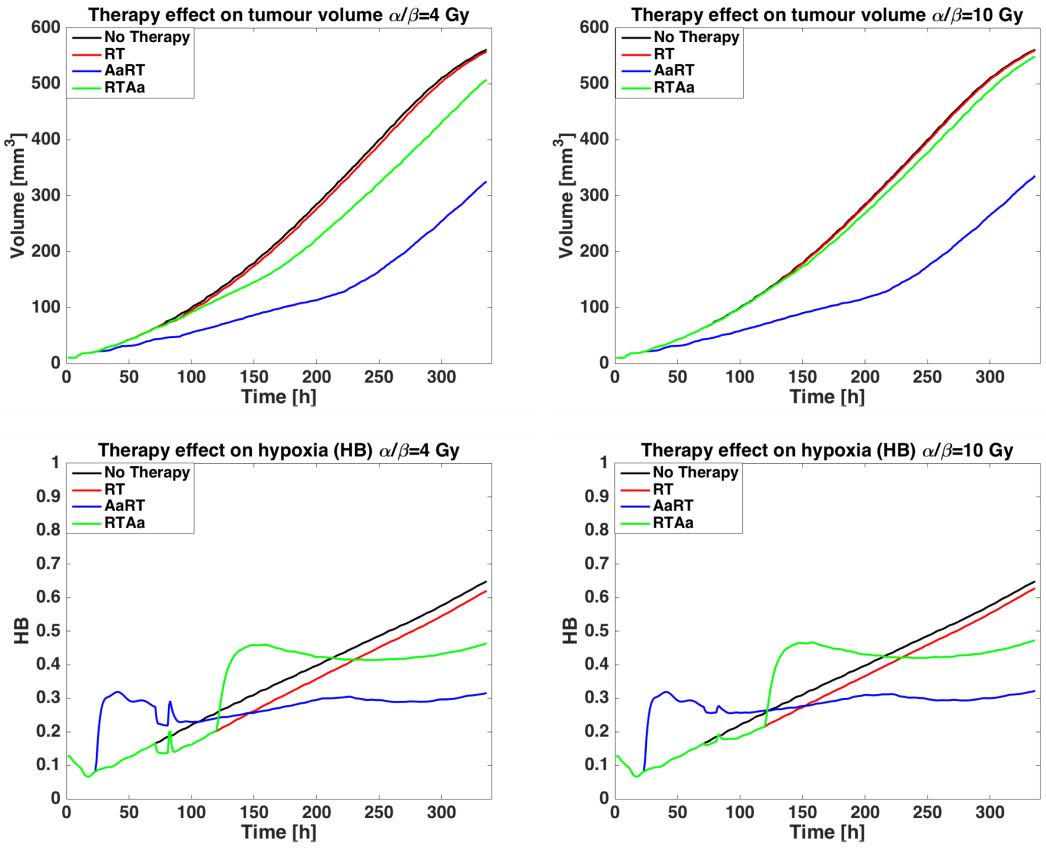


Figure 6.5: Effect of combined anti-angiogenic (Avastin) and radiotherapy schedule on volume and hypoxia evolution for $\alpha/\beta = 4\ Gy$ and $\alpha/\beta = 10\ Gy$. For all three schedules and the untreated case we simulate tumour growth for 14 days (336 hours) to be able to assess the growth delay effect of each treatment schedule.

A more quantitative measure of the effects on tumour growth by the different treatment schedules of Avastin and radiation are shown in Tab. 6.3. Quadruple time represents the time it took for tumour volume to quadruple starting from

	Breast ($\alpha/\beta = 4\,Gy$)		Brain ($\alpha/\beta = 10\,Gy$)	
	Quadruple Time (h)	Growth Delay (h)	Quadruple Time (h)	Growth Delay (h)
No therapy	188	0	188	0
RT	192	4	188	0
AvRT	302	**114**	296	**108**
RTAv	219	31	194	6

Table 6.3: The effects on tumour growth delay by multiple treatment schedules of Avastin and radiation.

the time point radiation was delivered (day 4). Growth delay is measured as the delay in quadruple time between each therapy modality and the case where no therapy was applied. Our results show that while for the simulated breast case ($\alpha/\beta = 4\ Gy$) radiotherapy (5 Gy) alone delayed quadrupling time by 4 hours, for the case of brain tumour, no growth delay was observed. For both cases, the greater effect on tumour growth (bold values) occurred when Avastin was administered before radiation treatment. Quadruple time was delayed by 31 and 6 hours when Avastin was delivered after radiotherapy, for $\alpha/\beta = 4\,Gy$ and $\alpha/\beta = 10\,Gy$, respectively. Overall, Avastin demonstrated larger tumour growth delays for the hypothetical breast (late-responding) than for the hypothetical brain (early-responding) tumour case.

6.3.2 Effect of fractionation on radiotherapy outcome

Figure 6.6 shows the cellular evolution of irradiated cells relative to the total number of cells for the untreated case for the cases of standard (red), hypo-fractionated (green) and hyper-fractionated (blue) therapies. The isoeffective doses used for each simulation are listed in 6.2. For all cases, the growth of an untreated tumour (Case 5) was simulated for 24 hours before treatment started. The simulation time range was of 288 hours for all cases. From Fig. 6.6 it becomes evident

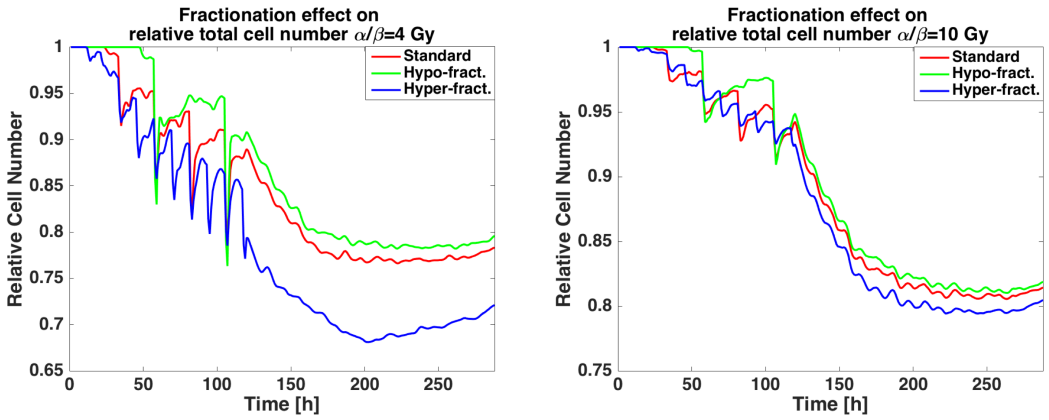


Figure 6.6: Effect of fractionation therapy on the relative cell number evolution (total cell number for the irradiated case to total cell number for the untreated case) for the fictitious cases of breast ($\alpha/\beta = 4\ Gy$) and brain ($\alpha/\beta = 10\ Gy$) tumours.

that the hyper-fractionated therapy had a higher effect on the fictitious breast tumour (left). Also for the case of case of brain tumour ($\alpha/\beta = 10\ Gy$) hyper-fractionated RT resulted in a smaller relative cell number, but the therapeutic gain was not as strong as the one observed for $\alpha/\beta = 4\ Gy$. This relatively small impact of radiotherapy on the cell evolution might be related to the assumption made in Chapter 3 that $G_{max} = 1 hour^{-1}$, so that the depending on the nutrient availability, high doubling times are simulated.

To evaluate the effect of different α and β values on therapy outcome, simulations for two sets of sensitivity parameters for each of the fictitious cases were performed. Fig. 6.7 shows the results for theses simulations in terms of hypoxic level, volume and tumour cell evolution for $\alpha = 0.08\ Gy^{-1}$ [150] and $\alpha = 0.36\ Gy^{-1}$ [135]; and $\alpha = 0.027\ Gy^{-1}$ [134] and $\alpha = 0.4\ Gy^{-1}$ [87] for breast and brain tumours, respectively. As observed in the case of combined therapy, the therapeutic gain appears to be related to the level of hypoxia, explaining the better performance of hyper-fractionation for the breast tumour case ($\alpha/\beta = 4\ Gy$, $\alpha = 0.08\ Gy^{-1}$) as compared to the brain tumour case ($\alpha/\beta = 10\ Gy$, $\alpha = 0.027\ Gy^{-1}$). For both tumour cases, higher α-values resulted in less hypoxia, higher cell kill and hence smaller tumour volumes for the treat-

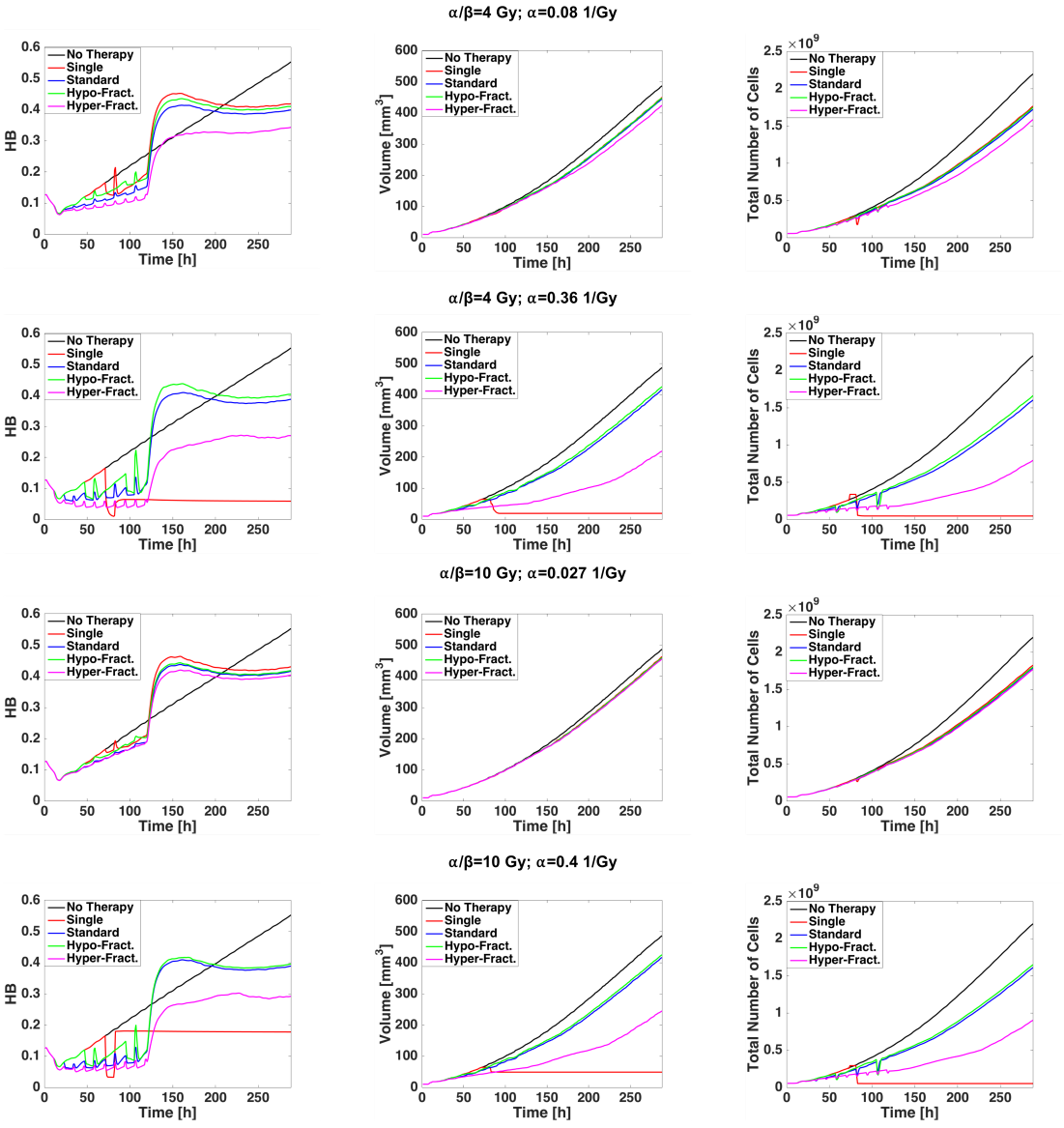


Figure 6.7: Effect of different α- and β-values on radiotherapy outcome.

ments using a single dose (red) and the hyper-fractionated scheme (magenta). The fact that using $\alpha/\beta = 4\ Gy$ and $\alpha = 0.36\ Gy^{-1}$ yielded very similar results for $\alpha/\beta = 10\ Gy$ and $\alpha = 0.4\ Gy^{-1}$, respectively, suggests that the sensitivity parameter β has just little influence on therapy outcome for higher values of α. For smaller α values, however, a clear difference can be observed for the case of hyper-fractionation, suggesting a higher dependence of this therapy schedule on the β sensitivity parameter. For all cases, no major differences could be observed between hypo-fractionated and standard therapies.

6.4 Discussion and Conclusions

In the present chapter, we have introduced an extension of the vascular model introduced in Chapter 5 to investigate the dynamic process of tumour growth and angiogenesis in response to anti-angiogenic therapy and radiotherapy. This model was chosen due to its demonstrated ability to predict vascular tumour growth at a macroscopic level whilst taking processes like proliferation, death and spread of tumour cells, as well as angiogenesis into account. A set of simulations were performed to inspect the effects of hypoxia, anti-angiogenic and fractionation on the reaction of tumour growth to radiotherapy. Our results agreed with behaviours observed in preclinical and clinical studies, demonstrating the feasibility of using maps of cellularity obtained from DCE-MRI analysis to obtain personalised predictions of tumour evolution and response to therapy.

Similar to other imaging-based models of tumour growth and reaction to therapy, our model is based on the reaction-diffusion mechanism and represents therapy response as a loss term in the cell evolution equation [134, 135, 100, 85, 136]. However, other than in these models, here the fact that we account for biological

processes such as hypoxia and angiogenesis, allows us not only to study different therapy dosing and schedules but also to include effects of anti-angiogenic therapy and tumour oxygenation on radiation response.

Accouting for two different, simulated tumour types (breast and brain) allowed us to test whether the model was able to report treatment outcomes depending on the tumour type at hand. Fig. 6.6 and Fig. 6.4 demonstrate that different types of tumour expressed damage of different levels and at different time points. Using three different therapy schedules, we were able to show that hyper-fractionation results in a therapeutic gain. This can be explained by the fact that hyper-fractionation allows for a higher total dose of radiation to be achieved in a total treatment duration as for standard radiotherapy (see Tab. 6.2). Hypo-fractionation has been shown to lead to better tumour control for the case of breast cancer [143, 142]. This improvement could, however, not be seen in our results. This might be due to two reasons. First, in our simulations we only compared iso-effective therapies (same BED). The results reported by [143, 142] were achieved using a hypo-fractionated scheme which had a higher BED than the one achieved for the standard therapy. As such, the overall delivered dose was higher, and might therefore have lead to the observed therapeutic gain. Second, because breast tumours are late-responding, the comparison in tumour control was performed months to years after the delivery of therapy. Our simulated time range, however, was of a few days and hence could not be used to inspect such late responses.

Our results also showed that it is not only relevant to estimate the α/β-ratios but rather each ratio component, as choosing α/β-ratios without knowing α can lead to considerably different results of the simulations and hence of the expected effect of therapy (see Fig. 6.7). It is therefore crucial to extract α and β values

from curves determined with *in-vitro* or *in-vivo* techniques, before using them for predictions. In addition, although the LQ-model is the most used model in the clinic to fit the cell surviving fraction curve, it is important to recall that the model does not have any biological basis, and hence that other models might provide more consistent and efficient estimators of model parameters, leading to better and more reliable predictions. Another limitation of the LQ-model is that it does not account for therapy delivery time. The fact that we already consider Borasi's formulation (Eq. 6.10) [148], is an advantage of our model over other reaction-diffusion based models [16, 83, 82]. However, to fully take advantage of this formulation we would need to have information on the drug delivery time, τ, as well as on the dose delivery rate, I. In the future this information should be included in the analysis.

As mentioned earlier, the resistance to therapy not only depends on the tissue being irradiated but can also be partly linked to the effects of the therapy on the vasculature. Therefore, we have also included the effect of anti-angiogenic therapy on the vasculature and performed simulations to assess whether our model can serve as a tool to determine the best delivery time point of anti-angiogenic therapy in combination with radiotherapy.

Studies have demonstrated direct effects of RT on the tumour vasculature [151]. In these studies, while high dose RT has been found to suppress angiogenesis, low dose radiotherapy appeared to promote angiogenesis in both *in vitro* and *in vivo*. Hence, in addition to anti-angiogenic therapy, radiotherapy also seems to directly affect angiogenesis depending on the chosen dose, scheduling and time interval after treatment [137]. In the future, the present model should be extended to account for this effect by introducing a constant that influences $HB(t-\tau)$ with dependence on the dose and the time lying between the application of the dose

and the current time point.

Even without accounting for the effect of RT on angiogenesis, our model was already able to mimic findings reported in pre-clinical studies. In [63] the authors found that Avastin given either 2 days before or after RT improved the effect of RT. Tumour growth delay was enhanced when RT was initiated within the tumour oxygenation window, i.e. the first fours days after Avastin delivery. Our results shown in Fig. 6.5 and Tab. 6.3, echo these findings since we also found that for both simulated tumour cases (breast and brain) using treatment schedule I, i.e.delivering anti-angiogenesis treatment 2 days before irradiation yielded the best results. These results are very promising as they show how our model could be used to develop a more precise treatment scheduling, ensuring RT is given during periods of higher radiosensitivity.

The results shown in Fig. 6.4 and Fig. 6.5 lead also to the conclusion that the higher the reductive effect on hypoxia, the higher the therapy gain. This not only agrees with findings reported in [63] but also highlights the importance of accounting for hypoxia and angiogenesis when modelling tumour growth and response to therapy. The model developed by Titz and Jeraj [89] also allowed for this hypoxic effect to be taken into account. However, the fact that in their approach each tumour cell is simulated individually renders the applicability of their model to the clinical not practicable.

Future work should include data with anti-angiogenic and radio-therapy to allow for calibration of the model. For instance, such data would allow calibration of the parameter k_{Aa}, here assumed to be $k_{Aa} = 100/AUC$ (see 6.1). Ultimately, this could lead to a tool not only able to estimate tumour response to different RT schedules and dosing but also to estimate the optimal time point to start combination therapy and hence to improve overall therapy outcome.

In this chapter we have presented a model of vascular tumour growth and reaction to therapy. The results achieved with this model are promising and can serve as proof of concept that models like these can be used as a potential aid in therapy planning. This model opens a myriad of avenues to be explored in the future, especially due to the increase in the availability of medical imaging based data. In the next chapter we will suggest some of the avenues that could be explored in the hope that this model can be improved even more, and hence be ultimately translated into the clinic.

Chapter 7

Conclusions and Future Work

7.1 Conclusions

The work presented in this thesis aimed to develop new methodologies to model solid tumour growth and reaction to therapy, which provide a framework for the integration of biological information extracted from medical anatomic and metabolic imaging. These methodologies are of great clinical interest, as they can integrate and quantify the various processes involved in tumour growth; but more importantly, they have the potential to enable the prediction of outcomes, and the selection and development of therapy schedules.

This thesis explores various models that can serve as pragmatic solutions to relevant clinical questions around cancer management, such as how a tumour will evolve if left untreated or what is the best treatment schedule for a specific patient regarding irradiation, anti-angiogenic therapy or a combination of both. While each model needs to be considered within its own context - with each chapter containing comprehensive discussion, comparison to current literature and conclusions, - collectively they form a wider narrative: an imaginary yellow brick road toward the long-sought objective of using patient-specific clinical medical

imaging data to predict cancer growth and treatment response.

Starting with the avascular case, we first demonstrated that it is possible to use cellularity maps derived from quantitative imaging analysis to feed a model of tumour growth to obtain predictions of tumour evolution (see Chapters 3 and 4). Using synthetic data, we were able to accurately predict future tumour growth, manifested in small volume errors and large Dice values, as compared to other studies [15], showing that the model *per se* is already a contribution to the field. A step towards a personalised prediction of tumour growth was presented in Chapter 4, in which we have developed and introduced a novel way of parametrising a model of avascular tumour growth using cellularity maps derived from a set of longitudinal DCE-MRI images of preclinical breast carcinoma. The results demonstrated the feasibility of using maps of cellularity to feed and calibrate tumour growth models to obtain subject-specific predictions of tumour evolution.

Although the results obtained in Chapters 3 and 4 were promising, the higher errors observed when the avascular model was applied to real data suggested that this model provided an incomplete description of tumour growth. This raised the question of whether including angiogenesis in the model would provide a more complete formulation and hence result in better growth predictions. To test this hypothesis, in Chapter 5, we developed and evaluated a model of vascular tumour growth. Vascularisation was taken into account in an indirect yet pragmatic way by focusing on the macroscopic changes that can be observed longitudinally on medical imaging scans due to angiogenesis, rather than following the migration of each endothelial cell as a response to TAF excretion and diffusion. Adding angiogenesis to the model not only produced more realistic results in terms of smaller volume errors and larger DICE values, but also in terms of local cellularity

predictions. The capability of accurately estimating vascular tumour growth at the local level is a major contribution of this thesis and provided encouragement to explore whether this vascular model of tumour growth could be expanded to account for tumour's response to therapeutic schemes.

The fact that the model of Chapter 5 included hypoxia-driven angiogenesis allowed us not only to expand the model to account for different radiotherapy schemes, but also to investigate whether by normalising the vasculature and reducing hypoxia we could observe an effect on radiotherapy outcome. The results presented in Chapter 6 served as a proof of concept that our updated model has the potential to serve as a valuable tool to support medical decision in the treatment and management of cancer patients.

All of our models are able to account for complex microscopic biological processes such as cell proliferation, hypoxia, necrosis, oxygenation, nutrient supply and molecular signals emitted by tumour cells, while retaining simplicity in terms of the number of parameters that require calibration. We consider this to be an advantage of our approach when compared to the ones available in the literature which are either too complex, relying on parameters that are difficult to measure in an intact living system and cannot be observed in medical images [5, 6, 7, 8]; or are too simplistic, focusing on tumour invasion and morphology without accounting for the biological processes underlying tumour growth [10, 11, 12, 13, 14, 16, 17, 15].

The cellularity maps used as input for all models represent in themselves an important contribution. To the best of our knowledge, this was the first attempt to quantify the number of proliferative, hypoxic and necrotic cells based only on DCE-MRI quantities. As such, the maps not only serve as input to tumour growth models but also as tumour descriptors that can be used amongst other

things as an aid to register images of subsequent time points over the tumour growth cycle, as we have demonstrated in a previous work [152].

By their straight-forward nature and promising results, these models open a myriad of avenues to be explored in the future. Nevertheless, in order to use them to predict cancer progression and treatment response on the basis of patient-specific clinical data, some limitations of the current methodologies will need to be overcome. In the next section, we suggest possible ways of doing so, in the hope that our models can realise their full potential.

7.2 Future Work

Next, we present recommendations for future work to improve the models' prediction accuracy, taking it a step forward in the direction of personalised medicine. We set out three categories in which future work could be undertaken. First, we suggest a possible way to increase confidence in the model's ability to predict the number of cells, by validation of the DCE-MRI based maps of tumour descriptors. Second, although our current model is constrained by a single modality (DCE-MRI), it does not mean that it is not extendible to other imaging modalities. We therefore suggest possible quantities that can be extracted from other imaging modalities to further personalise the model and potentially improve its prediction power. Finally, we suggest ways to expand the model of tumour reaction to therapy to account for important aspects known to influence treatment as well as how the model can be explored to aid radiotherapy planning.

Validating DCE-MRI based maps

DCE-MRI can be used to estimate parameters such as blood flow, volume of distribution and permeability of the vessels. In our models, cells proliferate, turn hypoxic or die depending either on the local oxygen level (delivered to tumour cells depending on the blood flow or/and permeability) or on the volume of distribution. Our proposed framework therefore links maps generated based on DCE-MRI to measurements of cellularity, proliferation, hypoxia, necrosis and vascularisation. The calibration process could, for instance, be extended by examining the match between the modelled and observed total numbers of proliferative, hypoxic and necrotic tumour cells; and vascular volume as well as total tumour volume. This more detailed calibration might allow individual fitting of more model parameters.

Given the novelty of our approach, in the future, these maps of cellularity and vascularisation should be validated against a ground truth. One way of validating these maps would be to perform histopathological/immunohistochemical staining at sacrifice, which could then be correlated with the maps extracted from the DCE-MRI data at the last longitudinal time point. Some of the possible staining analyses that could be performed to assess each of the processes stated above are listed below:

1. Tumour cellularity (cell density) could be assessed using nuclei staining (Hematoxylin and Eosin for cell counting) as proposed by [30].

2. Proliferation could be assessed through the labelling index of the antigen Ki-67, which can serve as a marker to determine the growth fraction of a given cell population [153, 154].

3. Hypoxia could be measured using 2-nitroimidazole agent EF5. One of the

advantages of EF5 over other hypoxia markers is that the resultant images used to provide absolute oxygen levels (e.g. pO_2 values) in cells and tissues [155].

4. Necrotic cells can be stained using Annexin V along with propidium iodide [156].

5. Vasculature could be assessed by:

   - Counting of intratumoural microvessel density (MVD) using immunostaining with anti-CD34 [112];
   - Using the Hoechst 33342 dye, a DNA-binding fluorescent stain which has been employed extensively as an *in vivo* marker of functional tumour vasculature [157].

Alternatively, some of these processes could be assessed using additional imaging modalities, which could lead to proportionality constants to be added to the relationship between 1) number of cells and the volume of distribution (Eq. 4.7; 2) maximum enhancement peak and proliferation (Eq. 4.8); and 3) flow and necrosis (Eq. 4.9). Some of the possible imaging modalities that could be included are:

1. Tumour cellularity could be assessed using DWI [26, 23];

2. Proliferation could be assessed using [18F]-FLT PET and tranformed into a quantitative measure as suggested by [89];

3. Hypoxia map could be obtained using 18F-fluoromisonidazole (FMISO) PET [26, 158];

4. Necrotic cells can be quantified by Gadophrin-3-enhanced T1-weighted images [159];

5. Vasculature could be assessed by Magnetic resonance elastography (MRE) in combination with DWI [160].

Adding information from other imaging modalities

Multi-modal information could not only help in the validation of the DCE-MRI based maps, but could also be used as model input in the absence of DCE-MRI data or as a means to further improve model predictions. In this section, we would therefore like to suggest ways by which our models could be expanded to accommodate complementary information on the microenvironment and on the surroundings of the tumour extracted from various imaging modalities.

Mechanical properties of the tumour and its surrounding

As the tumour cellularity increases with respect to time, the tumour naturally tends to expand outward. However, the surrounding biochemical and mechanical environment of the host tissue exerts an inhibiting force upon the growing tumour, which is dependent upon the surrounding environment. In the future, mechanical properties (such as stiffness, stress, pressure and elasticity) of the host tissue (e.g. brain) should be included in the model.

Magnetic resonance elastography provides a way of extracting such properties due to its ability to non-invasively and quantitatively assess tissue stiffness. The resulting maps of stiffness could, for instance, represent the resistance of the tissue to deformation and displacement by an expanding tumour; or be used to compute maps of the complex shear modulus [129, 160]. Both metrics could inform the model about the preferred direction of cell invasion into the host tissue; namely, the one of least resistance.

Alternatively, expansive pressure, $P(t)$, could be assessed using the relationship suggested in [129], $P(t) = N(t)/V(t)$, where $N(t)$ and $V(t)$ are the total cell number and the tumour volume occupied currently by the tumour, respectively. This is global value does not take tumour heterogeneity into account. A more heterogeneous metric could be obtained using the tumour interstitial fluid pressure ($TIFP$), which can be derived from DCE-MRI parameters [161]. Such an interstitial fluid pressure map could be used to drive the diffusion law introduced in this thesis, so that the local cellularity measure, $r(\mathbf{x}, \mathbf{t})$, in $D(\mathbf{x}, t) = D_0 \exp(-r(\mathbf{x}, t)/\kappa)$, would be replaced by $TIFP(\mathbf{x}, \mathbf{t})$.

For the specific case of gliomas, MRI diffusion tensor imaging (DTI) can be used to determine the 3D geometry of white matter tracts. Glioma cells are known to spread along fibre tracts of the white matter, so therefore DTI data have the potential to provide information on the anisotropic diffusion of glioma cells [11]. To implement DTI data into the reaction-diffusion model it is necessary to replace D by a second order tensor $\boldsymbol{D}$, as suggested by [11].

Accounting for these mechanical properties individually or collectively might ultimately improve the morphological prediction of finger-shaped tumours, like the ones seen in Cases 2 and 4 (Chapter 5).

Tumour microenvironment

Cells under hypoxic conditions need to derive their energy from glycolysis, which results in lactic acid production and consequently, in an acidic extracellular pH (pHe) in tumours. The pHe can be the cause of transformation, mutation and angiogenesis [162]. Therefore, precise measurement of pHe *in vivo* not only has clinical value but could also be used in a future version of our models. For example, 31(P) Magnetic Resonance Spectroscopy (MRS) upon injection of exogenous

probes such as 3-aminopropylphosphonate (3-APP) could be used to measure this parameter *in vivo* [163].

In addition to increasing the pHe, acute hypoxia can also lead to necrosis. In our models we already account for this mechanism. However, this is not the only mechanism by which tumour cells die. Apoptosis is a naturally occurring programmed cell death, that can be included in a future version of our model of tumour growth.

For the case of avascular tumour growth, we have inspected whether accounting for apoptosis would increase prediction accuracy of the model. Our results demonstrated that increasing the number of parameters led to less accurate predictions, so we have chosen not to include apoptosis in the models presented in this thesis. In the future, input data could include information on apoptosis assessed by imaging or staining [164]. This would eliminate the need to optimise the cell loss rate due to apoptosis, potentially yielding for more accurate results in terms of predicted number of necrotic cells.

Throughout this thesis, we have stressed the importance of pO_2 to tumour growth and response to therapy, and hence to models of tumour growth. Most studies derive the pO_2 map from PET-Scans using markers such as [61Cu]Cu-ATSM known to accumulate in hypoxic regions [89]. However, this method of pO_2 map generation has two main disadvantages: the low spatial resolution of PET and the fact that it requires injection of a radioactive isotope.

To overcome these disadvantages, one could in the future extract the pO_2 map through DCE-MRI. Using the relationship derived in [165] between pO_2 and the microvessel density (MVD) and assuming that v_D is directly related to MVD, yields:

$$pO_2(v_D(\mathbf{x},t)) = \frac{60 \cdot (K_{pO_2} \cdot v_D(\mathbf{x},t))^{1.95}}{(K_{pO_2} \cdot v_D(\mathbf{x},t))^{1.95} + 0.015^{1.95}} \tag{7.1}$$

where K_{pO_2} is the proportionality constant. Matsumoto *et al.*, using Overhauser enhanced MRI (OMRI), developed a non-invasive imaging modality able to simultaneously acquire quantitative information on pO_2 and microvascular permeability. If the relationship between the microvascular permeability assessed by OMRI and by DCE-MRI could be stated, one could obtain a direct mapping between pO_2 (assessed via OMRI) and v_D (assessed by DCE-MRI), and use the data to calibrate K_{pO_2}.

Expanding the model of tumour response to therapy

As mentioned earlier, pO_2 availability to cells is not only crucial to promote tumour growth but has a considerable impact on therapy outcome. Treatment failure in radiotherapy due to hypoxia can be attributed primarily to the decreased sensitivity of hypoxic tumour cells to ionising radiation. In our model of tumour reaction to therapy, we have adopted the approach introduced by Stamatakos *et al.*, which incorporates the effects of oxygen status to the sensitivity parameters depending on whether cells were proliferative or hypoxic [21]. We have assumed the that this protective effect of hypoxia on cells against radiation, generally expressed as the oxygen enhancement ratio (OER), was spatially constant.

Spatial dependence could be added using an alternative approach like the one adopted in [166]. To quantify reductions in radiosensitivity parameters, the authors introduced a hypoxia reduction factor HRF as a function of the oxygen partial pressure $p(r)$, which in turn was expressed as a function of radial distance r. The HRF was defined "as the ratio of the dose at a specific level of hypoxia to the dose under fully aerobic conditions to achieve equal cell killing" and was computed using [166]:

$$HRF(p(r)) = \frac{mK + p(r)}{K + p(r)}, \tag{7.2}$$

where m and K represent the maximum HRF and the pO_2 at which HRF is half the maximum value, respectively. They assumed HRF to be at its maximum for anoxic conditions with a value of 2.8 and to decrease to 1 as the cells near normoxic conditions.

If a map of pO_2 were available (e.g. from PET or OMRI), then $HRF(p(r))$ could be transformed into $HRF(pO_2(\mathbf{x}, t))$ and hence a local (voxel-wise) effect of hypoxia on the survival curve could be obtained. The updated, local survival curve would read:

$$S(\mathbf{x}, t) = exp[-(\alpha_p / HRF(pO_2(\mathbf{x}, t))) \cdot d - (\beta_p / HRF(pO_2(\mathbf{x}, t))^2) \cdot d^2], \tag{7.3}$$

where α_p and β_p are the radiosensitivity parameters for normoxic (proliferative) conditions, and d a single fraction of radiation dose.

Aiding radiotherapy planning

Maps like the ones introduced in this thesis and the ones discussed above could aid adaptive radiotherapy by informing on or predicting temporal changes in tumour anatomy (e.g. tumour growth and shrinkage), biology or function (e.g. hypoxia, proliferation). This could for instance enable care-givers to customise the radiation dose by varying the amount of radiation given to different parts of the area being treated. Such a customisation is even more likely if we consider how image-guided radiation therapy has vastly improved the management of geometric

uncertainties in radiotherapy practice [167].

A model-driven dosing plan has not only the potential to increase precision, accuracy and outcome of RT but also to reduce toxicity of healthy tissue. This opens the possibility for safe dose escalation, increasing the clinical interest in single dose and hypo-fractionated regimens. However, for hypo-fractionation treatments with larger doses, the LQ-model underestimates the surviving fraction $S(d)$. Therefore, to simulate the reaction to higher radiation doses other models should be explored. For instance, one could use the linear-quadratic-linear (LQ-L) formulation, which has been found to better fit the experimental data across a wider dose range [168, 141].

With appropriate additional imaging information, the modelling framework presented throughout this thesis could become even more relevant to clinical practice. Modellers and clinical practitioners need to collaborate on experimental design, and implement a feedback loop that enables at once the use of personalised data to constrain the models, and the validation of the models based on direct comparison of predictions with clinical outcomes. Whether the vision of predicting the therapy outcome for each individual patient will become a reality is largely dependent on how successfully imaging scientists, clinicians and modellers can take on this challenge.

References

[1] "World health organization, cancer fact sheet, february 2018." http://www.who.int/mediacentre/factsheets/fs297/en/. Accessed: 2018-04-14. iii, 1, 9

[2] B. W. Stewart and C. P. Wild, "World cancer report 2014," tech. rep., 2014. 1, 9

[3] "The economics of cancer presvention and control, 2014." http://issuu.com/uicc.org/docs/wcls2014_economics_of_cancer_final?e=10430107/10454633. Accessed: 2018-05-02. 1

[4] D. Hanahan, R. a. Weinberg, and S. Francisco, "The Hallmarks of Cancer Review," *Cell*, vol. 100, pp. 57–70, 2000. 2, 10, 11, 12, 72, 146

[5] M. E. Orme and M. A. J. Chaplain, "A Mathematical Model of Vascular Tumour Growth and Invasion," *Mathl. Comput. Modelling*, vol. 23, no. 10, pp. 43–60, 1996. 3, 41, 210

[6] H. M. Byrne and M. Chaplain, "Apoptosis and necrosis as distinct cell loss mechanisms in avascular tumour growth," vol. 1, pp. 223–235, 1998. 3, 41, 176, 210

[7] J. A. Sherratt and M. A. J. Chaplain, "Mathematical biology a new math-

ematical model for avascular tumour growth," vol. 312, pp. 291–312, 2001. 3, 41, 68, 70, 110, 210

[8] V. Cristini and J. Lowengrub, *Multiscale Modeling of Cancer: An Integrated Experimental and Mathematical Modeling Approach*. Cambridge University Press, 2010. 3, 41, 69, 147, 210

[9] A.-S. Qi, X. Zheng, D. Chan-Ying, and B.-S. An, "A Cellular Automaton Model of Cancerous Growth," *Journal of Theoretical Biology*, vol. 161, pp. 1–12, 1993. 3

[10] K. R. Swanson, C. Bridge, J. Murray, and E. C. Alvord, "Virtual and real brain tumors: using mathematical modeling to quantify glioma growth and invasion," *Journal of the Neurological Sciences*, vol. 216, pp. 1–10, Dec. 2003. 3, 4, 45, 63, 69, 90, 113, 153, 210

[11] S. Jbabdi, E. Mandonnet, H. Duffau, L. Capelle, K. R. Swanson, M. Pélégrini-Issac, R. Guillevin, and H. Benali, "Simulation of anisotropic growth of low-grade gliomas using diffusion tensor imaging.," *Magnetic Resonance in Medicine*, vol. 54, pp. 616–624, Sept. 2005. 3, 44, 45, 63, 67, 69, 100, 101, 174, 210, 215

[12] O. Clatz, M. Sermesant, P. Y. Bondiau, H. Delingette, S. K. Warfield, G. Malandain, and N. Ayache, "Realistic simulation of the 3-D growth of brain tumors in MR images coupling diffusion with biomechanical deformation," *IEEE Transactions on Medical Imaging*, vol. 24, no. 10, pp. 1334–1346, 2005. 3, 4, 44, 45, 53, 54, 63, 69, 99, 101, 135, 137, 173, 174, 192, 210

[13] C. Hogea, C. Davatzikos, and G. Biros, "An image-driven parameter estimation problem for a reaction-diffusion glioma growth model with mass

effects," *Journal of Mathematical Biology*, vol. 56, pp. 793–825, 2008. 3, 45, 69, 210

[14] P. Tracqui, "Biophysical models of tumour growth," *Reports on Progress in Physics*, vol. 72, p. 056701, May 2009. 3, 45, 69, 210

[15] D. Hormuth, J. Weis, S. Barnes, M. Miga, E. Rericha, V. Quaranta, and T. Yankeelov, "Predicting in vivo glioma growth with the reaction diffusion equation constrained by quantitative magnetic resonance imaging data," *Physical Biology*, vol. 12, no. 4, p. 046006, 2015. 3, 45, 63, 81, 85, 99, 135, 136, 137, 154, 172, 173, 192, 209, 210

[16] K. R. Swanson, R. C. Rockne, J. Claridge, M. A. Chaplain, E. C. Alvord, and A. R. A. Anderson, "Quantifying the role of angiogenesis in malignant progression of gliomas: in silico modeling integrates imaging and histology.," *Cancer research*, vol. 71, no. 24, pp. 7366–75, 2011. 3, 48, 63, 99, 135, 137, 146, 148, 154, 173, 174, 192, 205, 210

[17] E. Konukoglu, O. Clatz, B. H. Menze, M.-A. Weber, B. Stieltjes, E. Mandonnet, H. Delingette, and N. Ayache, "Image Guided Personalization of Reaction-Diffusion Type Tumor Growth Models Using Modified Anisotropic Eikonal Equations," *IEEE Transactions on Medical Imaging*, vol. 29, no. 1, pp. 77–95, 2010. 3, 63, 69, 85, 90, 113, 137, 153, 154, 173, 210

[18] J. M. Murray, "Optimal Drug Regimens in Cancer Chemotherapy for Single Drugs that Block Progression through the Cell Cycle," vol. 193, pp. 183–193, 1994. 3, 42, 67

[19] B. Titz and R. Jeraj, "An imaging-based tumour growth and treatment response model: investigating the effect of tumour oxygenation on radiation

therapy response," *Physics in Medicine and Biology*, vol. 53, pp. 4471–4488, Sept. 2008. 3, 4, 99

[20] B. Titz, K. R. Kozak, and R. Jeraj, "Computational modelling of anti-angiogenic therapies based on multiparametric molecular imaging data," *Physics in Medicine and Biology*, vol. 57, no. 19, pp. 6079–6101, 2012. 3, 4, 100

[21] G. S. Stamatakos, V. P. Antipas, and N. K. Uzunoglu, "A spatiotemporal,patient individualized simulation model of solid tumor response to chemotherapy in vivo: The paradigm of glioblastoma multiforme treated by temozolomide," *IEEE Trans Biomed Eng*, vol. 53, no. 8, pp. 1467–1477, 2006. 3, 5, 55, 57, 61, 63, 80, 99, 102, 177, 178, 218

[22] M. D. Szeto, G. Chakraborty, J. Hadley, R. Rockne, M. Muzi, E. C. Alvord, K. a. Krohn, A. M. Spence, and K. R. Swanson, "Quantitative metrics of net proliferation and invasion link biological aggressiveness assessed by MRI with hypoxia assessed by FMISO-PET in newly diagnosed glioblastomas.," *Cancer research*, vol. 69, pp. 4502–9, May 2009. 4, 46, 69, 101

[23] N. C. Atuegwu, L. R. Arlinghaus, X. Li, A. B. Chakravarthy, V. G. Abramson, M. E. Sanders, and T. E. Yankeelov, "Parameterizing the Logistic Model of Tumor Growth by DW-MRI and DCE-MRI Data to Predict Treatment Response and Changes in Breast Cancer Cellularity during Neoadjuvant Chemotherapy," *Translational Oncology*, vol. 6, pp. 256–264, June 2013. 4, 5, 58, 69, 102, 192, 213

[24] V. P. Antipas *et al.*, "A spatio-temporal simulation model of the response of solid tumours to radiotherapy in vivo : parametric validation concerning

oxygen enhancement ratio and cell cycle duration," *Physics in Medicine and Biology*, vol. 49, no. 8, pp. 1485–1504, 2004. 5, 47

[25] B. M. Ellingson, T. F. Cloughesy, A. Lai, P. L. Nghiemphu, and W. B. Pope, "Cell invasion, motility, and proliferation level estimate (cimple) maps derived from serial diffusion mr images in recurrent glioblastoma treated with bevacizumab," *Journal of Neuro-Oncology*, vol. 105, no. 1, pp. 91–101, 2011. 5, 59, 61, 102

[26] N. C. Atuegwu, J. C. Gore, and T. E. Yankeelov, "The integration of quantitative multi-modality imaging data into mathematical models of tumors," *Physics in medicine and biology*, vol. 55, pp. 2429–2449, 2010. 5, 49, 61, 100, 102, 213

[27] T. E. Yankeelov, N. Atuegwu, D. Hormuth, J. A. Weis, S. L. Barnes, M. I. Miga, and E. C. Rericha, "Clinically relevant modeling of tumor growth and treatment response," vol. 5, no. 187, pp. 1–5, 2013. 5, 48, 61, 71, 102, 176

[28] P. S. Tofts, G. Brix, D. L. Buckley, J. L. Evelhoch, E. Henderson, M. V. Knopp, H. B. Larsson, T.-Y. Lee, N. A. Mayr, G. J. Parker, R. E. Port, J. Taylor, and R. M. Weisskoff, "Estimating kinetic parameters from dynamic contrast-enhanced t1-weighted mri of a diffusable tracer: Standardized quantities and symbols," *Journal of Magnetic Resonance Imaging*, vol. 10, no. 3, pp. 223–232, 1999. 5, 31, 103, 106

[29] R. Venkatasubramanian, R. B. Arenas, M. a. Henson, and N. S. Forbes, "Mechanistic modelling of dynamic MRI data predicts that tumour heterogeneity decreases therapeutic response.," *British journal of cancer*, vol. 103, pp. 486–497, Aug. 2010. 5

[30] M. P. Aryal, T. N. Nagaraja, K. a. Keenan, H. Bagher-Ebadian, S. Panda, S. L. Brown, G. Cabral, J. D. Fenstermacher, and J. R. Ewing, "Dynamic contrast enhanced MRI parameters and tumor cellularity in a rat model of cerebral glioma at 7 T.," *Magnetic resonance in medicine*, vol. 71, pp. 2206–14, June 2014. 5, 109, 212

[31] D. Hanahan and R. A. Weinberg, "Hallmarks of cancer: The next generation," *Cell*, vol. 144, pp. 646–674, 2011. 10, 12

[32] R. J. Gillies, N. Raghunand, G. S. Karczmar, and Z. M. Bhujwalla, "MRI of the tumor microenvironment.," *Journal of magnetic resonance imaging : JMRI*, vol. 16, pp. 430–50, Oct. 2002. 12, 31

[33] M. Brady, R. Highnamb, B. Irving, and J. A. Schnabel, "Oncological image analysis," *Medical Image Analysis*, vol. 33, pp. 7–12, 2016. 13

[34] M. E. Van Dort, A. Rehemtulla, and B. D. Ross, "Pet and spect imaging of tumor biology: New approaches towards oncology drug discovery and development," *Current Computer-Aided Drug Design*, vol. 4, no. 1, pp. 46–53, 2008. 14

[35] J. Czernin, "Clinical applications of fdgpet in oncology," *Acta Medica Austriaca*, vol. 29, no. 5, pp. 162–170, 2002. 14

[36] D. Mankoff, A. F. Shields, and K. A. Krohn, "Pet imaging of cellular proliferation," *Radiologic Clinics of North America*, vol. 43, no. 1, pp. 153–167, 2005. 14

[37] J. Overgaard, "Hypoxic radiosensitization: Adored and ignored," *Journal of Clinical Oncology*, vol. 25, no. 26, pp. 4066–4074, 2007. 15

[38] G. N. Hounsfield, "Computed medical imaging," *Medical Physics*, vol. 7, no. 4, pp. 283–290. 16

[39] T.-Y. Lee, "Functional ct: physiological models," *Trends in Biotechnology*, vol. 20, no. 8, pp. 3–9. 17

[40] K. Miles, "Functional computed tomography in oncology," *European Journal of Cancer*, vol. 38, no. 16, pp. 2079 – 2084, 2002. 17

[41] P. C. Lauterbur, "Image formation by induced local interactions: Examples employing nuclear magnetic resonance," *Nature*, vol. 242, pp. 190–191, 1973. 17

[42] M. A. Brown and R. C. Semelka, *MRI Basic Principles and Applications*. Wiley-Liss, 2003. 18

[43] D. Patterson, A. R. Padhani, and D. J. Collins, "Technology insight: water diffusion mri: a potential new biomarker of response to cancer therapy," *Nature Clinical Practice Oncology*, vol. 5, pp. 220–233, 2008. 24, 25

[44] G. J. M. Parker, "Analysis of mr diffusion weighted images," *The British Journal of Radiology*, vol. 77, no. suppl_2, pp. S176–S185, 2004. 24

[45] T. E. Yankeelov, "Integrating Imaging Data into Predictive Biomathematical and Biophysical Models of Cancer.," *ISRN biomathematics*, vol. 2012, 2012. 24, 26

[46] S. Bonekamp, C. P. CoronaVillalobos, and I. R. Kamel, "Oncologic applications of diffusion weighted mri in the body," *Journal of Magnetic Resonance Imaging*, vol. 35, no. 2, pp. 257–279, 2012. 24, 25

[47] E. R. Gerstner and A. G. Sorensen, "Diffusion and diffusion tensor imaging

in brain cancer," *Seminars in Radiation Oncology*, vol. 21, no. 2, pp. 141 – 146, 2011. 25, 26, 27

[48] A. Anderson, J. Xie, J. Pizzonia, R. Bronen, D. Spencer, and J. Gore, "Effects of cell volume fraction changes on apparent diffusion in human cells," *Magnetic Resonance Imaging*, vol. 18, no. 6, pp. 689 – 695, 2000. 25

[49] P. Basser, J. Mattiello, and D. LeBihan, "Mr diffusion tensor spectroscopy and imaging," *Biophysical Journal*, vol. 66, no. 1, pp. 259 – 267, 1994. 26

[50] S. Mori and P. C. M. van Zijl, "Fiber tracking: principles and strategies a technical review," *NMR in Biomedicine*, vol. 15, no. 78, pp. 468–480, 2002. 26

[51] D. Leclercq, C. Delmaire, N. M. de Champfleur, J. Chiras, and S. Lehricy, "Diffusion tractography: Methods, validation and applications in patients with neurosurgical lesions," *Neurosurgery Clinics*, vol. 22, no. 2, pp. 253 – 268, 2011. 27

[52] S. Mori and J. Zhang, "Principles of diffusion tensor imaging and its applications to basic neuroscience research," *Neuron*, vol. 51, no. 5, pp. 527 – 539, 2006. 27

[53] B. Rosen, J. W. Belliveau, J. Vevea, and T. Brady, "Perfusion imaging with nmr contrast agents.," *Magnetic resonance in medicine*, vol. 14 2, pp. 249–65, 1990. 28

[54] R. Weisskoff, C. S. Zuo, J. L. Boxerman, and B. R. Rosen, "Microscopic susceptibility variation and transverse relaxation: Theory and experiment," *Magnetic Resonance in Medicine*, vol. 31, no. 6, pp. 601–610, 1994. 28

[55] G.-H. Jahng, G.-H. Li, L. Ostergaard, and F. Calamante, "Perfusion magnetic resonance imaging: A comprehensive update on principles and techniques," *Korean Journal of Radiology*, vol. 15, pp. 554–577, 2014. 28, 29, 31

[56] L. stergaard, R. M. Weisskoff, D. A. Chesler, C. Gyldensted, and B. R. Rosen, "High resolution measurement of cerebral blood flow using intravascular tracer bolus passages. part i: Mathematical approach and statistical analysis," *Magnetic Resonance in Medicine*, vol. 36, no. 5, pp. 715–725, 1996. 29, 31, 106

[57] P. Meier and K. L. Zierler, "On the theory of the indicator-dilution method for measurement of blood flow and volume," *Journal of Applied Physiology*, vol. 6, no. 12, pp. 731–744, 1954. 29

[58] B. K. L. Zierler, "Circulation Research," vol. XVI, no. 4, pp. 309–322, 1965. 29

[59] S. P. Sourbron and D. L. Buckley, "Classic models for dynamic contrast-enhanced MRI," *NMR in Biomedicine*, vol. 26, no. February, pp. 1004–1027, 2013. 30, 31, 32, 107, 139

[60] G. J. M. Parker, J. Suckling, S. F. Tanner, A. R. Padhani, P. B. Revell, J. E. Husband, and M. O. Leach, "Probing tumor microvascularity by measurement, analysis and display of contrast agent uptake kinetics," *Journal of Magnetic Resonance Imaging*, vol. 7, no. 3, pp. 564–574, 1997. 31, 106

[61] F. Khalifa, A. Soliman, A. El-Baz, M. Abou El-Ghar, T. El-Diasty, G. Gimel'farb, R. Ouseph, and A. C. Dwyer, "Models and methods for analyzing DCE-MRI: a review.," *Medical physics*, vol. 41, p. 124301, Dec. 2014. 31

[62] T. E. Yankeelov and J. C. Gore, "Dynamic contrast enhanced magnetic resonance imaging in oncology: Theory, data acquisition, analysis, and examples," *Current Medical Imaging Reviews*, vol. 3, p. 91107, 2009. 31

[63] R. P. Dings, M. Loren, H. Heun, E. McNiel, A. W. Griffioen, K. H. Mayo, and R. J. Griffin, "Scheduling of radiation with angiogenesis inhibitors anginex and avastin improves therapeutic outcome via vessel normalization," *Clinical Cancer Research*, vol. 13, no. 11, pp. 3395–3402, 2007. 32, 39, 40, 179, 187, 193, 197, 206

[64] P. Price and K. Sikora, *Treatment of Cancer Sixth Edition*. CRC Press, 2014. 32, 39

[65] G. Barnett, C. West, A. Dunning, R. Elliott, C. Coles, P. Pharoah, and N. Burnet, "Normal tissue reactions to radiotherapy: Towards tailoring treatment dose by genotype," *Nature Reviews Cancer*, vol. 9, pp. 134–142, 2 2009. 33, 176

[66] O. F. Nygaard, H. I. Adler, and W. K. Sinclair, *Radiation Research*. Academic Press, San Diegp, 1975. 34

[67] "The four r's of radiotherapy," vol. 5 of *Advances in Radiation Biology*, pp. 241 – 271, Elsevier, 1975. 35

[68] G. G. Steel, T. McMillan, and J. Peacock, "The 5rs of radiobiology," *International Journal of Radiation Biology*, vol. 56, no. 6, pp. 1045–1048, 1989. 35, 36

[69] J. A. McKnight, "Principles of chemotherapy," *Clinical Techniques in Small Animal Practice*, vol. 18, no. 2, pp. 67 – 72, 2003. Medical Oncology. 37, 38

[70] R. K. Jain, "Normalization of tumor vasculature: An emerging concept in antiangiogenic therapy," *Science*, vol. 307, no. 5706, pp. 58–62, 2005. 39, 178, 179

[71] D. Lambrechts, H.-J. Lenz, S. de Haas, P. Carmeliet, and S. J. Scherer, "Markers of response for the antiangiogenic agent bevacizumab," *Journal of Clinical Oncology*, vol. 31, no. 9, pp. 1219–1230, 2013. 39, 41

[72] R. Hlushchuk, O. Riesterer, O. Baum, J. Wood, G. Gruber, M. Pruschy, and V. Djonov, "Tumor recovery by angiogenic switch from sprouting to intussusceptive angiogenesis after treatment with ptk787/zk222584 or ionizing radiation," *The American Journal of Pathology*, vol. 173, no. 4, pp. 1173 – 1185, 2008. 39, 40

[73] J. A. Delgado-SanMartin, J. I. Hare, A. P. S. de Moura, and J. W. T. Yates, "Oxygen-driven tumour growth model: A pathology-relevant mathematical approach," *PLOS Computational Biology*, vol. 11, pp. 1–20, 2015. 41

[74] P. Tracqui, G. C. Cruywagen, D. E. Woodward, G. T. Bartoo, J. D. Murray, and E. C. Alvord, "A mathematical model of glioma growth: the effect of chemotherapy on spatio-temporal growth," *Cell Proliferation*, vol. 28, no. 1, pp. 17–31, 1995. 43

[75] K. R. Swanson, E. C. Alvord, and J. D. Murray, "A quantitative model for differential motility of gliomas in grey and white matter," *Cell Proliferation*, vol. 33, no. 5, pp. 317–329. 43

[76] K. R. Swanson, E. C. A. Jr, and J. D. Murray, "Virtual brain tumours (gliomas) enhance the reality of medical imaging and highlight inadequacies of current therapy," pp. 14–18, 2002. 43, 53, 56, 57, 59

[77] P.-Y. Bondiau, O. Clatz, M. Sermesant, P.-Y. Marcy, H. Delingette, M. Frenay, and N. Ayache, "Biocomputing: numerical simulation of glioblastoma growth using diffusion tensor imaging.," *Physics in medicine and biology*, vol. 53, pp. 879–93, Feb. 2008. 45

[78] C. Suarez, F. Maglietti, M. Colonna, K. Breitburd, and G. Marshall, "Mathematical modeling of human glioma growth based on brain topological structures: study of two clinical cases," *PloS one*, vol. 7, no. 6, pp. 1932–6203, 2012. 46

[79] G. S. Stamatakos, D. D. Dionysiou, E. I. Zacharaki, N. A. Mquravliansky, K. S. Nikita, and N. K. Uzunoglu, "In silico radiation oncology: Combining novel simulation algorithms with current visualization techniques," *Proceedings of the IEEE*, vol. 90, no. 11, pp. 1764–1777, 2002. 46, 62, 80, 99, 177, 178, 191

[80] O. Saut, J.-B. Lagaert, T. Colin, and H. M. Fathallah-Shaykh, "A multilayer grow-or-go model for gbm: Effects of invasive cells and anti-angiogenesis on growth," *Bulletin of Mathematical Biology*, vol. 76, no. 9, pp. 2306–2333, 2014. 47, 59

[81] A. M. Kellerer and H. H. Rossi, "Rbe and the primary mechanism of radiation action," *Radiation Research*, vol. 47, no. 1, pp. 15–34, 1971. 51, 180

[82] R. Rockne, J. K. Rockhill, M. Mrugala, A. M. Spence, I. Kalet, K. Hendrickson, T. Cloghesy, E. C. Alvors, and K. R. Swanson, "Predicting efficacy of radiotherapy in individual glioblastoma patients in vivo: a mathematical modeling approach," *Physics in Medicine and Biology*, vol. 55, no. 12, p. 32713285, 2010. 52, 189, 205

[83] R. Rockne, E. C. Alvord, J. K. Rockhill, and K. R. Swanson, "A mathematical model for brain tumor response to radiation therapy," *Journal of Mathematical Biology*, vol. 58, no. 4, pp. 561–578, 2008. 52, 189, 205

[84] B. H. Unkelbach, Janand Menze, E. Konukoglu, F. Dittmann, N. Ayache, and H. A. Shih, "Radiotherapy planning for glioblastoma based on a tumor growth model: implications for spatial dose redistribution," *Physics in Medicine and Biology*, vol. 59, no. 3, p. 771, 2014. 52

[85] E. Konukoglu, O. Clatz, H. Delingette, and N. Ayache, "Personalization of reaction-diffusion tumor growth models in mr images: Application to brain gliomas characterization and radiotherapy planning," in *Multiscale Cancer Modeling* (T. S. Deisboeck and G. Stamatakos, eds.), CRC Press, 2010. 54, 177, 203

[86] M. L, H. Delingette, J. Kalpathy-Cramer, E. R. Gerstner, T. Batchelor, J. Unkelbach, and N. Ayache, "Personalized radiotherapy planning based on a computational tumor growth model," *IEEE Transactions on Medical Imaging*, vol. 36, no. 3, pp. 815–825, 2017. 54

[87] D. D. Dionysiou, G. S. Stamatakos, N. K. Uzunoglu, K. S. Nikita, and A. Marioli, "A four-dimensional simulation model of tumour response to radiotherapy in vivo: Parametric validation considering radiosensitivity, genetic profile and fractionation," *Journal of Theoretical Biology*, vol. 230, pp. 1–20, 2004. 55, 177, 178, 195, 201

[88] D. D. Dionysiou and G. S. Stamatakos, "Applying a 4D multiscale in vivo tumor growth model to the exploration of radiotherapy scheduling: The effects of weekend treatment gaps and p53 gene status on the response of

fast growing solid tumors," *Cancer Informatics*, vol. 2, pp. 113–121, 2006. 55, 177, 178

[89] B. Titz and R. Jeraj, "An imaging-based tumour growth and treatment response model: investigating the effect of tumour oxygenation on radiation therapy response," *Physics in Medicine and Biology*, vol. 53, pp. 4471–4488, Sept. 2008. 55, 62, 178, 206, 213, 217

[90] T. Roque, L. Risser, V. Kersemans, S. Smart, D. Allen, P. Kinchesh, S. Gilchrist, A. L. Gomes, J. A. Schnabel, and M. A. Chappell, "A dce-mri driven 3-d reaction-diffusion model of solid tumor growth," *IEEE Transactions on Medical Imaging*, vol. 37, pp. 724–732, March 2018. 63, 103

[91] P. F. Verhulst, "Notice sur la loi que la population suit dans son accroissement," *Curr. Math. Phys*, vol. 10, pp. 113+, 1838. 66

[92] B. Gompertz, "On the nature of the function expressive of the law of human mortality, and on a new mode of determining the value of life contingencies," *Philosophical Transactions of the Royal Society of London*, vol. 115, pp. 513–583, 1825. 66

[93] H. Murphy, H. Jaafari, and H. M. Dobrovolny, "Differences in predictions of ode models of tumor growth: a cautionary example," *BMC Cancer*, vol. 16, no. 1, p. 163, 2016. 66

[94] J. Tannehill, D. Anderson, and R. Pletcher, *Computational Fluid Mechanics and Heat Transfer*. Taylor & Francis, 1997. 73, 76

[95] L. H. Thomas, "Elliptic problems in linear differential equations over a network," tech. rep., Columbia University, 1949. 73, 76, 78

[96] F. K. C. R. Lewy, H., "Ueber die partiellen differenzengleichungen der mathematischen physik," *Mathematische Annalen*, vol. 100, pp. 32–74, 1928. 74

[97] R. Courant, E. Isaacson, and M. Rees, "On the solution of nonlinear hyperbolic differential equations by finite differences," *Communications on Pure and Applied Mathematics*, vol. 5, no. 3, pp. 243–255, 1952. 75

[98] P. Vaupel and L. Harrison, "Tumor hypoxia: Causative factors, compensatory mechanisms, and cellular response," *The Oncologist*, vol. 9, no. suppl 5, pp. 4–9, 2004. 80

[99] I. P. Torres Filho, M. Leunig, F. Yuan, M. Intaglietta, and R. K. Jain, "Noninvasive measurement of microvascular and interstitial oxygen profiles in a human tumor in scid mice," *Proceedings of the National Academy of Sciences*, vol. 91, no. 6, pp. 2081–2085, 1994. 81

[100] K. R. Swanson, H. L. P. Harpold, D. L. Peacock, R. Rockne, C. Pennington, L. Kilbride, R. Grant, J. M. Wardlaw, and E. C. Alvord, "Velocity of radial expansion of contrast-enhancing gliomas and the effectiveness of radiotherapy in individual patients: a proof of principle.," *Clinical oncology (Royal College of Radiologists (Great Britain))*, vol. 20, pp. 301–8, May 2008. 81, 177, 203

[101] J. Pan, J.-F. Shang, G.-Q. Jiang, and Z.-X. Yang, "Ligustrazine induces apoptosis of breast cancer cells in vitro and in vivo," *Journal of Cancer Research and Therapeutics*, vol. 11, no. 2, pp. 454–458, 2015. 84

[102] M. Vakkala, K. Lähteenmäki, H. Raunio, P. Pääkkö, and Y. Soini, "Apoptosis during breast carcinoma progression," *Clinical Cancer Research*, vol. 5, no. 2, pp. 319–324, 1999. 84, 100

[103] S. Marino, I. Hogue, C. Ray, and D. Kirschner, "A methodology for performing global uncertainty and sensitivity analysis in systems biology.," *Journal of theoretical biology*, vol. 254 1, pp. 178–96, 2008. 86, 89, 150

[104] E. Mehrara, E. Forssell-Aronsson, H. Ahlman, and P. Bernhardt, "Specific growth rate versus doubling time for quantitative characterization of tumor growth rate," *Cancer Research*, vol. 67, no. 8, pp. 3970–3975, 2007. 86

[105] E. Mehrara, E. Forssell-Aronsson, H. Ahlman, and P. Bernhardt, "Quantitative analysis of tumor growth rate and changes in tumor marker level: Specific growth rate versus doubling time," *Acta Oncologica*, vol. 48, no. 4, pp. 591–597, 2009. 86, 120

[106] M. Rohrer, H. Bauer, J. Mintorovitch, M. Requardt, and H.-J. Weinmann, "Comparison of magnetic properties oof mri contrast media solutions at different magnetic field strengths," *Investigative Radiology*, vol. 40, no. 11, pp. 715–724, 2005. 107

[107] Y. Shen, F. Goerner, C. Snyder, J. Morelli, D. Hao, X. Lu, and V. Runge, "T1 relaxivities of gadolinium-based magnetic resonance constrast agents in human whole blood at 1.5, 3 and 7t," *Investigative Radiology*, vol. 50, no. 5, pp. 330–338, 2015. 107

[108] M. R. Orton, J. a. D'Arcy, S. Walker-Samuel, D. J. Hawkes, D. Atkinson, D. J. Collins, and M. O. Leach, "Computationally efficient vascular input function models for quantitative kinetic modelling using DCE-MRI.," *Physics in medicine and biology*, vol. 53, no. 5, pp. 1225–1239, 2008. 108

[109] M. Heilmann, C. Walczak, J. Vautier, J. L. Dimicoli, C. D. Thomas, M. Lupu, J. Mispelter, and A. Volk, "Simultaneous dynamic T1 and T2*

measurement for AIF assessment combined with DCE MRI in a mouse tumor model.," *Magma (New York, N.Y.)*, vol. 20, pp. 193–203, 2007. 108

[110] O. Wu, L. Ø stergaard, R. M. Weisskoff, T. Benner, B. R. Rosen, and a. G. Sorensen, "Tracer arrival timing-insensitive technique for estimating flow in MR perfusion-weighted imaging using singular value decomposition with a block-circulant deconvolution matrix.," *Magnetic Resonance in Medicine*, vol. 50, pp. 164–74, July 2003. 109

[111] K. L. Zierler, "Theoretical Basis of Indicator-Dilution Methods For Measuring Flow and Volume," *Circulation Research*, vol. 10, pp. 393–407, Mar. 1962. 109

[112] O. Fernández-Guinea, A. Andicoechea, L. O. González, S. González-Reyes, A. M. Merino, L. C. Hernández, A. López-Muniz, P. García-Pravia, and F. J. Vizoso, "Relationship between morphological features and kinetic patterns of enhancement of the dynamic breast magnetic resonance imaging and clinico-pathological and biological factors in invasive breast cancer," *BMC cancer*, vol. 10, p. 8, 2010. 109, 213

[113] S. Kirkpatrick, C. D. Gelatt, and M. P. Vecchi, "Optimization by simulated annealing," *Science*, vol. 220, no. 4598, pp. 671–680, 1983. 112, 149

[114] K. A. Christensen, D. M. Grant, E. M. Schulman, and C. Walling, "Optimal determination of relaxation times of fourier transform nuclear magnetic resonance. determination of spin-lattice relaxation times in chemically polarized species," *The Journal of Physical Chemistry*, vol. 78, no. 19, pp. 1971–1977, 1974. 115

[115] V. L. Yarnykh, "Actual flip-angle imaging in the pulsed steady state: A method for rapid three-dimensional mapping of the transmitted radiofre-

quency field," *Magnetic Resonance in Medicine*, vol. 57, no. 1, pp. 192–200, 2007. 116

[116] S. F. Parker, Geoffrey J. M.and Tanner and M. O. Leach, "Pitfalls in the measurement of tissue permeability over short time-scales using multi-compartment models with a low temporal resolution blood input function.," *Procedures 4th Annual Meeting ISMRM*, 1996. 139

[117] J. Folkman, "Tumor angiogenesis: therapeutic implications," *The New England Journal of Medicine*, vol. 285, pp. 1182–1186, 1971. 140, 143

[118] M. A. J. Chaplain and A. Anderson, "Mathematical modelling, simulation and prediction of tumour-induced angiogenesis.," *Invasion and Metastasis*, vol. 16 4-5, pp. 222–34, 1996. 141

[119] T. Alarcon, H. Byrne, P. Maini, and J. Panovska, "20 mathematical modelling of angiogenesis and vascular adaptation," in *Multidisciplinary Approaches to Theory in Medicine* (R. Paton and L. A. McNamara, eds.), vol. 3 of *Studies in Multidisciplinarity*, pp. 369 – 387, Elsevier, 2005. 141

[120] S. Pillay, H. M. Byrne, and P. K. Maini, "Modeling angiogenesis: A discrete to continuum description," *Phys. Rev. E*, vol. 95, p. 012410, Jan 2017. 141

[121] A. R. Anderson and M. A. Chaplain *Mathematical Biology*, vol. 60, pp. 857–899, 1998. 141

[122] Y. Cai, S. Xu, J. Wu, and Q. Long, "Coupled modelling of tumour angiogenesis, tumour growth and blood perfusion," *Journal of Theoretical Biology*, vol. 279, no. 1, pp. 90 – 101, 2011. 141

[123] J. Lyu, J. Cao, P. Zhang, Y. Liu, and H. Cheng, "Coupled hybrid

continuum-discrete model of tumor angiogenesisand growth," *Plos One*, vol. 10, no. 11, 2016. 141

[124] I. J. Stamper, H. M. Byrne, M. R. Owen, and P. K. Maini, "Modelling the role of angiogenesis and vasculogenesis in solid tumour growth," *Bulletin of Mathematical Biology*, vol. 69, no. 8, pp. 2737–2772, 2007. 141

[125] B. L. Krock, N. Skuli, and C. M. Simon, "Hypoxia-induced angiogenesis: Good and evil," *Genes and Cancer*, vol. 2, pp. 1117–1133, 2011. 143

[126] B. Muz, P. de la Puente, F. Azab, and A. K. Azab, "The role of hypoxia in cancer progression, angiogenesis, metastasis, and resistance to therapy," *Hypoxia*, vol. 3, pp. 83–92, 2015. 143

[127] W. F. Orr, M. R. Buchanan, and L. Weiss, *Microcirculation in Cancer Metastasis*. CRC Press, Inc, 1991. 143

[128] M. A. J. Chaplain and A. M. Stuart, "A mathematical model for the diffusion of tumour angiogenesis factor surrounding host tissue," *Journal of Mathematics Applied in Medicine and Biology*, vol. 8, pp. 191–220, 1991. 145

[129] R. Wasserman and R. Acharya, "A patient-specific in Vivo tumor model," *Mathematical biosciences*, 1996. 100, 174, 214, 215

[130] K. R. Swanson, G. Chakraborty, C. H. Wang, R. Rockne, H. L. P. Harpold, M. Muzi, T. C. H. Adamsen, K. a. Krohn, and A. M. Spence, "Complementary but distinct roles for MRI and 18F-fluoromisonidazole PET in the assessment of human glioblastomas.," *Journal of nuclear medicine*, vol. 50, pp. 36–44, Jan. 2009. 174, 177

[131] H. M. Byrne and M. a. J. Chaplain, "Growth of non-necrotic tumours in the presence and absence of inhibitors," *Math. Biosci.*, vol. 130, pp. 151–181, 1995. 176

[132] H. Byrne and L. Preziosi, "Modelling solid tumour growth using the theory of mixtures.," *Mathematical medicine and biology : a journal of the IMA*, vol. 20, pp. 341–366, 2003. 176

[133] B. Jones and R. G. Dale, "Mathematical models of tumour and normal tissue response," *Acta Oncologica*, vol. 38, pp. 883–893, 1999. 177, 183

[134] G. Powathil, M. Kohandel, S. Sivaloganathan, A. Oza, and M. Milosevic, "Mathematical modeling of brain tumors: effects of radiotherapy and chemotherapy," *Physics in Medicine and Biology*, vol. 52, pp. 3291–3306, 2007. 177, 192, 195, 201, 203

[135] G. S. Stamatakos and D. D. Dionysiou, "Introduction of hypermatrix and operator notation into a discrete mathematics simulation model of malignant tumour response to therapeutic schemes in vivo. Some operator properties," *Cancer Informatics*, vol. 7, pp. 239–251, 2009. 177, 195, 201, 203

[136] M. Lê, H. Delingette, J. Kalpathy-Cramer, E. R. Gerstner, T. Batchelor, J. Unkelbach, and N. Ayache, "Personalized Radiotherapy Planning Based on a Computational Tumor Growth Model," *IEEE Transactions on Medical Imaging*, p. 11, 2016. 177, 203

[137] E. A. Kleibeuker, A. W. Griffioen, H. M. Verheul, B. J. Slotman, and V. L. Thijssen, "Combining angiogenesis inhibition and radiotherapy: A double-edged sword," *Drug Resistance Updates*, vol. 15, no. 3, pp. 173 – 182, 2012. 178, 179, 205

[138] F. Winkler, S. V. Kozin, R. T. Tong, S.-S. Chae, M. F. Booth, I. Garkavtsev, L. Xu, D. J. Hicklin, D. Fukumura, E. di Tomaso, L. L. Munn, and R. K. Jain, "Kinetics of vascular normalization by vegfr2 blockade governs brain tumor response to radiation," *Cancer Cell*, vol. 6, pp. 553–563, 2004. 179

[139] W. S. Kamoun, C. D. Ley, C. T. Farrar, A. M. Duyverman, J. Lahdenranta, D. A. Lacorre, and R. K. Jain, "Edema control by cediranib, a vascular endothelial growth factor receptortargeted kinase inhibitor, prolongs survival despite persistent brain tumor growth in mice," *Journal of Clinical Oncology*, vol. 27, p. 25422552, 2009. 179

[140] D. J. Brenner, "The linear-quadratic model is an appropriate methodology for determining iso-effective doses at large doses per fraction," *Seminars in radiation oncology*, vol. 18, pp. 234–239, 2008. 181

[141] T. Roque, Z. Kalkan, and W. Zylka, "Biological effectiveness in hypofractionation: Modeling tumor survival probability for large doses with a stochastic cell-cycle model," *Biomedizinische Technik. Biomedical engineering*, vol. 57 Suppl 1, pp. 202–205, Jan. 2012. 182, 220

[142] M. Joiner and A. v. d. Kogel, *Basic clinical radiobiology*. London : Hodder Arnold, 2009. 183, 184, 204

[143] T. J. Whelan, K. Do-Hoon, and J. Sussman, "Clinical experience using hypofractionated radiation schedules in breast cancer," *Seminars in radiation oncology*, vol. 18, pp. 257–284, 2008. 184, 204

[144] N. Ferrara and R. S. Kerbel, "Angiogenesis as a therapeutic target," *Nature*, vol. 438, pp. 967 – 94, 2005. 184

[145] "European medicine agency, scientific discussion." `http://www.ema.europa.eu/docs/en_GB/document_library/EPAR_-_Scientific_`

Discussion/human/000582/WC500029262.pdf. Accessed: 2018-04-06. 185, 187

[146] L. M. Berezhkovskiy, "Determination of volume of distribution at steady state with complete consideration of the kinetics of protein and tissue binding in linear pharmacokinetics," *Journal of Pharmaceutical Sciences*, vol. 93, pp. 364–374, 2004. 187

[147] X. Wu, F. Nekka, and J. Li, "Steady-state volume of distribution of two-compartment models with simultaneous linear and saturated elimination," *Journal of Pharmacokinetics and Pharmacodynamics*, vol. 43, no. 4, pp. 447–459, 2016. 187

[148] G. Borasi and A. Nahum, "Modelling the radiotherapy effect in the reaction-diffusion equation," *Physica Medica*, vol. 32, no. 9, pp. 1175 – 1179, 2016. 189, 190, 205

[149] A. Dasu and J. Denekamp, "New insights into factors influencing the clinically relevant oxygen enhancement ratio," *Radiotherapy and Oncology*, vol. 46, pp. 269–277, 1997. 190

[150] X. S. Qi, J. White, and A. Li, "Is alpha/beta for breast cancer really low?," *Radiotherapy and Oncology*, vol. 100, pp. 282–288, 2011. 192, 195, 201

[151] L. Geng, E. Donnelly, G. P. McMahon, C. Lin, E. Sierra-Rivera, H. Oshinka, and D. E. Hallahan, "Inhibition of vascular endothelial growth factor receptor signaling leads to reversal of tumor resistance to radiotherapy," *Cancer Research*, vol. 61, pp. 2413 – 2419, 2001. 205

[152] T. Roque, B. W. Papiez, V. Kersemans, S. Smart, D. Allen, M. Chappell, and J. A. Schnabel, "Tumor growth estimation via registration of dce-mri

derived tumor specific descriptors," in *2016 IEEE Conference on Computer Vision and Pattern Recognition Workshops (CVPRW)*, pp. 507–515, June 2016. 211

[153] R. K. Vartanian and N. Weidner, "Correlation of intratumoral endothelial cell proliferation with microvessel density (tumor angiogenesis) and tumor cell proliferation in breast carcinoma," *American Journal of Pathology*, vol. 144, pp. 1189–1194, 1994. 212

[154] H. C. Roberts, T. P. Roberts, A. W. Bollen, S. Ley, R. C. Brasch, and W. P. Dillon, "Correlation of microvascular permeability derived from dynamic contrast-enhanced mr imaging with histologic grade and tumor labeling index: A study in human brain tumors," *Academic Radiology*, vol. 8, no. 5, pp. 384 – 391, 2001. 212

[155] C. K. Koch, "Measurement of absolute oxygen levels in cells and tissues using oxygen sensors and 2-nitroimidazole ef5," *Methods in Enzymology*, vol. 352, pp. 3–31, 2002. 213

[156] L. C. Crowley, B. J. Marfell, A. P. Scott, and N. J. Waterhouse, "Quantitation of apoptosis and necrosis by annexin v binding, propidium iodide uptake, and flow cytometry," *Cold Spring Harbor Protocols*, vol. 2016, no. 11, p. pdb.prot087288, 2016. 213

[157] D. J. Arndt-Jovin and T. M. Jovin, "Analysis and sorting of living cells according to deoxyribonucleic acid content.," *Journal of Histochemistry & Cytochemistry*, vol. 25, no. 7, pp. 585–589, 1977. 213

[158] Z. Xu, X.-F. Li, H. Zou, X. Sun, and B. Shen, "18f-fluoromisonidazole in tumor hypoxia imaging," *Oncotarget*, vol. 53, no. 8, p. 9496994979., 2017. 213

[159] S. Metz, H. E. Daldrup-Link, T. Richter, C. Rth, W. Ebert, M. Settles, E. J. Rummeny, T. M. Link, and M. Piert, "Detection and quantification of breast tumor necrosis with mr imaging: Value of the necrosis-avid contrast agent gadophrin-," *Academic Radiology*, vol. 10, no. 5, pp. 484 – 490, 2003. 213

[160] L. Jug, B.-T. Doan, J. Seguin, M. Albuquerque, B. Larrat, N. Mignet, G. G. Chabot, D. Scherman, V. Paradis, V. Vilgrain, B. E. Van Beers, and R. Sinkus, "Colon tumor growth and antivascular treatment in mice: Complementary assessment with mr elastography and diffusion-weighted mr imaging," *Radiology*, vol. 264, no. 2, pp. 436–444, 2012. 214

[161] M. P. Aryal, T. N. Nagaraja, R. Elmgghribi, K. a. Keenan, S. Panda, G. Cabral, S. L. Brown, and J. R. Ewing, "Dynamic contrast enhanced mri estimate of tumor interstitial fluid pressure in solid brain tumors," in *Proc. Intl. Soc. Magn. Reson. Med 23*, p. 669, 2015. 215

[162] V. Estrella, T. Chen, M. Lloyd, J. Wojtkowiak, H. H. Cornnell, A. Ibrahim-Hashim, K. Bailey, Y. Balagurunathan, J. M. Rothberg, B. F. Sloane, J. Johnson, R. A. Gatenby, and R. J. Gillies, "Acidity generated by the tumor microenvironment drives local invasion," *Cancer Research*, vol. 73, no. 5, pp. 1524–1535, 2013. 215

[163] N. Raghunand, M. I. Altbach, R. van Sluis, B. Baggett, C. W. Taylor, Z. M. Bhujwalla, and R. J. Gillies, "Plasmalemmal ph-gradients in drug-sensitive and drug-resistant mcf-7 human breast carcinoma xenografts measured by 31p magnetic resonance spectroscopy," *Biochemical Pharmacology*, vol. 57, no. 3, pp. 309 – 312, 1999. 216

[164] T. Takei, Y. Kuge, S. Zhao, M. Sato, H. W. Strauss, F. G. Blankenberg,

J. F. Tait, and N. Tamaki, "Time course of apoptotic tumor response after a single dose of chemotherapy: comparison with 99mtc-annexin v uptake and histologic findings in an experimental model," *Journal of Nuclear Medicine*, vol. 45, pp. 2083–2087, 2004. 217

[165] V. Adhikarla and R. Jeraj, "An imaging-based stochastic model for simulation of tumour vasculature," *Physics in medicine and biology*, vol. 57, pp. 6103–24, Oct. 2012. 217

[166] D. J. Carlson, P. J. Keall, B. W. Loo, Z. Chen, and J. M. Brown, "Hypofractionation results in reduced tumor cell kill compared to conventional fractionation for tumors with regions of hypoxia.," *International journal of radiation oncology, biology, physics*, vol. 79, pp. 1188–95, 2011. 218

[167] T. Gupta and C. A. Narayan, "Image-guided radiation therapy: Physicians perspectives," *Journal of Medical Physics*, vol. 37, p. 174182, 2012. 220

[168] M. Astrahan, "Some implications of linear-quadratic-linear radiation dose-response with regard to hypofractionation," *Medical physics*, vol. 35, pp. 4161– 4172, September 2008. 220